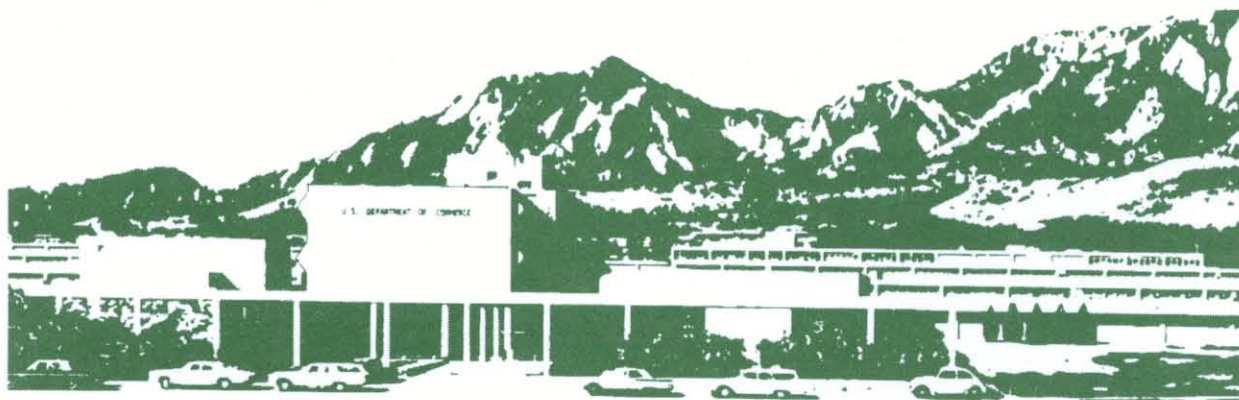


NIST Special Publication 1024

Technical Digest: Symposium on Optical Fiber Measurements, 2004

Sponsored by the National Institute of Standards and Technology
in cooperation with the IEEE Lasers and Electro-Optics Society
and the Optical Society of America



NIST Special Publication 1024

Technical Digest: Symposium on Optical Fiber Measurements, 2002



Digest of a symposium sponsored by the
National Institute of Standards and Technology
in cooperation with the
IEEE Lasers and Electro-Optical Society
and the Optical Society of America

September 28-30, 2004
National Institute of Standards and Technology
Boulder, Colorado 80305

Edited by
P. A. Williams
G. W. Day

September 2004



U.S. Department of Commerce
Donald L. Evans, Secretary

Technology Administration
Phillip J. Bond, Under Secretary for Technology

National Institute of Standards and Technology
Arden L. Bement, Jr., Director

National Institute of Standards and Technology Special Publication 1024
Natl. Inst. Stand. Technol. Spec. Publ. 1024, pages (September 2004)
CODEN: NSPUE2

U.S. GOVERNMENT PRINTING OFFICE
WASHINGTON: 2004

For sale by the Superintendent of Documents, U.S. Government Printing Office
Internet: bookstore.gpo.gov Phone: (202) 512-1800 Fax: (202) 512-2250
Mail: Stop SSOP, Washington, DC 20402-0001

PREFACE



Welcome to SOFM 2004, the quarter-of-a-century mark for this meeting that has taken place every other year since 1980. Since that time, SOFM has provided this glimpse of what's going on in the area of measurements relating to optoelectronics. This year, we again see a broad range of topics including wavelength metrology, nonlinear measurements, OTDR improvements, fiber index characterization, fiber Bragg grating measurement techniques, and PMD.

This year, we also see an unusually strong international participation with two thirds of the papers originating outside the U.S. We have also added some variety to the Symposium by organizing workshop on the "last mile" fiber solutions and related metrology.

Please enjoy your visit, the technology, the mountains and the people.

Happy reading,

Paul Williams
Gordon Day
Boulder, Colorado
September 2004

Except where attributed to NIST authors, the content of individual sections of this volume has not been reviewed or edited by the National Institute of Standards and Technology. NIST therefore accepts no responsibility for comments or recommendations therein. The mention of trade names in this volume by no means implies any endorsement or recommendation by the National Institute of Standards and Technology.

SYMPOSIUM COMMITTEE



G.W. Day, *NIST*, General Chair

P.A. Williams, *NIST*, Program Chair

M. Artiglia, *Pirelli*

A. Barlow, *PerkinElmer*

T.J. Drapela, *NIST*

S.C. Fleming, *Sydney University*

D. Franzen, *NIST*

N. Gisin, *University of Geneva*

M. Hackert, *U.S. Navy*

T.A. Hanson, *Corning*

D. Humphreys, *NPL*

J. Jackel, *Telcordia*

J. Jones, *Heriot-Watt University*

W. Reed, *OFS*

K.B. Rochford, *NIST*

G. W. Schinn, *EXFO*

C. Shaar, *Photon Kinetics*

K. Takada, *Gunma University*

CONTENTS

PREFACE	iii
SYMPOSIUM COMMITTEE	iv
The Era of Coherent Optical Frequency References (invited)	
L. Hollberg, C.W. Oates, S. Diddams, G. Wilpers, A. Bartels, C. Hoyt, Z. Barber, NIST	1
Generation of Standard Frequency References over the C and L Bands Using an Acetylene Cell and Four-Wave Mixing Enhanced by Raman Amplification	
A. Carrasco-Sanz, S. Martín-López, M. González- Herraéz, P. Corredera, M.L. Hernanz, Instituto de Física Aplicada (CSIC)	7
Infrared Frequency Comb for Frequency Metrology Based on a Tunable Repetition Rate Fiber Laser	
B.R. Washburn, S.A. Diddams, N.R. Newbury, NIST; J.W. Nicholson, K. Feder, P.S. Westbrook, OFS Laboratories; C.G. Jørgenson, OFS Fitel	11
Accuracy Limits for Simple Molecular Absorption Based Wavelength References	
W.C. Swann, S.L. Gilbert, NIST	15
Fast-Fourier-Transformation De-convolutions for a Fabry-Perot Filter Based OSA: Demonstration of 15.0 dB Increase of Optical-Rejection-Ratio at ± 25.0 GHz from Peak	
K.-C. Zeng, Sunrise Telecom, Inc.	19
Stimulated Brillouin Scattering: An Overview of Measurements, System Impairments, and Applications (invited)	
A.B. Ruffin, Corning, Inc.	23
Coherence Effect on the Measurement of Optical Fiber Nonlinear Coefficient in Continuous-Wave Dual Frequency Method	
S.K. Kim, H.S. Moon, R.K. Kim, J.-C. Seo, Korea Research Institute of Standards and Science	29
ITU-T Round Robin Measurement for Nonlinear Coefficient (n_2/A_{eff}) of Various Single Mode Optical Fibers	
Y. Namihiro, University of the Ryukyus	33
Broadband Continuous-Wave Source Based on Fiber Nonlinearity	
M. González-Herráez, S. Martín-López, P. Corredera, M.L. Hernanz, A. Carrasco, Instituto de Física Aplicada (CSIC)	37
Characterization of Photonic Crystal Structures (invited)	
J. O'Brien, J.-R. Cao, A. Stapleton, M.-H. Shih, W. Kuang, W.J. Kim, Z.-J. Wei, S.-J. Choi, P.D. Dapkus, University of Southern California	41
Ultrasensitive Measurement Method for Refractive Index Difference between Two Wavelengths	
M. Legré, M. Wegmuller, N. Gisin, University of Geneva	47
Tomographic Reconstruction for Arbitrary Refractive Index Distribution of Optical Fibre Preforms	
Y.C. Zhao, S. Fleming, K. Lyytikainen, M.A. van Eijkelenborg, Australian Photonics CRC, Optical Fibre Technology Centre, University of Sydney	51

Micro-Analytical Techniques for Imaging Erbium Doped Optical Fibers F. Sidirolou ¹ , S.T. Huntington ¹ , R. Stern ² , G. Baxter ³ , A. Roberts ¹ , ¹ University of Melbourne; ² Victoria University; ³ University of Western Australia	55
Measuring Electro-Optic Coefficients of Poled Polymers Using Fiber-Optic Mach-Zehnder Interferometer Y.-P. Wang, J.-P. Chen, X.-W. Li, J.-X. Hong, X.-H. Zhang, J.-H. Zhou, A.-L. Ye, State Key Laboratory on Local Fiber-Optic Communication Networks and Advanced Optical Communication Systems, Shanghai Jiao Tong University	59
Concepts and Techniques for Short Optical Pulse Characterization (invited) C. Dorrer, Bell Laboratories-Lucent Technologies	63
High Spatial Resolution PON Measurement Using an OTDR Enhanced with a Dead-Zone-Free Signal Analysis Method N. Araki, H. Izumita, Y. Koshikiya, M. Nakamura, NTT Corporation	69
A Bi-Directional Optical Time Domain Reflectometry Technique Optimised for Short LAN Fibers N.D. Channon, Megger Limited; A.G. Hallam, Halcyon Optical Services	73
An Improved Method for the Distributed Measurement of the Chromatic Dispersion of an Optical Fiber Using a Wavelength Tunable OTDR S.G. Murdoch, University of Auckland; D.A. Svendsen, Photon Kinetics (UK)	77
Inter-Comparison of Chromatic Dispersion Reference Fibre Measurements: Results of Euromet Project 666 J. Morel, Swiss Federal Office of Metrology and Accreditation (METAS)	81
Generalized Interferometric Method for Accurate Match with DGD Measurements and Comparison against Standard References (invited) N. Cyr, EXFO Electrical Optical Engineering	85
Study of Variation of the Laplacian Parameter of DGD Time Derivative with Fiber Length Using Measured DGD Data P.K. Kondamuri, C. Allen, University of Kansas; D.L. Richards, Sprint Corporation	91
The Long-Term Distribution of Differential Group Delay in a Recirculating Loop H. Xu ¹ , B.S. Marks ^{1,2} , J. Zweck ³ , L. Yan ¹ , C.R. Menyuk ¹ , G.M. Carter ^{1,2} , ¹ Department of Computer Science and Electrical Engineering, University of Maryland Baltimore County; ² Laboratory for Physical Sciences; ³ Department of Mathematics and Statistics, University of Maryland, Baltimore County	95
Experience in Reflectometry and PMD Measurements for WAN in Costa Rica L.D. Marin-Naranjo, University of Costa Rica, Photonics and Laser Laboratory LAFTLA	99
Locating High PMD Sections of an Overhead Cable Using Polarization-OTDR A.B. Connibear ¹ , F.J. Visser ² , F. Audet ³ , R. Salmi ³ , A.W.R. Leitch ¹ , ¹ University of Port Elizabeth; ² Telkom S.A.; ³ EXFO	103
Effects of Polarization-Mode Dispersion on Four-Wave Mixing Efficiency M. González- Herráez, J. Pelayo, P. Corredera, M.L. Hernanz, J.A. Méndez, S. Martín-Lopez, A. Carrasco, Instituto de Física Aplicada (CSIC)	107

Calibration of a Polarisation Rotator, to Launch Defined Polarisation States D. Ives, NPL	111
Extraction of Orthogonal Incident State of Polarization Spectra Using Mueller Matrix Approach É. Desfonds, K. Pimenov, MetroPhotonics; T.J. Hall, University of Ottawa	115
Detailed Polarization Properties Comparison for Three Completely Different Species of Highly Birefringent Fibers M. Wegmuller, M. Legré, N. Gisin, University of Geneva, K.P. Hansen, T.P. Hansen, C. Jakobsen, Crystal Fibre A/S	119
Determination of the Phase and Group Birefringence of Single-Mode Optical Fibers Based on the Twist M. Legré, M. Wegmuller, N. Gisin, University of Geneva	123
An Improved Lyot Fibre Depolariser M. Matar ¹ , I.M. Bassett ¹ , B. Gordon ² , J.H. Haywood ¹ , A. Michie ¹ , ¹ Australian Photonics CRC, Optical Fibre Technology Centre; ² Cochlear, Ltd	127
Measurement Issues in Microwave Photonics (invited) J. Capmany, D. Pastor, B. Ortega, S. Sales, Universidad Politécnica de Valencia	131
Applications of Metrology for Optical Coherence Tomography (invited) T.E. Milner, N.J. Kemp, C.G. Rylander, D.P. Davé, University of Texas at Austin	137
High-Power Nonlinearity of Optical Fiber Power Meters I. Vayshenker ¹ , R. Swafford ² , S. Yang ¹ , ¹ NIST; ² OZ Optics	145
Characterization of a High Power and High Accuracy Integrating Sphere Radiometer for Fiber Applications P. Corredera, M.L. Hernanz, M. González-Herráez, S. Martín-López, A. Carrasco-Sanz, Instituto de Física Aplicada (CSIC)	149
Insertion Loss Measurement of Low Loss Fiber Optic Splices L. Wesson, Aurora; P. Arrowsmith, R. Suurmann, Celestica; D. Gignac, Nortel Networks; S. Pradham, Sanmina-SCI; J. Garren, Solectron; T. Watanabe, Sumitomo Electric; E. Mies, Vytran	153
Quantum Cryptography in Optical Networks and Supporting Metrology (invited) R.J. Runser ¹ , P. Toliver ¹ , S. McNown ² , T.E. Chapuran ¹ , M.S. Goodman ¹ , J. Jackel ¹ , R.J. Hughes ³ , J.E. Nordholt ³ , C.G. Peterson ³ , K. Tyagi ³ , P. Hiskett ³ , K. McCabe ³ , ¹ Telcordia Technologies; ² Laboratory for Telecommunication Science; ³ Los Alamos National Laboratory	159
Measurement of Phase Diagrams of Optical Communication Signals Using Sampled Coherent Detection M.G. Taylor, University College London	163
Demonstration of Birefringence in a Bulk Semiconductor Optical Amplifier and Its Application to All-Optical Wavelength Conversion L.Q. Guo, M.J. Connelly, University of Limerick	167
Effects of Optical Coherence and Polarization in Optical ANA D.A. Humphreys, NPL	171

Characterization of Multimode Fiber for 10+ Gb/s Operation by Predicting ISI from Bandwidth Measurement Data J.S. Abbott, Corning	175
Fibre Sensing: Specifying Components and Systems (invited) B. Culshaw, University of Strathclyde; W. Habel, Federal Institute for Materials Research and Testing (BAM)	179
Accurate Index Profile Measurements for Fiber Bragg Gratings and Sensor Application X. Chapeleau ¹ , D. Leduc ¹ , P. Casari ² , Y. Quiquempois ³ , J. Lebon ² , F. Lopez ³ , C. Lupi ¹ , C. Boisrobert ¹ , ¹ Université de Nantes; ² Institut de Recherche en Génie Civil et Mécanique (GéM); ³ Université des Sciences et Technologies de Lille	191
Analysis of a Fiber Bragg Grating Writing Process Using Low-Coherence Interferometry and Layer-Peeling R.J. Espejo, M. Svalgaard, S.D. Dyer, NIST	195
CO ₂ -Laser Induced LPFG's Torsion Characteristics Depending on the Length of the Twisted Fiber Y.P. Wang, J.-P. Chen, State Key Laboratory on Local Fiber-Optic Communication Networks and Advanced Optical Communication Systems; Y.-J. Rao, Department of Optoelectronic Engineering, Chongqing University	199
AUTHORS INDEX	203
APPENDIX I - PROGRAM	205

The Era of Coherent Optical Frequency References

L. Hollberg, C.W Oates, S. Diddams, G. Wilpers, A. Bartels, C. Hoyt, and Z. Barber
NIST, Boulder, CO

(Contribution of NIST, not subject to copyright)

In the past four years have shown a dramatic improvement in the performance of optical frequency references and in the methods by which they are calibrated and utilized. These revolutionary changes result from better stabilized lasers that probe narrow-linewidth transitions in laser-cooled atoms and ions, and from the development of a convenient method for synthesizing, measuring and distributing optical frequencies based on mode-locked lasers.

Physical Wavelength References

Frequency stabilized lasers are usually controlled by some type of physical artifact that has good mechanical stability and that uses optical interference to provide wavelength discrimination and selectivity. High spectral resolution is made possible with high quality optics and optical interference. An optical interferometer might consist of optical gratings, solid etalons, Fizeau or Michelson interferometers, or Fabry-Perot cavities. The very best of these instruments can provide outstanding stability on short time scales and reasonable accuracy (10^{-4} to 10^{-9} fractionally). For short time intervals and in highly controlled environments Fabry Perot cavities provide very high spectral resolution ($\frac{\Delta\lambda}{\lambda} \approx 10^{-12}$) and the very best short-term stability (eg. $\frac{\Delta\lambda}{\lambda} = 10^{-15}$ for times $\tau < 20$ s).ⁱ The geometrical stability of even the best physical artifacts is limited by material properties, environmental effects and history. If the interferometer path-length is not entirely evacuated the temperature dependence of the refractive index combined with temperature fluctuations can dominate the wavelength instability (e.g. $10^{-5}/\text{K}$ for quartz). In addition, even the best physical artifacts show dimensional changes with time due to material aging and creep. This might be on the order of $10^{-7}/\text{yr}$ for good materials, and depends strongly dependant on environmental history. For transportable instruments it seems quite challenging to achieve better than ~ 100 MHz frequency uncertainty in the visible (~ 500 THz) even using high quality vacuum-spaced temperature controlled Fabry-Perot cavities. When higher accuracy and better long-term stability are required, atomic and molecular transitions provide a good solution.

Quantum Frequency References

Atomic and molecular energy levels provide discrete frequency references determined by quantum mechanical interactions ($E_i - E_j = h\nu_{ij}$). These can serve as high accuracy frequency markers to control laser frequencies. A fundamental difference between physical artifacts and quantum systems for frequency control is that physical references act as wavelength references while atomic transitions are frequency references. Interferometers depend directly on geometrical factors (optical path lengths, angles, index of refraction, etc.) and discriminate wavelengths by multi-path interference, whereas atomic/molecular transitions depend on quantum mechanical energy differences and hence optical frequency. The physical parameters of artifacts are difficult to control

with high accuracy and for long periods of time. Quantum references provide much better long-term stability and accuracy, but have some disadvantages that include: signals that are generally weaker than those achieved with physical references, quantum transitions are usually not conveniently distributed in wavelength, and the detection of atomic states is generally more complex and less robust than physical references. They can however provide an absolute frequency reference which is known (with varying degrees of accuracy) in terms of the fundamental constants and SI units, in particular the Cs atomic frequency (9 192 631 770 Hz) that defines the SI “second”. Rough estimates of the performance achieved with common types of optical wavelength/frequency references are provided in the figure 1.


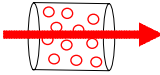
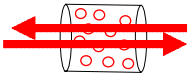


	Line Q	Potential Reproducibility
 Optical cavity	10^7 - 10^{13}	100 kHz-100 MHz
 Vapor cell	10^7 - 10^9	5 kHz-10 MHz
 Vapor cell	10^7 - 10^9	5 kHz-10 MHz
 Atomic beam	10^{10} - 10^{11}	< 100 Hz
 Atom trap	10^{12} - 10^{15}	< 1 Hz

Figure 1. Approximate frequency reproducibility attained with different types of optical frequency references. The second column gives the range of spectral line Q’s that is achieved, where $Q = (\text{center frequency})/(\text{linewidth})$. The third column gives approximate frequency reproducibility assuming a center frequency near 500 THz. The wide range of values shown here results from the fact that the performance depends strongly on the actual system and environmental conditions. Two different types of vapor cell systems are illustrated. The single laser beam system represents Doppler broadened transitions, while the two-beam system corresponds to Doppler-free methods, such as saturated absorption or two-photon transitions. The atom/ion trap example is for laser-cooled atoms/ions with near zero thermal velocity.

Most of the atomic/molecular transitions that are commonly used as optical frequency references have been reviewed elsewhere, so Table 1 lists only a few representative examples that illustrate the distribution in wavelength and the performance that has been demonstrated. Some research groups are studying optical atomic frequency standards for their potential in providing the highest possible frequency stability and accuracy for the next generation of atomic clocks, while other groups are developing simpler compact

optical frequency references with more modest performance that can be used as calibration references for field applications such as WDM systems.^{ii,iii,iv,v,vi,vii,viii ix,x} Some representative examples of quantum transitions currently being used for optical frequency references are provided in Table 1.

<u>Atom</u>	<u>λ (nm)</u>	<u>Linewidth (kHz)</u>
Ca	657	0.4
Sr	689	7
Mg	457	0.4
Cs	852 & 891	5000
Rb	780 & 795	5000
Rb	778	300
I ₂	500-700	50-5000
H	243	0.5
C ₂ H ₂	1530-1560	<1000
CH ₄	3392	3
Hg ⁺	281	0.006
Yb ⁺	435	0.010
Sr ⁺	674	0.050

Table 1. Some representative optical frequency references. The first column lists the atom/ion/molecule, the second column gives the wavelength of the reference transition(s), and the third column provides an approximate spectral linewidth observed experimentally on that transition. More details can be found in the references.

Optical Frequency Combs

Modern mode-locked lasers can now be actively stabilized to produce a fixed comb of optical frequencies which can be used to translate optical frequencies coherently from one spectral region to another, ranging from the ultraviolet to the microwave region. The basic concept of performing optical frequency synthesis using mode-locked lasers is based on ideas from T. Hänsch and others.^{xi,xii} Today, ultra-fast mode-locked lasers have repetition rates of 50-1000 MHz and produce optical pulses with pulse widths in the 5 to 100 fs range. This repetitive train of optical pulses, with pulse-width Δt_p and repetition rate f_{rep} , has a Fourier domain spectrum that consists of a comb of optical frequencies separated by f_{rep} and covering a spectral-width of Δf_{opt} as illustrated in figure 2. When appropriately stabilized and viewed in the Fourier domain, the pulse train corresponds to an evenly spaced array of modes (e.g. an “optical frequency comb”) that covers a significant portion of the optical spectrum (~100 THz). The frequency of all the modes can even be determined with accuracy equal to that of the best atomic clocks.

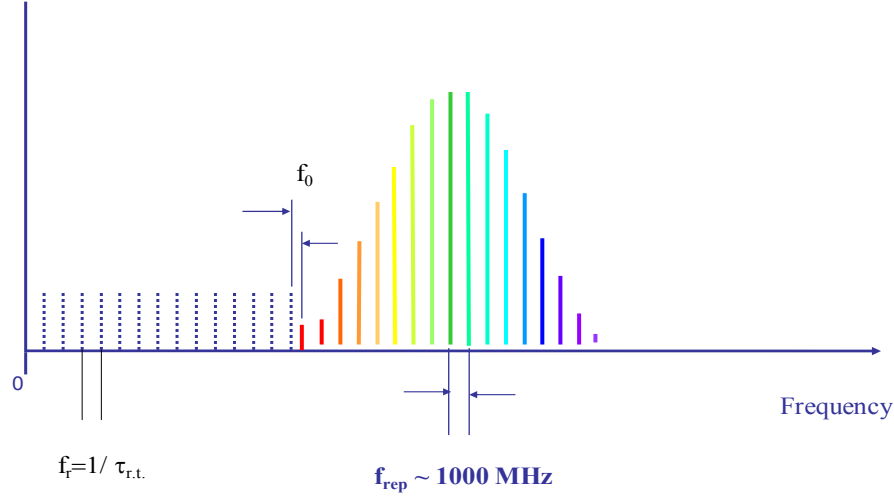


Fig. 2. Schematic representation of an optical frequency comb showing the mode spacing set by the pulse repetition frequency f_{rep} and offset from zero by f_0 when extrapolated to zero frequency. The series of dotted lines represents an imaginary comb of modes that starts at zero frequency and progresses toward higher frequencies with a mode spacing equal to f_{rep} .

The frequency of any arbitrary mode N (an integer) of the optical comb can be written simply as $f_N = Nf_{\text{rep}} + f_0$ where f_0 is an offset frequency of the comb from zero (if it was hypothetically extended all the way back from optical to zero frequency). The repetitive optical pulses, or equivalently their frequency domain comb of modes serve as the key component of the new optical frequency synthesizers. As can be seen in the equation above, there are two free parameters to the comb: the spacing of the comb modes determined by f_{rep} and the offset of the entire comb f_0 . To know the exact optical frequency of all the modes of the comb requires that we determine and control two free parameters. These could be f_{rep} and f_0 (two frequencies in the radio frequency domain), or the frequency of two specific optical modes f_i and f_j (in the optical domain), or f_0 and a specific optical mode f_i . The most powerful approach is the “self reference” method demonstrated in 2000.^{xiii} In that method some low frequency comb modes are frequency doubled and then compared with a some high frequency modes, generating a beatnote that provides a radio frequency output equal to the offset frequency f_0 , thus $2(kf_{\text{rep}} + f_0) - [2kf_{\text{rep}} + f_0] = f_0$, where i is an integer. Table 2 lists some examples of mode-locked laser based optical frequency combs that are being used for optical frequency measurements.

Type of mode-locked laser	f_{rep} (MHz)	Pulse-width (fs)	External broadening	Wavelength range (nm) approx. w/ broadening	Freq. Meas.	Self-Referencing method
Ti:sapphire	80 to 1000	<50	Microstructure fiber	500-1200	Yes	f-2f
Ti:sapphire	1000 and 100	<10	None required	550-1100	Yes	2f-3f and f-2f
Fiber laser	50	50-100	Highly nonlinear fiber and microstructure fiber	800-2200	Yes	f-2f
Cr:Forsterite	430	40	Highly nonlinear fiber	1000-2200	Yes	f-2f
Cr:LiSAF	90	40	Microstructure fiber	550-1100 nm	No	f-2f

Table 2. Some optical frequency combs based on mode-locked lasers that are being used for optical frequency measurement, distribution and control.

Summary

The new tools and methods outlined very briefly enable precise control of the phase and frequency of laser fields. The key ingredients making the advances possible are: stabilized optical frequency combs, highly stabilized continuous-wave lasers, and precision spectroscopy of laser-cooled atoms and ions. Combining these technologies in just four years has led to ~ 1000 times improvement in the performance of optical frequency references. These capabilities represent a new era in optical frequency synthesis, metrology, and coherent optical control. Obviously, there is a direct analogy and correspondence with the well-known coherent techniques now widely used in RF and microwave electronics, and perhaps there will be similar widespread applications in optics in the future. Phase and frequency control methods are improving spectral resolution by many orders of magnitude. For example, it is challenging to get 7 digits of wavelength accuracy by interferometric methods, whereas 15 digits of frequency accuracy has been demonstrated at optical frequencies. In spite of this, we must still recognize that the five most significant digits are still most easily determined interferometrically rather than by the methods of optical frequency metrology. Some combination of the two approaches, interferometry and frequency metrology, seems most widely useful and applicable. Coherent optical methods are not a new idea; they were suggested long ago for numerous applications including optical communication systems, sensing, lidar etc. However, now is the time that these ideas are coming to fruition and becoming an experimental reality. This enables many older ideas and applications, and

opens new frontiers such as optical atomic clocks, timing and synchronization with femtosecond precision, ultra-low phase-noise microwave sources, and, no doubt other applications to come.

References

-
- ⁱ B. C. Young, F. C. Cruz, W. M. Itano, et al., “Visible lasers with subhertz linewidths” *Physical Review Letters* 82, 3799 (1999).
- ⁱⁱ J. L. Hall, “Optical frequency measurement: 40 years of technology revolutions”, *IEEE Journal of Selected Topics in Quantum Electronics* 6, 1136 (2000).
- ⁱⁱⁱ L. Hollberg, C.W. Oates, E.A. Curtis, et al. “Optical Frequency Standards and Measurements, *IEEE J. Quantum Elect.* 37, 1502 (2001).
- ^{iv} J. Ye et al., “Molecular Iodine Clock,” *Phys. Rev. Lett.*, 87, 270801-1 to -4, Dec. 2001
- ^v D. J. E. Knight, “A Tabulation of Absolute Laser-Frequency Measurements,” *Metrologia* 22, 251 (1986).
- ^{vi} A. A. Madej and J. E. Bernard, “Single-Ion Optical Frequency Standards and Measurements of their Absolute Optical Frequency,” in *Frequency Measurements and Control: Advanced Techniques and Future Trends*, edited by A. N. Luiten (Springer-Verlag, Heidelberg, New York, 2001), Vol. *Topics in Applied Physics*, p. 153.
- ^{vii} S.L. Gilbert, W.C. Swann, and T. Dennis, “Wavelength Control and Calibration for Wavelength Division Multiplexed Optical Communication Proc., *IEEE Int'l Frequency Control Symp.*,” Jun 6-8, 2001, Seattle, WA, pp. 122-126 (2001)
- ^{viii} T. Dennis, E.A. Curtis, C.W. Oates, et al., “Wavelength References for 1300 nm Wavelength Division Multiplexing,” *J. Lightwave Technol.* 20, pp. 804-810 (2002)
- ^{ix} J.L. Hall, M. Zhu, and P. Buch “Prospects for Using Laser-Prepared Atomic Fountains for Optical Frequency Standards Applications,” *J. Opt. Soc. Am. B* 6, 2194 (1989).
- ^x T. Quinn “Practical Realization of the Definition of the Metre, including Recommended Radiations of Other Optical Frequency Standards (2001),” *Metrologia* 40, 103 (2003).
- ^{xi} T. Udem, R. Holzwarth, and T. W. Hansch, “Optical frequency metrology,” *Nature* 416, 233 (2002).
- ^{xii} Long-Shen Ma, Zhiyi Bi, A. Bartels, et al., “Optical Frequency Synthesis and Comparison with Uncertainty at the 10^{-19} Level,” *Science* 303, 1843 (2004).
- ^{xiii} D. J. Jones, S. A. Diddams, J. K. Ranka, et al. “Carrier-envelope phase control of femtosecond mode-locked lasers and direct optical frequency synthesis,” *Science* 288, 635 (2000).

GENERATION OF STANDARD FREQUENCY REFERENCES OVER THE C AND L BANDS USING AN ACETYLENE CELL AND FOUR-WAVE MIXING ENHANCED BY RAMAN AMPLIFICATION.

A. Carrasco-Sanz, S. Martín-López, M. González-Herraez, P. Corredera & M. L. Hernanz.
Instituto de Física Aplicada (CSIC), Serrano 144, 28006. MADRID, SPAIN. pcorredera@ifa.cetef.csic.es

Abstract: This paper describes the stabilization of a tuneable laser diode on an acetylene cell, for its use as a frequency standard in the S and C bands. We also describe a method based on Four-Wave Mixing enhanced by Raman to extend the previous frequency reference to the C and L-bands.

Introduction

Wavelength-Division Multiplexing (WDM) demands standard frequency references along the spectral range of the C and L-bands (1510-1625 nm). The stabilization of lasers in the atomic or molecular transitions of some specific gases ($^{12}\text{C}_2\text{H}_2$, $^{13}\text{C}_2\text{H}_2$, HCN, ...) is an interesting method to generate reference frequencies in these transmission bands^(1,2,3,4), but due to the limitation in the number of absorption lines and suitable gas specimens, other procedures are necessary to complete the full frequency range.

This paper describes the process of stabilization of a tuneable laser diode on the absorption lines of an acetylene cell (1512-1542 nm) and the generation of additional reference lines in the 1542-1570 nm range using Four-Wave Mixing enhanced by Raman.

Stabilization of a calibrated reference frequency pattern based in acetylene $^{12}\text{C}_2\text{H}_2$

A 5 cm-long cell manufactured and calibrated by NIST was used as primary standard⁽⁵⁾. This cell has 6.7 kPa of pressure and the uncertainties belonging to the frequencies given by the NIST are around 13 and 77 MHz (0.1 and 0.6 pm).

Fig.1 shows the experimental setup employed in the stabilization of a tuneable laser in this cell simultaneously with the wavelength meter calibration. A tuneable external cavity laser GN Nettest TUNICS Plus with a resolution of 0.01 GHz (0.08 pm) is used. The output of the laser is connected to the acetylene cell and to the wavelength meter which is going to be calibrated, through a 90/10 coupler. The light that passes through the cell is received by an InGaAs detector. The whole system is controlled by a computer which tunes the laser in order to get the deepest absorption. To fix the laser in the deepest absorption, the data collected from the system is fitted to a Lorentzian function which determines the accurate working frequency.

We have studied the error sources that contribute to the uncertainties of the reference frequencies. The main sources of uncertainties are: the uncertainties assigned by NIST, the wavelength resolution of the laser, the pressure and temperature influence, the stability of the locked laser and the precision of the fitting. The stability and fitting errors depend on the absorption depth of the line. Eight lines with different absorptions were studied. The results for 1dB-signal decay in the InGaAs detector are shown in figure 2. The total combined uncertainty ($k=2$) is shown in table 1.

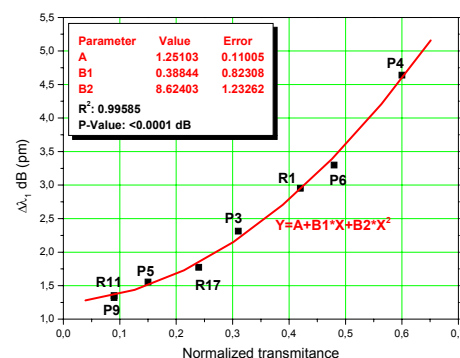


Fig. 2 Wavelength shift obtained for eight lines against normalized absorption for 1 dB signal decay

R Branch						P Branch					
Frequency (GHz)		Uncer. (GHz)	Frequency (GHz)		Uncer. (GHz)	Frequency (GHz)		Uncer. (GHz)	Frequency (GHz)		Uncer. (GHz)
29	198310.823	0.112	14	197522.916	0.102	1	196487.337	0.118	15	195419.304	0.062
28	198263.871	0.111	13	197464.045	0.068	2	196416.006	0.097	16	195337.329	0.097
27	198216.112	0.105	12	197404.403	0.100	3	196343.923	0.050	17	195254.595	0.062
26	198167.572	0.110	11	197343.971	0.055	4	196271.065	0.090	18	195171.119	0.097
25	198118.226	0.109	10	197282.747	0.065	5	196197.441	0.050	19	195086.902	0.062
24	198068.068	0.109	9	197220.749	0.064	6	196123.051	0.090	20	195001.933	0.098
23	198017.124	0.108	8	197157.974	0.063	7	196047.895	0.062	21	194916.214	0.063
22	197965.383	0.107	7	197094.409	0.051	8	195971.976	0.097	22	194829.747	0.092
21	197912.845	0.106	6	197030.056	0.097	9	195895.296	0.062	23	194742.545	0.092
20	197859.513	0.106	5	196964.930	0.061	10	195817.862	0.050	24	194654.599	0.093
19	197805.387	0.073	4	196899.032	0.096	11	195739.663	0.062	25	194565.915	0.100
18	197750.469	0.104	3	196832.351	0.060	12	195660.701	0.097	26	194476.496	0.101
17	197694.761	0.061	2	196764.889	0.096	13	195580.992	0.050	27	194386.348	0.102
16	197638.276	0.103	1	196696.674	0.047	14	195500.524	0.090			
15	197580.989	0.069									

introduction of the Raman pump gives an overall gain of ~20 dB in the converted power all along the band of interest.

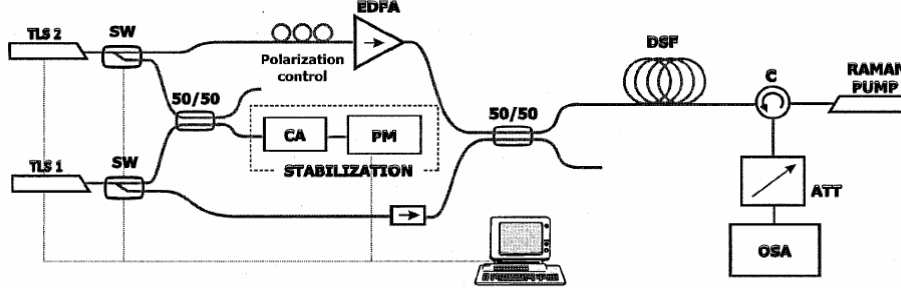


Fig. 3 Experimental setup used

In our experiment, the wavelength and power settings are basically the same than the considered in the theoretical case. The outputs of the two tunable lasers are delivered either to the fiber or to the stabilization loop by the switches SW_1 and SW_2 . Through a control program we can manage to stabilize the two lasers in different absorption lines of the gas cell. In this way it is possible to update the state of the lasers in periods not longer than a few hundreds of milliseconds. To compare with theoretical results ⁽⁶⁾, we lock the wavelength of the laser TLS2 on the P27 absorption line of the acetylene $^{12}C_2H_2$, which is centred in $\lambda_2=1542.2508$ nm. With the TLS1 laser we sweep all the band between 1500 and 1540 nm, while we measure the converted power. The acetylene ($^{12}C_2H_2$) has absorption lines between 1511 and 1540 nm, so we are capable of generating lines with precisely known frequencies covering the whole C band and some part of L band (up to 1574 nm). We can see that, along all this band, the generation using Raman pump has powers higher than -50 dBm. Also notice that in some points close to 1544 nm, the generated power is as high as -5 dBm.

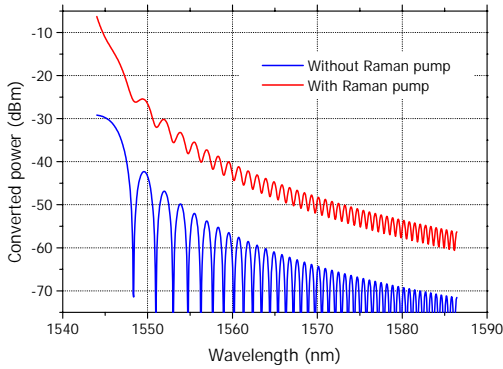


Fig. 4 Theoretical results

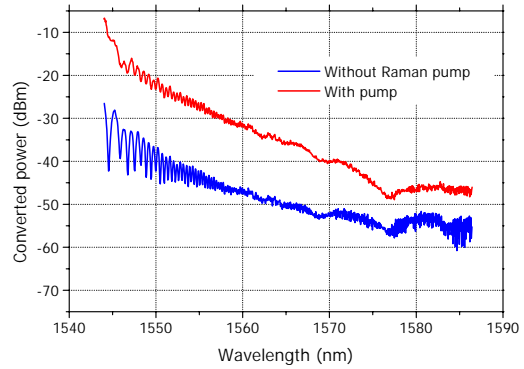


Fig. 5 Experimental results

Application to ITU's frequencies.

With the method proposed in this paper along with the results and the uncertainty values obtained, it is possible to study the calibration of the OCA and OSA in the ITU grid. If we use the acetylene ($^{12}C_2H_2$) absorption cell, we can generate reference frequencies in the region between 1540 and 1574 nm. In table 2 there are some input frequencies (with the corresponding

absorption line), together with the generated frequency and the uncertainty obtained for the new frequency, Δf_{FWM} . A problem might arise in our setup when trying to make this configuration more efficient. Due to the four-wave mixing process, the line width of the generated wave is several times bigger than the original waves. In the present configuration of the experiment, no issue has been detected concerning the line width of the generated wave, that is, the line width of the generated wave remains negligible respecting to the stabilization uncertainty. However, as the frequency conversion process is more efficient, the line width of the four-wave mixing grows accordingly. For higher conversion efficiencies, a trade off would probably be established between the conversion efficiency and the uncertainty in the generated wave.

Table 2

f_1 (GHz)	f_2 (GHz)	f_{FWM} (GHz)	f_{ITU} (GHz)	$ f_{\text{FWM}} - f_{\text{ITU}} $ (MHz)	Δf_1 (GHz)	Δf_2 (GHz)	Δf_{FWM} (GHz)
197522,92 (R18)	194386.35 (P27)	191249,78	191250	220	0,10	0,10	0,141
194565,91 (R15)	197580.99 (P25)	191550,83	191550	830	0,10	0,10	0,141
197282,75 (R10)	197580.99 (P25)	191849,07	191850	930	0,06	0,10	0,117
196832,35 (R3)	197580.99 (P25)	192299,47	192300	530	0,06	0,10	0,117
195001,93 (R12)	197404.40 (P20)	192599,46	197400	540	0,10	0,10	0,141
196123,05 (P6)	194386.35 (P27)	192649,65	192650	350	0,09	0,10	0,135
195971,98 (P8)	194386.35 (P27)	192800,72	192800	720	0,10	0,10	0,141
195580,99 (P13)	197580.99 (P25)	193550,83	193550	830	0,05	0,10	0,112

Conclusions

We have described a method to stabilize a tuneable laser based on the absorption lines of the acetylene $^{12}\text{C}_2\text{H}_2$. We have demonstrated that it is possible to generate new reference frequencies from another one, by means of fiber Raman-enhanced four-wave mixing. We have shown that our configuration is extremely efficient for the generation of new references over a broad range of wavelengths. The uncertainty of the new frequency is basically comparable to the uncertainty in the stabilization of the original four-wave mixing pump waves. A possible application of this method might be used in the calibration of wavelength meters, optical spectrum analyzers and optical channels analyzers with an uncertainty of less than 120 MHz (1 pm).

Acknowledgements

This work was supported by Spanish Commision Interministerial de Ciencia y Tecnologia, projects TIC2000-02005&TIC2003-01867 and by Comunidad Autonoma de Madrid through project 07T/0041/2003.

References

- 1) W.C. Swann and S. L. Gilbert “Pressure-produced shift and broadening of 1510-1540-nm acetylene wavelength calibration lines” J. Opt. Soc. Am. B, 17, 1263-1270 (2000).
- 2) K. Nakagawa, M. de Labachellerie. Y. Awaji and M. Kourogi “Accurate optical frequency atlas of the 1.5 μm bands of acetylene” J. Opt. Soc. Am. B, 13, 2708-2714 (1996).
- 3) M. de Labachellerie, K. Nakagawa and M. Othsu “Ultrannarrow $^{13}\text{C}_2\text{H}_2$ saturated-absorption lines at 1.5 μm ” Opt. Lett. 19, 840-842 (1994).
- 4) Y. Awaji, M. de Labachellerie, M. Othsu, H. Sasada “Optical frequency measurement of the $\text{H}^{12}\text{C}^{14}\text{N}$ Lamb-dip-stabilized 1.5 μm diode laser” Opt. Lett. 20, 2024-2026 (1995).
- 5) S. L. Gilbert and W. C. Swam, “Standard Reference Material: Acetylene $^{12}\text{C}_2\text{H}_2$ Absorption Reference for 1510 nm to 1540 nm Wavelength Calibration—SRM 2517a,” NIST Spec. Publ. **260-133** _National Institute of Standards and Technology, Gaithersburg, Md., 2001.
- 6) S. Martín López, M. González Herráez, P. Corredera, M. L. Hernanz and A. Corróns “Reference frequency generation using Raman-enhanced four-photon mixing” App.Opt.. 43 3185-3190 (2004).

Infrared frequency comb for frequency metrology based on a tunable repetition rate fiber laser

B. R. Washburn, S. A. Diddams, and N. R. Newbury

*National Institute of Standards and Technology, 325 Broadway, Boulder, CO 80305
email: brianw@boulder.nist.gov, phone: 303-497-4447, fax: 303-497-3387*

J. W. Nicholson, K. Feder, and P. S. Westbrook

OFS Laboratories, 700 Mountain Avenue, Murray Hill, New Jersey 07974

C. G. Jørgensen

OFS Fitel Denmark I/S, Priorparken 680, 2605 Brøndby, Denmark

Abstract

A phase-locked, all-fiber supercontinuum source based on an ultrashort fiber ring laser with a tunable repetition rate is presented. The supercontinuum output is composed of a frequency comb with a spacing set by the laser repetition rate and an offset frequency determined by the carrier-envelope offset frequency. The laser repetition rate can be scanned over 400 kHz while the offset frequency remains phase-locked to a stable RF source.

Introduction

A phase-locked, all-fiber supercontinuum source based on an ultrashort fiber laser has been developed for precision IR frequency metrology [1]. This source generates an octave-spanning supercontinuum [2] that is used to detect the carrier envelope offset (CEO) beat frequency [3-5]. The phase-locked supercontinuum exhibits narrow comb linewidths, which is an attractive feature for precision metrology of optical frequencies [6,7].

We have recently developed a second, all-fiber supercontinuum source based on an ultrashort fiber ring laser [8] with a tunable repetition rate. The compact design of the fiber laser allows us to easily change its repetition rate using a free-space delay line. The repetition rate can be scanned over a 400 kHz range while the laser remains mode-locked *and* the CEO beat frequency remains phase-locked to a stable RF source. The attractive features of the tunable repetition rate supercontinuum source are that it can be used to match the repetition rate of another pulsed source, it can be used for precision metrology without a wavelength meter [9], and it can be used to precisely scan the frequency of a cw laser locked to the comb. If a 1500 nm cw laser is locked to a tooth of the supercontinuum frequency comb, a change in repetition rate of 400 kHz would correspond to a 1.5 THz change in optical frequency of the cw laser.

Experimental Measurements

Figure 1 depicts the supercontinuum source, which consists of an additive pulse mode-locked erbium fiber ring laser, an erbium-doped fiber amplifier (EDFA), and a length of UV exposed dispersion-flattened, highly nonlinear, dispersion-shifted fiber (HNLF) [10]. The additive-pulse mode-locked erbium fiber ring laser was operated in soliton mode, producing ultrashort pulses with 20 nm spectral bandwidth. A fiber-coupled free-space delay line in the fiber laser cavity allowed the repetition rate to be changed from 49.32 MHz to 50.14 MHz. The pulses from the laser were amplified and compressed to less than 100 fs in the EDFA before being injected into the UV exposed HNLF. The HNLF uses a combination of Ge and F dopants, in the unexposed fiber, to produce a nonlinear coefficient of $\gamma \sim 10.6 \text{ W}^{-1} \text{ km}^{-1}$, a dispersion of 1.74 ps/(nm km), and a dispersion slope of 0.009 ps/(nm² km) at 1550 nm. The exposure of the HNLF to UV radiation

increases the refractive index of the Ge-doped core, enhancing the short wavelength (<1100 nm) portion of the supercontinuum. From a 30 cm length of UV exposed HNLF, the resulting supercontinuum spanned from 1000 nm to 2300 nm (~ 140 THz wide).

The CEO beat frequency was measured by mixing 1030 nm light with frequency-doubled 2060 nm light in an f-to-2f interferometer [3]. The 1030 nm and 2060 nm portions of the supercontinuum are shown in Fig. 2(a) along with the corresponding offset beat, Fig 2(b). The CEO beat frequency can be phase locked to a stable RF source. The repetition rate could also be phase locked to a stable RF source using a piezoelectric transducer (PZT) fiber stretcher in the laser cavity.

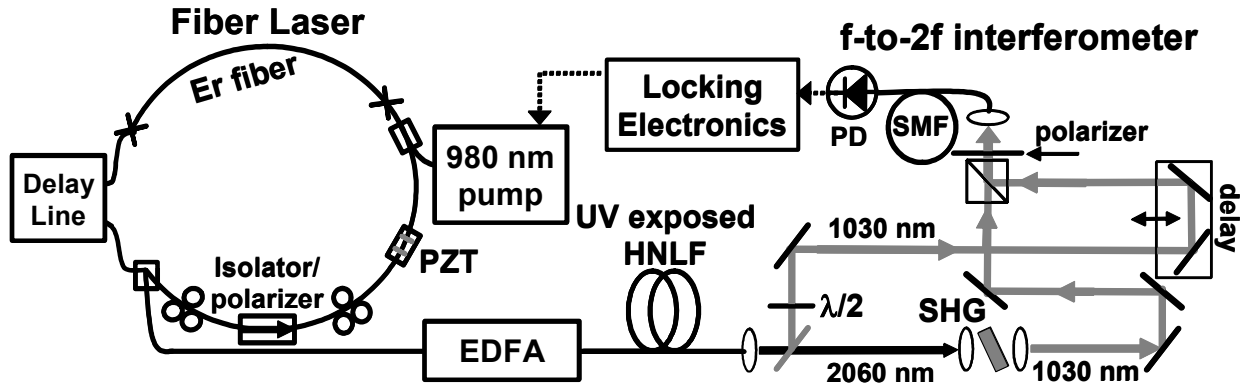


Fig 1. Schematic of the mode-locked fiber laser, erbium-doped fiber amplifier (EDFA), UV exposed highly nonlinear fiber (HNLF), and f-to-2f interferometer. The CEO beat frequency is detected by a photodetector (PD), and is used to control the 980 nm pump diode current. The thick solid lines represent free-space optical paths, the thin solid lines represent fiber optic paths and the dotted lines represent electrical paths.

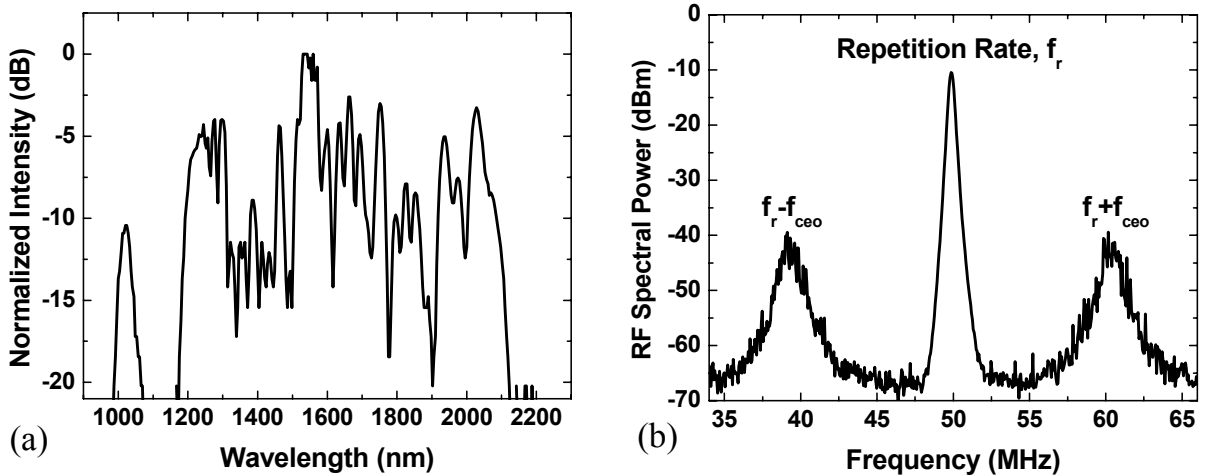


Fig 2. (a) The octave-spanning supercontinuum generated by the UV-exposed highly nonlinear fiber. (b) RF power spectrum from mixing the 1030 nm portion of the supercontinuum with the frequency-doubled 2060 nm portion. The repetition rate signal (f_r) at 49.8 MHz and CEO beat frequency (f_{CEO}) are clearly seen.

To demonstrate the utility of the variable repetition rate laser, the CEO beat frequency was locked and the repetition rate was scanned over a range by moving the in-cavity delay line.

The repetition rate was free-running for this experiment. To lock the CEO beat frequency, negative feedback to the 980 nm pump diode current was used. The RF signal from the f-to-2f interferometer was filtered at 120 MHz (this beat is at $2f_r + f_{\text{CEO}}$), mixed up to 1120 MHz and divided in frequency by 256 (Fig. 3). The divided-down signal at 4.375 MHz was compared to a synthesizer, and the resulting phase error was used to control the 980 nm pump diode current. The divided-down and phase-locked CEO beat frequency had a standard deviation of ≤ 25 mHz.

Figure 4 shows the divided-down CEO beat frequency for repetition rate scans over 20 kHz and 400 kHz. The occasional cycle slips occurred due to non-optimization of the control electronics. Only one cycle slip was recorded over a 20 kHz range and four were recorded over the 400 kHz range. We are currently improving the CEO beat frequency lock to prevent phase slips from occurring over the full repetition rate scan of 0.82 MHz.

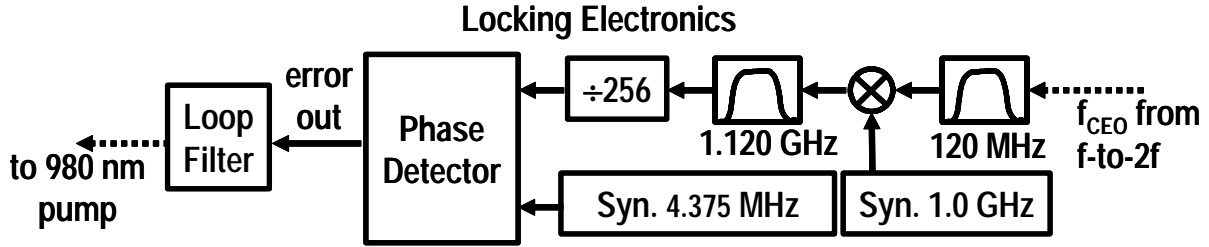


Fig. 3. The electronics used to phase-lock the CEO beat frequency. The f_{CEO} signal from the f-to-2f interferometer was filtered at 120 MHz, mixed with a 1 GHz signal, and divided by 256 in frequency. This signal is compared to a 4.375 MHz signal by a digital phase detector, and the error signal is used to control the 980 nm pump laser current. All synthesizers were referenced to a common time base.

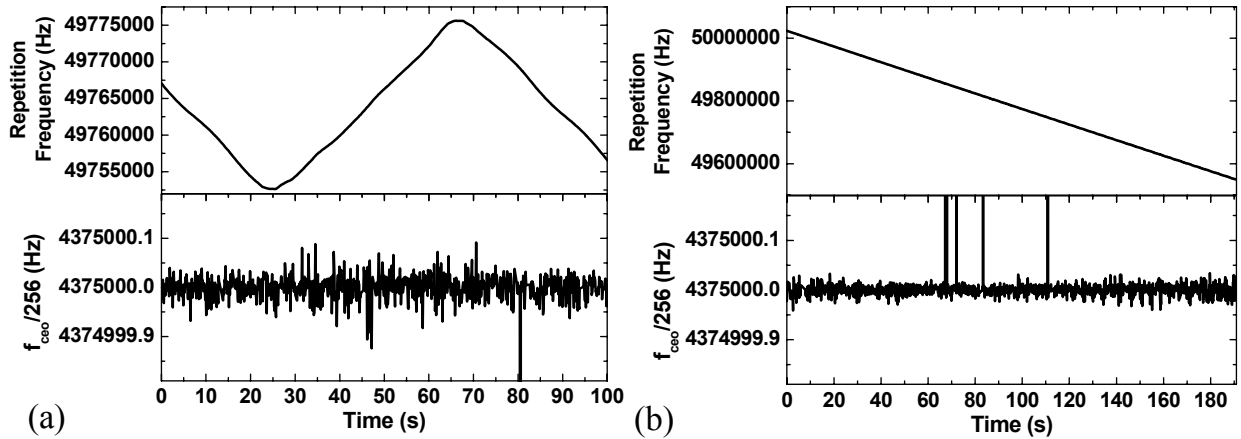


Fig. 4. Scanning the laser repetition rate while the CEO beat frequency (f_{CEO}) is locked. (a) The divided-down CEO frequency experiences one phase slip as the repetition rate is scanned over a 20 kHz span in 100 s. (b) The divided-down CEO beat frequency remains locked over a 400 kHz span in 180 s.

A phase-locked frequency comb with a variable comb tooth separation has many potential uses for IR frequency metrology. For example, the ability to sweep the comb tooth separation allows one to distinguish the mode number of a single comb tooth without using a wavelength meter [9]. Also, a cw laser can be precisely scanned in frequency by locking it to a single comb tooth of the supercontinuum. With the CEO frequency phase-locked to the

synthesizer, a change in repetition rate of 400 kHz would correspond to a 1.5 THz change in the optical frequency of a comb tooth around 1500 nm. A cw laser locked to this comb tooth would then experience continuous tuning over 1.5 THz (12 nm). Finally, the tunable repetition rate will allow synchronization between two optical frequency combs for tests of comb stability [11].

Conclusion

We have demonstrated the ability to phase-lock the CEO frequency of an all-fiber supercontinuum source while scanning its repetition rate, thus altering the comb spacing while the CEO frequency is fixed. A phase-locked near-IR frequency comb with a variable comb tooth separation has many potential benefits for near-IR frequency metrology.

References

- [1] B. R. Washburn, S. A. Diddams, N. R. Newbury, J. W. Nicholson, M. F. Yan, and C. G. Jørgensen, "A phase-locked, erbium fiber laser-based frequency comb in the near infrared," *Opt. Lett.*, vol. 29, pp. 250-252, 2003.
- [2] J. W. Nicholson, M. F. Yan, P. Wisk, J. Fleming, F. DiMarcello, E. Monberg, A. Yablon, C. Jorgensen, and T. Veng, "All-fiber, octave-spanning supercontinuum," *Opt. Lett.*, vol. 28, pp. 643, 2003.
- [3] D. J. Jones, S. A. Diddams, J. K. Ranka, A. Stenz, R. S. Windeler, J. L. Hall, and S. T. Cundiff, "Carrier-Envelope Phase Control of Femtosecond Mode-Locked Lasers and Direct Optical Frequency Synthesis," *Science*, vol. 288, pp. 635, 2000.
- [4] F. Tauser, A. Leitenstorfer, and W. Zinth, "Amplified femtosecond pulses from an Er: fiber system: Nonlinear pulse shortening and self-referencing detection of the carrier-envelope phase evolution," *Opt. Express*, vol. 11, pp. 594-600, 2003.
- [5] F.-L. Hong, K. Minoshima, A. Onae, H. Inaba, H. Takada, A. Hirai, H. Matsumoto, T. Sugiura, and M. Yoshida, "Broad-spectrum frequency comb generation and carrier-envelope offset frequency measurement by second harmonic generation of a mode-locked fiber laser," *Opt. Lett.*, vol. 28, pp. 1-3, 2003.
- [6] R. Fox and L. Hollberg, "Wavelength references for precision metrology in air," presented at Conference on lasers and electro-optics, CTuO4, CLEO 2004 Technical Digest, San Francisco, CA, USA, 2004.
- [7] K. Minoshima, T. R. Schibli, and H. Matsumoto, "Study on cyclic errors in a distance measurement using a frequency comb generated by a mode-locked laser," presented at Conference on lasers and electro-optics, CTuH6, CLEO 2004 Technical Digest, San Francisco, CA, USA, 2004.
- [8] K. Tamura, H. A. Haus, and E. P. Ippen, "Self-starting additive pulse mode-locked erbium fiber ring laser," *Electron. Lett.*, vol. 28, pp. 2226-7, 1992.
- [9] L.-S. Ma, M. Zucco, S. Picard, L. Robertsson, and R. S. Windeler, "A new method to determine the absolute mode number of a mode-locked femtosecond-laser comb used for absolute optical frequency measurements," *IEEE Journ. Select. Topics Quant. Electron.*, vol. 9, pp. 1066-1071, 2003.
- [10] P. S. Westbrook, J. W. Nicholson, K. Feder, and A. D. Yablon, "UV processing of highly nonlinear fibers for enhanced supercontinuum generation," presented at Optical fiber conference, PDP27, OFC 2004 Technical Digest, Los Angeles, CA, USA, 2004.
- [11] L.-S. Ma, Z. Bi, A. Bartels, L. Robersson, M. Zucco, R. S. Windeler, G. Wilpers, C. Oates, L. Hollberg, and S. A. Diddams, "Optical frequency synthesis and comparison with uncertainty at the 10^{-19} level," *Science*, vol. 303, pp. 1843-1845, 2004.

Accuracy limits for simple molecular absorption based wavelength references

W. C. Swann and S. L. Gilbert
National Institute of Standards and Technology
325 Broadway, Boulder, CO 80305
swann@boulder.nist.gov

Abstract: We present limitations on the characterization and use of molecular absorption lines for wavelength calibration purposes. These limits assume a Doppler and pressure-broadened absorption spectrum obtained by transmitting light through a simple gas cell. Attempting to define the line centers to ever-higher accuracy reveals limits associated with effects of cell pressure uncertainty, weak features in the spectrum, increasing complexity in the line profile model, and accuracy limits of wavelength meters.

Introduction: Absorption line based wavelength references have gained widespread acceptance as calibration references throughout the near infrared wavelength region. Introduced to the optical telecommunications industry for instrument calibration [1], these references have also proven useful in fields such as optical sensing and spectroscopy. A typical reference consists of a short gas filled cell that is optical fiber-coupled for attachment to a light source and the instrument being calibrated [Fig. 1]. This format offers reliable service while remaining simple to use. Typical line center uncertainties range from

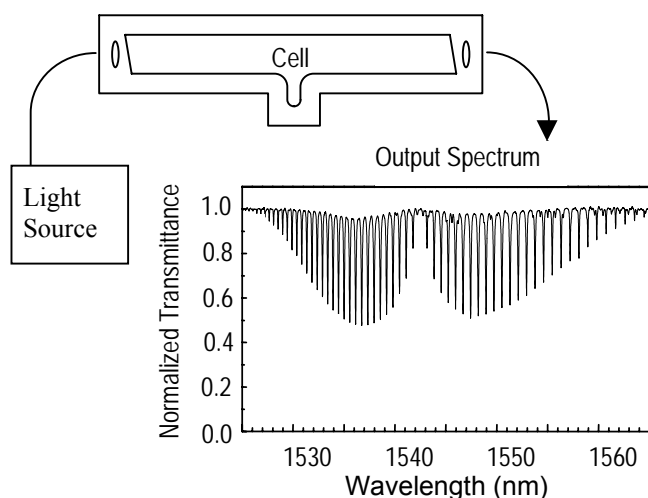


Figure 1: Molecular absorption wavelength reference. The source may be an LED and the output spectrum displayed on a spectrum analyzer, or the source could be a tunable laser and the spectrum measured by a photodiode.

about ± 0.1 pm to ± 1 pm, and linewidths are of order 5 to 50 pm, making these references ideal for calibrating measurement apparatus such as optical spectrum analyzers, tunable lasers, and wavelength meters. The need for higher accuracy references, driven by development of high density wavelength division multiplexed (WDM) systems, fiber Bragg grating sensor systems, and sophisticated swept wavelength test and measurement apparatus, has prompted NIST to investigate the suitability of absorption lines to meet these needs. We found that, for simple references of the format described above, an uncertainty limit of about 0.01 pm is reached where the line centers become difficult to define and measure without abandoning the simplicity and resorting to significantly more complex apparatus and measurement techniques, such as Doppler-free spectroscopy.

Absorption line characterization: At very low temperature and gas pressures, an absorption line has a narrow “natural” linewidth and a well-defined and essentially invariant line center [2]. At room temperature this line is Doppler broadened to about 3.5 pm (~ 450 MHz) for the molecules typically used as wavelength references in the 1550 nm region. The line is also collision (pressure) broadened linearly with increasing pressure. This collisional broadening, described by a Lorentzian profile, is convolved with the Gaussian Doppler profile to yield the Voigt profile that closely represents a typical absorption line. Often a wavelength reference will be tailored to have a specific linewidth by adjusting the gas pressure to obtain the desired collisional broadening. Additionally, the line center shifts slightly with pressure [1]. Characterization of an absorption spectrum for use as a wavelength reference typically involves measuring the line center and width at several pressures and extrapolating to zero pressure to obtain the shift and broadening coefficients, as well as the zero-pressure line centers.

Effect of pressure shift and adjacent small lines: The pressure shift of absorption lines is significant for high accuracy applications; it is as large as 0.5 pm for some $\text{H}^{13}\text{C}^{14}\text{N}$ lines at a pressure of 3.3 kPa (25 Torr). If these HCN lines were used for calibration with an intended uncertainty of 0.01 pm, the pressure shift coefficient for that line and the absolute pressure within the cell would need to be known with an uncertainty of better than 2 %. Alternatively, a lower pressure cell, or lines with a smaller pressure shift coefficient could be used.

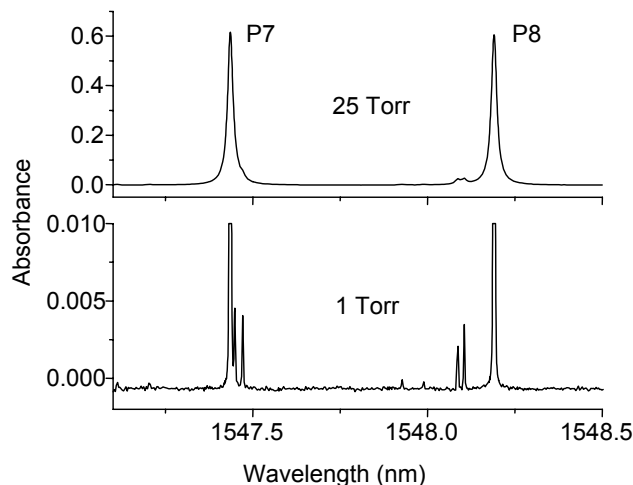


Figure 2: $\text{H}^{13}\text{C}^{14}\text{N}$ lines P7 and P8, showing adjacent small features. The lower trace is expanded 70 \times and the main lines are truncated. Features visible at 0.13 kPa (1 Torr) are blended into line P7 in the 3.3 kPa (25 Torr) spectrum.

of the adjacent feature, we find that only a very few lines in the spectrum are shifted by more than 0.005 pm. This points out to the need for a thorough understanding of the spectrum, including all weak features, and the need for careful fitting, when attempting to obtain high accuracy results from molecular reference spectra. The $^{12}\text{C}_2\text{H}_2$ spectrum, another commonly used wavelength reference, suffers from hot-band transitions that are stronger than those in the HCN spectrum, and even more care needs to be taken when using this reference at high accuracy.

Subtle effects on line shape: Figure 3 shows $\text{H}^{13}\text{C}^{14}\text{N}$ line P16 at a pressure of 3.3 kPa (25 Torr), and a Voigt fit to this line. Although the fitting function appears indistinguishable from the data, examination of the fit residuals shows a systematic difference between the data and fit function and indicates potential errors in the linewidth and center returned by the fit. This difference is an indicator of other contributions to the line profile, chief among which is collisional narrowing. This is best explained as a narrowing of the Doppler width caused by collisions between the absorbing molecule and other molecules during the interaction time of a photon and the absorbing molecule [3]. A simple Galatry function accounts for this collisional narrowing and better represents the data. Furthermore,

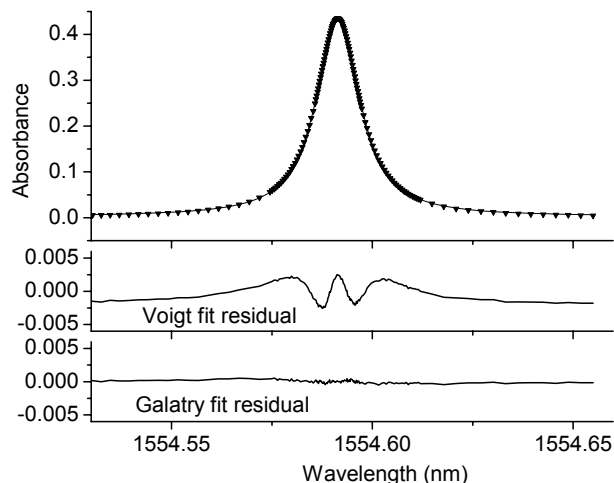


Figure 3: $\text{H}^{13}\text{C}^{14}\text{N}$ line P16. Residuals for both Voigt and Galatry fits are shown on expanded scales.

asymmetry in the residuals points to an asymmetric line shape; fitting such a shape with a symmetric Voigt or Galatry function leads to an ambiguity in the line center. This asymmetry arises from a correlation between the velocity changing collisions responsible for collisional narrowing, and the state perturbing collisions that result in collisional (pressure) broadening. Generalized versions of the Galatry functions, which include a complex velocity-changing frequency term, account for this asymmetry and include a parameter that defines the line center shift with increasing pressure. Using these functions, however, requires a deep understanding of the molecular collision dynamics so that several parameters may be initialized to values specific to the line number and state conditions. Furthermore, subtle offsets and distortions in the detection of light transmitted through the cell can give structure in the residuals that can mask or be confused with effects of collision dynamics.

In both the characterization and use of molecular absorption based wavelength references it is valuable to have a fitting function that returns useful information under a variety of conditions without the undue burden on the user, such as the need to recalculate initial parameters for each set of conditions. The Voigt function satisfies this, at the expense of increasing the uncertainty somewhat on parameters such as the line centers and broadening. We estimated the line center error caused by using a Voigt function to fit an asymmetric line shape by fitting an absorption line using a Voigt function over different widths, and observing the shift in line center. Performing this operation on a high precision scan of a typical molecular reference line, $\text{H}^{13}\text{C}^{14}\text{N}$ line P16 at 25 Torr, revealed a shift of -0.007 pm as the fitted portion was decreased from 5 times to 0.4 times the linewidth. A similar shift is seen for this line at a pressure of 1 Torr. Line P9 showed a shift of $+0.005$ pm, while lines R23 and P24 at 25 Torr showed shifts of only -0.003 pm and $+0.002$ pm, respectively, indicating the variation in behavior of different lines within the same spectrum.

Wavelength meter errors: Of the different means of characterizing molecular absorption spectra, the combination of a tunable laser and a wavelength meter (WLM) remains the most versatile. Here, a laser is stepped across an absorption line, and for each step the transmittance of the absorbing gas and the laser's wavelength are measured. Difference frequency methods, based on the measurement of the difference frequency between a laser locked to a reference line and a second laser locked to a fundamental reference such as a rubidium line [4], offer the highest accuracy but tend to be complicated, and a stable optical frequency comb is required to perform measurements over a molecular band. Fourier transform spectroscopy offers good signal-to-noise ratio, but mitigation of offset and linearity errors requires a set of accurately known calibration lines. Grating based spectrometers suffer these same problems and additional resolution limits. The laser/WLM combination offers measurement bandwidths limited only by the tunable laser's bandwidth, often about 100 nm, and accuracy limited by the WLM.

Wavelength meters of the swept Michelson interferometer variety [5] work by comparing an interference fringe count of a measurand light source with that of a known-wavelength reference source as the interferometer's path difference is swept. Since the fringe count increases with the length of the swept path difference, increasing the interferometer's size will increase the WLM's resolution. A swept path difference of two meters will, at a reference wavelength of 633 nm, give about 6×10^6 fringes per sweep. The resolution is often further increased through splitting the fringe count by up to 100. With fringe splitting, the resulting resolution will be $633 \text{ nm} \div 6 \times 10^8$, or around 0.001 pm at this wavelength. If the WLM is operated in ambient atmosphere, the fringe counts are corrected for the air's refractive index n_{air} at their respective wavelengths, using either the Ciddor or Edlen equation [6], to obtain the wavelength in vacuum. The WLM fractional uncertainty due to this correction is approximately the index uncertainty δn_{air} . Stone [6] gives a $(2\sigma) \delta n_{\text{air}}$ of 2×10^{-8} , independent of λ , for air under laboratory conditions. Ciddor [7], claims δn_{air} can be as high as 5×10^{-8} (1σ), and furthermore cautions that infrared absorption bands of H_2O and CO_2 have not been included in any refractive index analysis. Our observations of WLM reading shifts vs. humidity are outside of what would be explained by δn_{air} given in Ref. 6 but within that given by Ref. 7, lending credence to the ambiguity of the uncertainty on n_{air} , especially with respect to the

humidity correction. Operation of the wavelength meter under vacuum would eliminate errors caused by ambient air, but such apparatus are complicated to construct and inconvenient to use, and a limit where errors dominated by optics alignment and aperture interference would soon be reached. Overcoming these error sources leaves the reference laser as the dominant contribution to the WLM's uncertainty. Simple polarization-stabilized helium-neon lasers [8], including commercially available models, offer stability limited to about one part in 10^8 , resulting in a WLM uncertainty of about 0.02 pm at 1550 nm. Iodine-stabilized reference lasers offer stability of better than one part in 10^{10} , but are expensive and complicated to operate. When using a WLM to accuracies greater than about 1 part in 10^6 , periodic calibration with a known reference near the measurand's wavelength is advisable. We frequently calibrate our NIST-built WLM against a 1560 nm rubidium-stabilized laser, thereby correcting for instabilities of the WLM reference laser, any changes in index of refraction due to atmospheric conditions, and alignment errors. This calibration step reduces our standard uncertainty to 0.004 pm (about 0.5 MHz) at 1560 nm. We verified that this accuracy was maintained at nearby wavelengths by measuring a series of $^{12}\text{C}_2\text{H}_2$ lines between 1528 nm and 1538 nm and comparing our results with values given in Ref. 4.

Conclusion: Expending only reasonable effort, the line center of a pressure broadened line typical of a molecular absorption wavelength reference cannot be defined to better than about ± 0.01 pm. This might be improved slightly by using apparatus such as vacuum wavelength meters and sophisticated fitting routines. While these approaches may be appropriate under some laboratory settings, they are time consuming and expensive where entire spectra need to be evaluated. Even if the line centers were to be defined to ± 0.001 pm, careful application of complicated fitting functions, which may lie beyond the means of the reference's user, would be needed to realize this accuracy in a practical setting. Fortunately, recent advances in frequency combs have increased their bandwidths to over 100 THz, making them an attractive alternative to the molecular absorption wavelength reference for high accuracy needs. Where high accuracy is desired and cost is less important, the comb itself can be used as a wavelength reference, or more appropriately an optical frequency reference. Molecular spectra would still satisfy the need for moderate accuracy references, but reevaluating the spectra against a frequency comb would remove any errors associated with the wavelength meter, and give the line centers unambiguously in frequency units. In fact, this reporting of optical spectra directly in frequency units skirts entirely the complications associated with the dependence of wavelength measurements on local refractive indices, and is expected to usher in a new era of optical spectral measurement.

References:

1. S. L. Gilbert and W. C. Swann, "Acetylene $^{12}\text{C}_2\text{H}_2$ absorption reference for 1510 nm to 1540 nm wavelength calibration – SRM 2517a," Natl. Inst. Stand. Technol. (US) Spec. Publ. 260-133 (2001); S. L. Gilbert, W. C. Swann, and C. M. Wang, "Hydrogen Cyanide $\text{H}^{13}\text{C}^{14}\text{N}$ absorption reference for 1530 nm to 1560 nm wavelength calibration-SRM 2519," Natl. Inst. Stand. Technol. (US) Spec. Publ. 260-137 (1998); S. L. Gilbert and W. C. Swann, "Carbon monoxide absorption references for 1560 nm to 1630 nm wavelength calibration-SRM 2514 ($^{12}\text{C}^{16}\text{O}$) and SRM 2515 ($^{13}\text{C}^{16}\text{O}$)," Natl. Inst. Stand. Technol. (US) Spec. Publ. 260-146 (2002).
2. W. Demtröder, *Laser Spectroscopy*, second printing (Springer-Verlag 1982) Chapter 3.
3. P. L. Varghese and R. K. Hanson, "Collisional narrowing effects on spectral line shapes measured at high resolution," Appl. Opt. **23**, pp. 2376-2385 (1984).
4. K. Nakagawa, M. de Labachellerie, Y. Awaji, and M. Kourogi, "Accurate optical frequency atlas of the 1.5- μm bands of acetylene," J. Opt. Soc. Am. B **13**, pp. 2708- 2714 (1996).
5. J. L. Hall and S. A. Lee, "Interferometric real-time display of cw dye laser wavelength with sub-Doppler accuracy," Appl. Phys. Lett. **29**, pp. 367-369 (1976).
6. J. A. Stone and J. H. Zimmerman, "Index of refraction of air," (<http://patapasco.nist.gov/mel/div821/Wavelength/Documentation.asp#IndexofRefractionofAir>).
7. P. E. Ciddor, "Refractive index of air: new equations for the visible and near infrared," Appl. Opt. **35**, pp. 1566-1573 (1996).
8. T. M. Niebauer, J. E. Faller, H. M. Godwin, J. L. Hall, and R. L. Barger, "Frequency stability measurements on polarization-stabilized He-Ne lasers," Appl. Opt. **27**, pp. 1285-1289 (1988).

Fast-Fourier-Transformation de-convolutions for a Fabry-Perot filter based OSA: demonstration of 15.0 dB increase of Optical-Rejection-Ratio at ± 25.0 GHz from peak

Ke-Cai Zeng^{a)}, Sunrise Telecom Inc, 302 Enzo Drive, San Jose, CA 95138, U.S. A.

Abstract: An optical spectrum analyzer (OSA) based on a tunable Fabry-Perot filter (TFPF) has been implemented. The TFPF has free spectrum range (FSR) of about 180 nm, finesse of about 7200, and 3-dB bandwidth of less than 80.0 pm. Its optical rejection ratio (ORR) at ± 25.0 GHz away from its main transmission peak is about 24.5 dB. We demonstrated that Fast-Fourier-Transformation (FFT) de-convolutions can be employed to enhance its ORR by more than 15 dB at ± 25.0 GHz. This is the first time that FFT de-convolutions have been demonstrated to greatly enhance the ORR of a TFPF for OSA applications (**with one patent pending**).

1. INTRODUCTION AND THEORY: Optical spectrum analysis is the measurement of optical power as a function of wavelength. Basic method is to pass the optical signal to be analyzed through a tunable optical filter, which resolves or picks out the individual components. Three basic types of filters are widely used to make optical spectrum analyzers, including diffraction gratings, Fabry-Perot (FP) filters, and Michelson interferometers. Applications include testing laser and/or LED light sources for spectral purity and power distribution, monitoring an optical transmission system of a wavelength division multiplexing (WDM) system for signal quality and noise figure, and testing transmission characteristics of various optical devices and components, and so on. The optical resolution of an OSA is the minimum wavelength spacing between two spectral components, which can be resolved reliably. To achieve high optical resolution, the filter should have a narrow enough 3-dB bandwidth (BW). For many measurements, the various spectral components to be measured are not equal amplitude. One such example is the measurement of side-mode suppression of a distributed feedback (DFB) laser. For this measurement, the bandwidth of the filter is not the only concern. Filter shape, which is specified in terms of optical rejection ratio (ORR) at certain distance, for example at ± 25 GHz, away from the main transmission, is also important. Among the three types of filters used, one of the commonly used filters is the FP filter [1]. A FP filter can be fabricated to have very narrow 3-dB BW and it thus provides very good spectral resolution. However, a FP filter's transmission profile normally has very broad skirt at 20 dB down as compared with a diffraction grating. This would limit its ORR and thus dynamic range for optical signal-to-noise measurements. In this paper, we described a method to overcome this hurdle of FP filter for OSA applications. The transmission profile of a FP filter is described by the Airy Function:

$$A(\lambda) = \frac{I_0}{1 + \left(\frac{2F}{\pi} \sin \frac{2\pi nL}{\lambda} \right)^2}, \quad (1)$$

where I_0 is the peak transmission optical intensity, F is the finesse of the FP filter, λ is the wavelength of the light wave. The above Airy function can be approximated by the following modified Lorentzian distribution:

$$L(f) = \frac{I_0}{1 + 4 \left(\frac{f - f_0}{B} \right)^2 \left[1 - \frac{1}{3} \left(\frac{\pi}{FSR} (f - f_0) \right)^2 \right]}, \quad \left(\text{for } \frac{f - f_0}{FSR} \ll 1 \right) \quad (2)$$

where f is the frequency of the transmitted lightwave, f_0 is the peak transmission frequency, FSR is the free spectrum range of the FP filter. The 3-dB bandwidth (BW) of the Lorentzian distribution is denoted by

$$BW = \frac{1 - r}{\sqrt{r}} \frac{c}{2\pi nL}, \quad \text{with } r \text{ the reflectivity of the filter mirrors, } c \text{ the light speed in vacuum, } n \text{ the index of}$$

refraction of the media inside the filter cavity, and L the length of the filter's cavity. We define this type of filter, which has Lorentzian transmission profile as "Lorentzian filter".

In the same time, the transmission profile of a diffraction grating is described by a Gaussian distribution:

$$G(f) = I_0 e^{-\frac{(f-f_0)^2}{2\sigma^2}}, \quad (3)$$

where σ defines the BW of the Gaussian distribution. We define this type of filter with a Gaussian transmission profile, as “Gaussian filter”.

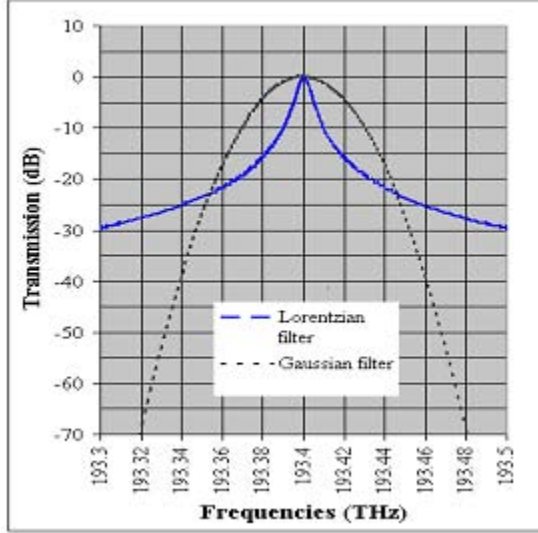


Figure 2 Atheoretical Lorentzian and Gaussian filter with a 3.0-dB BW of about 6.6 GHz and 33.0 GHz, respectively. The Lorentzian filter shows an ORR of about 23.0 dB at 50.0 GHz away and 29.0 dB at 100 GHz away from the main transmission, while the Gaussian filter shows an ORR of about 25.0 dB at 50.0 GHz away and greater than 70.0 dB at 100.0 GHz away from the main transmission.

Tunable FP filters or diffraction gratings can both be used to construct OSAs. For a tunable FP filter (TFPF), one of the major problems experienced for DWDM applications is the relative broad skirt of its transmission profile, as compared with a diffraction grating with the same 3.0-dB BW. The transmission profile of a diffraction grating has a much steeper skirt. Due to its relative broad skirt of a Lorentzian filter, it will also pick up signals from channels other than the channel around the filter's main transmission. This effect of the FP filter would limit the OSA's dynamic range (DR) for optical signal-to-noise measurements (OSNR). Figure 2 shows a comparison between a Lorentzian and a Gaussian filter with a 3-dB BW of about 6.6 GHz and 33.0 GHz, respectively. The Lorentzian filter shows an ORR of about 23.0 dB at ± 50.0 GHz and 29.0 dB at ± 100.0 GHz away from the main transmission peak. The Gaussian filter shows an ORR of about 25.0 dB at ± 50.0 GHz away from the transmission peak (similar to the Lorentzian filter), but it shows an ORR of greater than 70.0 dB at ± 100.0 GHz away from the transmission peak. Although the 3-dB BW of the Lorentzian filter is only 1/5 of that of the Gaussian filter, it has a much lower ORR at ± 100.0 GHz away from the filter's peak transmission due to its broad skirt. Figure 2 reveals the main reason why all the existing OSAs based on FP filters have much lower DR for OSNR measurements than those based on diffraction gratings. In the following, we will show that Fast-Fourier-Transformations (FFT) de-convolutions can be used to greatly enhance the DR for OSNR measurements of an OSA made with FP filter.

Any measured optical spectrum can be described as an integral of convolution of the OSA's filter with the original optical signal. If we denote the original optical signal by $R(f)$, the spectrum measured with a Lorentzian filter by $P_L(f)$, and that measured with a Gaussian filter by $P_G(f)$, then we have the following integrals of convolution:

$$P_L(f) = \int_{-\infty}^{+\infty} R(f_0) L(f - f_0) df_0, \quad (4)$$

$$P_G(f) = \int_{-\infty}^{+\infty} R(f_0) G(f - f_0) df_0, \quad (5)$$

where $L(f - f_0)$ and $G(f - f_0)$ are functions of Lorentzian and Gaussian distributions centered at f_0 , respectively. According to the theory of Fourier Transformations for integrals of convolution [2-3], we can have:

$$F[P_L(f)] = F[R(f)] \cdot F[L(f)], \quad (6)$$

$$F[P_G(f)] = F[R(f)] \cdot F[G(f)], \quad (7)$$

where $F[P_L(f)]$, $F[R(f)]$, $F[L(f)]$, $F[P_G(f)]$, and $F[G(f)]$ are the Fourier Transformations of $P_L(f)$, $R(f)$, $L(f)$, $P_G(f)$, and $G(f)$, respectively. We can then deduct the following equation:

$$P_G(f) = F^{-1} \left[\frac{F[P_L(f)]}{F[L(f)]} \cdot F[G(f)] \right], \quad (8)$$

Equation (8) is the base of our FFT de-convolution method, which will be further discussed in the following section.

2. RESULTS: We implemented an OSA using a TFPF for the 1470 nm to 1630 nm wavelength range. The tunable FP filter used has a FSR of about 180 nm, a finesse of about 7200, and a 3-dB BW of less than 80.0 pm. Its narrow 3-dB BW enables the OSA to have good spectral resolution. The filter's optical rejection ratio at 25.0 GHz and 50.0 GHz away from the filter peak transmission is about 24.5 dB and 30.0 dB, respectively. This means that the highest OSNR, which this OSA can measure, is less than 24.5 (30.0) dB for 50.0 (100.0) GHz spacing optical signals.

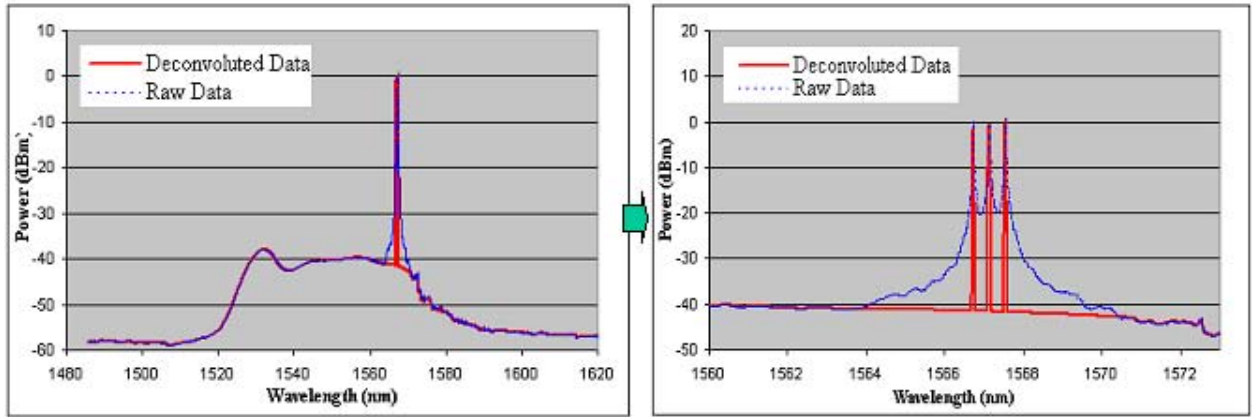


Figure 3 A comparison between the unprocessed raw data spectrum and the de-convoluted spectrum measured with our FP OSA. The deconvoluted spectrum shows an increase of optical rejection ratio at ± 25.0 GHz of more than 15.0 dB.

We have implemented software programs, based on equation (8), to perform Fast Fourier Transformations on the measured optical spectrum very efficiently. For an optical spectrum from 1470 to 1630 nm, our OSA acquires about twenty thousands of effective data points for the wavelength range of 1470 to 1630 nm, which gives a wavelength resolution better than 8.0 pm. The total time needed to perform the FFT de-convolutions on the whole spectrum is less than 1 second on a PC with a Pentium III processor.

Figure 3 shows a comparison between an un-transformed raw data spectrum measured with our FP filter OSA and the processed spectrum after FFT de-convolutions. The de-convoluted spectrum shows an increase of ORR of about 15.0 dB. This is due to that FFT de-convolution has made the filter skirt much steeper. The OSNR values measured for all the three channels based on the raw data spectrum are around 20.0 dB in this case. However, OSNR measured based on the transformed spectrum is around 40.0 dB. This enhancement of the OSNR measurement is directly due to the FFT de-convolutions, which have removed the channel cross talk greatly. Figure 4 shows three DWDM channels with imbalanced powers. The power of the middle channel is about -34.5 dBm and that of the other two channels is about 0.0 dBm. Power imbalance is about 34.5 dB. The raw data spectrum fairly resolves the weak

power channel since it is covered under the skirts of its left and right neighboring channels. However, the de-convoluted spectrum clearly resolves the weak power channel. The power cross talk has been almost fully removed by the FFT de-convolutions. And thus the spectrum gives a much better contrast for the weak power channel.

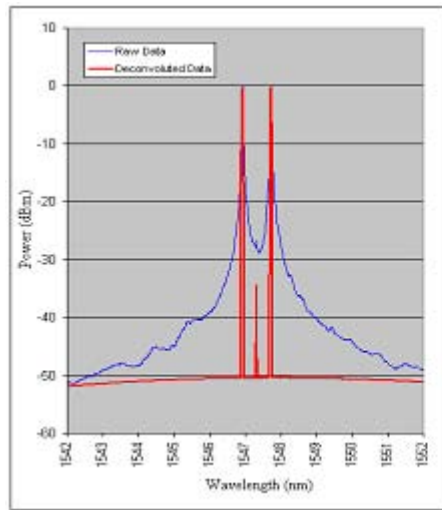


Figure 4 Three DWDM channels, of which the middle channel is at about -34.0 dBm and the other two channels are at about 0.0 dBm, show a power-imbalance greater than 34.0 dB. The raw data spectrum fairly resolves the weak power channel since it is buried under the skirts of its left and right channels. The de-convoluted spectrum clearly resolves the weak power channel.

Figure 5 shows a comparison between an un-transformed raw optical spectrum, which includes more than forty 50-GHz-spacing DWDM channels, and its FFT de-convoluted spectrum. The OSNR results measured from the de-convoluted spectrum are very close to their real values, which was confirmed by the tests made on another commercial OSA based on diffraction grating with very high DR for OSNR measurements. Again, it is obvious that the FFT de-convolution method, which we developed, is very effective.

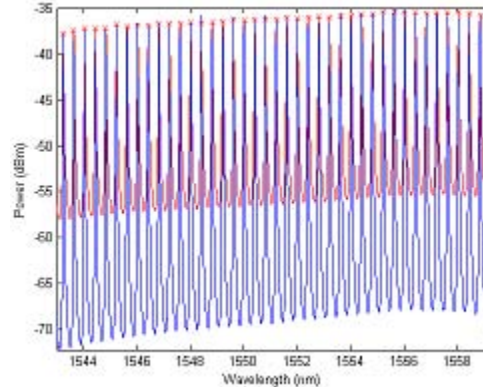


Figure 5 A comparison between a Unprocessed raw spectrum (Red), which consists of more than 40 50-GHz-spacing DWDM channels, and the deconvoluted spectrum (blue).

3. CONCLUSION AND DISCUSSIONS: An optical spectrum analyzer based on TFPF has been demonstrated. FFT de-convolutions have been employed to enhance its ORR and thus its DR for OSNR measurements by more than 15.0 dB at ± 25.0 GHz. To the best of our knowledge, this is the first time that FFT de-convolutions have been employed to enhance the DR for OSNR measurements of a FP Filter based OSA. The FFT de-convolution method, which we have developed and demonstrated, can overcome one of the major hurdles of FP Filters for high dynamic range OSA applications. This has made it possible that OSAs, constructed with FP filter, can provide not only excellent spectral resolution, but also very high dynamic range for OSNR measurements for WDM systems, and etc.

REFERENCES:

- (a) E-mail address: kzeng@SunriseTelecom.com
- [1] Hernandez, G. (1986), FP Interferometers, Cambridge, England: Cambridge University Press.
- [2] Bracewell, R. (1965), "The Fourier Transform and Its Applications," McGrawHill, New York.
- [3] Papoulis, A. (1962), "The Fourier Integral and its Applications," McGraw-Hill, New York.

Stimulated Brillouin Scattering: An Overview of Measurements, System Impairments, and Applications

A. Boh Ruffin

Corning, Inc., 1 Science Dr., Corning, NY 14831, ruffinab@corning.com

Abstract— Basic concepts of stimulated Brillouin scattering are reviewed together with Brillouin gain spectrum characterization techniques, system impairments, and applications.

Keywords— Stimulated Brillouin Scattering (SBS), SBS measurement techniques, SBS impairments

I. INTRODUCTION

LIGHT scattering in optical communication fiber is omnipresent regardless of the amount of optical power present in the fiber. It can be categorized into two regimes: spontaneous and stimulated scattering [1,2]. Spontaneous light scattering refers to the process of scattering under conditions such that the optical material properties are unaffected by the presence of the incident electric field. For input optical fields of sufficient intensities spontaneous light scattering can become quite intense; thus in this stimulated regime the nature of the scattering process grossly modifies the optical properties of the material system and vice versa. Furthermore, spontaneous and stimulated scattering can result from Rayleigh, Raman, and Brillouin scattering events. Rayleigh scattering occurs from non-propagating density fluctuations, and can be referred to as scattering from entropy fluctuations. Raman scattering arises from the interaction of light with the vibrational modes of the constituent molecules in the scattering medium; equivalently this can be considered as the scattering of light from optical phonons. Brillouin scattering arises from the interaction of light with propagating density waves or acoustic phonons. Each of these scattering processes are always present in optical fiber as no fiber is free from microscopic defects or thermal fluctuations which drive the three processes. Of the three types of scattering events stimulated Brillouin scattering (SBS) is recognized as the dominant optical fiber nonlinearity. Hence this review article will emphasize this subject matter.

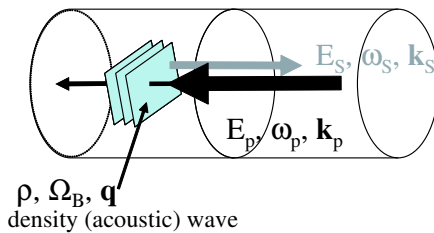


Fig. 1. Schematic diagram of the stimulated Brillouin scattering process in an optical fiber.

At high enough input powers, SBS will convert transmitted light in the fiber to a scattered, Stokes-shifted (down shifted) reflection well above typical Rayleigh scattering power levels. As illustrated in Fig. 1 this phenomena arises from the interaction between the optical field and acoustic phonons in the fiber, driven through an electrostrictive process where the medium becomes more dense in regions of high optical density. As shown in Fig. 1 an incident optical field of sufficient intensity interferes with ubiquitously scattered optical fields, which give rise to density and pressure variations (electrostriction). The incident optical field then scatters off the refractive index perturbations as a result of the aforementioned density variations. The scattered light is Stokes shifted and will add constructively with the Stokes radiation which produced the acoustic disturbance. The incident light can add energy to the acoustic waves as it interferes with the scattered Stokes light and thus significantly increase the probability of scattering more of the incident light through Bragg diffraction. Since energy and momentum are conserved during these scattering events, the frequencies and wave vectors of the pump (incident), scattered, and acoustic fields are given by

$$\Omega_B = \omega_p - \omega_s, \vec{q} = \vec{k}_p - \vec{k}_s, \quad (1)$$

where $\omega_{p,s}$ and $k_{p,s}$ are the optical frequencies and wave vectors of the pump and Stokes shifted fields, respectively. The Brillouin frequency, Ω_B , and the wave vector of the acoustic field, q , are related by the phonon dispersion relation

$$\Omega_B = |\vec{q}|v_A \approx 2v_A|\vec{k}_p|\sin\left(\frac{\theta}{2}\right), \quad (2)$$

where v_A is the speed of sound in the medium and θ is the angle between the pump and Stokes fields. However, in a single-mode optical fiber the relevant θ values are 0 and π , hence the Brillouin frequency shift is given by $\nu_B = 2nv_A/\lambda_p$. Typical values of a Brillouin frequency shift in optical fiber at 1550 nm range approximately between 9-12 GHz.

The previously described interaction between the three fields can be represented via a set of coupled mode equations in steady state as follows [3,4]

$$\begin{aligned} \frac{dA_p}{dz} &= -\frac{i\gamma_e\omega}{2\rho_0nc} \rho A_s - \alpha A_p \\ \frac{dA_s}{dz} &= -\frac{i\gamma_e\omega}{2\rho_0nc} \rho^* A_p + \alpha A_s \end{aligned} \quad (3)$$

where the amplitude of the density (acoustic) wave, $\rho(z, t)$, is approximated by

$$\rho(z, t) = \frac{\gamma_e q^2}{4\pi} \frac{A_p A_S^*}{\Omega_B^2 - \Omega^2 - i\Omega\Gamma_B}. \quad (4)$$

Also in Eq. 3 $A_{p,S}$ are the electric field amplitudes of the pump and Stokes waves, respectively, Γ_B is the phonon lifetime, and ρ_o is the density of the material. Also, γ_e represents the electrostrictive coupling coefficient of the medium and is expressed as $\gamma_e = \rho \frac{\partial \epsilon}{\partial \rho}$, where ϵ is the dielectric constant of the material. A steady state solution of Eq. 3 is offered in Ref. [1].

Algebraic manipulation of Eqs. 3 and 4 results in the definition of a complex Brillouin gain coefficient:

$$g(\Omega) = \frac{g_B}{(\Omega_B^2 - \Omega^2) + i\Omega\Gamma_B} \quad (5)$$

where the peak value is defined as,

$$g_B(\Omega = \Omega_B) = \frac{\gamma_e^2 \omega^2}{2n\rho_o c^3 n\Gamma_B} \quad (6)$$

The coupling term, $g(\Omega)$, is an important parameter as most limitations or attributes of Brillouin scattering can be assessed from its value. For example, extracting the functional form of this parameter makes it possible to determine the SBS critical power [5], characterize the Brillouin gain spectrum [3,6], as well as the SBS induced phase shift of the optical pump signal [7]. In an optical fiber the gain spectrum can be manipulated by affecting the strain or temperature anywhere along the length of the strand. Also, the gain spectrum is readily affected by perceptible changes in the fiber design [8,9]. In this regard, this review article will discuss several measurement techniques used to extract relevant optical parameters such as the gain factor, SBS-induced phase shift, and SBS-induced noise. Furthermore, systems which are limited by SBS effects will also be considered together with applications for SBS.

II. AN OVERVIEW OF MEASUREMENTS

A. Critical power, Brillouin gain spectrum, SBS-induced phase shift

Consider the transcendental expression for determining the critical power or SBS power threshold, P_c ,

$$\frac{\exp[-\gamma_B(1 - e^{-\alpha L})]}{\frac{1}{\gamma_B} + e^{-\alpha L}} \gamma_B^{\frac{3}{2}} = \frac{\sqrt{\pi}}{2} kT \frac{\nu_S}{\nu_A} \Delta\nu_B \frac{g_B}{\alpha A_e} \quad (7)$$

$$\gamma_B = \frac{g_B P_c}{\alpha A_e}$$

where kT is the thermal energy of the acoustic phonons, $\nu_{S,A}$ are the frequencies of the Stokes wave and acoustic phonon, respectively, L is the length of the fiber, A_e is the effective area of the optical fiber, and $\Delta\nu_B$ is the full-width-at-half-max (FWHM) Brillouin linewidth [5,10]. The term γ_B is a unitless parameter that characterizes the strength of the nonlinear interaction due to Brillouin scattering. Eq.

7 leads to the more familiar closed-form expression of the SBS power threshold for fibers much longer than their effective length (L_{eff}),

$$P_{th}^{SBS} = \frac{21\alpha A_e}{(1 - e^{-\alpha L})g_B} \left(\frac{\Delta\nu_B \otimes \Delta\nu_L}{\Delta\nu_B} \right) \quad (8)$$

where the convolution term is a multiplicative factor for the Brillouin gain factor to account for the influence of pump laser's spectral linewidth ($\Delta\nu_L$) [11]. While Eq. 8 is based on the condition when the reflected Stokes optical power at $z = 0$ is equal to the input pump power ($P_{in} = P_{reflect}$)¹, there are various definitions of the SBS threshold in optical fibers [12,13]. However, one can also arbitrarily define the SBS power threshold to be the input power where the reflected power is equal to some fraction, η , of the pump, $P_{reflect} = \eta \times P_{in}$. One might also identify the SBS threshold based on the change in slope of the output power due to pump depletion, or the maximum change in slope (second derivative) of the reflected power curve (in linear dimensions).

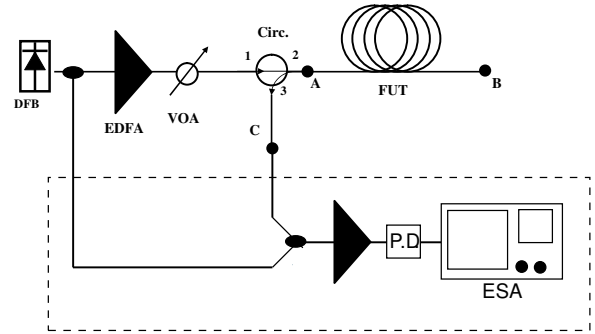


Fig. 2. Top: The experimental configuration for measuring stimulated Brillouin scattering power threshold and heterodyne method for measuring the BGS (highlighted in the box).

SBS power measurements (illustrated in Fig. 3) are by far the most common and simplest of means to quantify the SBS threshold. As shown in Fig. 2, a narrow linewidth laser source of sufficient output power (or available amplification), a means to control and measure the input power, and an optical circulator are required to complete the measurement. A calibration of the variable optical attenuator (VOA) settings is required such that the launch power at point A is always known. The three-port optical circulator couples the pump signal into the fiber under test through ports $1 \Rightarrow 2$, but directs the backscattered Stokes signal through port $3 \Leftarrow 2$. Thus, it is possible to measure the reflected or transmitted optical powers at points B and C in the diagram, respectively, in order to characterize the SBS threshold. The effects of SBS in single-mode fiber are also demonstrated in Fig. 3a wherein the output and reflected power as a function of input power is plotted. When plotted on a logarithmic scale one can readily observe that

¹This definition assumes the absence of pump depletion. However this is not experimentally observable since pump depletion inevitably occurs, thus the backscattered power is always less than the pump power.

the reflected power increases sigmoidally with input power. The output power curve in Fig. 3a also shows that the signal power becomes depleted beyond a certain input power. This deleterious result will effectively clamp the signal output power, but continue to transfer power to the Stokes (reflected) signal via the electrostrictive process which underlies the stimulated Brillouin phenomenon.

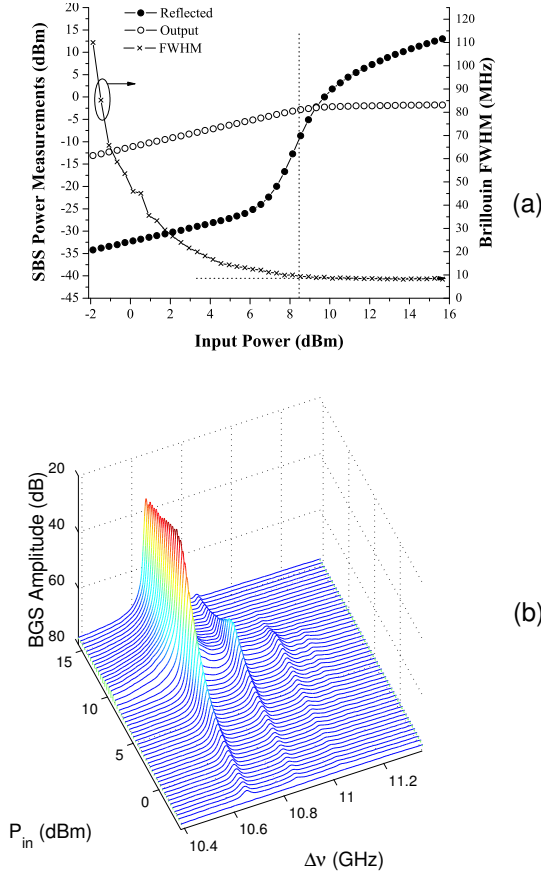


Fig. 3. (a) SBS threshold measurements for an NZ-DSF overlaid with FWHM data from above data. The vertical line represents the boundary from spontaneous to stimulated Brillouin scattering and the onset of SBS-induced pump depletion. (b) Measure Brillouin gain spectrum at various input powers using the configuration in Fig. 2.

A complement to the previously described power measurement could include spectral characterization to quantify the Brillouin frequency shift, linewidth, gain shape, and peak gain coefficient. It has been observed that the Brillouin spectrum is influenced by the material composition of the fiber, ambient fiber temperature, or fiber strain, thus evaluating the spectral information can also be advantageous as a means of fiber design feedback for suppressing or exploiting Brillouin scatter attributes in a fiber [14]. Several methods to access the Brillouin gain spectrum (BGS) are widely deployed to characterize the SBS nonlinearity in various fiber types [3]. One of the first techniques in quantifying the BGS of bulk silica was introduced by Krishnan in 1950 [15]. Techniques have since evolved with improved spectral resolution and sensitivity such that the transition from spontaneous to stimulated Brillouin scattering can be delineated or the absolute peak gain factor

can be determined. A direct method to obtain the Brillouin gain spectral shape in optical fiber is derived from the heterodyne method [3, 16]. This approach interferes the pump signal with its Stokes counterpart (unique to the fiber under test) and subsequently converts the amplified beat signal into the electrical domain where it is spectrally resolved using an electric spectrum analyzer (ESA). Yeniay *et al.* implemented such an approach to study the Brillouin spectral shape and monitor the evolution from spontaneous to stimulated scattering for several fiber types. While this technique does not yield an absolute value for the peak Brillouin gain factor, it provides another means to ascertain an SBS threshold at the spontaneous-stimulated boundary by observing the effects of gain narrowing in the Brillouin spectrum (Fig. 3b) [17]. As illustrated in the secondary plot in Fig. 3a, the transition from spontaneous to stimulated Brillouin scattering is demarcated on the curve where the FWHM of the first order acoustic mode becomes constant.

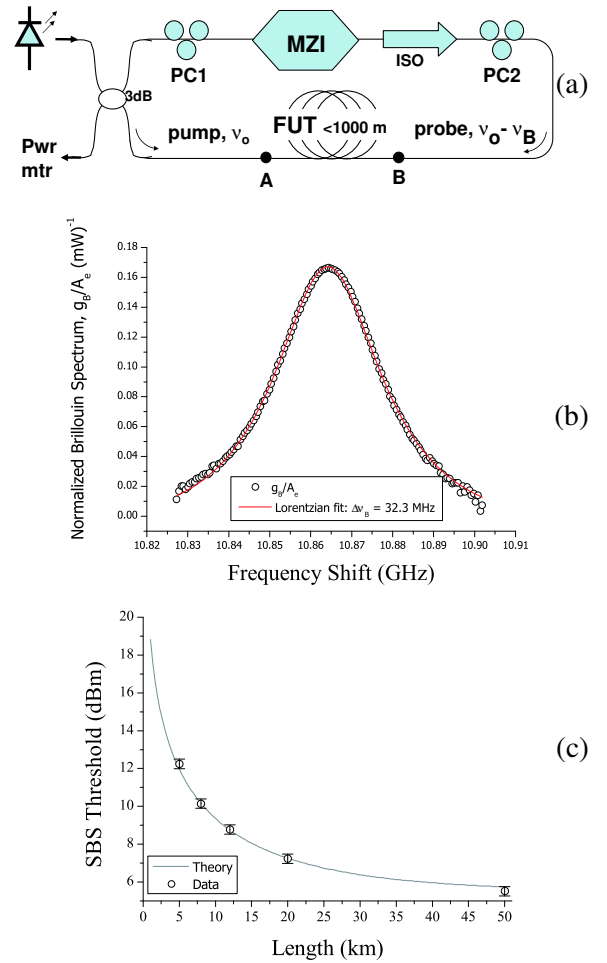


Fig. 4. (a) Experimental setup for measuring the Brillouin gain spectrum based on Ref. [6] (b) Measure Brillouin gain spectrum of a step-index, single-mode fiber. (c) The corresponding SBS threshold length dependence using measured results in (b) and Eq. 7.

Alternatively, Nikl s *et al.* developed an original approach for measuring the absolute magnitude of the gain spectrum in a manner that was insensitive to the polariza-

tion of the pump signal. As illustrated in Fig. 4c their method used a signal pass Brillouin amplifier where the pump signal counterpropagated with a carrier-suppressed replica (with sidebands offset near the Brillouin shift of the fiber under test). By sweeping the RF driving frequency of the electrooptic modulator used to generate the carrier suppressed probe signal they were able to measure the BGS and determine the peak gain coefficient. In light of this technique and from Eq. 7 it is reasonable to define a figure of merit for which most measurements characterizing SBS in different fiber types can be normalized as $g_{FOM}^B = \frac{g_B}{\alpha A_e}$. Thus a measurement of the gain factor alone can characterize the Brillouin spectral shape and linewidth, as well as determine the power threshold as a function of length using Eq. 7. as noted in Fig. 4.

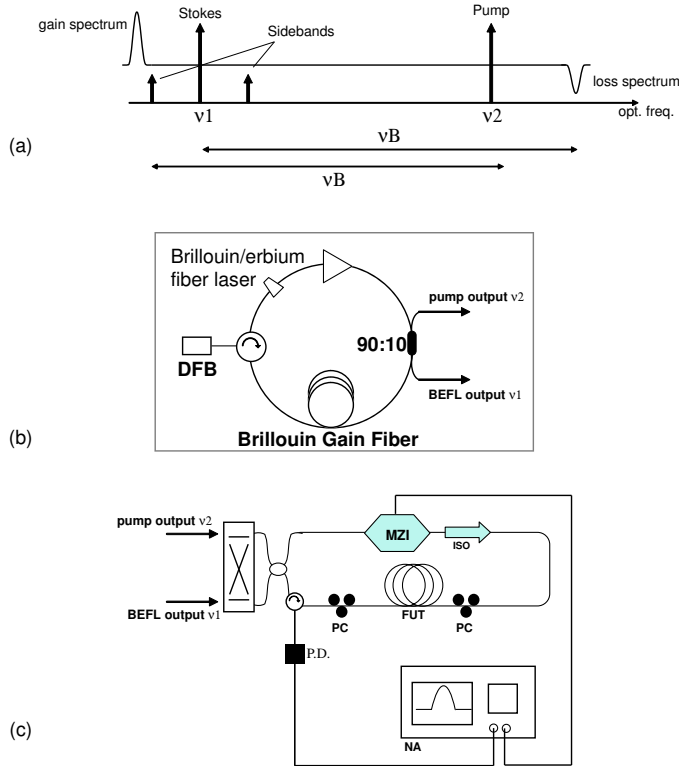


Fig. 5. (a) The basic concept of Loayssa *et al.* technique [18]; either a pump or Stokes wave is used to measure the Brillouin gain or loss close to an amplitude modulated carrier. (b) Brillouin-erbium fiber laser. (c) Setup of the Brillouin or loss spectrum, depending on the output of the BEFL. The spectrum is generated by sweeping the RF signal to the optical modulator.

Because the Brillouin gain spectrum is complex, a Hilbert transformation of the measured data can be used to derive the imaginary component, or ultimately obtain the magnitude of the SBS-induced phase shift. Alternatively, it is possible to directly measure the SBS-induced phase shift under various pump or Stokes intensity values. [7, 18]. Peral *et al.* experimental results confirmed that this phase shift originates from the imaginary part of the BGS,

$$\Delta\varphi(z) = -\frac{\text{Im}\{g_B\}}{2} \int_0^z |A_S|^2 dz. \quad (9)$$

Loayssa *et al.* developed a high resolution technique to di-

rectly measure the Brillouin gain spectrum, the loss spectrum of the pump signal, and the SBS-induced phase shift using the output of a Brillouin-Erbium fiber laser (BEFL) in concert with a Brillouin amplifier and network analyzer (NA). This system is illustrated in Fig. 5. Such a measurement technique is useful in applications where the phase of the optical carrier requires some manipulation (optical signal processing), or when characterizing the induced phase shift as a function of input pump power.

B. SBS-induced system limitations

Stimulated Brillouin scattering is known to grossly limit the design of several optical transmission systems, amplifiers, and lasers. As depicted by the output power plot in Fig. 3a, the generation of the Stokes signal during SBS process can induce a loss of power of the pump signal above the intrinsic fiber loss. This effect can obviously limit the maximum power that can be transported through an optical fiber which can impact the efficiency of fiber lasers, fiber parametric oscillators and dispersion compensation consisting of nonlinear fibers, and Raman amplifiers. In analog

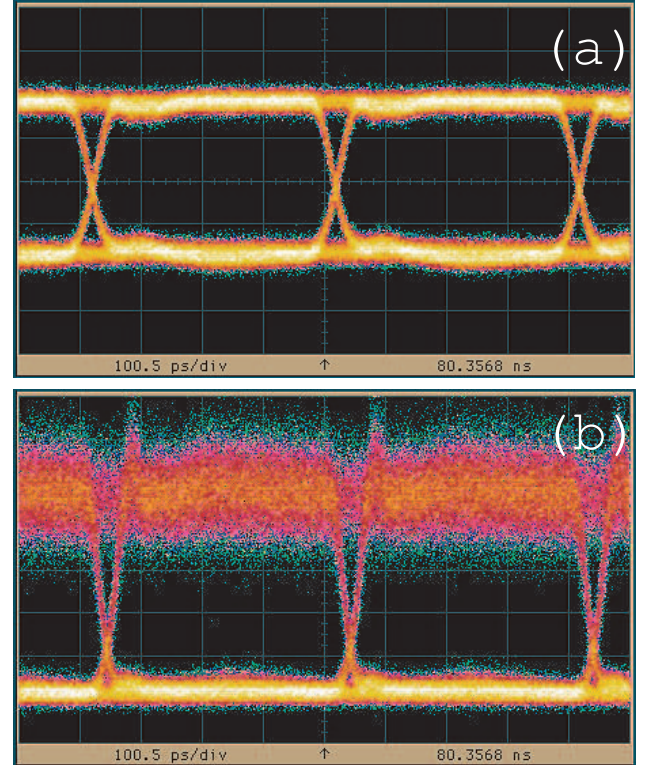


Fig. 6. An OC-48 signal propagated through 50-km of NZ-DSF with launch powers (a) below and (b) above the SBS threshold.

or digital lightwave communication systems the aforementioned phase shift of the carrier can exacerbate the total system relative intensity noise (RIN) [19, 20]. This rise in system RIN results from a conversion of phase noise to intensity noise due to mixing of the pump signal and Rayleigh scattered Stokes signal at the optical detector. This phenomena of SBS can drastically reduce the received signal quality. Digital optical systems can be susceptible to the

deleterious effects of SBS, but because the amplitude modulation format broadens the optical spectrum (thereby reducing the overall power in the optical carrier) these systems exhibit some resistance to SBS-induced noise [21]. For example, the SBS threshold for amplitude shift keying format is given by,

$$P_{th}^{ASK} = \frac{P_{th}^{CW}}{1 - \frac{B}{2\Delta\nu_B}(1 - e^{-\frac{\Delta\nu_B}{B}})} \quad (10)$$

where B is the bit rate of the modulation. Still, at high enough input the bit error ratio of these systems can degrade as a result of SBS adding noise on the 'one' level, as depicted in Fig. 6. Common approaches in both digital and analog communication systems to actively increase the SBS threshold in laser sources include phase modulation and bias dithering. However, these approaches are tempered by dispersion penalties resulting from an increased optical spectrum.

Analog lightwave (HFC/CATV) systems are especially susceptible to such SBS-induced impairments since these optical transmission systems are typically loss-limited and requires high launch powers to maintain acceptable signal quality levels at the receiver. The performance of an analog lightwave communication system is typically characterized using the carrier-to-noise ratio. Each element of the transmission link can contribute to the total noise spectral power such that the accumulative effect burdens the photoreceiver. Also the CSO (composite second-order) and CTB (composite triple beat) distortions are used to characterize the spurious beat product count of the received signal that arise as a result of nonlinear mixing of tones within the RF signal. The effects of SBS on the quality of a

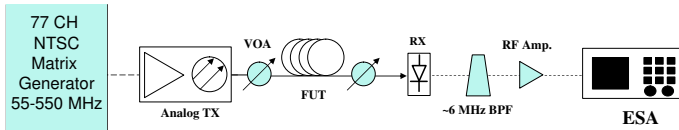


Fig. 7. Analog transmission experimental setup

video signal of an analog lightwave system are best demonstrated in the experimental configuration illustrated in Fig. 7. Here, a comb of 77 NTSC RF video carrier-signals drive a commercially-available,externally-modulated, analog transmitter, rated with an 18 dBm SBS threshold². A variable optical attenuator located after an EDFA (27 dBm, NF= 6 dB) was used to incrementally vary the output power of the transmitter over a range of powers before it was coupled into the fiber under test. A second VOA at the output of the fiber was used to maintain a constant power at the photoreceiver regardless of the power launched into the fiber. The converted electrical signal was then analyzed for the CNR, CSO, and CTB values by filtering the other 76 channels. The CNR, CSO, and CTB of a channel under test was then analyzed from the RF spectrum using an electrical spectrum analyzer. The results in Fig. 8

²The laser source used here actively increased the SBS threshold via phase modulation and bias dithering

illustrate the effects of SBS on CNR, CSO, and CTB metrics on RF video carriers over various input powers in two fiber types. The SBS-induced degradation on the CNR of the RF channels is largely due to a dramatic rise in the system's RIN levels, and not necessarily due to the additive loss resulting from pump depletion. However, SBS-induced pump depletion of the optical carrier exacerbates the second- and third-order distortions [22]. A comparison of the analog metrics in Fig. 8 shows that a 4 dB SBS threshold advantage can be passively achieved using Corning's NexCorTM fiber (G.652.D compliant) over standard G.652.D fiber. This passive means of SBS suppression compliments the active means employed in the transmitter to increase the SBS suppression beyond the rating of the transmitter. Here, we observe the onset of SBS-induced degradations at 17.5 dBm and 21.5 dBm, respectively for standard single mode fiber and the SBS suppressive fiber.

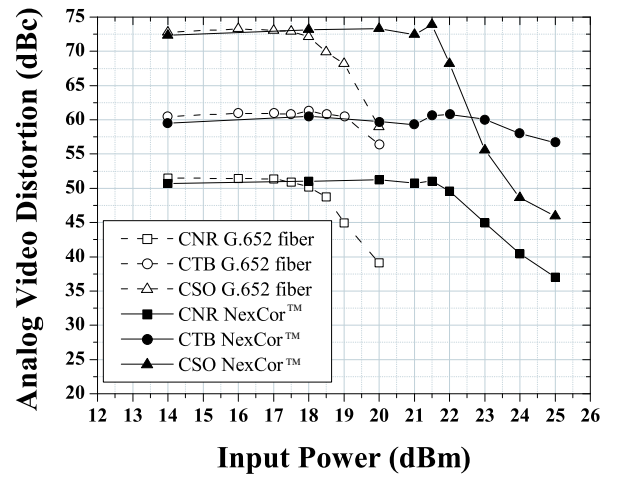


Fig. 8. (a) Comparison of CATV metrics on NTSC CH14 (121.25 MHz) as a function of launch power for two fiber G.652.D fibers.

C. Applications

Nonlinear phenomena in optical fibers can also be exploited for a wide variety of device and systems applications. For example, attributes such as the narrowband BGS and high nonlinear Brillouin coefficient make SBS in fibers ideal for wavelength conversion, frequency selectivity, carrier suppression, and amplification. The influence of temperature and strain on the peak gain value and Brillouin frequency shift has been recognized as ideal traits for distributed fiber sensors [23]. Microwave photonic systems have been developed to utilize the narrow BGS bandwidth in order to selectively amplify a weak data carrying optical sideband without perturbing an unmodulated carrier. At the photoreceiver these two signals can beat together to increase the modulation index of the received RF signal [24]. The Brillouin interaction can be used to nondestructively analyze attenuation characteristics in optical fiber using Brillouin optical-fiber time-domain (BOTDR) analysis using low power lasers; such methods exhibit high dynamic range in comparison to traditional OTDR methods [25]. Concepts such as optical carrier Brillouin processing

(OCBP) has recently been developed to control the amplitude and phase of the optical carrier of a modulated signal; such systems are implemented to suppress an optical carrier or to compensated for dispersion induced penalties in optical links [26]. Efficient, narrow linewidth, low frequency jitter Brillouin fiber lasers have also been developed for applications such as laser Doppler velocimetry, two-photon spectroscopy [27, 28].

III. SUMMARY

This paper discussed the fundamentals of stimulated Brillouin scattering and cited several measurement techniques to extract critical parameters such as the Brillouin gain coefficient and power threshold. System limitations resulting from SBS-induced noise for digital and analog optical communication systems were also considered. Optical signal processing methods, sensors, lasers, and other devices which have been developed to utilized the attributes of SBS were also noted.

REFERENCES

- [1] Robert Boyd. *Nonlinear Optics*. Academic Press, 1992.
- [2] G.P. Agrawal. *Nonlinear Fiber Optics*. Academic Press, 3rd edition, 2001.
- [3] A. Yeniay, M.-M. Delavaux, and J. Toulouse. Spontaneous and stimulated brillouin scattering gain spectra in optical fibers. *J. Lightwave Tech.*, 20(8):1425–1432, 2002.
- [4] R.W. Boyd, K. Rzaewski, and P. Narum. Noise initiation of stimulated brillouin scattering. *Phys. Rev. A*, 42(9):5514–5520, 1990.
- [5] R.G. Smith. Optical power handling capacity of low-loss optical fibers as determined by stimulated raman and brillouin scattering. *Appl. Opt.*, 11:2489–2494, 1972.
- [6] Marc Niklès, Luc Thénaz, and Philippe A. Robert. Brillouin gain spectrum characterization in single-mode optical fibers. *J. Lightwave Tech.*, 15(10):1842–1851, 1997.
- [7] Eva Peral and Amnon Yariv. Degradation of modulation and noise characteristics of semiconductor lasers after propagation in optical fiber due to a phase shift induced by stimulated brillouin scattering. *IEEE J. Quantum Elect.*, 35(8):1185–1195, 1999.
- [8] N. Shibata, K. Okamoto, and Y. Azuma. Longitudinal acoustic modes and brillouin-gain spectra for GeO_2 -doped-core single-mode fibers. *J. Opt. Soc. Am. B*, 6(6):1167, 1989.
- [9] E. Buckland. Mode-profile dependence of the electrostrictive response in fibers. *Opt. Lett.*, 24(13):872–874, 1999.
- [10] A. Kobaykov, M. Mehendale, M. Vasilyev, S. Tsuda, and A.F. Evans. Stimulated brillouin scattering in raman-pumped fibers: A theoretical approach. *J. Lightwave Tech.*, 20(8):1635–1643, 2002.
- [11] D. Cotter. Stimulated brillouin scattering in monomode optical fiber. *J. Opt. Comm.*, 4(1):10–19, 1983.
- [12] D. Cotter. Observation of stimulated brillouin scattering in low-loss silica fiber at $1.3 - \mu\text{m}$. *Elec. Lett.*, 18(12):495–496, 1982.
- [13] W.B. Gardner. Appendix on nonlinearities for G.650. ITU Document COM 15-273-E, ITU, 1996.
- [14] and S. Sato Y. Koyamada, S. Nakamura, and a nd W. Chujo H. Sotobayashi. Simulating and designing brillouin gain spectrum in single-mode fibers. *J. Lightwave Tech.*, 22(2):631–639, 2004.
- [15] R.S. Krishnan. *Nature*, page 933, 1950.
- [16] R.W. Tkach, A.R. Chraplyvy, and D.M. Derosier. Spontaneous brillouin scattering for single-mode optical fibre characterisation. *Elec. Lett.*, 22(19):1011–1013, 1986.
- [17] K. Rzaewski, M. Lewenstein, and M.G. Raymer. Statistics of stimulated stokes pulse energies in the steady-state regime. *Opt. Commun.*, 42(6):451–5454, 1982.
- [18] A. Loayssa, R. Hernández, D. Benito, and S. Galech. Characterization of stimulated brillouin scattering spectra by use of optical single-sideband modulation. *Opt. Lett.*, 29(6):638–640, 2004.
- [19] A.R. Chraplyvy. Limitation on lightwave communication imposed by optical fiber nonlinearities. *J. Lightwave Tech.*, 8(10):1548–1557, 1990.
- [20] M. Horowitz, A.R. Chraplyvy, and J.L. Zyskind. Broadband transmitted intensity noise induced by stokes and anti-stokes brillouin scattering in single-mode fibers. *IEEE Photonics Tech. Lett.*, 9(1):124–126, 1997.
- [21] D.A. Fishman and J.A. Nagel. Degradations due to stimulated brillouin scattering in multigigabit intensity-modulated fiber optic systems. *J. Lightwave Tech.*, 11(11):1721–17–28, 1993.
- [22] M.R. Phillips and D.M. Ott. Optical fiber nonlinearities in 1550 nm analog transmission systems. In *European Conference on Optical Communications, Technical Digest*, pages II–190. Institute of Electrical and Electronics Engineers, 1999.
- [23] M. Niklès, L. Thèvenaz, and P.A. Robert. Simple distributed fiber sensor based on brillouin gain spectrum analysis. *Opt. Lett.*, 21(10):758–760, 1996.
- [24] X.S. Yao. Brillouin selective sideband amplification of microwave photonic signals. *Photonic Tech. Lett.*, 10(1):138–140, 1998.
- [25] T. Horiguchi and M. Tateda. Botda-nondestructive measurement of single-mode optical fiber attenuation characteristics using brillouin interaction: Theory. *J. Lightwave Tech.*, 7(8):1170–1176, 1989.
- [26] A. Loayssa, D. Benito, and M.J. Garde. Applications of optical carrier brillouin processing in microwave photonics. *Opt. Fiber Tech.*, 8, 2002.
- [27] J.C Yong, L. Thèvenaz, and B.Y. Kim. Brillouin fiber laser pumped by a dfb laser diode. *J. Lightwave Tech.*, 21(2):546–554, 2003.
- [28] S.P. Smith, Z. Zarinetchi, and S. Ezekiel. Narrow-linewidth stimulated brillouin fiber laser and applications. *Opt. Lett.*, 16(6):393–395, 1991.

Coherence effect on the measurement of optical fiber nonlinear coefficient in continuous-wave dual frequency method

Seung Kwan Kim, Han Seb Moon, Ryun Kyung Kim, Jung-Chul Seo

Center for Information and Telecommunication Standards

Korea Research Institute of Standards and Science

1 Doryong-Dong, Yuseong-Gu, Daejeon 305-340, Korea

Tel: +82-42-868-5701; Fax: +82-42-868-5022; skkfiber@kriss.re.kr

We examined the source coherence effect on the optical fiber nonlinear coefficient measurement in a direct continuous-wave dual frequency method. Highly coherent dual frequency source was constructed with an external cavity laser diode and an acousto-optic frequency shifter. In a highly coherent case, we obtained nonlinear coefficients of ~ 3 % higher than those of an incoherent case.

Continuous-wave dual frequency methods (CWDFM's) based on the self phase modulation effect can offer simple direct measurement of optical fiber nonlinear coefficient with moderate accuracy [1-3]. Two optical frequency components produce a beat signal that propagates through an optical fiber experiencing frequency chirp owing to the intensity dependent refractive index. The frequency chirp produces side bands in wavelength domain that can be easily measured by an optical spectrum analyzer (OSA).

The two optical frequencies are normally prepared with two independent laser sources, such as distributed feedback laser diodes (DFB LD's) [1] and external cavity laser diodes (ECL's) [2]. Since the laser source has finite coherence time, the beat signal of the two independent laser sources has random phase change and frequency jitter. They may affect the determination of nonlinear coefficient because CWDFM assumes that each frequency component is monochromatic.

In this paper, we constructed highly coherent dual frequency source using an ECL and an acousto-optic frequency shifter (AOFS), and examined how the laser coherence would affect the optical fiber nonlinear coefficient measurement.

The dual frequency source used in this experiment is shown in Fig. 1. One of the dual laser outputs of an ECL (Agilent 81640A) was split by a 3-dB coupler, and delivered into an AOFS (IntraAction 501E5C) with a frequency shift of 50 MHz and a variable optical attenuator, respectively. The two output ports were connected to a conventional CWDFM setup. The fiber under test (FUT) was a 1 km-long non-zero dispersion shifted fiber with a chromatic dispersion of 7.9 ps/nm/km and an attenuation of 0.21 dB/km at 1550 nm.

Since the two frequencies were separated by 50 MHz, we analyzed the final output signal with a radio frequency spectrum analyzer (RFSA, Agilent E4440A) instead of an OSA after detecting the light by an InGaAs pin photo-receiver (New Focus 1611) with a bandwidth of 1 GHz. In order to view the fundamental modes and 1st side modes

simultaneously, we combined the output from the FUT with another output from the ECL after shifting the optical frequency by another AOFS (Brimrose AMM-150) with a frequency shift of 150 MHz, opposite sign to the previous one. Then, the beat signal between the fundamental modes of the dual frequency source appeared at 50 MHz, the beat signal between ECL and the fundamental modes at 150 and 200 MHz, and the beat signal between ECL and the 1st side modes at 100 and 250 MHz, respectively, as shown in Fig. 2.

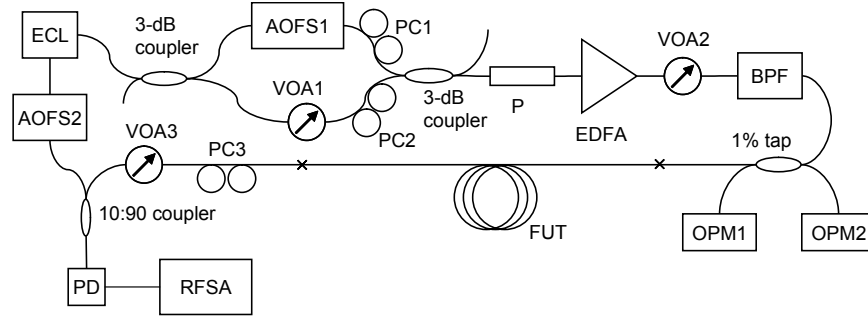


Fig. 1. Experimental setup for the highly coherent CWDFM. AOFS, acousto-optic frequency shifter; BPF, band pass filter; ECL, external cavity laser diode; EDFA, Erbium-doped fiber amplifier; FUT, fiber under test; OPM, optical power meter; P, polarizer; PD, photo diode; RFSA, RF spectrum analyzer; VOA, variable optical attenuator.

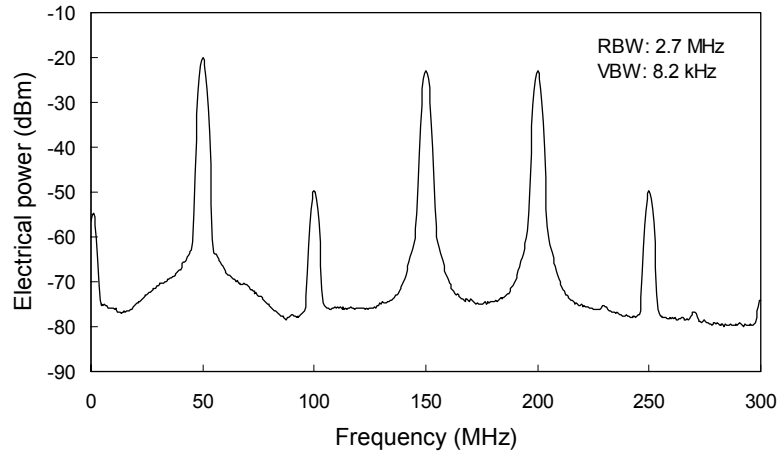


Fig. 2. RF spectrum showing beat signals between ECL and the output from FUT (Input power = 55 mW).

Since the RFSA measures the electrical power of the signal delivered by the photo-receiver as a function of electrical frequency, each spectral power on the RFSA is proportional to the optical power of each mode from the FUT multiplied by the optical power of the frequency shifted ECL mode. Therefore, the nonlinear phase shift can be calculated by the electrical power ratio of 1st side mode to the fundamental mode.

The nonlinear phase shifts were plotted as a function of input power as shown in Fig. 3 for five independent measurements. The data points for linear fitting were chosen in the range between 20 mW and 60 mW considering

signal-to-noise ratio and stimulated Brillouin scattering induced error. The slope was determined to be 3.155 ± 0.015 rad/W and the corresponding nonlinear coefficient was calculated to be $3.98 \pm 0.02 \times 10^{-10}$ W⁻¹. The nonlinear refractive index n_2 was then calculated to be $2.54 \pm 0.01 \times 10^{-20}$ m²/W assuming the measured effective area of $63.9 \mu\text{m}^2$ is correct.

When two DFB LD's were used with 0.2 nm separation for CWDFM, the slope of the same FUT was measured to be 2.72 rad/W and the corresponding nonlinear refractive index was 2.19×10^{-20} m²/W. The discrepancy of 16.0 % is mainly caused by electrostrictive nonlinearity contribution because the frequency of the beat signal in the FUT was far less than 1 GHz [4].

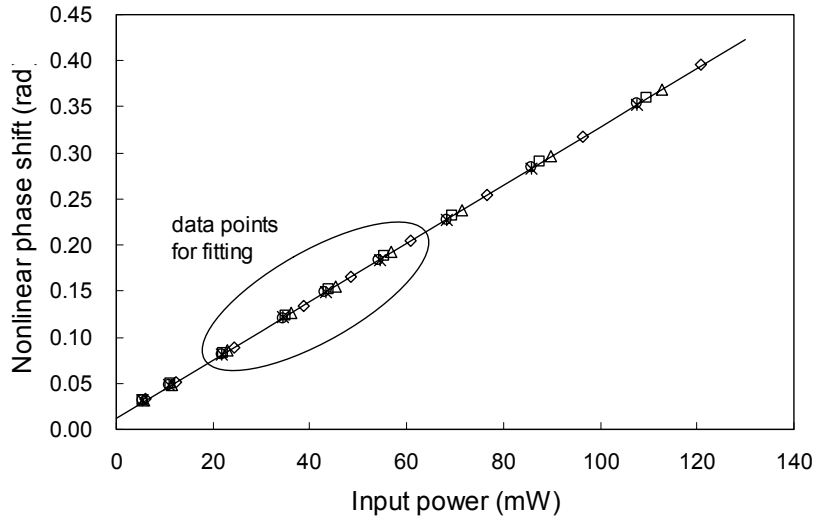


Fig. 3. Nonlinear phase shift versus input power. Solid lines are linear fitting curves. Symbols correspond to five independent measurements.

In order to examine the source coherence effect, we inserted a 22.5 km-long fiber delay line of ordinary single mode fiber between AOFS1 and PC1. Since the two frequency components became incoherent, the beat signal generated by them exhibited optical phase fluctuation and frequency jitter. The beat note at 50 MHz on the RFSA showed the maximum frequency jitter was ~ 3 MHz, that is approximately the twice of the long term line width of the ECL. Accordingly, the beat note at 250 MHz, that was the frequency of 1st side mode, showed the maximum frequency jitter of ~ 6 MHz, twice of the frequency jitter at 50 MHz.

The slope of the nonlinear phase shift versus input power was determined to be 3.054 ± 0.042 rad/W, that was 3.2 % lower than the case without delay. Relative deviation of all the data points from the fitting line without delay was plotted in Fig. 4 showing that the relative difference of 3.2 % was clearly outside of the deviation of each data group.

These experimental results compare the coherent case with the incoherent case for low frequency separation (50 MHz), so that the electrostrictive nonlinearity contribution is involved in the measured nonlinear coefficients. We

are able to say that the source coherence does affect the accuracy of the overall nonlinear coefficient measurement using CWDFM. However, it is not yet resolved whether the source coherence effect does influence the Kerr type nonlinear coefficient measurement which is interested in optical fiber communications. Highly coherent optical dual frequency generation in > 10 GHz range can resolve the problem by suppressing the electrostrictive contribution.

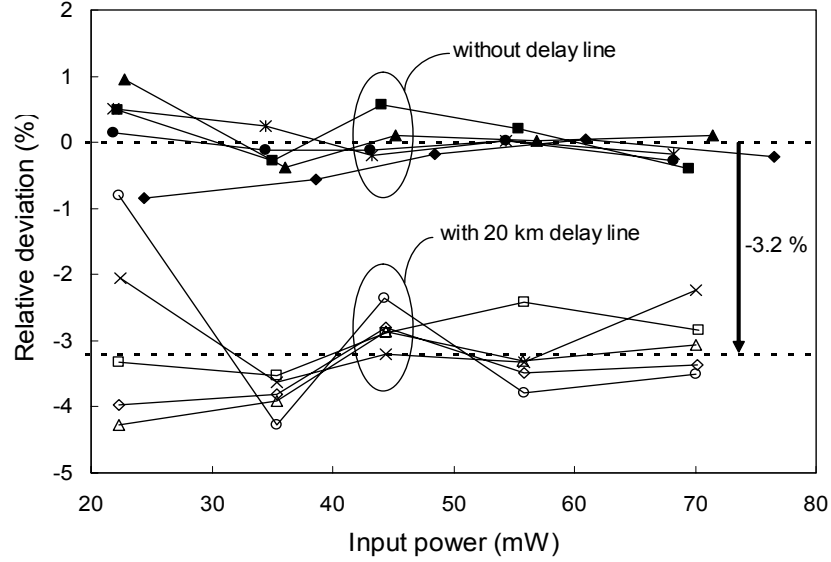


Fig. 4. Relative deviations of measured nonlinear phase shifts from average fitting line without delay.

In conclusion, we examined the source coherence effect on the measurement of optical fiber nonlinear coefficient using CWDFM by comparing the case of using highly coherent dual frequency source with that of incoherent source. We determined that the CWDFM with two independent laser source may measure smaller nonlinear coefficient than the correct value by $\sim 3\%$.

REFERENCES

- [1] A. Boskovic, et. al., Opt. Lett. 21 (24), 1966 (1996).
- [2] D. L. Philen, Technical Digest of SOFM 2000, NIST Special Publication 953, 39 (2000).
- [3] T. Omae, K. Nakajima, and M. Ohashi, IEEE Photon. Technol. Lett. 13 (6), 571 (2001).
- [4] E. L. Buckland and R. W. Boyd, Opt. Lett. 21 (5), 1117 (1996).

ITU-T Round Robin Measurement for Nonlinear Coefficient (n_2/A_{eff}) of various Single Mode Optical Fibers

Yoshinori Namihiro

University of the Ryukyus, 1 Senbaru, Nishihara, Okinawa 903-0213, Japan
Phone/Fax: +81-98-895-8700, E-mail: namihiro@eee.u-ryukyu.ac.jp

Abstract Final report of ITU-T round robin measurement for nonlinear coefficient (n_2/A_{eff}) of various optical fibers using Pulsed-LD SPM, CW-LD SPM, XPM and Modulated signal-SPM methods is presented. The relationship between (n_2/A_{eff}) and effective area (A_{eff}), and also between nonlinear refractive index n_2 and A_{eff} are first demonstrated.

Introduction: Accurate determination of the nonlinear coefficient (n_2/A_{eff}) { n_2 is the nonlinear refractive index, A_{eff} is the effective area } of optical fibers is required for the ultra-long amplified optical transmission systems. To date, the (n_2/A_{eff}) has been measured by using the self-phase modulation (SPM) method with a pulsed laser diode (LD) (P-SPM) [1,2], the SPM method with dual CW-LDs (CW-SPM) [3], the cross-phase modulation (XPM) method [4], self-aligned Interferometric (INT) method [5], four wave mixing (FWM) method [6], and modulated signal-SPM (M-SPM) method [7,8].

To compare these methods, ITU-T round robin measurements of (n_2/A_{eff}) and n_2 of various optical fibers, coordinated by Y. Namihiro of Univ. of the Ryukyus (formerly KDD) have been successfully performed [9-11].

This paper presents the final report of ITU-T round robin measurements for (n_2/A_{eff}) of various optical fibers such as standard single mode fiber (SMF), cut-off shifted fiber (CSF), dispersion shifted fiber (DSF), non-zero DSF (NZDSF) and large effective area DSF (LEDSF), and dispersion compensating fiber (DCF) using four different techniques such as the P-SPM [1,2], CW-SPM [3], XPM [4], and M-SPM [7,8] methods at 1550nm.

Experiments and methods: The experimental set-up of the (n_2/A_{eff}) measurements for various single mode optical fibers is shown in Fig.1. In Fig.1, (a), (b), (c) and (d) are P-SPM method, CW-SPM method, XPM method, and M-SPM method, respectively. Here, n_2 can be estimated by (n_2/A_{eff}) multiplying the A_{eff} [11]. The A_{eff} was measured by the far-field scan (FFS) technique [12]. The A_{eff} values of six kinds of single mode optical fibers are shown in Tables 1 and 2. These fibers were circulated to the twelve Laboratories such as University of the Ryukyus, KDD, NTT, Furukawa, Fujikura, Sumitomo, and Muroran Institute of Technology in Japan, University of Geneva and Pirelli Labs., in EU and Tyco Submarine Systems Labs., Corning OFS Fitel (formerly Lucent Technology) in USA. However, Interferometric method [4] from University of Geneva, FWM method [5] from Muroran Institute of Technology, and the results of OFS Fitel were not included in this paper because of measurement accuracy and other reasons.

1) P-SPM method: In Fig.1(a), the mode-locked Nd:YAG laser was used as light source [1]. The output optical pulse due to SPM was measured by the optical spectrum analyzer (OSA). As the input optical power increases, the maximum phase shift increases in proportion to the input peak power. The (n_2/A_{eff}) can be obtained from the numbers of peaks in the SPM broadened spectra [1].

2) CW-SPM method: In Fig.1(b), the optical beat signal was derived from dual CW-LDs operating at around 1550nm [3]. The beat signal was then amplified by a preamplifier (EDFA) and transmitted through an optical band pass filter to suppress the amplified stimulated emission and a polarizer to a following high power EDFA.

3) XPM method: In Fig.1(c), the probe signal power is set relatively weak so that the (n_2/A_{eff}) is dominantly caused by amplified strong pump CW-LD through XPM and that the effect of SPM is negligible. When pump CW-LD or CW-SLD is modulated in its intensity, probe CW-LD is modulated in this phase through XPM [4].

4) M-SPM method: In Fig.1 (d), the M-SPM method is based on SPM effect estimation. This technique consists simply in propagating an optical signal modulated by means of an electro-optical LiNbO₃ modulator. The γ -factor estimation is achieved using a simulation tool capable of reproducing the evolution of signal spectra along the fiber and doing a comparison between acquired experimental data and simulation result [7,8].

Results and discussions: The results of ITU-T round robin measurements for (n_2/A_{eff}) and n_2 at 1550nm in random polarization states (RP) using four different techniques of the P-SPM, CW-SPM, XPM, and M-SPM for a SMF, a CSF, two kinds of DSFs, two kinds of NZDSFs, a LEDSF and a DCF at 1550nm are summarized in Tables 1 and 2, respectively.

In Tables 1 and 2, $n_2(\text{RP}) = \eta n_2(\text{LP})$, $\eta = 1.0$ for P-SPM, $\eta = 8/9$ for CW-SPM and M-SPM, and the polarization factor $\eta = 2/3$ for XPM were used [11]. Here, LP represents the linear polarization state.

Fig. 2 shows measured values of (n_2/A_{eff}) at 1550nm in random polarization states for various optical fibers as a function of the A_{eff} values of various optical fibers.

The relationship between (n_2/A_{eff}) and A_{eff} can be expressed as empirical equation:

$$(n_2/A_{\text{eff}}) = \alpha A_{\text{eff}}^{-\beta} \quad [x \cdot 10^{-10} \text{ W}^{-1}] \quad (1)$$

where, $\alpha \cong 420 [W^{-1} \mu\text{m}^{-(2-\beta)}]$, $\beta \cong 1.15$, $A_{\text{eff}} [\mu\text{m}^2]$

Fig. 3 indicates the estimated values of n_2 at 1550nm in random polarization states for four different measurement methods as a function of the A_{eff} values for various optical fibers.

The empirical equation between n_2 and A_{eff} can be expressed as

$$n_2 = (\alpha/100) A_{\text{eff}}^{-(\beta-1)} \quad [x \cdot 10^{-20} \text{ m}^2/\text{W}] \quad (2)$$

where, $\alpha \cong 420 [W^{-1} \mu\text{m}^{-(2-\beta)}]$, $\beta \cong 1.15$, $A_{\text{eff}} [\mu\text{m}^2]$

From Tables 1 and 2, it was found that the average values of (n_2/A_{eff}) at RP of SMF, CSF, DSF1, DSF2, NZDSF1, NZDSF2, LEDSF and DCF were $\sim 2.55, 2.28, 4.94, 5.07, 4.07, 4.46, 3.14$ and $12.0 \times 10^{-10} [1/\text{W}]$, respectively. Also, the averaged values of n_2 at RP for SMF, CSF, DSF1, DSF2, NZDSF1, NZDSF2, LEDSF and DCF were $\sim 2.21, 2.14, 2.25, 2.31, 2.32$, and $2.78 \times 10^{-20} [\text{m}^2/\text{W}]$, respectively.

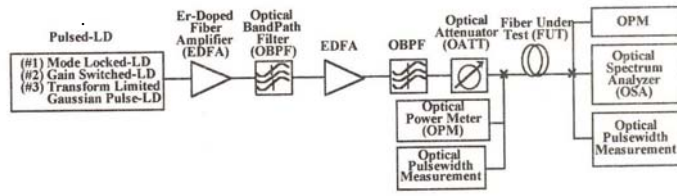
In Tables 1 and 2, Offset (%) = (Each measured values – Participant's averaged values) / Participant's averaged values $\times 100$ (%). Zero (%) means the same as the Participant's averaged values. The offset value of CW-SPM1 method was the best method, the values was less than 4.5%. The next groups are the P-SPM, CW-SPM2, CW-SPM3, the offset value was less than 5% except for one fiber sample was less than 8.9%. The third group was M-SPM1, the offset value was less than 5% except for two fiber samples were less than 10%. The last groups of CW-SPM4, XPM1, XPM2, and M-SPM2 were very scattered, the offset values were less than 16%.

Conclusions: From the ITU-T round robin nonlinear coefficient (n_2/A_{eff}) measurement for various optical fibers, the P-SPM, CW-SPM-1, 2, 3 and M-SPM1 were found to be more accurate measurement method than the XPM-1, 2 and M-SPM2 methods. The relationship between (n_2/A_{eff}) and A_{eff} , and n_2 and A_{eff} were first proposed as empirical equation of $(n_2/A_{\text{eff}}) = \alpha A_{\text{eff}}^{-\beta} [x \cdot 10^{-10} 1/\text{W}]$, and $n_2 = (\alpha/100) A_{\text{eff}}^{-(\beta-1)} [x \cdot 10^{-20} \text{ m}^2/\text{W}]$, respectively. It was confirmed that the average values n_2 at 1550nm in random polarization state obtained from these different methods were $2.0 \sim 2.3 \times 10^{-20} [\text{m}^2/\text{W}]$ for SMF, CSF, DSF1, DSF2, NZDSF1, NZDSF2 and LEDSF except for DCF of $\sim 3.0 \times 10^{-20} [\text{m}^2/\text{W}]$, respectively.

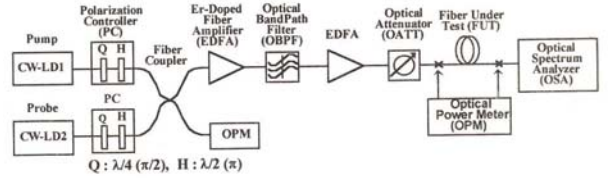
Acknowledgements: Author express special thanks to the following organizations: KDD, NTT, Fujikura, Furukawa, Sumitomo, Univ. of Muroran Institute of Technology and Univ. of the Ryukyu in Japan, University of Geneva and Pirelli Labs., in EU and Tyco Submarine Systems Labs., Corning and OFS Fitel in USA, also thanks Mr. K. Nakachi of Univ. of the Ryukyus for his cooperation.

References :

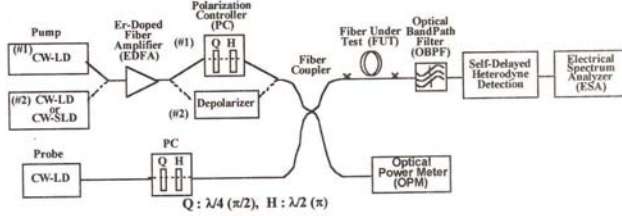
- [1] K. S. Kim et al., "Measurement of the non-linear index of silica core and dispersion-shifted fibers," Optics Lett., vol.19, no.14, pp.257-259, 1994.
- [2] Y. Namihiro et al., "Nonlinear coefficient measurements for dispersion shifted fibres using self-phase modulation method at 1.55 μm ," Electron. Lett., vol.30, no.14, pp.1171-1172, 1994.
- [3] A. Boskovic, et al., "Direct continuous-wave measurement of n_2 in various types of telecommunication fiber at 1.55 μm ," Optics Letters, vol. 21, no. 24, pp. 1966-1968, 1996.
- [4] T. Kato et al., "Measurement of nonlinear refractive index in optical fibers by cross phase modulation method using depolarized pump light," Optics Lett., 20, p.988, 1995.
- [5] C. Vinegoni et al., "Interlaboratory measurements of the nonlinear coefficient of standard SMF and DSF fibers using an interferometric method and an SPM based cw dual-frequency method", OFMC'01, pp.59-62, Cambridge, UK, 2001.
- [6] K. Kawanami et al., "Polarization effects on determination of nonlinear refractive index by four-wave mixing in a dispersion shifted fiber", OECC'02, Yokohama, Japan, 2002.
- [7] Y. Namihiro et al., "Novel fibre nonlinear coefficient (n_2/A_{eff}) measurement technique based on SPM method with modulated signal", submitted to Electron. Lett., 2004.
- [8] G. Pietra: "Sinusoidally modulated SPM method", Private communications, May, 2002.
- [9] Y. Namihiro et al., "Interim report of ITU-T nonlinear coefficient (n_2/A_{eff}) round robin measurement results in Japan", OFMC'01, pp.63-66, Cambridge, UK, 2001.
- [10] Y. Namihiro, et al., "A comparison of six techniques for nonlinear coefficient measurements for various optical fibers in Japan, USA, Switzerland and Italy", ECOC/IOOC 2003, We4, P.40, p.636-637, Rimini, Italy, 2003.
- [11] Y. Namihiro: "ITU-T nonlinear coefficient (n_2/A_{eff}) round robin measurements of various single mode optical fibers", SOFM, NIST, p.15-18, 2002.
- [12] Y. Namihiro: "Relationship between nonlinear effective area and mode field diameter for dispersion shifted fibers", Electron. Lett., vol.30, no.3, p.262, 1994



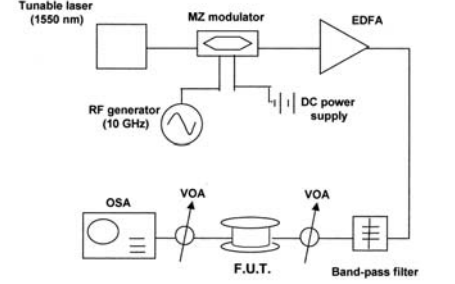
(a) Pulsed-LD SPM (P-SPM)



(b) CW-LD SPM (CW-SPM)



(c) XPM method



(d) Modulated signal SPM (M-SPM)

Fig.1 Experimental set up for four different (n_2/A_{eff}) measurement methods.

(a) Pulsed LD SPM(P-SPM), (b) CW-LD SPM (CW-SPM), (c) XPM, (d) Modulated signal SPM (M-SPM)

Table 1 Measured values of (n_2/A_{eff}) at 1550nm in random polarization states for various optical fibers using four different methods.

Fibers	Effective Area	Measurement Methods for Nonlinear Coefficient (n_2/A_{eff})																		Ave $\times 10^{-10}$ [1/W]	σ $\times 10^{-10}$ [1/W]
		P-SPM		CW-SPM1		CW-SPM2		CW-SPM3		CW-SPM4		XPM1		XPM2		M-SPM1		M-SPM2			
	$(n_2/A_{eff}) \times 10^{10}$ [1/W]	$(n_2/A_{eff}) \times 10^{10}$ [1/W]	$(n_2/A_{eff}) \times 10^{10}$ [1/W]	$(n_2/A_{eff}) \times 10^{10}$ [1/W]	$(n_2/A_{eff}) \times 10^{10}$ [1/W]	$(n_2/A_{eff}) \times 10^{10}$ [1/W]	$(n_2/A_{eff}) \times 10^{10}$ [1/W]	$(n_2/A_{eff}) \times 10^{10}$ [1/W]	$(n_2/A_{eff}) \times 10^{10}$ [1/W]	$(n_2/A_{eff}) \times 10^{10}$ [1/W]	$(n_2/A_{eff}) \times 10^{10}$ [1/W]	$(n_2/A_{eff}) \times 10^{10}$ [1/W]	$(n_2/A_{eff}) \times 10^{10}$ [1/W]	$(n_2/A_{eff}) \times 10^{10}$ [1/W]	$(n_2/A_{eff}) \times 10^{10}$ [1/W]	$(n_2/A_{eff}) \times 10^{10}$ [1/W]	$(n_2/A_{eff}) \times 10^{10}$ [1/W]				
	Measured	Offset(%)	Measured	Offset(%)	Measured	Offset(%)	Measured	Offset(%)	Measured	Offset(%)	Measured	Offset(%)	Measured	Offset(%)	Measured	Offset(%)	Measured	Offset(%)			
SMF	84.6	2.62	2.75	2.58	1.18	2.61	2.35	2.54	-0.39	2.66	4.31	2.50	-1.96	2.39	-6.27	2.61	2.35	2.90	13.73	2.55	0.97
CSF	88.5	2.45	7.46	2.39	4.82	2.21	-3.07	2.32	1.75	2.33	2.19	2.05	-10.09	2.23	-2.19	2.51	10.22	2.65	16.23	2.28	0.13
DSF1	46.7	4.81	-2.63	5.15	4.25	4.77	-3.44	5.10	3.24	5.36	8.50	4.59	-7.09	4.78	-3.24	4.76	-3.68	5.05	2.23	4.94	0.27
DSF2	45.6	4.88	-3.75	5.30	4.54	5.05	-0.39	5.15	1.58	5.60	10.45	4.56	-10.06	4.92	-2.96	4.73	-6.80	5.12	0.99	5.07	0.33
NZDSF1	55.5	4.08	0.25	4.13	1.47	4.43	8.85	4.22	3.69	4.24	4.18	3.51	-13.76	3.88	-4.67	3.99	-1.97	4.75	16.71	4.07	0.30
NZDSF2	51.3	4.31	-3.36	4.54	1.79	4.63	3.73	4.73	6.05	4.91	10.09	3.98	-10.76	4.15	-6.95	4.36	-2.24	4.75	6.50	4.46	0.33
LEDSF	72.7	3.01	-4.14	3.15	0.32	3.16	0.52	3.32	5.73	3.37	7.32	3.11	-0.96	2.89	-7.96	3.06	-2.55	3.51	11.78	3.14	0.17
DCF	22.8	11.90	-0.83	11.60	-3.33	12.37	3.11	11.30	-5.83	10.90	-9.17	12.82	6.83	13.18	9.83	11.44	-4.67	10.12	-15.67	12.00	0.81

Table 2 Estimated values of n_2 at 1550nm in random polarization states for various optical fibers using four different methods.

Fibers	Effective Area	Measurement Methods for Nonlinear Refractive Index n_2																		Ave $\times 10^{-20}$ [m ² /W]	σ $\times 10^{-20}$ [m ² /W]
		P-SPM		CW-SPM1		CW-SPM2		CW-SPM3		CW-SPM4		XPM1		XPM2		M-SPM1		M-SPM2			
	(A_{eff}) [μm ²]	(n_2) $\times 10^{-20}$ [m ² /W]	(n_2) $\times 10^{-20}$ [m ² /W]	(n_2) $\times 10^{-20}$ [m ² /W]	(n_2) $\times 10^{-20}$ [m ² /W]	(n_2) $\times 10^{-20}$ [m ² /W]	(n_2) $\times 10^{-20}$ [m ² /W]	(n_2) $\times 10^{-20}$ [m ² /W]	(n_2) $\times 10^{-20}$ [m ² /W]	(n_2) $\times 10^{-20}$ [m ² /W]	(n_2) $\times 10^{-20}$ [m ² /W]	(n_2) $\times 10^{-20}$ [m ² /W]	(n_2) $\times 10^{-20}$ [m ² /W]	(n_2) $\times 10^{-20}$ [m ² /W]	(n_2) $\times 10^{-20}$ [m ² /W]	(n_2) $\times 10^{-20}$ [m ² /W]					
	@ 1550nm	Measured	Offset(%)	Measured	Offset(%)	Measured	Offset(%)	Measured	Offset(%)	Measured	Offset(%)	Measured	Offset(%)	Measured	Offset(%)	Measured	Offset(%)	Measured	Offset(%)		
SMF	84.6	2.21	2.31	2.18	0.93	2.21	2.31	2.15	-0.46	2.25	4.17	2.11	-2.31	2.02	-6.48	2.20	1.85	2.45	13.43	2.16	0.08
CSF	88.5	2.16	7.46	2.11	4.98	1.96	-2.49	2.05	1.99	2.05	1.99	1.80	-10.45	1.97	-1.99	2.21	9.95	2.34	16.42	2.01	0.12
DSF1	46.7	2.25	-2.60	2.41	4.33	2.23	-3.46	2.39	3.46	2.52	9.09	2.14	-7.36	2.23	-3.46	2.22	-3.90	2.36	2.16	2.31	0.13
DSF2	45.6	2.24	-3.86	2.44	4.72	2.32	-0.24	2.37	1.72	2.57	10.30	2.08	-10.73	2.25	-3.43	2.16	-7.30	2.33	0.00	2.33	0.16
NZDSF1	55.5	2.27	0.44	2.30	1.77	2.47	9.29	2.35	3.98	2.36	4.42	1.95	-13.72	2.15	-4.87	2.22	-1.77	2.63	16.37	2.26	0.17
NZDSF2	51.3	2.24	-3.03	2.35	1.73	2.40	3.90	2.45	6.06	2.54	9.96	2.04	-11.69	2.13	-7.79	2.23	-3.46	2.43	5.19	2.31	0.18
LEDSF	72.7	2.26	-1.74	2.29	-0.43	2.30	0.00	2.42	5.22	2.46	6.96	2.26	-1.74	2.10	-8.70	2.22	-3.48	2.55	10.87	2.30	0.12
DCF	22.8	2.73	-1.09	2.68	-2.90	2.84	2.90	2.60	-5.80	2.52	-8.70	2.92	5.80	3.01	9.06	2.60	-5.80	2.31	-16.30	2.76	0.17

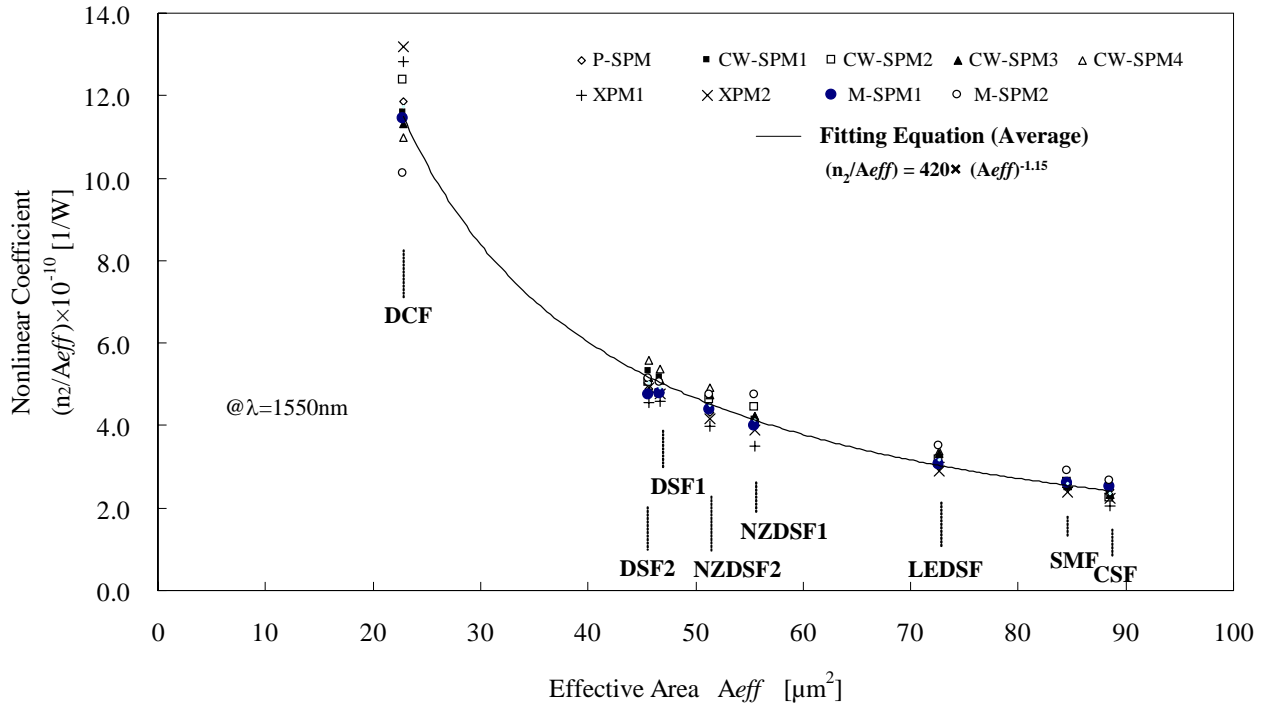


Fig.2 Measured values of (n_2/A_{eff}) at 1550nm in random polarization states for various optical fibers as a function of four different measurement methods.

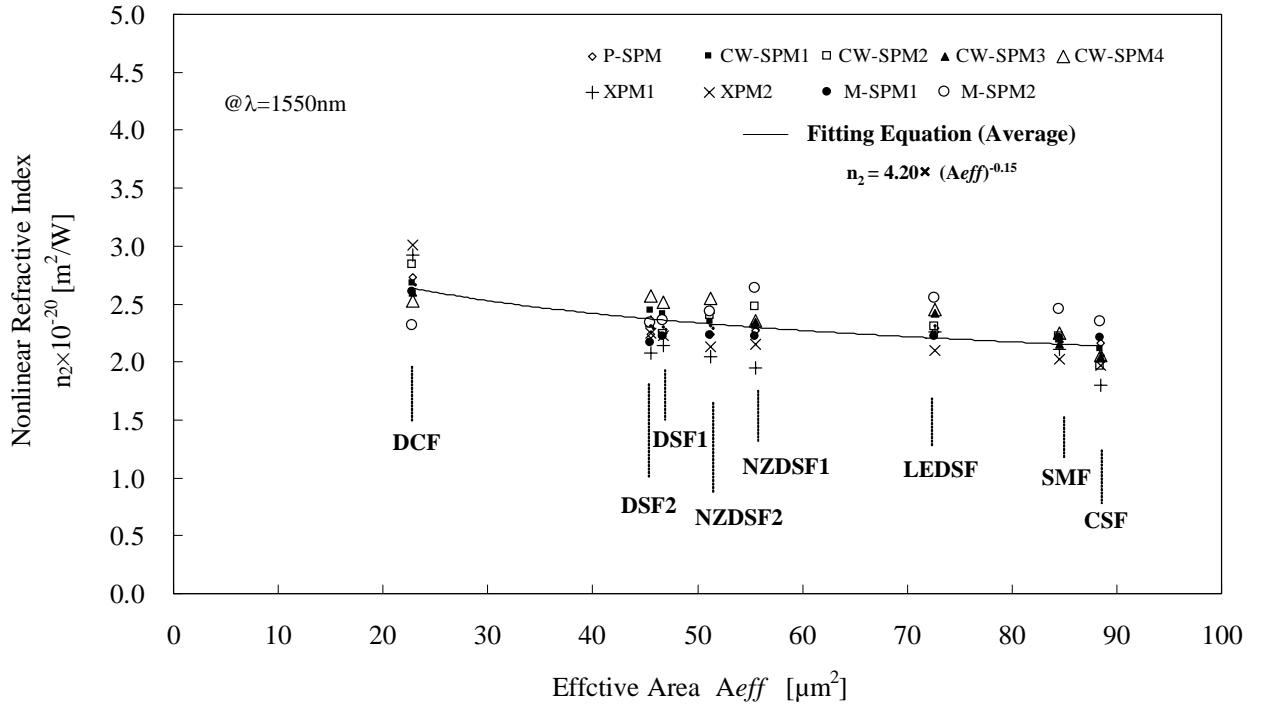


Fig.3 Estimated values of n_2 at 1550nm in random polarization states for four different measurement methods as a function of various single mode optical fibers.

Broadband continuous-wave source based on fiber nonlinearity

M. González-Herráez, S. Martín-López, P. Corredera, M. L. Hernanz and A. Carrasco
Instituto de Física Aplicada, CSIC. Serrano 144, 28006 Madrid. Spain

A supercontinuum, nearly flat spectrum covering the S, C and L transmission bands of the optical fiber is obtained by pumping a conventional nonzero dispersion-shifted fiber with a continuous-wave Raman fiber laser tuned to the region of small anomalous dispersion. By using a long fiber with low loss, complete power transfer from the pump to the supercontinuum is reached. We demonstrate that this supercontinuum can be used to perform accurate, long-range (> 200 km) measurements of polarization mode dispersion in fibers.

1 Introduction

Supercontinuum (SC) generation in optical fibers and waveguides is a phenomenon of increasing interest that has found applications in fields like time-resolved spectroscopy [1], ultrashort pulse compression [2], multiwavelength optical sources for WDM [3] and optical frequency metrology [4]. Most of the experiments performed up to now have been accomplished using pulsed laser sources and special fibers; in reference [5], for example, supercontinuum generation over 600 nm in the visible-near infrared region was obtained with short lengths of a specially designed photonic crystal fiber. Supercontinuum generation using continuous-wave laser sources was demonstrated only recently [6, 7], but the initial results demonstrate that powerful, broadband supercontinua (more than 250 nm in [7]) can be achieved with good long-term stability. In this paper we use a continuous wave source at 1455.3 nm to pump a fiber with small anomalous dispersion. The output supercontinuum covers the S, C and L transmission bands of the optical fiber. We believe that such a source can have very interesting applications in optical fiber characterization. As a sample application, we show that this source can be used to measure polarization mode dispersion (PMD) accurately with a very large dynamic range (> 50 dB).

In our pumping conditions, supercontinuum generation is caused by the combined effect of modulational instability and Raman processes. These processes are both stimulated, and so they can be thought of as seeded by the pump laser noise and spontaneous photons emitted along the fiber. Efficient generation of a broad modulational instability spectrum can only be achieved in the region of very small anomalous dispersion ($D > 0$ or $\beta_2 < 0$). Photonic crystal fibers can be easily designed to show the adequate dispersion and nonlinearity properties in the desired wavelength range. Although losses and guidance issues are being dramatically reduced in these fibers, still they are far from being optimized in these aspects. Thus, only short lengths can be used and the power transfer from pump to SC is (normally) far from complete. Conventional fibers, though, are much more constrained in the design but they exhibit excellent loss and guiding characteristics. Long lengths can be used at low cost and nearly complete power transfer from the pump to the SC can be achieved. The spectral width of this SC is far from the values reached with specially designed fibers, but it is still enough for some applications.

2 Supercontinuum generation

The pump used in our experiment was a continuous-wave Raman Fiber Laser (RFL) tuned at 1455.3 nm. The laser output is depolarized and the maximum output power reaches 2.1 W. We monitor this

power with a special integrating sphere radiometer with a 1% uncertainty [8]. A feedback control ensures that the output power of the RFL remains constant and controlled with an accuracy of ± 10 mW. Figure 1(a) shows the spectrum of the RFL alone for different power levels. The linewidth of the RFL grows as the power is increased. For a pump power of 2.1 W, the full width at half maximum (FWHM) of the laser output is 1.1 nm. The spectrum of the RFL shows clearly one of the resonances of the laser at 1365 nm. This resonance is effectively suppressed at the laser output (side mode suppression ratio is $\simeq 20$ dB).

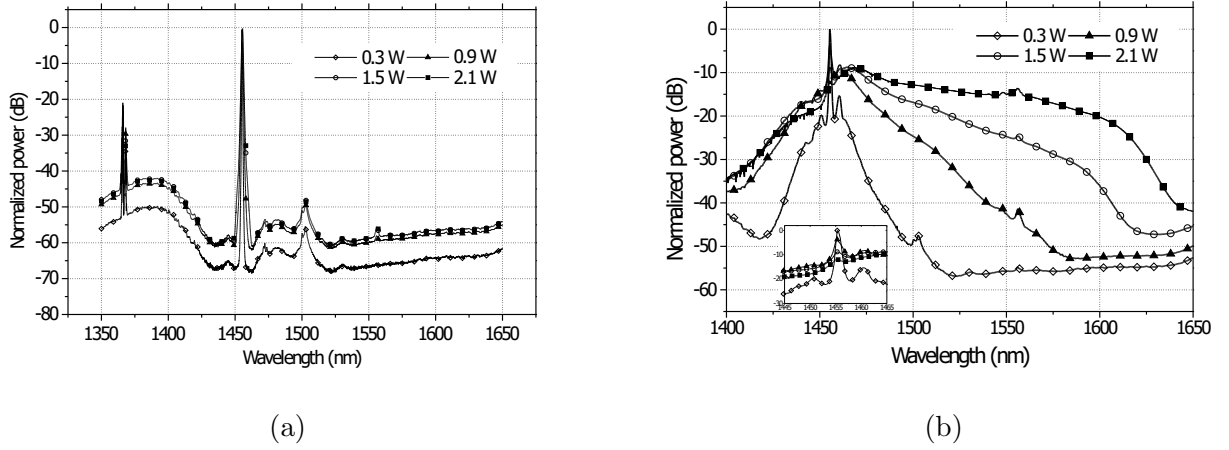


Figure 1: (a) Normalized output spectrum of the RFL. (b) Spectrum of the generated supercontinuum. Inset shows how increasing pump power leads to a more efficient pump depletion.

We use a 7-km-long spool of nonzero dispersion-shifted fiber with a measured end-to-end zero dispersion at approximately 1452.8 nm. The dispersion slope is $0.043 \text{ ps}\cdot\text{nm}^{-2}\cdot\text{km}^{-1}$. Thus, the expected dispersion at the wavelength of interest is roughly $0.081 \text{ ps}\cdot\text{nm}^{-1}\cdot\text{km}^{-1}$. The fiber loss at the wavelength of 1550 is 0.25 dB/km, and it remains mostly flat in the range from 1450-1620. Figure 1(b) shows the spectrum at the fiber output for the same power levels. At 300 mW, the effect of modulational instability (MI) is clearly visible as two nearly symmetric noise sidebands around the center frequency. The asymmetry between the two side bands is caused by Raman amplification of the lower frequencies and attenuation of the higher frequencies. As the power at the fiber input grows, the SC becomes broader. For a power level of 2.1 W, the 20-dB bandwidth of the output supercontinuum is 207 nm (from 1416.5 nm to 1624.0 nm). This effectively covers the S, C and L bands of the optical fiber. A further increase of the pump power would achieve a broader SC. Note that for power levels beyond 1500 mW, nearly complete pump depletion is achieved (the pump power is fully transferred to the supercontinuum). The feedback control in the output power of the RFL ensures a good stability of the SC. The temperature of the laser environment is controlled to ensure wavelength stability.

3 Application to polarization-mode dispersion measurements

To demonstrate the applicability of the generated supercontinuum, we performed measurements of polarization-mode dispersion (PMD) on a single fiber spool. We use the mean level crossing method reported in reference [9]. These measurements require a broadband source and an optical spectrum analyzer. The resolution and uncertainty of the measurement is strongly dependent on the bandwidth of the source. As the bandwidth of the source is increased, the uncertainty becomes smaller. In conventional tests, superluminescent light emitting diodes (SLED) are used as broadband sources. These typically have a bandwidth of less than 100 nm and an output power of a few hundred

microwatts. Our supercontinuum seems specially suited to perform these kind of measurements since large bandwidths (more than 200 nm) and high power densities (~ 1 mW/nm) can be achieved. More specifically, this source is adequate for the characterization of long lengths of fiber with a low uncertainty.

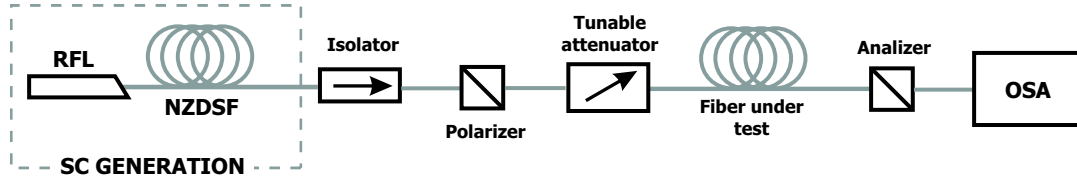


Figure 2: Setup for measuring PMD.

We use the experimental setup depicted in figure 2. After the NZDSF, an isolator prevents any reflection from coming back to the RFL. One polarizer ensures that the full SC spectrum is polarized in the same direction. After propagation through the fiber under test, we measure the transmitted power as a function of the frequency with and without analyzer (we denote these spectra as $P_a(\omega)$ and $P_w(\omega)$). With the resulting spectra we compute the transmission coefficient $T(\omega) = P_a(\omega)/P_w(\omega)$ and we analyze the mean-level crossing statistics. According to the model developed in [9], the mean differential group delay of the fiber is:

$$\langle \Delta\tau \rangle = 4 \frac{\langle N_m \rangle}{\Delta\omega} \quad (1)$$

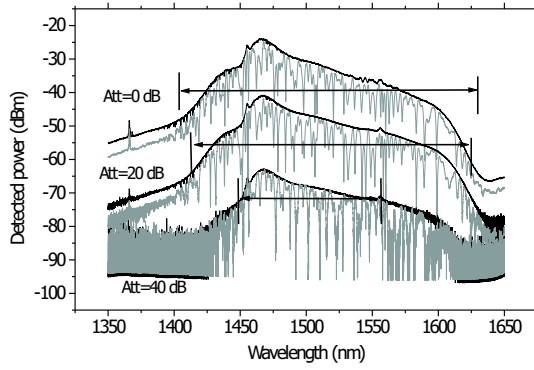
where $\langle N_m \rangle$ is the mean number of crossings through the mean value in a span of $\Delta\omega$. The uncertainty σ of the measurement is related to the frequency span over which the measurement has been performed. Since we perform a single measurement of DGD, we must expect that the number of mean level crossings in our measurement (N_m) is reasonably close to $\langle N_m \rangle$. In fact, the uncertainty is given by the following relationship:

$$\frac{\sigma^2}{\langle \Delta\tau \rangle} \simeq 0.44 \frac{2\pi}{\langle \Delta\tau \rangle \Delta\omega} \simeq \frac{0.7}{N_m} \quad (2)$$

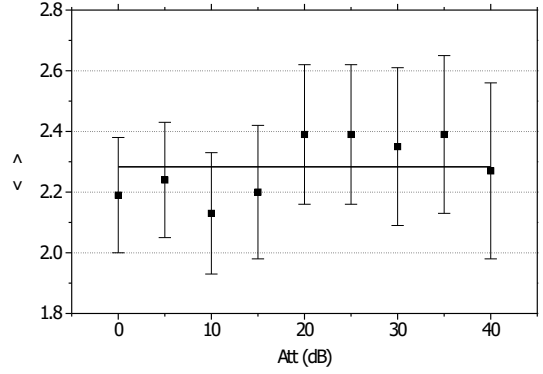
The power delivered by the pump in this case is tuned to 1.8 W. The 20-dB bandwidth of the generated SC is 191 nm. The accumulated losses (including isolator, first polarizer, fiber and splices) at the input of the second analyzer is approximately 11 dB at 1550 nm. This is mainly caused by the initial polarizer (3 dB loss, since the input is depolarized), splicing issues (the fiber under test is a dispersion-shifted fiber) and insertion losses of the tunable attenuator. To analyze the dynamic range of the measurement setup, we modify the attenuation in the tunable attenuator from 0 to 40 dB. The measurements are performed consecutively, so that the DGD remains more or less constant over the whole range of attenuation. Figure 3(a) shows measured spectra for 0, 20 and 40 dB of attenuation. Each spectrum shows the wavelength span in which the mean level crossing analysis has been made. Figure 3(b) shows the results of the measured DGD for different values of the attenuation. Note that as the attenuation grows, the range over which the calculus of the DGD is made becomes smaller, and thus the uncertainty increases.

4 Conclusions

We have demonstrated supercontinuum generation over bandwidths of more than 200 nm using a continuous wave Raman fiber laser and conventional nonzero dispersion-shifted fiber. The generated supercontinuum covers the S, C and L transmission bands of the fiber. We believe that



(a)



(b)

Figure 3: (a) Measurement of $P_a(\lambda)$ and $P_w(\lambda)$ for different values of attenuation, and the corresponding frequency span used in the calculation of PMD (b) Measured values of DGD for different values of attenuation

this source might have a wide range of applications for optical fiber metrology. We have used this supercontinuum to perform accurate measurements of polarization-mode dispersion in optical fibers.

We acknowledge financial support from the Spanish Ministerio de Ciencia y Tecnología through project TIC2000-2005. M. González Herráez acknowledges support from the Comunidad Autónoma de Madrid through a "Formación de Personal Investigador" grant.

References

- [1] C. Lin and R. H. Stolen, Appl. Phys. Lett. 28 (1976) 216
- [2] M. Nisoli, S. De Silvestri and O. Svelto, Appl. Phys. Lett. 68 (1996) 2793
- [3] T. Morioka, K. Mori and M. Saruwatari, Electron. Lett. 29 (1993) 862
- [4] S. A. Diddams, D. J. Jones, J. Ye, S. T. Cundiff, J. L. Hall, J. K. Ranka, R. S. Windeler, R. Holzwarth, T. Udem, and T. W. Hansch, Phys. Rev. Lett. 84 (2000) 5102
- [5] S. Coen, A. Hing Lun, R. Leonhardt, J. D. Harvey, J. C. Knight, W. J. Wadsworth and P. St. J. Russell, J. Opt. Soc. Am B 19 (2002) 753
- [6] M. Prabhu, N. S. Kim and K. Ueda, Jpn. J. Appl. Phys. 39 (2000) L291
- [7] A. Abeeluck, K. Brar, J. Boutellier, C. Headley and S. Radic, in *Proceedings of the Optical Fiber Communications Conference 2003* OSA Technical Digest Series (Optical Society of America, Washington D. C. 2003) paper ThT1.
- [8] P. Corredera, J. Campos, M. L. Hernanz, J. L. Fontecha, A. Pons and A. Corrons, Metrologia 35 (1998) 273
- [9] C. D. Poole and D. L. Favin, J. Lightwave Technol., 12, (1994) 917

Characterization of Photonic Crystal Structures

John O'Brien, Jiang-Rong Cao, Andrew Stapleton, Min-Hsiung Shih, Wan Kuang, Woo Jun Kim, Zhi-Jian Wei, Sang-Jun Choi, P. Daniel Dapkus

Department of Electrical Engineering
University of Southern California
Los Angeles, CA 90089-0271

Abstract

The basic device characteristics of photonic crystal lasers and passive components are introduced followed by a more detailed discussion of the experimental characterization of these devices.

Modern nanofabrication techniques allow the index of refraction in semiconductor photonic devices to be patterned on a scale that is small compared to the wavelength of operation of these devices. This allows the electromagnetic fields inside these photonic devices to be designed in microscopic detail. It is a serious challenge, however, to understand how to utilize this freedom in order to improve device performance. Two-dimensional photonic crystal devices are one technology that uses this freedom in patterning the dielectric constant to create small, potentially densely integrable devices, and are the subject of this work. Once the designed devices are constructed, it is also challenging to verify that the designed device properties are realized in practice rather than being obscured by fabrication imperfections. Close ties between numerical electromagnetic models and experimental characterization of these devices are necessary in order to verify that the predicted device properties are, in fact, realized.

Our work has included efforts on photonic crystal lasers as well as photonic crystal waveguides, junctions, and interferometers. Our electromagnetic modeling effort utilizes large-scale finite difference time-domain (FDTD) and finite element (FEM) calculations to design and predict the behavior of these devices. These calculations are run in a large-scale parallel processing environment. These numerical tools allow us to calculate device dispersion relations, modal fields, resonant frequencies, quality factors, and radiation patterns. All of these properties are, in principle, subject to experimental verification. In the following sections, a discussion of the properties of photonic crystal

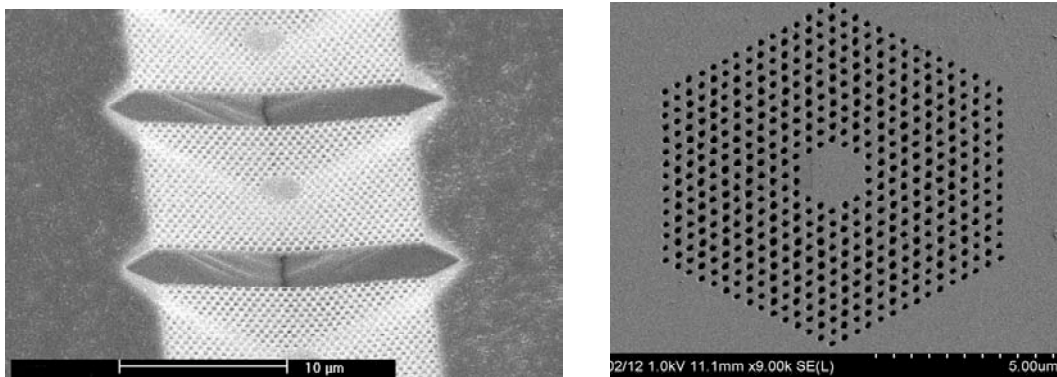


Figure 1 Electron micrographs of photonic crystal resonant cavities. The image on the left shows the suspended membrane geometry, while the image on the right is of a sapphire-bonded semiconductor membrane.

lasers is followed by a discussion of the properties of passive photonic crystal components.

Lasers with photonic crystal resonant cavities can be formed by patterning a two-dimensional photonic crystal lattice into a thin semiconductor membrane with a quantum well active region. We have investigated both a suspended membrane geometry in which the semiconductor membrane has air as upper and lower waveguide cladding layers and a geometry in which the semiconductor membrane is bonded to a sapphire substrate that acts as the lower waveguide cladding while facilitating heat dissipation. Figure 1 shows electron micrographs of these two cavity geometries. The cavities in these images are about 2.5 microns across and are formed by the elimination of 19 holes from a triangular lattice. These cavities are formed using relatively standard nanofabrication techniques [1,2]. The semiconductor membrane is an InGaAsP based heterostructure that is about one-half wavelength thick and contains four InGaAsP quantum wells. These cavities are multi-moded. Figure 2 shows both an optically pumped subthreshold spectrum along

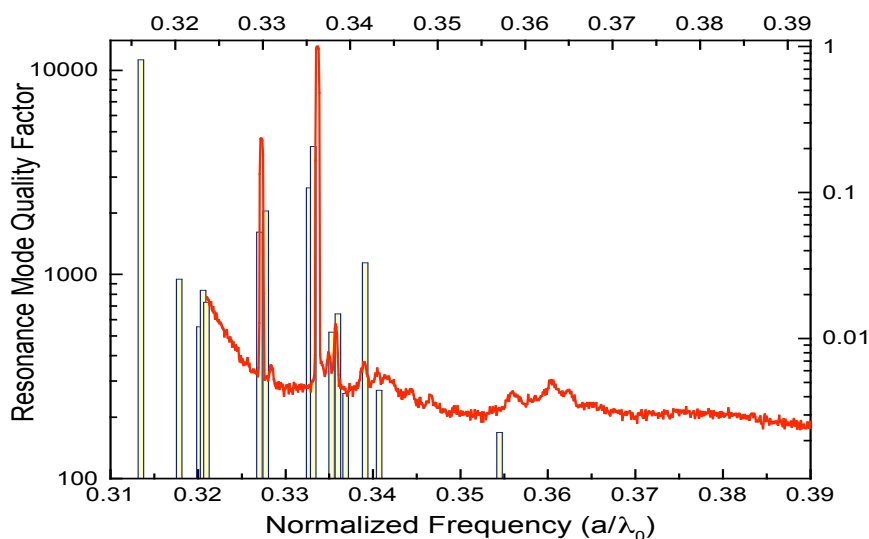


Figure 2 Subthreshold spectrum from a suspended membrane photonic crystal cavity plotted on the same axis as the numerical predictions of the resonant frequencies and their quality factors for this cavity.

with an FDTD calculation of the resonant frequencies and their predicted quality factors. The observed resonant frequencies differ only by about 1% from their predicted values.

A diagram of the optical pumping setup is shown in figure 3. The pump laser beam was

generated by an 850nm edge-emitting laser (IQ1H85(852-100B)G3D2 made by Power Technology, Inc.) with a corrected circular output. The pumping laser beam was focused onto the photonic crystal microcavities by a microscope objective lens, such as a Mitutoyo NIR 100x long working distance lens or a Newport 60x standard microscope objective lens. The precise alignment between the pump laser spot and the photonic crystal microcavity was achieved by flipping up/down a silver mirror placed in front of the white light source while imaging the location of the pumping spot and the laser cavity on a TV monitor receiving a video signal from the CCD camera, as illustrated in figure 3. The out-of-plane radiation from the photonic crystal microcavities was collimated by the same microscope objective lens, and was coupled into a multimode optical fiber after passing through a dichroic beamsplitter and a double polished GaAs wafer. The long wave pass dichroic beamsplitter was designed to transmit most of the 1.5μm band signal,

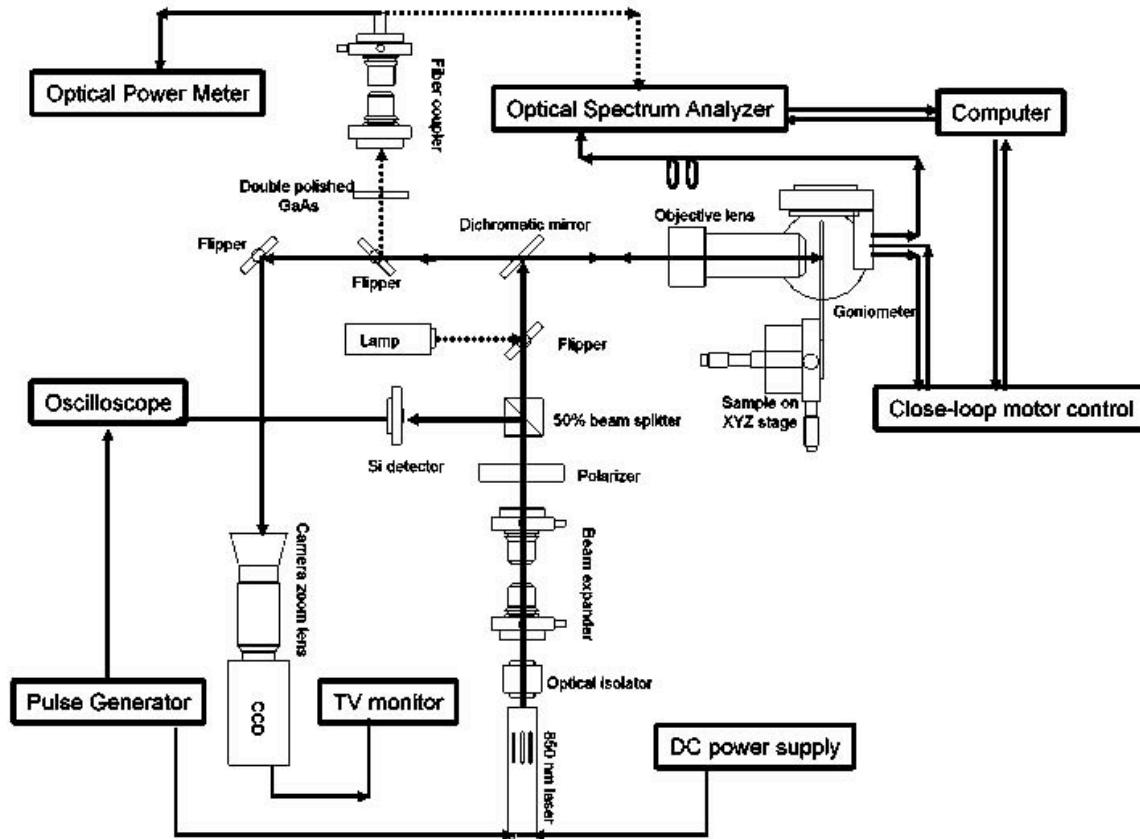


Figure 3. An illustration showing the optical characterization layout for the photonic crystal microcavity measurements, including optical pump, pump spot alignment, laser spectrum collection, and far-field scan.

from the photonic crystal laser while reflecting most of the 850nm band signal incident at a 45° angle regardless of the polarization of the light. The cutoff wavelength is 1025 nm. Once the optical signal was collected into a multimode fiber, it was directed either to an optical spectrum analyzer (OSA) or to a power meter. The GaAs wafer was used as an optical filter to absorb the remaining 850 nm pump laser signal reflected from the sample surface and transmitted through the dichromatic mirror. The polarizer placed in the path of the pump laser beam allows the continuous adjustment of the incident pump power by rotating this polarizer with respect to the linearly polarized axis of the pump beam. Also, a thermal electrical cooler (TEC) was placed on the sample mounting stage, when the photonic crystal microcavity lasers were characterized at elevated temperatures. Since the sapphire substrate is transparent to the emission wavelength of these microcavity lasers, the sapphire-bonded devices could be characterized through the sapphire substrate, while they were optically pumped on the front side. A far-field scanning apparatus was set up on the backside of the sample to study the radiation patterns. This was implemented using a goniometer formed by two orthogonally oriented rotary stages.

In addition to obtaining good agreement between the observed and predicted resonant frequencies, we have also obtained good agreement between the observed and predicted mode degeneracies, and between the observed and predicted radiation patterns from these lasers. The degeneracy breaking was modeled by applying group theoretic

projection operations to the modal fields obtained by an FDTD calculation [3]. The radiation patterns were calculated using a Green's function to obtain the far-field using an FDTD calculated near field [4].

Photonic crystal waveguides, waveguide branches and junctions, and interferometers have also been investigated in our group. These devices are formed by removing a single row of holes from a triangular lattice photonic crystal patterned into a suspended membrane. The fabrication of these devices is very similar to the fabrication of the laser cavities discussed above. We have formed photonic crystal waveguides in both the InGaAsP and SOI material systems. Figure 4 shows two electron micrographs of photonic crystal waveguide components.

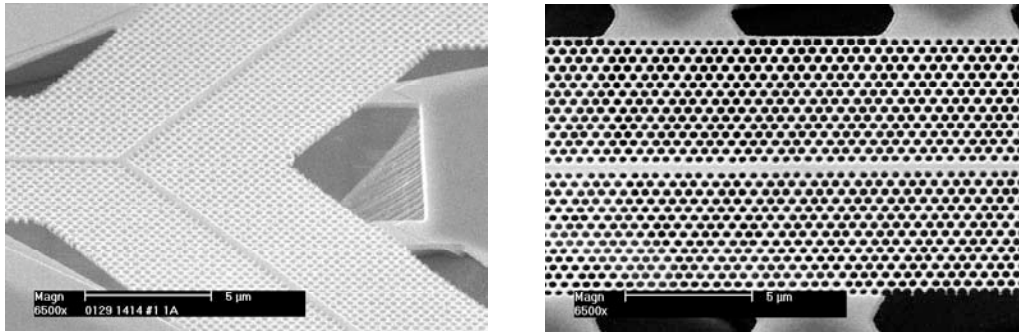


Figure 4 Electron micrographs showing, on the left, a photonic crystal y-branch, and on the right, a section of a straight waveguide.

We are interested in the waveguide dispersion, the optical losses, and the reflectivity of any waveguide junctions in these structures. Much of this information is directly accessible from the measured transmission spectrum. Our experimental setup for measuring the transmission characteristics of photonic crystal waveguides is shown in figure 5. Multiple tunable diode lasers enable us to characterize waveguides over the 1400nm to 1600nm wavelength range. Our setup utilizes free space optics throughout. The high numerical aperture microscope lenses used to couple light in and out of the waveguide are designed to give us an improvement in coupling efficiency compared to using cleaved or lensed fiber. The light generated by the tunable laser passes through several optical elements before reaching the waveguide. After the optical isolator, the light goes through a half wave plate allowing us to rotate the linearly polarized laser light to any arbitrary orientation. The signal then passes through a beam expander that enlarges the roughly 1 millimeter diameter beam from the tunable laser to several millimeters. Before the input coupling objective lens, a linear polarizer allows us to analyze the polarization state of the beam before it enters the waveguide. The 60x microscope lens used to couple light into the waveguide is a high numerical aperture aspheric lens that has been anti-reflection coated for near infrared wavelengths. At the output of the waveguide device under test, a high numerical aperture compound microscope lens (100x) is used to collect the light that is transmitted through the waveguide. An image of the facet is formed on an iris that functions as a spatial filter to remove all the light that does not originate from the waveguide core. The small minimum iris diameter along with the high magnification of the imaging system allow us to get effective minimum aperture sizes of approximately 2 microns. Following the iris

and subsequent focusing lens is a thermoelectrically cooled InGaAs detector that is capable of measuring signals down to -90dBm.

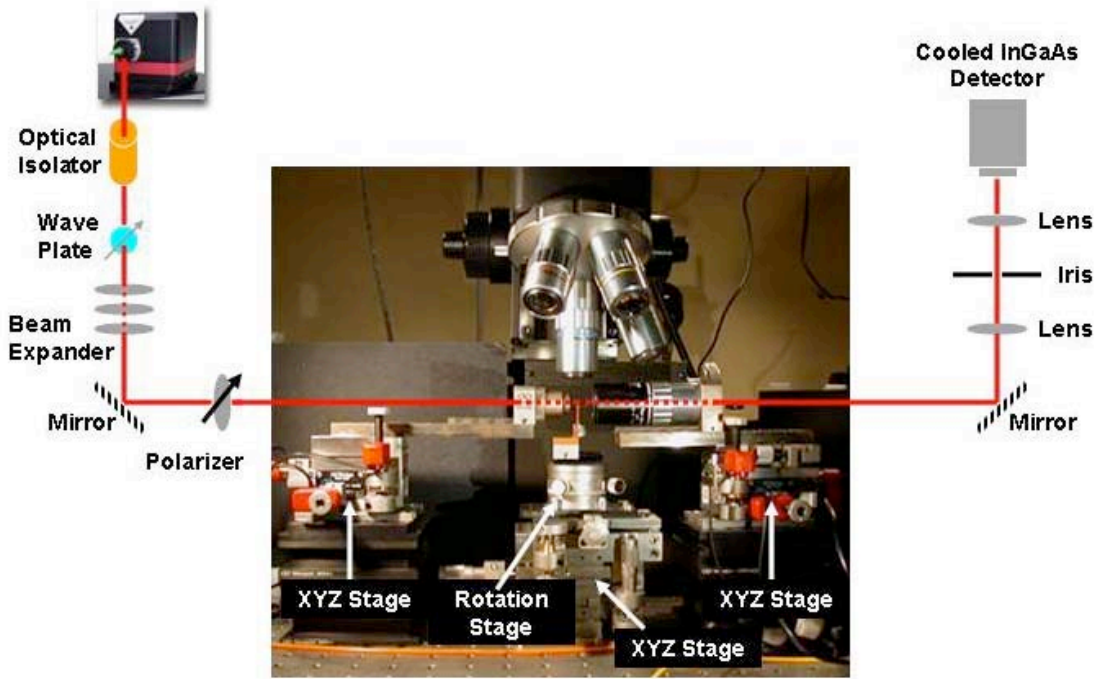


Figure 5. Diagram of the waveguide characterization setup including a photograph of the coupling assembly.

Figure 6 shows the dispersion relation and group velocity calculated by FEM for a single mode waveguide for three different photonic crystal hole diameters. We obtain good agreement between the calculated and measured transmission bandwidth. We can

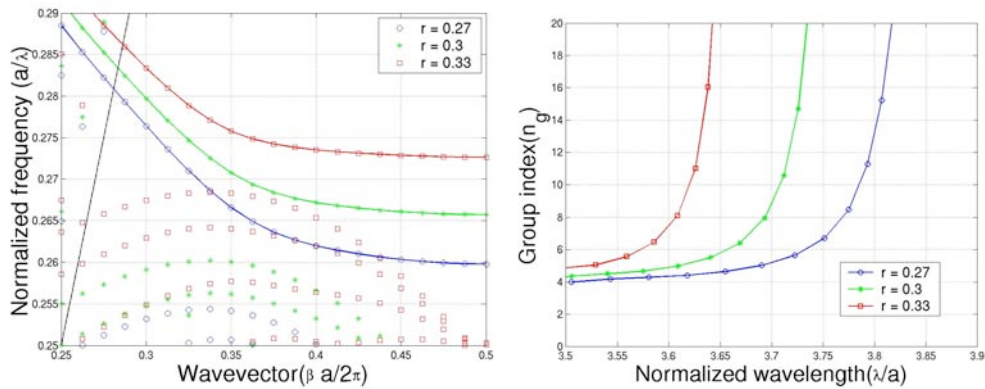


Figure 6. Calculated dispersion relation and group index for a single mode photonic crystal waveguide for three photonic crystal hole diameters.

also extract information about the waveguide dispersion from the transmission data. Since the facets of our waveguide are cleaved, Fabry-Perot oscillations occur in the

transmission spectra. The period of these oscillations contains information about the group index at that frequency. Figure 7 shows a measured transmission spectrum taken in a spectral region in which there is little group velocity dispersion in the waveguide. Also shown in the figure is the Fourier transform of the transmission spectrum scaled so that it is plotted as a function of the group index. Similarly, reflections from waveguide junctions give rise to Fabry-Perot oscillations in the transmission spectra. The peak-to-valley ratio of these oscillations can be used to infer the reflectivity as a function of wavelength of these junctions. We have made these measurements for waveguide bends

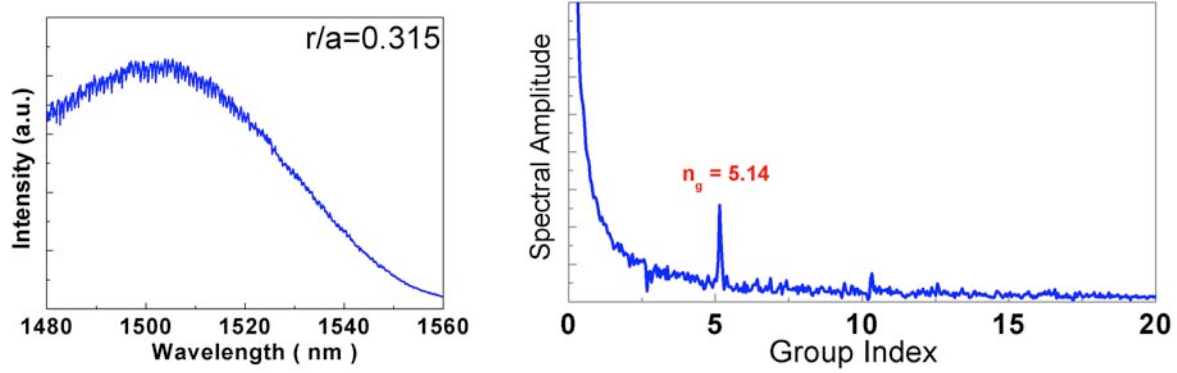


Figure 7. On the left is the transmission spectrum of a straight waveguide with a lattice constant of 420 nm and an r/a value of 0.315. On the right is the Fourier transform of this data scaled so that it can be plotted as a function of the group index.

and have again obtained excellent agreement between the numerical predictions and the experimental observations.

References

- [1]. J. R. Cao, P.-T. Lee, S.-J. Choi, R. Shafiiha, S.-J. Choi, J. D. O'Brien, P. D. Dapkus, "Nanofabrication of Photonic Crystal Membrane Lasers", *J. Vac. Sci. and Tech. B.*, 30, pp. 618-621 (2002).
- [2] J.-R. Cao, Z.-J. Wei, S.-J. Choi, W. Kuang, H. Yu, J. D. O'Brien, P. D. Dapkus, "Sapphire bonded photonic crystal microcavity lasers", paper TuE5, OSA Annual Meeting, Tuscon AZ (2003).
- [3] Wan Kuang, J. R. Cao, Tian Yang, Sangjun Choi, John D. O'Brien, P. Daniel Dapkus, "Classification of Modes in Multi-Moded Photonic Crystal Microcavities", CTuDD, Conference on Laser and Electro-Optics (CLEO), San Francisco, California (2004)
- [4] J. R. Cao, Wan Kuang, Zhijian Wei, Sang-Jun Choi, John D. O'Brien, and P. Daniel Dapkus, "Far-Fields of Photonic Crystal Microcavity Lasers", CTuR, Conference on Laser and Electro-Optics (CLEO), San Francisco, California (2004)

Ultrasensitive Measurement Method for Refractive Index Difference between Two Wavelengths

Matthieu Legré, Mark Wegmuller, Nicolas Gisin

Group of Applied Physics, University of Geneva,
20 rue de l'Ecole-de-Medecine, CH-1205 Genève, Switzerland.

Abstract: A novel method for the measurement of ultra small refractive index differences between two wavelengths is demonstrated. The method is based on the change of the phase matching conditions of a nonlinear process in two nonlinear crystals separated by a dispersive medium. We demonstrate the performance of our technique by measuring the refractive index difference of air between 775nm and 1550nm with an air column of only 33cm.

I. INTRODUCTION

$\chi^{(2)}$ processes obtained with one nonlinear crystal are very well understood, but the effect obtained with two successive crystals were less investigated. However, configurations with two nonlinear crystals are very common in the quantum optics field, where they are used to create entangled photon pairs [1]. Di Giuseppe *et al* have studied in [2] the properties of entangled photon pairs generated by two nonlinear crystals separated by a dispersive medium. They demonstrated that the phase-matching properties of the nonlinear process are changed by the presence of this dispersive medium. We are demonstrating in the following that it is possible to determine the refractive index difference between two wavelengths from the change of the phase-matching properties. First, the theory behind our measurement method is explained, and then we illustrate it with the experimental determination of the refractive index difference of air between 775nm and 1550nm.

II. THEORY OF THE EXPERIMENT

If we consider a simple experiment of second harmonic generation (SHG, see figure 1.a), the evolution of the two waves in a nonlinear crystal can be calculated under the hypothesis of *slowly varying amplitudes* and of *plane-wave fixed-field approximation*. One finds the following equations [3]:

$$E_{\omega}(z) = E_{\omega} \quad (\text{constant because of fixed-field approximation}) \quad (1)$$

$$\frac{dE_{2\omega}(z)}{dz} = i \frac{\omega}{n_2 c} \chi^{(2)} E_{\omega}^2 e^{-i\Delta k z} \quad \text{with } \Delta k = k(2\omega) - 2k(\omega) \quad (2)$$

with ω the optical frequency of the pump, n_2 the refractive index of the crystal for a frequency 2ω , c the velocity of light in vacuum, $\chi^{(2)}$ the dielectric susceptibility of the nonlinear material, and $k(\omega)$ the wavevector of the light at ω . The fixed-field approximation implies that the amplitude of the pump wave (E_{ω}) is constant along the crystal (equation (1)). Integration of equation (2) provides the SHG signal at the end of the crystal,

$$E_{2\omega}(L) = i \frac{\omega}{n_2 c} \chi^{(2)} E_{\omega}^2 e^{-i\Delta k L/2} \frac{\sin(\Delta k L/2)}{\Delta k/2} \quad (3)$$

, where $\chi^{(2)}$ is considered independent of z and L is the length of the nonlinear crystal. Equation (3) demonstrates that the nonlinear process is efficient only for waves in accordance with the phase-matching condition ($\Delta k=0$). The dependence of the conversion efficiency when Δk varies around zero allows to compute the output intensity generated in a nonlinear crystal for different pump laser wavelengths. A typical result is shown in figure 1.b. The dependence of the generated intensity on the pump wavelength follows a *sinc* function, whereas the bandwidth $\delta\lambda_{1/2}$ of the curve is determined by the physical properties of the crystal (length, refractive index, see equation (3)).

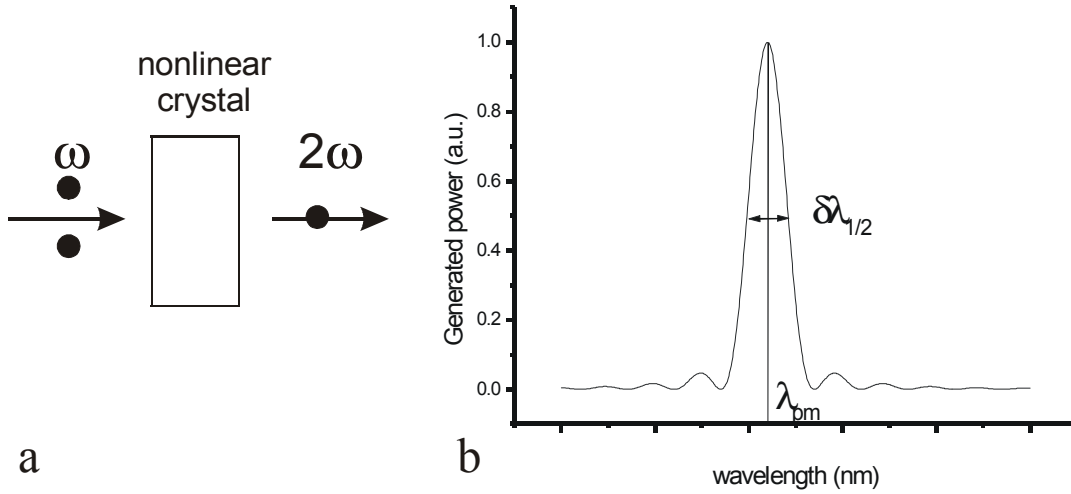


Figure 1.a Sketch of a SHG experiment. ω is the frequency of the pump source, 2ω is the frequency of the generated wave.

Figure 2.b Theoretical pump wavelength dependence of the SHG signal power. λ_{PM} : wavelength corresponding to the phase-matching condition, $\delta\lambda_{1/2}$: phase-matching bandwidth.

Now, let us consider an experiment with two nonlinear crystals having the same phase-matching conditions, separated by a dispersive medium as shown in figure 2. Using the same approximations as before, the generated SHG power becomes:

$$I_{2\omega} = \left(\frac{\sin(\Delta k L_1/2)}{\Delta k/2} \right)^2 + \left(\frac{\sin(\Delta k L_2/2)}{\Delta k/2} \right)^2 + \frac{2 \sin(\Delta k L_1/2) \sin(\Delta k L_2/2) \cos(\Delta k(L_1 + L_2)/2 + \Delta k' d)}{(\Delta k/2)^2} \quad (4)$$

with $L_{1,2}$ the length of the first and second crystal, respectively, d the length of the dispersive medium, k' the wavevector in the dispersive medium, and the parameter of interest $\Delta k' = k'(2\omega) - 2k'(\omega)$. If the parameters Δk , L_1 , L_2 , and d have been previously measured, it is possible to determine $\Delta k'$ by fitting the measured SHG power as a function of the wavelength of the input laser. The refractive index difference in the dispersive index, $\Delta n' = n'(2\omega) - n'(\omega)$, can be easily determined from $\Delta k' = 2\pi \Delta n' / \lambda_{\omega}$.

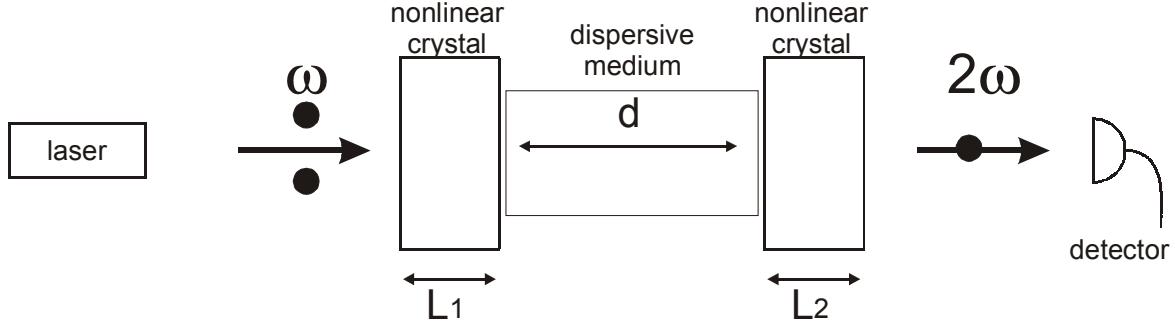
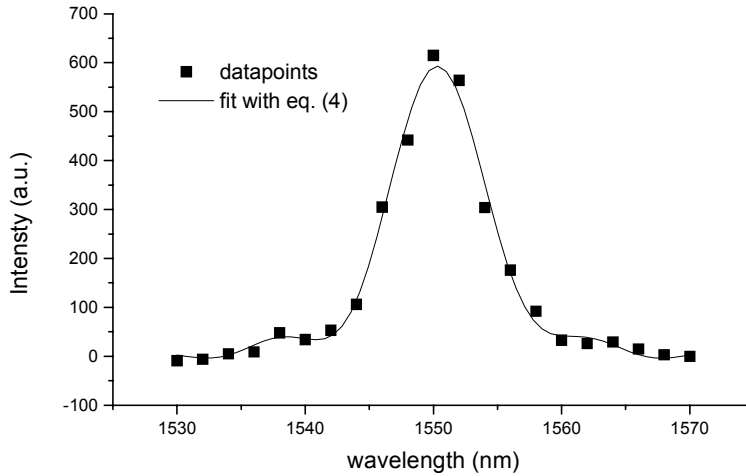


Figure 2 : Setup of the experiment with two nonlinear crystals separated by a dispersive medium. L_1 and L_2 are the lengths of the first and second crystal, respectively. d is the length of the dispersive medium.

III. EXPERIMENTAL RESULTS

To underline the great sensitivity of our measurement technique, we extract the value of the refractive index difference between 775nm (ω) and 1550nm (2ω) of air, which is known to have a very small dispersion. Our experimental setup is outlined in figure 2. The light source is a tunable laser at 1550nm, the nonlinear crystals are type II KTP of 3mm length cut for SHG at 1550nm, and the dispersive medium is a 33cm long air column. The SHG signal is measured with a silicon photon counting detector, preceded by low-pass filters to remove the pump light at 1550nm.



δd (nm)	$\Delta n'$
0	2.29934E-06
2	2.31028E-06
4	2.31713E-06
6	2.32165E-06
8	2.33347E-06

Table 1 : Values of the refractive index difference determined for several distances d

Figure 3 : SHG signal power as a function of pump wavelength for normal incidence.

First, we characterize the phase-matching properties of each of the two crystals. This is done by measuring the SHG power for different pump wavelengths and normal incidence. From the corresponding results, similar to the curve shown in figure 1.b, the phase-matching wavelength (λ_{PM}) and the phase-matching bandwidth ($\delta\lambda_{1/2}$) can be extracted. Considering just the first order in λ , ΔkL can be determined from λ_{PM} and $\delta\lambda_{1/2}$ with the relation $\Delta k(\lambda)L = 2\pi(\lambda - \lambda_{PM})/\delta\lambda_{1/2}$. Then we measure the length of the air column d with an OFDR [4] using a refractive index of $n=1$ (1550nm). Now that we know the parameters, $\Delta k(\lambda)$, L_1 , L_2 , and d , we measure the

SHG wave after the succession of both crystals for different wavelengths. A typical result is shown in figure 3. The form of the curve is slightly different from the theoretical one obtained with one crystal (figure 1.b). By fitting these data points with equation (4), we extract $\Delta k'$, respectively $\Delta n' = \lambda_o \Delta k' / 2\pi = 2.3 \cdot 10^{-6}$.

This value has to be compared with the one computed with empirical laws like the Gladstone-Dale law (general law for gases), or more specific laws for air [5]. We compute a value of $2.1 \cdot 10^{-6}$ for $n_{air}(775nm) - n_{air}(1550nm)$ at a temperature of 20°C and a pressure of $1.1 \cdot 10^5$ Pa (notice that the value depends strongly on pressure and temperature). There is a good agreement between the measured and the calculated value. In order to control the reproducibility of our measurement, we repeated the experiment five times each time increasing the distance d by 2mm. The corresponding results are summarize in table 1. As one can see, all the values are almost identical, with a maximum relative error of 1%, demonstrating the good reproducibility of our measurement method. Notice however that the measured $\Delta n'$ increased with δd , which can certainly be explained by a small change of λ_{PM} . In fact, λ_{PM} has been measured quite precisely for the first measurement ($\delta d = 0$ mm), and we supposed that it did not change for the others. This assumption is maybe not true because we translate a bit the second crystal and then it is certainly thoughtlessly turned at the same time (a small turn already considerably changes the phase-matching wavelength λ_{PM}). We calculate that a change of 1nm of λ_{PM} produces an error of 5% on the measured value of $\Delta n'$.

IV. CONCLUSIONS

We have presented a novel method to measure ultra low refractive index differences. It is based on the change of the phase-matching properties of a nonlinear process when a dispersive medium separates the two nonlinear crystals. Using SHG, we precisely determined the refractive index difference of air between wavelengths of 775nm and 1550nm. The measurement has been done with an air space of only 33cm, which proves the good sensitivity of this measurement technique. The results are very reproducible, and agree very well with the values found in the literature.

In this letter, where we use SHG, we were only able to measure the refractive index difference between a frequency and its double. However, the use of different nonlinear processes like sum frequency generation, difference frequency generation, or four wave mixing, should allow to make the measurement more versatile, so that the chromatic dispersion of the medium can be more easily extracted.

Acknowledgements: Financial support from EXFO Inc (Vanier, Canada) and NCCR (Switzerland) are acknowledged.

References

- 1- "Ultrabright source of polarization-entangled photons", P. G. Kwiat, E. Waks, A. G. White, I. Appelbaum, and P. H. Eberhard, *PRA*, **60**, pp. R773-776 (1999)
- 2- "Entangled-photon generation from parametric down-conversion in media with inhomogeneous nonlinearity", G. Di Giuseppe, *et al.*, *PRA*, **66**, 013801 (2002).
- 3- "Handbook of nonlinear optical crystals", V.G. Dmitriev, G.G. Gurzadyan, and D.N. Nikogosyan, *Third Revised Edition*, Springer (1999).
- 4- "On the characterization of optical fiber network components with optical frequency domain reflectometry", J.P. vondes Weid, R. Passy, G. Mussi, and N. Gisin, *J. Lighthwave Tech.*, **15**, 1131-1141 (1997)
- 5- B. Edlen, *Metrologia*, **2**, 71 (1966)

Tomographic Reconstruction for Arbitrary Refractive Index Distribution of Optical Fibre Preforms

Y. C. Zhao, S. Fleming, K. Lyytikainen, M. A. van Eijkelenborg
 Australian Photonics CRC, Optical Fibre Technology Centre
 University of Sydney, NSW, Australia
 Tel: +61 02 9351 1939, Fax: +61 02 9351 1911
 y.zhao@ofc.usyd.edu.au

Abstract: We demonstrate a tomographic method to measure arbitrary refractive index profiles of silica and polymer optical preforms. The preform is rotated through 180 degrees and the deflection angle data collected, then the back projection technique and spline interpolation algorithm are used in the computed tomographic two-dimensional profile distribution. An improved formula for calculating the optical path length from the deflection function is derived. To minimize the computing time, the spatial Nyquist frequency is used to estimate the angle sampling number of views and the numbers of points per scan in advance.

1. Introduction

Optical fibres, especially those with complex internal structure and made from novel material demand a non-destructive technique to accurately determine the refractive index profile in the optical fiber preform. Chu first reported a non-destructive method to measure circularly symmetric conventional optical fibre preforms [1]. A laser beam was used to scan radially across the preform and the beam deflection angle was measured, from which the refractive index profile was calculated by using the Abel inversion method. Marcuse proposed an experimentally more convenient method [2]. With *a priori* knowledge of near circular or elliptical preforms, several methods were proposed for non-circularly symmetric conventional preform measurements [3,4]. A nondestructive measurement of the two-dimensional refractive index profile for arbitrary preform index distribution without *a priori* knowledge of the preform was proposed by using the tomography method [5]. A non-destructive method for measuring the profile of a Holey Fibre Preform (HFP) was proposed by using two types of matching oil [6]. This paper presents a new method by which the deflection data can be used to reconstruct a two-dimensional refractive index profile with weakly varying, arbitrary index distribution. The principle of this method is based on the representation of optical path length difference by a modified formula and the back projection method is performed. A spline interpolation algorithm is used to interpolate the radial points to the points on a square grid.

2. Theory

Under the assumption of a preform with small numerical aperture, we analytically derived the relationship between the optical path difference and deflection function. Fig. 1 shows the geometry of the launching arrangement for the noncircular arbitrary index distribution preform, which is surrounded by a medium of index matching oil. A ray is shown to enter the preform at a distance ρ from the origin O and at an angle θ with respect to the x-axis. Let $n(r, \theta)$ denote the refractive index distribution of the preform, and the surrounding medium refractive index be n_c , the index distribution can be expressed as a Taylor's series

$$n(r, \theta) = n_c + \Delta n(r) + \delta n(r, \theta) \quad (1)$$

where

$$\Delta n(r) = (-n_c + n_0) + \frac{1}{1!} r \left. \frac{\partial n(r, \theta)}{\partial r} \right|_{(0,0)} + \frac{1}{2!} r^2 \left. \frac{\partial^2 n(r, \theta)}{\partial r^2} \right|_{(0,0)} + \frac{1}{3!} r^3 \left. \frac{\partial^3 n(r, \theta)}{\partial r^3} \right|_{(0,0)} + \dots \quad (2)$$

and

$$\delta n(r, \theta) = \frac{1}{1!} \theta \left. \frac{\partial n(r, \theta)}{\partial \theta} \right|_{(0,0)} + \frac{1}{2!} \left[2r\theta \left. \frac{\partial^2 n(r, \theta)}{\partial r \partial \theta} \right|_{(0,0)} + \theta^2 \left. \frac{\partial^2 n(r, \theta)}{\partial \theta^2} \right|_{(0,0)} \right] + \dots \quad (3)$$

When the preform is immersed in the matching oil, the light ray trajectory changes its direction continuously and the optical path length between the launching plane AA' to the output observation plane BB' can be approximated as

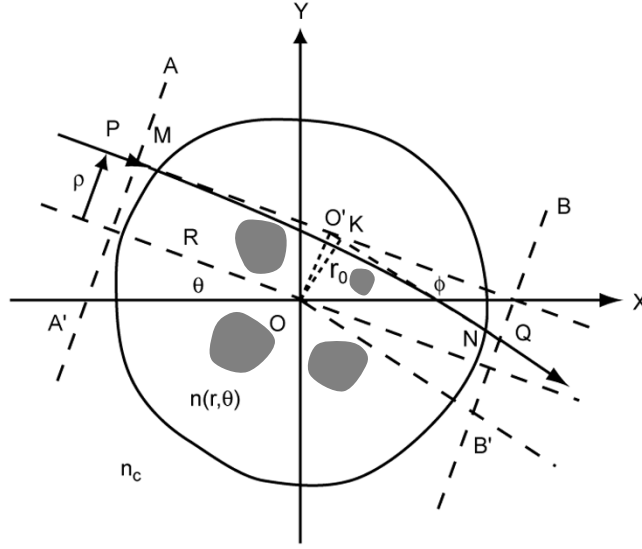


Fig. 1 Ray trajectory in an arbitrary preform cross section

$$\int_P^Q n(r, \theta) ds = n_c \overline{PM} + \int_M^N n(r, \theta) ds + n_c \overline{NQ}$$

$$\approx n_c \int_0^\rho \phi(\xi, \theta) d\xi - n_c \rho \phi + n_c (1 + \sec \phi) \left(R - \rho \tan \frac{\phi}{2} \right) + \Delta E + \Delta G \quad (4)$$

where

$$\Delta E = \frac{\partial}{\partial \theta} \int_0^\rho n_c \phi(\xi, \theta) d\xi \cdot \Delta \theta \quad (5)$$

is a modification term. In the circularly symmetric case $\Delta E = 0$ and

$$\Delta G = 2 \int_0^R \Delta n(r) dr \quad (6)$$

is a constant. Also, without the preform, the optical path length between the launching plane and observation plane PO'Q can be approximated as

$$\int_P^Q n_c ds \approx -2n_c \rho \tan \frac{\phi}{2} + n_c (1 + \sec \phi) \left(R - \rho \tan \frac{\phi}{2} \right) \quad (7)$$

where $2R$ is the distance between the launching and observation planes, and the optical path length difference, which is attributed to the optical fiber preform, can be expressed as

$$\Psi(\rho, \theta) = n_c \int_0^\rho \phi(\xi, \theta) d\xi + \frac{n_c \rho}{12} \phi(\rho, \theta)^3 + \Delta E + \Delta G \quad (8)$$

Although the light rays passing through the preform are refracted and follow a curved path, the main hypothesis of the reconstruction is based on the assumption that the optical preform may be regarded as a phase object. This implies a perfect index matching between the matching oil and the preform, and the actual ray trajectory can be approximated by a straight line between the launching and observation planes. This assumption does not incur any significant error due to the small numerical apertures of practical optical fiber preforms. Theoretical analysis shows that the mismatch effect becomes negligible when the index mismatch is less than 0.005 [5]. In our experiment, the mismatch is less than 0.003.

3. Reconstruction algorithm

In the Cartesian coordinate system, if the optical path differences are known for all θ between zero and π , the normalized index profile can be reconstructed by the discrete integral [7]

$$f(x, y) \approx \frac{\pi}{N} \sum_{l=1}^N g_{\theta_l} (x \cos \theta_l + y \sin \theta_l) \quad (9)$$

where the angles θ_l with $l=1,2,\dots,N$ are those for which the optical path length differences are known. Values $g_\theta(\rho)$ are calculated by inverse Fourier transforms

$$g_\theta(\rho) = \int_{-\infty}^{\infty} S_\theta(k) k \exp(i2\pi k \rho) dk \quad (10)$$

where k is the spatial frequency and $S_\theta(k)$ is the Fourier transform of path length difference function of $\Psi_\theta(\rho)$, which is given by

$$S_\theta(k) = \int_{-\infty}^{\infty} \Psi_\theta(\rho) \exp(-i2\pi k \rho) d\rho \quad (11)$$

$S_\theta(k)$ and $g_\theta(\rho)$ can be obtained efficiently by applying a fast Fourier transform and an inverse fast Fourier transform, respectively.

To obtain the index profile of the holey fiber preforms, the first step is to use the laser-scanning method to measure the deflection function $\phi(\rho, \theta)$ for N_θ orientations. For each orientation, the whole preform is scanned transversely with an increment $\delta\rho$. Then the optical path length differences $\Psi_\theta(\rho)$ are calculated by using Eq. (8) and the FFT is applied to the optical path length difference function to obtain $S_\theta(k)$. The back-projecting filtered function $g_\theta(\rho)$ is obtained by using the inverse FFT in Eq. (10). For each point (x,y), the normalized index profile is obtained by numerical integration over the rotation angle θ by using Eq. (9). The value of $x \cos \theta_l + y \sin \theta_l$ in (9) may not correspond to one of the values of ρ for which $g_\theta(\rho)$ is determined in (10). In this case, $g_\theta(\rho)$ for such ρ is approximated by spline interpolation. To minimize the influence of measurement noise, which is generally of higher frequencies, $S_\theta(k)$ is multiplied with a Hamming window function $H(k)$ before taking the inverse FFT. Superior reconstructions are usually obtained by applying such a window to filter the projection.

4. Experiments and results

To illustrate the technique for reconstructing the refractive index distribution, two different special preforms (manufactured at Optical Fibre Technology Centre, Sydney University) were measured. The deflection functions are measured by using a NetTest PK2600 preform analyzer. The measurements are performed at a wavelength of 632.8 nm, and the raw data from the position sensitive detector are used for the index reconstruction.

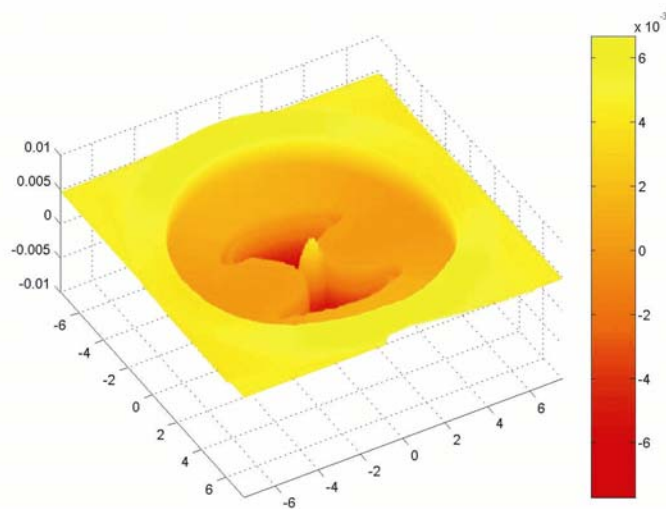


Fig. 2 Bow-tie fibre preform tomography plot

Preform A is a hi-birefringence design with bow-tie profile. Preform B is a microstructured polymer fibre preform. In the first case, the bow-tie preform with elliptical cladding shape was immersed in index matching

oil. The three dimensional display of preform A is shown in Fig. 2. The tomography result tallies with the design parameters.

The second preform measurement was performed on a PMMA (polymethylmethacrylate) polymer preform with a refractive index of $n_{\text{PMMA}} = 1.4897$ at 632.8 nm. Due to polymer's high index contrast to silica, two types of index matching oil were used to minimize the mismatch influence. The holes of the polymer HFP were filled with matching oil whose index is close to the polymer index, ($n = 1.4822$), the preform was placed in a silica tube filled with the same oil, and the silica tube was then immersed into another oil whose index ($n = 1.4609$) is close to that of silica. This layered arrangement is required in order not to contaminate the oil bath of the PK2600, and maintain the capacity to measure both silica and polymer preforms without a complete changeover of the oil in the instrument. The reconstructed three-dimensional index profile of the polymer filled HFP is shown in Fig.4.

Since only a finite amount of discrete data is available to reconstruct the refractive index, the resolution is limited by the accuracy of the deflection measurement. The spline interpolation algorithm is used to suppress the aliasing errors.

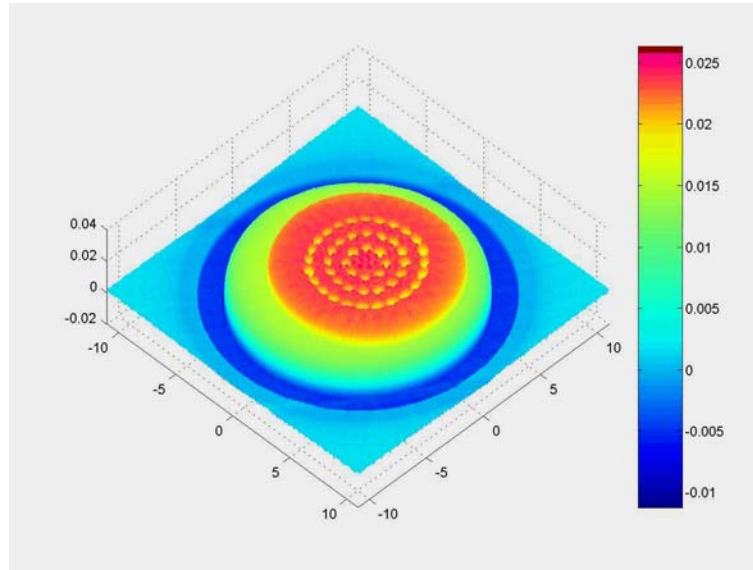


Fig. 3 Polymer holey fibre preform tomography plot

This paper describes the use of the back projection method to reconstruct the preform index distribution from the information of the deflection function. Based on the ray tracing principle, we derive an improved optical path length formula from the deflection function. The complete tomographic method makes it possible to reconstruct the fiber preform index distribution accurately without *a priori* knowledge of the preform. This method is very valuable for determining the refractive index profile and structural integrity of new structured holey fibre preforms in a non-destructive manner.

REFERENCES

- [1] P. L. Chu, "Nondestructive measurement of index profile of an optical fibre preform", Electron. Lett., Vol.13, No.24, pp. 736-738, Nov. 1977.
- [2] D. Marcuse, "Refractive index determination by the focusing method", Appl. Opt., Vol.18, No. 1, pp. 9-13, Jan. 1979.
- [3] P. L. Francois, I. Sasaki, M. J. Adams, "Practical three-dimensional profiling of optical fibre preforms", IEEE J. Quantum. Electron., Vol. 18, No. 4, pp.524-534. Apr.1982.
- [4] C. Saekeang, P. L. Chu, T. W. Whitbread, "Nondestructive measurement of refractive-index profile and cross sectional geometry of optical fibre preforms", Appl. Opt., Vol. 19, No.12, pp. 2025-2030, Jun. 1980.
- [5] Y. C. Zhao, S. Fleming, K. Lyytikainen, L. Poladian, "Nondestructive measurement for arbitrary RIP distribution of optical fibre preforms" IEEE J. of Lightwave Technol., Vol. 22 No. 2, pp.478-486, Feb. 2004.
- [6] Y. C. Zhao, K. Lyytikainen, M. A. van Eijkelenborg, S. Fleming, "Nondestructive measurement of refractive index profile for holey fibre preforms", Opt. Express, Vol. 11, No.20, pp.2474-2479, Oct. 2003.
- [7] C. R. Crawford, A. C. Kak, "Aliasing artefacts in computerized tomography," Appl. Opt. Vol. 18, No.21, pp. 3704-3711, Nov. 1979.

Micro-analytical techniques for imaging erbium doped optical fibers

F. Sidiroglou^{*}, S.T. Huntington^{*}, R. Stern[♦], G. Baxter[†], A. Roberts^{*}

^{*}School of Physics, University of Melbourne, Victoria, 3010, Australia

[†]School of Communications and Informatics, Victoria University, PO Box 14428, Melbourne, Victoria, 8001, Australia

[♦]Centre for Microscopy and Microanalysis, M010, The University of Western Australia, 35 Stirling Highway Crawley, WA 6009, Australia

Abstract

In this paper we demonstrate the application of two microscopic imaging techniques, Raman Fluorescence Intensity Confocal Optical Microscopy and Nano-Secondary Ion Mass Spectroscopy (NanoSIMS), to the determination of the relative erbium ion distribution in optical fibers. We also employ Quantitative Phase Microscopy (QPM) for the acquisition of the refractive index profile of one of the investigated samples. As well as being able to acquire two dimensional profiles of the relative erbium ion distribution, these methods can also provide valuable information on a sub-micron level regarding physical and optogeometric parameters of the examined samples.

Introduction

Rare-earth doped optical fibers are now being used extensively for fiber lasers and fiber amplifiers [1]. The capabilities of these devices have found tremendous use in a range of scientific and industrial environments among which the field of optical communications has been influenced the most. Since the development of the erbium-doped fiber amplifier (EDFA) [2], the quest for optimizing the design and manufacture of such devices has become a continuing challenge to optical scientists and engineers. It has been demonstrated that the properties and performance of Er-doped fiber (EDF) lasers and amplifiers are related to a number of parameters such as the fiber glass material, the waveguide characteristics, and the erbium ion distribution profile. The accurate knowledge of the latter has been found to be vital for the optimal design and operation of these devices [3].

To date, in the most common approach employed for the determination of the erbium ion distribution in optical fibers, analytical chemistry based techniques (i.e., SIMS [4], EPMA [5], and EXAFS [6]) have been applied to fiber preforms from which the fiber is drawn, in order to investigate the erbium distribution profile. The information extracted from the preform is then scaled down to match fiber dimensions assuming that there are no changes during the drawing process that can alter the compositional profile of the drawn fiber. However, there is no guarantee that during fiber drawing the compositional profile of the resulting fiber will be the same as the original preform. It is expected that due to dopant diffusion some redistribution of the erbium ions will occur during the drawing process.

In this paper we present the results from the application of a Raman confocal imaging system to determine the erbium ion distribution directly in germanosilicate optical fibers. The advantage of this technique is that it can provide submicron information about the relative erbium ion distribution by exploiting the superior wavelength resolution of a Raman spectrometer together with the reduced depth of field and the high spatial resolution of a confocal microscope.

The acquired relative erbium ion distribution is then correlated to the refractive index profile determined using Quantitative Phase Microscopy (QPM). The latter is a relatively new non-interferometric technique that can be used to quantitatively determine the phase of a transparent specimen. QPM is based on the transport of intensity equation where variations within the phase introduced into the lightfield by a specimen are manifested as variations in the transmitted intensity as the distance is varied [7].

In addition, we also present preliminary measurements for an experimental erbium doped fiber sample acquired by NanoSIMS. The obvious benefit of this method is that investigation of the erbium ion traces as well as that of the silica atoms it can be achieved at a high sensitivity and at a spatial resolution of 500 nm.

Raman Fluorescence Intensity Confocal Optical Microscopy

The profiling scheme adopted for the imaging of the Er-ion distribution from the endface of freshly cleaved fiber samples is outlined as follows. Pump light from an argon ion laser ($\lambda=514$ nm, $P\sim 1$ mW) is focused by a microscope objective ($\times 100$, $NA=0.9$) to a submicron spot incident on the endface of the freshly cleaved fiber (around 5 mm long). In the core region, where the erbium ions are located, the incident pump excites the ions from the ground state ($4I_{15/2}$) to the $2H_{11/2}$ upper energy level. Radiative decay back to the ground state from this level, and non-radiative relaxation to the next lowest level, $4S_{3/2}$, followed by radiative emission to the ground state, yields fluorescence bands centered on 520 and 550 nm, respectively (Figure 1a). The 550 nm resulting fluorescence peak is then collected by the same microscope objective and is spectrally analyzed with the Raman (Renishaw) system (Figure 1b).

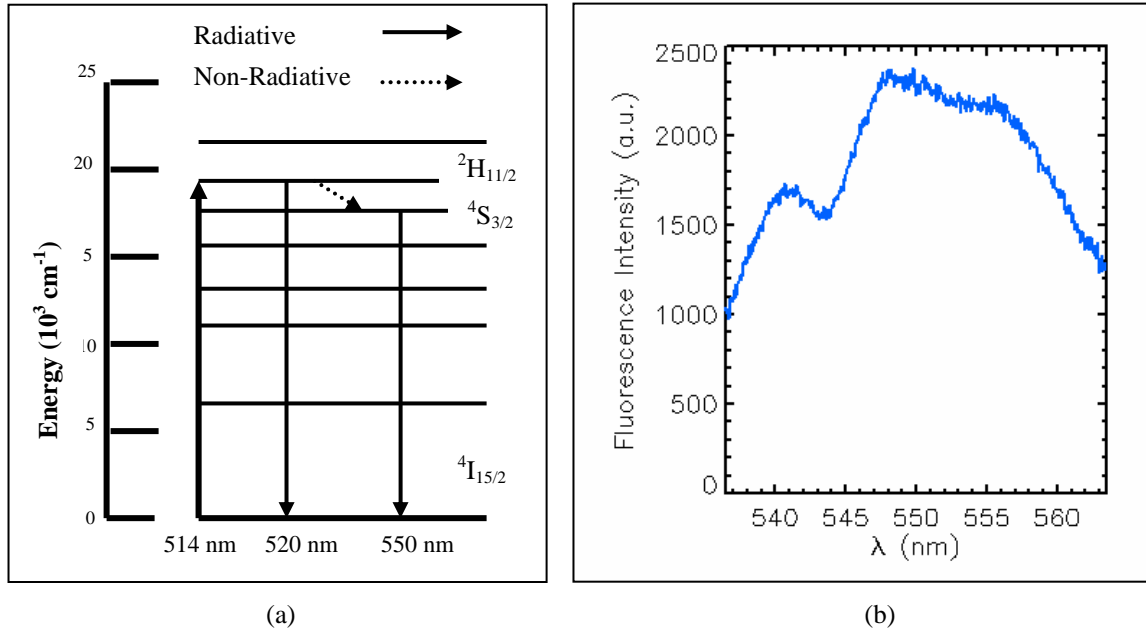


Figure 1: (a) Partial energy level diagram for erbium in germanosilicate host (b) The 550 nm fluorescence peak collected by the Raman system.

The integrated fluorescence intensity over the wavelength range of 537.5-562.5 nm from each point is taken as an indication of the local dopant concentration. A two-dimensional fluorescence profile is then formed by scanning the core area in steps of $0.25 \mu\text{m}$ in both the x and y direction. As a result, a two-dimensional map of the relative ion distribution is obtained. A typical fluorescence image of an erbium doped optical fiber (Commercial grade erbium doped fiber available from the Optical Fiber Technology Centre) is shown in Figure 2. Information about the optogeometric parameters of the core area, along with the well-known depression in erbium concentration at the central core region, is clearly visible.

Quantitative Phase Microscopy

QPM was performed using transverse images obtained with a standard bright-field microscope (Olympus BX-60 microscope, $0.95 \times 40\times$ UplanApo microscope objective). The condenser numerical aperture was set to 0.2 and a bandpass filter with a central wavelength of 521 nm and a passband of 10 nm was included in the light path. The aforementioned EDFA sample was first

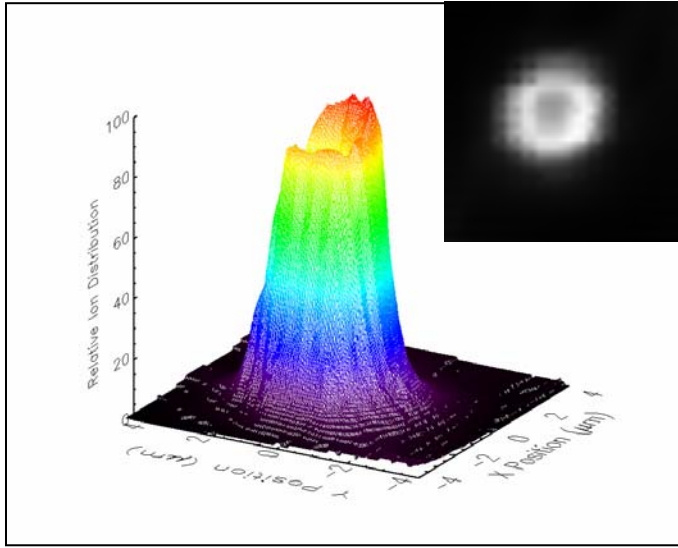


Figure2: Two dimensional fluorescence profile detected from the endface of the freshly cleaved EDFA sample.

A transverse profile through the centre of the core of the fiber showing the relative erbium ion distribution, extracted from the fluorescence image in Figure 2, is also displayed. Clearly evident is a resemblance of the erbium distribution profile to that of the refractive index including the depleted region in the core centre. It can be seen, however that there appear to be subtle differences in these profiles that are the subject of current investigation.

Nano-Secondary Ion Mass Spectroscopy (NanoSIMS)

The NanoSIMS method was applied for the direct analysis of an experimental highly doped erbium doped optical fiber. This technique provides a direct measurement of the concentration of ion species present in a sample and is an important tool for investigating the relationship between the erbium ion concentration and the fluorescence intensities obtained using the Raman method described above. The measurements were performed using a commercial Cameca NanoSIMS 50 ion microprobe located at the Centre for Microscopy and Microanalysis (CMM) at the University of Western Australia. Chemically reactive primary ions of $^{16}\text{O}^-$ were utilized with impact energies of 16keV in order to bombard the polished endface of the fiber sample at an angle normal to the sample surface. In addition, the ion beam was scanned across the endface of the fiber so that two dimensional images of the erbium as well as the silica ions could be obtained. The detection of both the erbium and silica ions was realized simultaneously. The raw erbium counts were then normalized to the silica background so that possible systematic errors due to variations in secondary ion yield would be minimized. The acquired image of the normalized erbium profile as well as its transverse linescan through the centre of the core is shown in Figure 4a. The same fiber

stripped of its plastic coating, cleaned and then immersed in index matching liquid (ThorLabs, A G608N) prior to imaging in order to minimize unwanted lens effects caused by the relatively large radius of curvature of the cladding/fluid interface. Three bright-field images of the EDFA sample were obtained. These consisted of an in-focus image and two defocused images at $\pm 2.0 \mu\text{m}$. These three images were then processed using an implementation of the inverse Abel transform as outlined in reference [7] so that the refractive index profile of the fiber under examination could be achieved. The acquired change in the refractive index for the central core region of the EDFA sample is shown in Figure 3. A

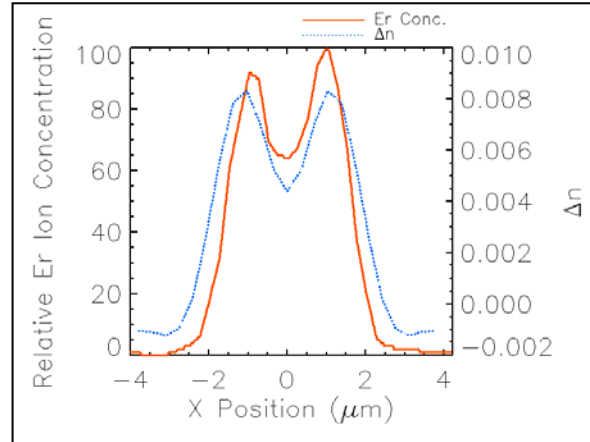


Figure 3: A transverse profile through the centre of the fiber showing the relative erbium ion distribution. Also shown is the average radial refractive index profile determined using QPM

sample was also examined using the Raman system, the results of which are displayed in Figure 4b. Although it is clear that both techniques have revealed the asymmetric configuration of the fiber, which is believed to be the outcome of an unsuccessful collapse during the fabrication process, there is still a significant divergence between the two techniques in regards to the exhibited depleted region in the core centre. A closer examination of this is the subject of ongoing research.

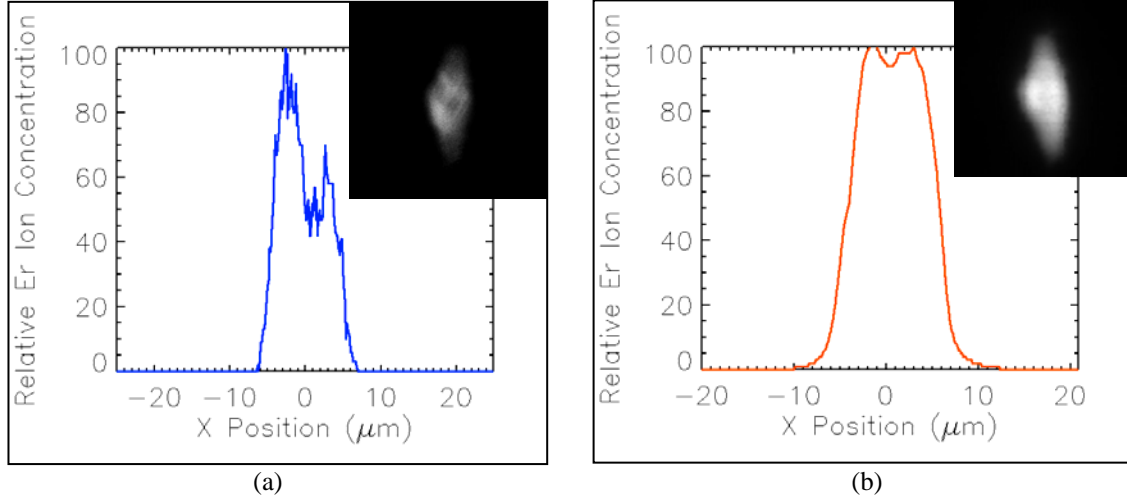


Figure 4: (a) Normalized two-dimensional erbium ion profile obtained by the NanoSIMS system. Also presented in this figure is the extracted transverse profile through the centre of the core of the fibre showing the relative ion distribution (b) Two-dimensional fluorescence profile Acquired by the Raman system. Also presented in this figure is the extracted transverse profile through the centre of the core of the fibre showing the relative ion distribution.

Conclusion

We have demonstrated the applicability of a variety of imaging systems to the characterization of erbium doped optical fibers at a submicron level. It is anticipated that further work with these systems on rare-earth doped fibers will enhance our understanding of the investigated topics and will offer new insights regarding the physical and optical parameters of fiber lasers and amplifiers.

Acknowledgements

The authors would like to thank John Canning of the Optical Fiber Technology Centre (OFTC), Australia, as well as Thinh Nguyen of Victoria University for the provision of the fiber specimens. Neal McNaughton (UWA) is thanked for fabricating the NanoSIMS sample mount. This work sponsored in part by the Australian Research Council NANO-MNRF.

References

1. Michel J.F. Digonnet, *Rare-earth-doped fiber lasers and amplifiers*, 2nd ed, New York: Marcel Dekker, 2001.
2. R. J. Mears, L. Reekie, I. M. Jauncey, and D. N. Payne, *Elect. Lett.* **23**, 1026, 1987.
3. E. Desurvire, J. L. Zyskind, and C. R. Giles, *IEEE J. Lightwave Technol.* **8**, 1730, 1990
4. N. Kagi, A. Oyobe, and K. Nakamura, *I.E.E.E J. Lightwave Tech.*, **8**, 1319, 1990.
5. T. Kashiwada, M. Shigematsu, T. Kougo, H. Kanamori, and M. Nishimura, *I.E.E.E. Photonics Tech. Lett.*, **3**, 721, 1991.
6. D. T. Bowron, R. J. Newport, J. S. Rigden, E. J. Tarbox, and M. Oversluizen, *J. Materials Science*, **38**, 485, 1996.
7. A. Roberts, E. Ampem-Lassen, A. Barty, K.A. Nugent, G.W. Baxter, N.M. Dragomir, and S.T. Huntington, *Opt. Lett.*, **27**, pp. 2061, 2002.

Measuring electro-optic coefficients of poled polymers using fiber-optic Mach-Zehnder interferometer

Yi-Ping Wang¹, Jian-Ping Chen, Xin-Wan Li, Jian-Xun Hong,
Xiao-Hong Zhang, Jun-He Zhou, and Ai-Lun Ye

State Key Laboratory on Local Fiber-Optic Communication Networks and Advanced Optical Communication Systems, Shanghai Jiao Tong University, Shanghai 200030, China,, ¹ E-mail: wangyp@sjtu.edu.cn

Abstract: It is proposed and demonstrated that fiber-optic Mach-Zehnder interferometer measures accurately the EO coefficients of, not only the poled polymer thin film, but also the poled polymer waveguide. Furthermore, the tensor components, both r_{13} and r_{33} , of EO coefficient can be measured simultaneously.

1. Introduction:

Poled polymers have received considerable attentions for the high electro-optic (EO) coefficient [1]. They can be used to fabricate high speed optical devices, such as EO modulator, optic switch, and waveguide grating. There are a number of methods measuring the EO coefficients of poled polymers. One popular method is simple reflection technique [2]. It is mainly used to measure the tensor component of EO coefficient, r_{33} , of polymer thin film without upper cladding or lower cladding, and its measurement precision is relatively low. A free space Mach-Zehnder (MZ) interferometer that can accurately measure the tensor components, r_{13} and r_{33} , of EO coefficients of poled polymer simultaneously, was reported [3]. Nevertheless, in contrast with the fiber-optic MZ interferometer [4], the free space MZ interferometer is subject to some problems, such as bulky optic elements, configuring hardness, complex experiment set-up and poor stability. In this paper, it is proposed and demonstrated that a novel fiber-optic M-Z interferometer system measures accurately the EO coefficients of, not only the poled polymer thin film, but also the poled polymer waveguide.

2. Principles:

The intensity, I , of light from a MZ interferometer with one arm modulated at frequency of Ω , is given as [3, 5]

$$I = \frac{1}{2} [E_{01}^2 + E_{02}^2 + 2E_{01}E_{02} \cos(\phi + A \cos \Omega t)] \quad (1)$$

where E_{01} and E_{02} are the field amplitudes in each arm of the interferometer, A is the modulation amplitude, and ϕ is the optical bias, i.e. the phase difference without the modulation. For small signal modulation, the modulation amplitude output is given by

$$I_{\text{sig}} = E_{01}E_{02}A|\sin \phi| \quad (2)$$

By varying the optical bias, ϕ , the maximum and the minimum intensities, I_{max} and I_{min} , of interference pattern can be determined. Thus, $E_{01}E_{02}$ can be given by

$$E_{01}E_{02} = (I_{\text{max}} - I_{\text{min}})/2 \quad (3)$$

According to the Fresnel relation, the refractive index n_θ and the EO coefficient tensor, r_θ , of poled polymer, corresponding to the incident light with a polarization angle, θ , relative to the x-axis (see Fig.1), can be given by [3]

$$\frac{1}{n_\theta^2} = \frac{\cos^2 \theta}{n_e^2} + \frac{\sin^2 \theta}{n_o^2} \quad (4)$$

$$r_\theta = r_{33} \cos^2 \theta + r_{13} \sin^2 \theta \quad (5)$$

where n_e and n_o are the refractive index corresponding to 'e' and 'o' light, respectively. If the poled polymer has a pair of parallel plate electrodes, as shown in Fig.1, the phase modulation amplitude, A , in Eq. (2) can be written as

$$A = \pi r_\theta n_\theta^3 V_{rms} / \lambda \quad (6)$$

where V_{rms} is the root mean square modulation voltage. According to Eqs. (2), (3) and (6), the EO coefficient tensor of poled polymer, r_θ can be determined by

$$r_\theta = \frac{2\lambda I_{sig}}{\pi n_\theta^3 V_{rms} (I_{max} - I_{min})} \quad (7)$$

where I_{sig} is the modulation amplitude measurement when the phase bias is $\phi = \pi/2$ or $\phi = 3\pi/2$. Thus, according to Eq. (5), r_{13} and r_{33} can be obtained by varying the polarization angle θ .

3. Experiments:

The fiber-optic MZ interference system measuring EO coefficient of poled polymer is shown in Fig. 1. The sample arm (arm1) of the MZ interferometer with a polarization controller has a pair of collimators allowing the measured polymer sample to be inserted. A section of fiber in another arm (arm2) is affixed on a piezoelectric transducer (PZT), which can vary the phase bias of MZ interferometer. The maximum and minimum intensities, I_{max} and I_{min} , of the DC interference fringes can be measured by adjusting the voltage applied on the PZT. The insert loss, caused by the polymer sample and the collimators, may results in an intensity difference in two arms. This was overcome by employing an optical passive coupler with a coupling ratio of 85:15. The coupling ratio of another coupler is 50:50. Thus, the high visibility of the interference stripes was maintained. For example, when a broadband ASE source was applied, the high stripe visibility was observed, and the transmission spectrum of the MZ interferometer is shown in Fig.2. The measured polymer sample may be either a poled polymer thin film with one transparent electrode or a poled polymer waveguide with a pair of parallel plate electrodes and pigtail fibers, as shown Fig. 1(b) and Fig. 1 (c). For polymer waveguide measurement, the pigtail fibers of the waveguide are directly coupled with the arm1 by connector instead of the collimators.

The polymer thin film sample was prepared by the following method. Firstly, indium-tin-oxide (ITO) was deposited on the SiO_2 wafer, as a transparent electrode. Secondly, the organic polymer doped with the dye molecules, PMMA-DR1, was spin-coated and cured on the ITO. Then, it was poled using the corona method [6]. This poled polymer thin film was inserted between two collimators in the arm1. Another transparent electrode can be obtained by employing the other ITO glass clinging to the polymer thin film, as shown in Fig. 1(b). When an AC modulation signal, V_{rms} , is applied to the poled polymer sample, the EO modulation was transformed to the output electric signal, I_{sig} , that can be read by the lock-in amplifier. Thus, according to Eq. (7), different EO coefficient tensor, r_θ , can be obtained by varying the polarization angle θ . The tensor components, r_{13} and r_{33} , of EO coefficient correspond to special polarization angle, $\pi/2$ and 0, respectively.

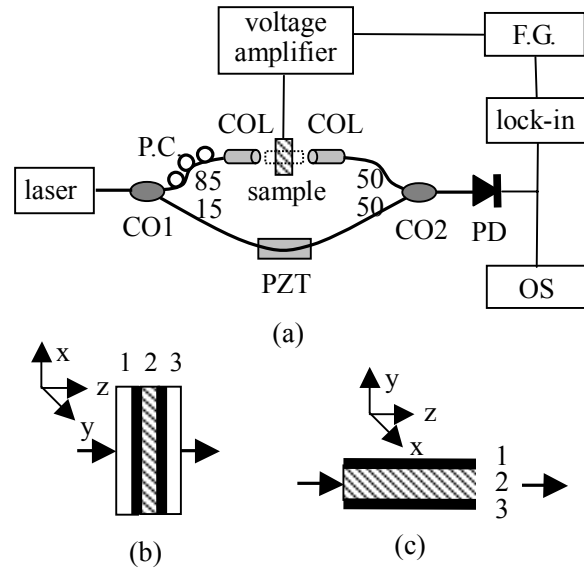


Fig. 1 (a) Fiber-optic MZ interference measurement system, OS: oscillograph, CO1 and CO2: coupler, COL: collimator, PC: polarization controller, PZT: piezoelectric transducer, F.G.: function generator, PD: photodiode; (b) Sample of polymer thin film, 1: ITO glass, 2: polymer thin film, 3: ITO glass; (c) Sample of polymer waveguide, 1: upper electrode, 2: polymer waveguide, 3: lower electrode

The EO coefficient measurements of the PMMA-DR1 sample are $r_{13} = 8.3 \text{ pm/V}$ and $r_{33} = 25.7 \text{ pm/V}$.

4. Conclusions:

A novel fiber-optic MZ interference system was present. This system can be used to measure EO coefficients of, not only the poled polymer thin film, but the poled polymer waveguide, corresponding to the light incidence being parallel and vertical to the modulation electric field direction, respectively. Furthermore, The tensor components, both r_{13} and r_{33} , of EO coefficients, can be measured simultaneously. In comparison with the free space MZ interferometer and other measurement methods, this method has many advantages, such as simple experiment configuration, easy operation, high measurement precision, good repeatability and easy sample preparation. The most outstanding advantage is that the second electrodes need not be fabricated on the top of polymer film before poling and measuring. Instead, the second electrodes can be provisionally replaced by other ITO glass. Therefore, it is especially suitable to measure EO coefficients of trial polymer samples. In addition, stringent environment stability requirement can be obviated by means of adjusting continually the phase bias of the MZ interferometer.

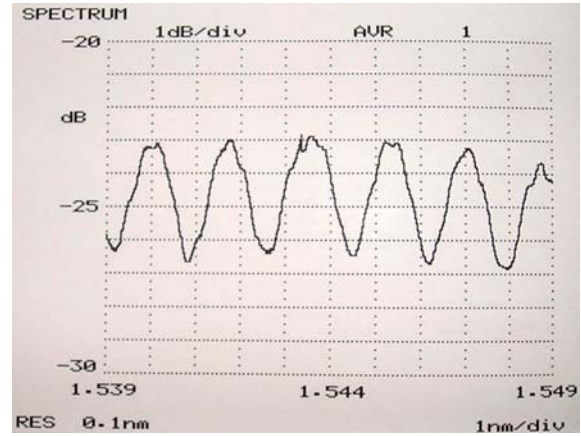


Fig. 2 Transmission spectrum with a high stripe visibility of fiber-optic MZ interferometer

5. Acknowledge:

This work was supported by the China Postdoctoral Science Foundation (No. 2003034258).

Interference

- [1] Oh M. C., Hua Zhang, Zhang C., Erlig H., Chang Y., Tsap B., Chang D., Szep A., Steier W. H., Fetterman H. R., and Dalton L. R.: 'Recent advances in electrooptic polymer modulators incorporating highly nonlinear chromophore', IEEE J. on Selected Topics in Quantum Electronics, 2001, **7**(5), pp. 826-835
- [2] Chen C. C., and Man H. T.: 'Simple reflection technique for measuring the electro-optic coefficient of poled polymers', Appl. Phys. Lett., **56**(18), 1990, pp. 1734-1736
- [3] Norwood, R. A., Kuzyk M. G., and Keosian, R. A.: 'Electro-optic tensor ratio determination of side-chain copolymers with electro-optic interferometry', J. Appl. Phys., 1994, **75**(4), pp. 1869-1874
- [4] Ahn, J. T., Lee, H. K., Kim, K. H., Jeon, M. Y., Lim, D. S., and Lee, E. H.: 'A stabilised fibre-optic Mach-Zehnder interferometer filter using an independent stabilisation light source', Opt. Communications, 1998, **157**, pp. 62-66
- [5] Singer, K. D., Kuzyk, M. G., Holland, W. R., Sohn, J. E., Lalama, S. J., Comizzoli, R. B., Katz, H. E., and Schilling M. L.: 'Electro-optic phase modulation and optical second-harmonic generation in corona-poled polymer films', Appl. Phys. Lett., 1988, **53**(19), pp. 1800-1802
- [6] Daoa, P. T., Williams, D. J., McKenna, W. P. and Kim G. B.: 'Constant current corona charging as a technique for poled organic nonlinear optical thin films' and the effect of ambient gas', J. Appl. Phys., 1993, **73** (5), pp. 2043-2050

Concepts and techniques for short optical pulse characterization

Christophe Dorrer

Bell Laboratories-Lucent Technologies

101 Crawfords Corner Road, Holmdel, NJ, 07733

Phone: 732 332 6463, Fax: 732 949 2473, email: dorrer@lucent.com

The measurement of the electric field of short optical pulses is an active domain of research and development as many applications demand accurate characterization. Characterization techniques can be classified according to general concepts that condition their properties and implementation. The concepts of spectrography, interferometry and tomography are reviewed and examples of corresponding techniques are presented.

I. Electric field, correlation functions and Wigner-Ville function

Pulse characterization aims at measuring the electric field of light as a function of time $E(t)$ (or equivalently frequency $\tilde{E}(\omega)$). While the spectrum $|\tilde{E}(\omega)|^2$ can easily be measured with a spectrometer (a time-stationary device), the intensity $|E(t)|^2$, the temporal phase $\psi(t)$ (from which the instantaneous frequency $-\frac{\partial\psi}{\partial t}$ is defined) and the spectral phase $\phi(\omega)$ (from which the group delay $\frac{\partial\phi}{\partial\omega}$ is defined) require some form of temporal resolution, i.e. a time-non-stationary device. A time-stationary and a time-non-stationary filter are needed to completely characterize the electric field of a pulse[1,2].

If the source under test emits a periodic train of pulses, appropriate characterization is obtained with the electric field. For a stochastic source, one can either sample the output of the source (either the intensity of the source, as is performed by electrical or optical sampling oscilloscopes[3], or the electric field as is performed by linear optical sampling[4,5]). One can also measure a correlation such as the two-time or two-frequency correlation functions $C(t, t') = \langle E(t) \cdot E^*(t') \rangle$ and $C(\omega, \omega') = \langle \tilde{E}(\omega) \cdot \tilde{E}^*(\omega') \rangle$, from which one can define the Wigner-Ville (W-V) function[6,7]:

$$W(\tau, \omega) = \int C(\tau - \frac{t}{2}, \tau + \frac{t}{2}) \exp(i\omega t) dt \quad (1)$$

This function is real, its time and frequency marginals are the temporal intensity and spectrum, and it behaves in some cases as would be expected from a probability density in the chronocyclic space (ω, τ) although it can take negative values (Fig. 1). For example chirp is represented by a correlation between time τ and frequency ω . The W-V function is useful to interpret pulse characterization strategies and contains information about the coherence of the source (i.e. how similar the pulses in a train of pulses are).

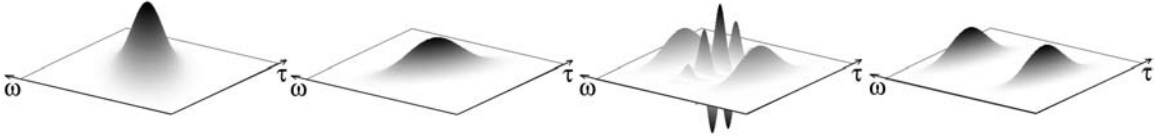


Fig.1: Wigner-Ville function of a Fourier-transform limited pulse, a chirped pulse, 2 mutually coherent chirped pulses and 2 mutually incoherent chirped pulses (from left to right). In the latter case, note the absence of the crossed terms between the two individual Wigner functions.

II. Spectrography

In spectrographic techniques, one typically operates sequentially in the two conjugate domains ω and τ . For example, a spectrogram is built by first applying a temporal gate $G(t)$ on the pulse, and then measuring the spectrum of the gated field (Fig. 2). A simplified view is that spectra measured at various delays between the pulse and the gate contain information about the chirp in the pulse, as different optical frequencies are present at different times. The spectrogram is mathematically given by:

$$S(\tau, \omega) = \left| \int E(t) \cdot G(t - \tau) \cdot \exp(i\omega t) dt \right|^2 \quad (2)$$

The spectrogram is a convolution of the W-V function of the pulse and the W-V function of the gate[6], and spectrographic techniques operate by using the gate W-V function as a probe in the chronocyclic space on the pulse W-V function. Spectrograms are widely used in ultrafast optics, where a suitable gate can be obtained using a nonlinear interaction with a replica of the pulse itself (such implementation is usually called Frequency Resolved Optical Gating[8]). In the telecommunication environment, a gate can be implemented with a nonlinear interaction[9,10] or a temporal modulator driven synchronously with the pulse[11,12]. Another way of operating is to first gate in

the spectral domain and then measure the temporal intensity of the filtered pulse, which leads to a sonogram[13,14].

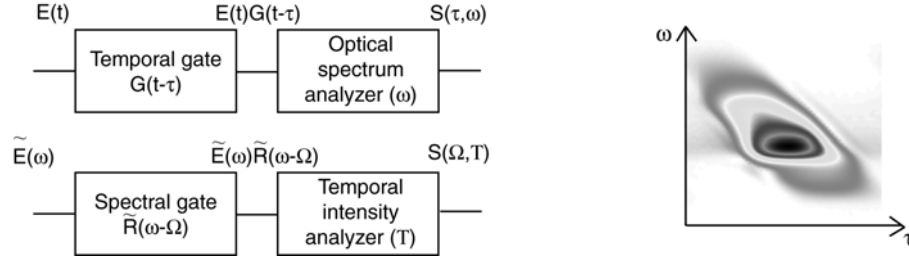


Fig. 2: General implementation of a spectrogram and sonogram (left upper and lower plots) and example of the spectrogram of a chirped pulse (right plot, note the coupling between τ and ω).

Sonograms and spectrograms can usually give a good picture of the chirp, thanks to the relation between their first order moments and the chirp[6]. However, in the most general case, obtaining the electric field of the pulse under test requires an iterative phase retrieval algorithm such as the Principal Component Generalized Projection Algorithm that can retrieve both $E(t)$ and $G(t)$ from $S(\tau, \omega)$ [15]. An implementation of this concept using an electroabsorption modulator as a gate is displayed on Fig. 3[11,12]. Such linear diagnostic is highly sensitive and can characterize trains of pulses with average power as low as -40 dBm. It was used for various characterization tasks such as the optimization of pulse carving and pulse compression setup and the characterization of semiconductor optical amplifiers[16].

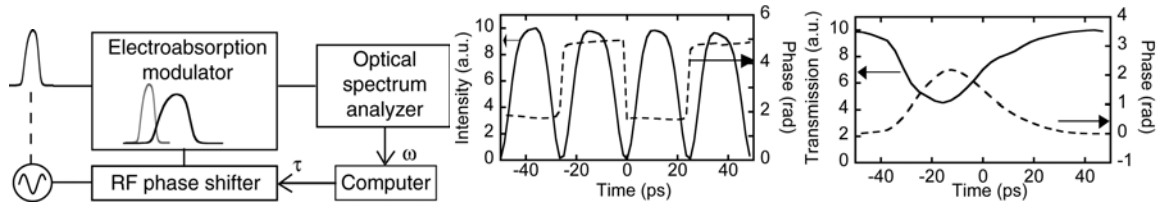


Fig. 3: spectrogram implemented using an electroabsorption modulator as a gate (left). The computer controls the delay between the gate and the pulse using a RF phase shifter operating on the driving signal to the EAM and records the spectra after modulation. Measured electric field of a CSRZ train of pulses (middle) and measured transmission of a gain-depleted SOA (right).

III. Interferometry

Interferometric techniques are powerful techniques for measuring electric fields. For short optical pulses, they usually operate by measuring the phase difference between two optical frequencies, and have the advantage of using an algebraic non-iterative inversion that leads to high accuracy and update rates. For example, if the spectrum is composed of

modes Ω_N separated by Ω (which is the case for a source with period $2\pi/\Omega$), it is only required to know the intensity of each mode (easily measured with an optical spectrum analyzer) and the phase of each mode, which can be obtained by measuring the relative phase between mode N and mode $N+1$ for all N . Various techniques are known to extract such phase difference (Fig. 4). For example, one can spectrally filter the two modes N and $N+1$ and measure the phase of the resulting temporal beating at $2\pi/\Omega$ (Fig. 4a)[17]. One can also modulate the pulse so that modes initially at different frequencies end up overlapping in the modulated pulse. A modulation at $\Omega/2$ leads to a sideband at $\Omega_N + \Omega/2$ for the modes N and $N+1$. As the intensity of such sideband depends on the phase difference between these 2 modes, it is possible to reconstruct the spectral phase of the pulse (Fig. 4b)[18]. In the spectral version of spatial shearing interferometry, one interferes the pulse under test $\tilde{E}(\omega)$ with its spectrally sheared replica in a spectrometer (Fig. 4c) [19,20]. The spectrum is in such case:

$$\left| \tilde{E}(\omega) + \tilde{E}(\omega - \Omega) \right|^2 = I(\omega) + I(\omega - \Omega) + 2 \left| \tilde{E}(\omega) \right| \left| \tilde{E}(\omega - \Omega) \right| \cos[\varphi(\omega) - \varphi(\omega - \Omega)] \quad (3)$$

which depends upon the relative phase between frequencies ω and $\omega - \Omega$. Such shearing can be performed using a nonlinear interaction (as in Spectral Phase Interferometry for Direct Electric-field Reconstruction[21]) or using linear temporal phase modulation which can be obtained by driving a phase modulator with a sine wave and synchronizing the pulse with one of the zero-crossings of the modulation[22,23].

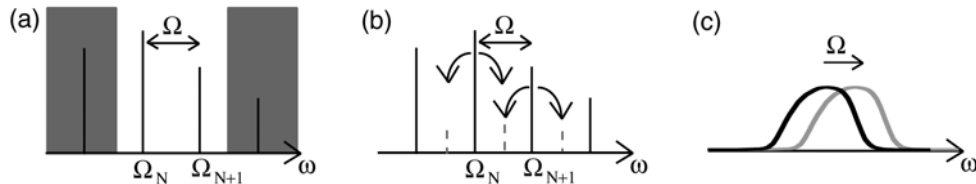


Fig. 4: various interferometric concepts. In (a), two modes are extracted and their phase difference is compared to a reference in the time domain. In (b), the modulation of the pulse at $\Omega/2$ leads to sidebands whose intensity is related to the phase difference between modes. In (c), the pulse is interfered with its spectrally sheared replica.

IV. Tomography

Tomography relates to the reconstruction of an object from a set of its projections[24]. A tomographic reconstruction of the W-V function can be implemented by measuring its projections on various axes, or equivalently rotating the W-V function by various angles

and measuring its projections on a fixed axis. A combination of spectral and temporal quadratic phase modulations can perform an arbitrary rotation in the chronocyclic space, and the projection of a W-V function on the frequency axis is the corresponding spectrum (Fig. 5a and 5b), and it is therefore possible to obtain a set of projections of the W-V function[25]. This set of projections (known as the Radon transform) corresponds to tomographic imaging with a non-diffracting parallel beams, and the reconstruction of the Wigner function can be achieved using a filtered back-projection algorithm. This would measure the W-V function independently of the coherence of the source, and the electric field could be calculated from the W-V function if the source is perfectly coherent. No experimental application has been made, but two simplified versions of tomography are known. In the time-to-frequency converter[26], the W-V function is rotated by $\pi/2$, therefore the measured spectrum corresponds to the temporal intensity of the initial pulse (Fig. 5c). Simplified chronocyclic tomography is based on a relation between the electric field, a projection of its W-V function for a given angle and the derivative of the projection with respect to the rotation angle[27,28]. If the rotation is implemented with a quadratic temporal phase modulation $\psi t^2 / 2$, the corresponding spectrum is I_ψ and one has:

$$\frac{\partial I_\psi}{\partial \omega} = \frac{\partial}{\partial \omega} \left[I(\omega) \cdot \frac{\partial \varphi}{\partial \omega} \right] \quad (4)$$

This relation combined with the spectral intensity of the pulse allows the reconstruction of the electric field. The derivative in Eq. 4 can be obtained from the difference between two spectra after small rotations of the W-V function (Fig. 5d).

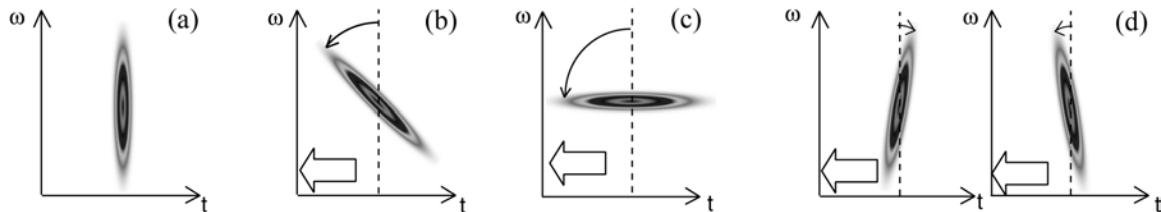


Fig. 5: tomographic concepts in the chronocyclic space. The W-V function (a) can be rotated via a combination of quadratic temporal and spectral modulation and projected on the frequency axis (b). Chronocyclic tomography uses a large number of projections, but the time-to-frequency converter (c) and simplified chronocyclic tomography (d) respectively use 1 and 2 projections.

An experimental implementation of simplified chronocyclic tomography is presented on Fig.6. The derivative in Eq. 4 is obtained by measuring two spectra after a positive and

negative phase modulation obtained by synchronizing the pulse with the maximum or minimum of a sinusoidal modulation.. A technique based on the direct measurement of the difference between the two spectra based on lock-in detection was also demonstrated[29].

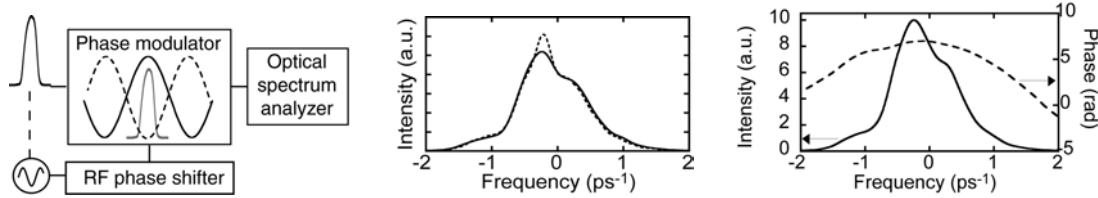


Fig. 6: setup for simplified chronocyclic tomography (left), spectra measured after positive and negative quadratic temporal phase modulation (dashed and continuous line), and reconstructed electric field.

References

1. V. Wong and I. A. Walmsley, *J. Opt. Soc. Am. B*, **12**, 1491-1499 (1995).
2. I. A. Walmsley and V. Wong, *J. Opt. Soc. Am. B*, **13**, 2453-2463 (1996).
3. P. A. Andrekson, *Optical Fiber Conference*, **TuO1**, (2004).
4. C. Dorrer et al, *IEEE Photon. Technol. Lett.*, **15**, 1746-1748 (2003).
5. C. Dorrer, J. Leuthold, and C. R. Doerr, *Optical Fiber Conference*, **PD33**, (2004).
6. L. Cohen, *Time-frequency analysis*, (Prentice Hall PTR, 1995).
7. J. Paye, *J. Opt. Soc. Am. B*, **28**, 2262-2273 (1992).
8. R. Trebino et al, *Rev. Sci. Instrum.*, **68**, 3277-3295 (1997).
9. J. M. Dudley et al, *IEEE J. Quantum Electron.*, **35**, 441-450 (1999).
10. P.-A. Lacourt et al, *Opt. Lett.*, **27**, 863-865 (2002).
11. C. Dorrer and I. Kang, *Opt. Lett.*, **27**, 1315-1317 (2002).
12. C. Dorrer and I. Kang, *Photon. Technol. Lett.*, **16**, 858-860 (2004).
13. V. Wong and I. A. Walmsley, *J. Opt. Soc. Am. B*, **14**, 944-949 (1997).
14. D. T. Reid et al, *Electron. Lett.*, **36**, 1141-1142 (2000).
15. D. J. Kane, *IEEE J. Quantum Electron.*, **35**, 421-431 (1999).
16. I. Kang and C. Dorrer, *Optical Fiber Conference*, **MF43**, (2004).
17. P. Kockaert et al, *IEEE Photon. Technol. Lett.*, **12**, 187-189 (2000).
18. J. Debeau, B. Kowalski, and R. Boittin, *Opt. Lett.*, **23**, 1784-1786 (1998).
19. V. A. Zubov and T. I. Kuznetsova, *Sov. J. Quantum Electron.*, **21**, 1285-1286 (1991).
20. V. Wong and I. A. Walmsley, *Opt. Lett.*, **19**, 287-289 (1994).
21. C. Iaconis and I. A. Walmsley, *Opt. Lett.*, **23**, 792-794 (1998).
22. C. Dorrer and I. Kang, *Opt. Lett.*, **28**, 477-479 (2003).
23. I. Kang, C. Dorrer, and F. Quochi, *Opt. Lett.*, **28**, 2264-2266 (2003).
24. A. C. Kak and M. Slaney, *Principles of computerized tomographic imaging*, (IEEE Press, New York, 1987).
25. M. Beck et al, *Opt. Lett.*, **18**, 2041-2043 (1993).
26. M. T. Kaufman et al, *Appl. Phys. Lett.*, **64**, 270-272 (1994).
27. T. Alieva, M. J. Bastiaans, and L. Stankovic, *IEEE Trans. Signal Processing*, **51**, 112-123 (2003).
28. C. Dorrer and I. Kang, *Opt. Lett.*, **28**, 1481-1483 (2003).
29. I. Kang and C. Dorrer, *Conference on Lasers and Electro-Optics*, **CTuZ6**, (2004).

High spatial resolution PON measurement using an OTDR enhanced with a dead-zone-free signal analysis method

Noriyuki Araki, Hisashi Izumita, Yusuke Koshikiya and Minoru Nakamura

NTT Access Network Service Systems Laboratories, NTT Corporation,

1-7-1 Hanabatake, Tsukuba-city, Ibaraki 305-0805, Japan

Phone: +81-29-868-6365, Fax: +81-29-868-6360 E-mail: noriyuki@ansl.ntt.co.jp

Abstract: This paper describes a high spatial resolution OTDR measurement technique for PON, which employs optical filters installed at the end of optical fiber lines. This technique can measure bending or splice losses in an attenuation dead zone just behind the Fresnel reflection of an optical splitter by using a dead-zone-free signal analysis method.

1. Introduction

Broadband optical access services are now commercially available [1]. NTT provides a high-speed IP connection service with a maximum bit rate of 100 Mbps. The number of FTTH subscribers in Japan is increasing rapidly and exceeded 0.89 million by the end of fiscal 2003. This number will reach more than 2 million by the end of fiscal 2004 [2]. Passive optical networks (PONs) provide the main FTTH service based on B-PON or GE-PON, where several customers share an OLT and an optical fiber [3]. Optical access networks are also expanding rapidly as the number of FTTH subscribers increases. Broadband network provision currently requires thousands of optical fibers to be accommodated in a central office for optical access networks. An optical fiber line testing system is essential for reducing maintenance costs and improving service reliability in optical fiber networks. The automatic optical fiber operations support system, AURORA, has already been deployed [4] and developed for application to wide band transmission systems and various network topologies [5]-[7]. We use the ultra long wavelength (U-band) of 1650 nm for maintenance testing in accordance with ITU-T recommendation L.41 [8]. We have also proposed a fault isolation technique for identifying a faulty optical fiber line below an optical splitter from a central office by using a high-resolution optical time domain reflectometer (H-OTDR) [6]. However, this approach cannot pinpoint the location of a fault in a branched optical fiber because the H-OTDR pulse width of 10 ns is very narrow and the dynamic range of the measurement is insufficient to determine the Rayleigh backscattered power from branched optical fibers. With a view to monitoring optical fiber cables in access networks, the OTDR installed in the testing system must provide a higher dynamic range and higher spatial resolution simultaneously. This is because optical access networks have many connection points (optical connectors, fusion and mechanical splices), complex network structures, short span cables with neighboring connection points, and externally installed optical splitters. However, it is very difficult to realize both requirements, because there is a tradeoff between dynamic range and spatial resolution [9]. Moreover, the spatial resolution is limited by the bandwidth of the OTDR receiver and the OTDR measurement parameters.

We therefore propose a new approach designed to improve the spatial resolution by using a new OTDR signal analysis method. This paper describes a high spatial resolution PON measurement technique that uses an FBG filter embedded in a termination cable and a dead-zone-free signal analysis method.

2. Optical fiber line testing system

Figure 1 shows the configuration of our optical fiber line testing system. The system consists of test equipment (TE) containing an optical time domain reflectometer (OTDR), and optical fiber selectors, and test access modules (TAMs) containing an optical coupler and optical filters. The TE and FSs are installed in the cable termination room of a central office. The TAMs introduce a test light into optical fiber lines. Termination cables with an optical filter are equipped at either end of the optical fiber line. The filter allows a communication light to pass but not a test light. The optical filters installed in front of the ONUs reflect the test light from the OTDR to identify faults between optical fiber lines and ONUs [7]. The control terminal orders the TE to perform various optical fiber tests through a data communication network (DCN). The TE controls the OTDR and FSs, and returns the test results to the control terminal. This system performs automatic OTDR measurements, reveals fiber characteristics, and isolates faults and their location with no degradation in the transmission quality.

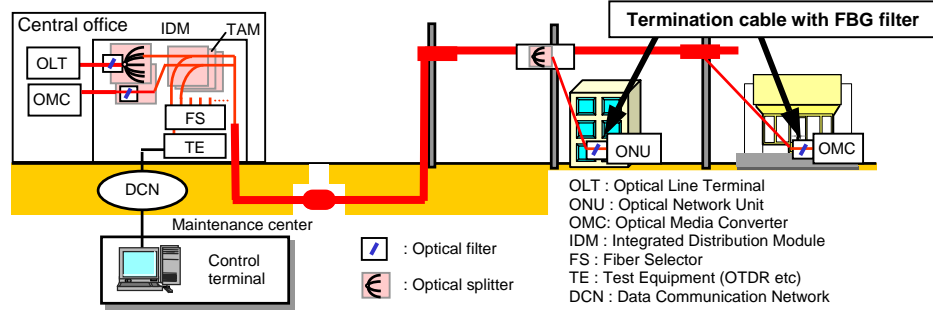


Fig. 1. Configuration of optical fiber line testing system with add-on type optical filter

Figure 2 shows insertion loss and reflection spectra of typical termination cables used in the field. We applied fiber Bragg grating (FBG) technologies to the optical filter, which is located in front of the ONU, to obtain a high return loss [6]. The average and maximum return losses for 30 sample FBG filters were 0.94 and 1.51 dB respectively. These FBG filter characteristics allow us to propose a dead-zone-free OTDR signal analysis method for analyzing a fault location just behind an optical splitter installed in an optical fiber line.

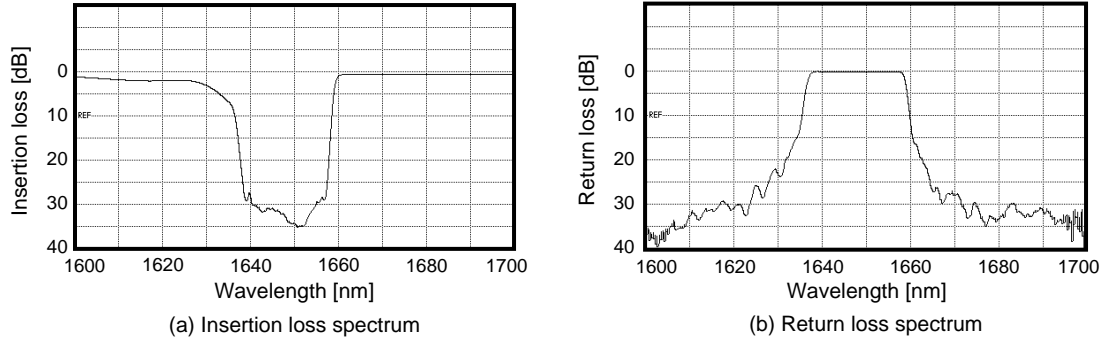


Fig. 2 Insertion loss and reflection spectra of a typical termination cable

3. Dead-zone- free OTDR signal analysis method

3.1 Principles

Figure 3 shows an OTDR trace to help explain the dead-zone-free signal analysis method. The wavelength of the OTDR test light is 1650 nm, and the SM optical fibers are 3 km long. An optical splitter is installed between the optical fibers by using SC connectors. When an FBG filter that reflects the 1650 nm test light is installed at the far end of the optical fiber line, we can observe an OTDR trace that consists of 2 sections, A and B. There is a large Fresnel reflection at the center of the OTDR trace that is caused by an FBG filter embedded in a termination cable. OTDR trace A shows the Rayleigh backscattering and the Fresnel reflections that originate from optical pulses input directly by the OTDR. OTDR trace B shows the Rayleigh backscattering and the Fresnel reflections that originate from optical pulses that are reflected by the FBG filter and that return to the OTDR with a time delay corresponding to the length of the optical fiber line. Namely, we also obtain an OTDR trace that is measured from the far end of the optical fiber line. This means we can obtain two OTDR traces for one end of the fiber line by performing a bi-directional OTDR measurement. We are able to analyze the characteristics of the optical fiber line more accurately by using these two OTDR traces.

There is a Fresnel reflection at the 4-branched optical splitter in OTDR trace A. The effect of the Fresnel reflection causes an attenuation dead zone [10] in which it is impossible to measure the fiber characteristics. When there is a bending loss just behind an optical splitter, we cannot detect it in OTDR trace A. This means we cannot isolate a fault between the optical splitter and the bending loss in the optical fiber line. Figure 4 shows the process of this dead-zone-free signal analysis method. Here, we describe how to replace the OTDR measurement data. First, we decide the attenuation dead zone in OTDR trace A, and a section (Section S_{att}), which corresponds to the length of

this dead zone in OTDR trace B. We then invert the slope of a line representing the fiber's backscatter signal and the location of the measurement samples in section S_{att} . Next we shift the Rayleigh backscattering level of section S_{att} to match that of the attenuation dead zone edge in OTDR trace A, and replace the measured data in the attenuation dead zone of OTDR trace A with the composed data in section S_{att} of OTDR trace B. The length of the attenuation dead zone depends on the height of the Fresnel reflection, the OTDR pulse width, the insertion loss, and the OTDR receiver bandwidth [9]. When a simple first-order low pass model is chosen for the approximation of the OTDR receiver function, the attenuation dead zone length L_{dz} is derived as given in Eq. 1.

$$L_{dz} = c/n [\tau - \ln\{(10^{0.2(Th-\rho)} - 10^{-0.2\rho}) / 10^{0.2\delta}\} / (2\pi Bw)]$$

Where, c is the speed of light in a vacuum, n is the group index of the optical fiber, τ is the OTDR pulse width, Th is the threshold of the vertical distance between the Rayleigh backscattering values, ρ is the insertion loss, δ is the height of the Fresnel reflection, and the Bw is the OTDR receiver bandwidth.

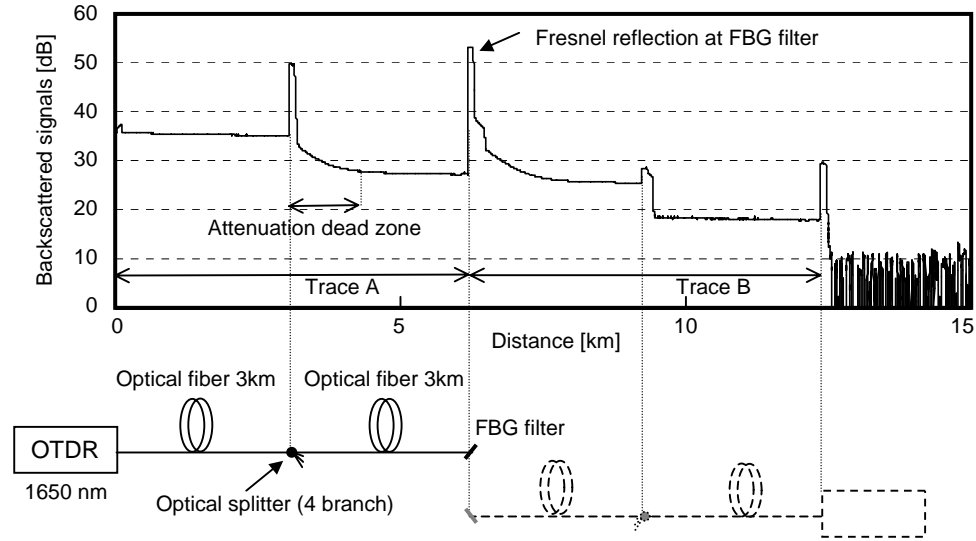


Fig. 3 OTDR trace of dead-zone-free signal analysis method

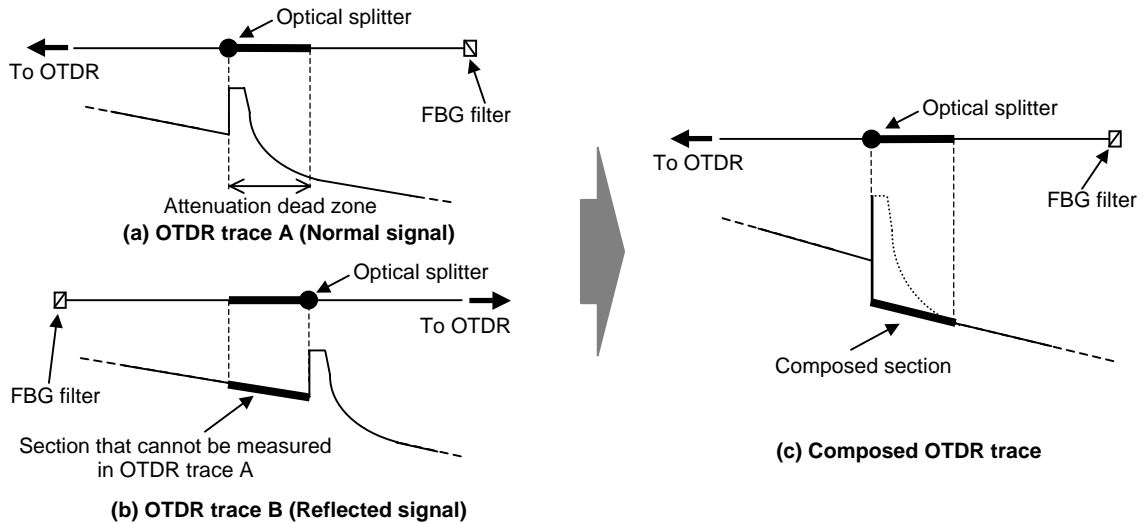


Fig. 4 Measured data replacement process of dead-zone-free signal analysis method

3.2 Experimental result

Figure 5 shows the experimental setup and the result obtained with the dead-zone-free OTDR signal analysis method. The experimental setup is the same as that shown in Fig. 3. The fibers before and after the optical splitter were both 3 km long. The insertion loss of the optical splitter was 6.6 dB, and the other 3 ports of the splitter were

not connected to fibers. The OTDR pulse width was 100 ns. The height of the Fresnel reflection at the optical splitter in OTDR trace A was 15.7 dB compared with the Rayleigh backscattering behind the optical splitter, and the length of the attenuation dead zone was about 450 meters. When we added a bending loss of 3.1 dB to the optical fiber line at a point 20 m behind the optical splitter. This bending loss was superimposed on the Fresnel reflection and it was impossible to measure it from OTDR trace A. Figure 5 (b) shows the reflected OTDR trace, which is the same when the OTDR testing is carried out from the other side of the optical fiber line. Therefore, the Fresnel reflection does not effect the measurement of the fiber section behind the optical splitter. The bending loss exactly 20 m behind the optical splitter was clearly measured. When the overlapped Rayleigh backscattering values from the branched optical fibers are measured in the OTDR trace, we are able to separate them by employing a fault location technique normally used for branched optical fiber networks [11], [12].

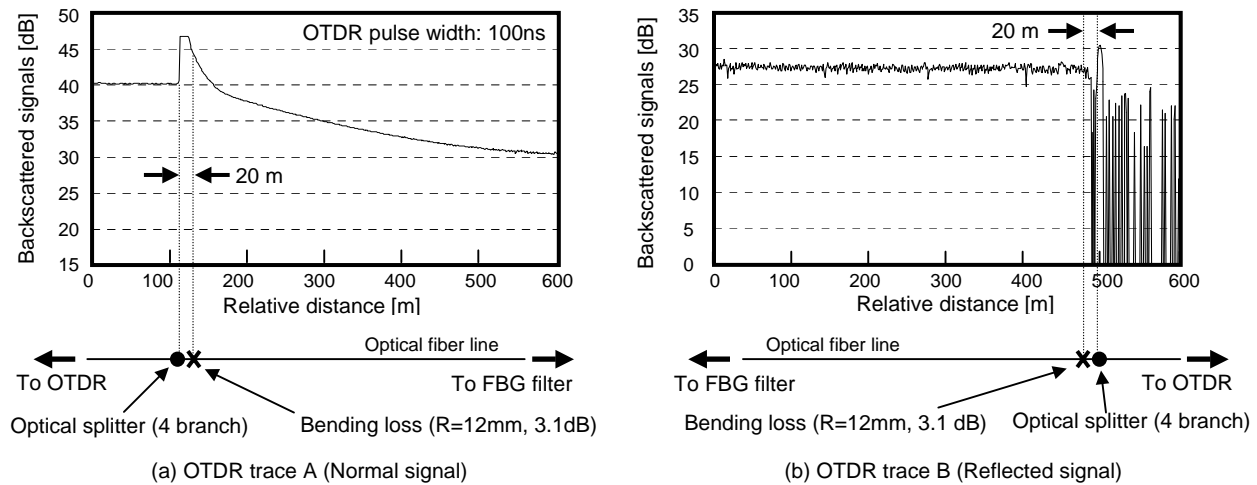


Fig. 5 Experimental setup and result of dead-zone-free signal analysis method

4. Conclusion

We have described an OTDR measurement technique with high spatial resolution for PON with an FBG filter at the end of an optical fiber line. We proposed a dead-zone-free signal analysis method that uses signals reflected at an FBG filter. We demonstrated the ability to measure bending loss with a spatial resolution of 20 m in the attenuation dead zone of the Fresnel reflection caused by a 4-branch optical splitter, when we used an OTDR pulse width of 100 ns. We also evaluated the required bandwidth of the OTDR receiver in relation to the length of the attenuation dead zone.

5. References

- [1] H. Shinohara, "NTT's deployment of FTTH services," *OFC2004 Technical Digest*, paper ThW2, Feb. 2004.
- [2] http://www.soumu.go.jp/joho_tsusin/eng/Statistics/number_usres.html
- [3] K. Okada, "The vision for HIKARI-soft services," *NTT Rev.*, vol. 13, no. 4, pp. 4-8, July 2001.
- [4] N. Nakao, H. Izumita, T. Inoue, Y. Enomoto, N. Araki, and N. Tomita, "Maintenance method using 1650-nm wavelength band for optical fiber cable networks," *J. Lightwave Technol.*, vol. 19, no. 10, pp. 1513-1520, Oct. 2001.
- [5] N. Araki, H. Izumita, N. Honda, and M. Nakamura, "Extended optical fiber line testing system using new eight-channel L/U-band crossed optical waveguide coupler for L-band WDM transmission," *J. Lightwave Technol.*, vol. 21, no. 12, pp. 3316-3322, Dec. 2003.
- [6] Y. Enomoto, H. Izumita, and M. Nakamura, "Over 31.5 dB dynamic range optical fiber line testing system with optical fiber fault isolation function for 32-branched PON," *OFC2003 Technical Digest*, paper ThAA3, pp. 608-610, 2003.
- [7] Y. Enomoto, N. Honda, H. Izumita, and M. Nakamura, "Optical fiber line testing system using test light bypass module for ADM ring networks," in *Proc. ECOC 2001*, vol. 3, We.B.1.6, 2001.
- [8] "Maintenance wavelength on fibres carrying signals", ITU-T Recommendation L.41, May 2000.
- [9] D. Derickson, "Fiber optic test and measurement", Prentice Hall Inc., 1997.
- [10] "Calibration of optical time-domain reflectometers (OTDRs)", IEC Standard, IEC 61746 Ed.1.0, 2001.
- [11] I. Sankawa, S. Furukawa, Y. Koyamada, H. Izumita, "Fault location technique for in-service branched optical fiber networks", *IEEE Photon. Technol. Lett.*, vol. 2, no. 10, pp. 766-768, October 1990.
- [12] F. Yamamoto, et al., *64th Optical Access Network PON-Workshop*, 6.2.1-6.2.7, 1994.

A Bi-Directional Optical Time Domain Reflectometry Technique Optimised for Short LAN Fibers.

N. D. Channon - Megger Limited, Dover England
A. G. Hallam - Halcyon Optical Services, Southampton England

Abstract: A process for constructing bi-directional OTDR traces is demonstrated that is better suited to the short fibers installed as part of local area networks (LANs). Reflections are eliminated from the processed trace and no fiber is obscured by dead zones.

Introduction

The optical time-domain reflectometer (OTDR) is a useful tool for characterising the losses along an optical fiber because it is a distributed measurement and the resulting trace represents the local loss at any point in the fiber. This loss is simply the gradient of the trace at the distance along the fiber or the magnitude of the step across an event such as a splice or connector.¹ The validity of these loss measurements depends on the consistency of the fiber before and after the event. They are only valid if the fiber used on both sides of an event is of the same physical construction and chemical composition. Bi-directional techniques, where an OTDR trace is obtained from both ends of the fiber, offer a way to combine the data into a more precise, and less fiber dependent measurement, of loss.² However, the conventional technique obscures useful data around each connector whereas the technique described here demonstrates an enhanced processing method that avoids this problem.

Conventional OTDR Measurement on a Duplex LAN fiber.

In LAN applications where the fiber under test (FUT) is duplex (two fiber cable) it is convenient to perform bi-directional measurements by attaching a loop-back patchcord at the far end of the link then measuring the resulting loop in both directions by shifting the OTDR between the duplex fibers.

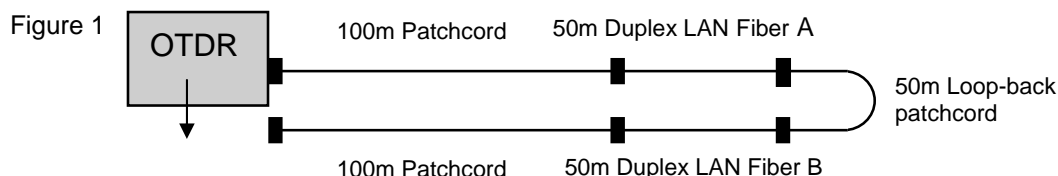


Figure 1 shows a 50m LAN fiber segment connected to an OTDR with a 100m duplex patchcord. A 50m loop-back patchcord has been attached to the far end and the resulting loop measured in both directions. Figure 2 shows the resulting OTDR traces with Trace B flipped so that the distance axis represents the same section of fiber on both traces. (It can also be seen from these traces that this FUT has a severe loss caused by a tight bend in it; a typical fault caused by poor installation)

When Trace A is examined, Figure 3, the connector between the launch patchcord and the FUT appears to have a negative loss of 0.03dB across it. However, the same connector, when measured in the reverse direction (Trace B) appears to have a loss of 0.07 dB shown in Figure 4 by the step down in power.

The problem is not unusual in the LAN environment and arises because the FUT and the loop-back are from different manufacturers of fiber and have slightly different optical properties such as numerical aperture. In the case of the Trace A, more scattered light is returned to the OTDR after the connector than before it giving rise to what is known as a “gainer”. The correct loss, the one that would be most likely to agree with a Light Source – Power Meter (LSPM) measurement, is probably the average of the two directions.³ Bi-directional analysis is one way to achieve this.

Figure 2

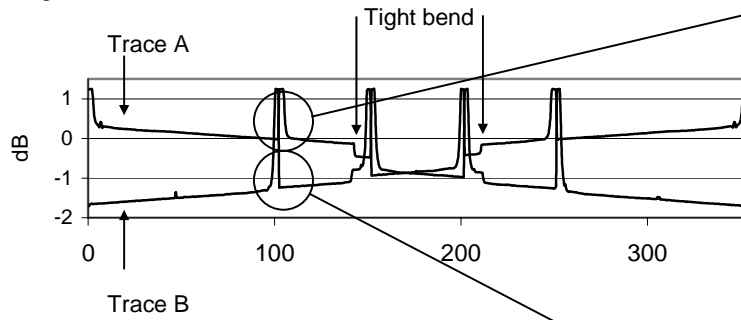
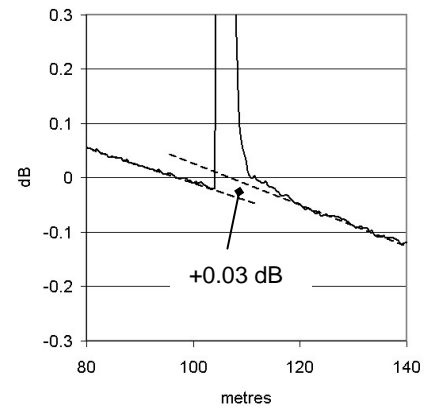


Figure 3



Conventional bi-directional processing proceeds by inverting Trace B, Figure 5, then taking the mean power of the two traces. The resulting trace is shown in Figure 6.

Figure 5

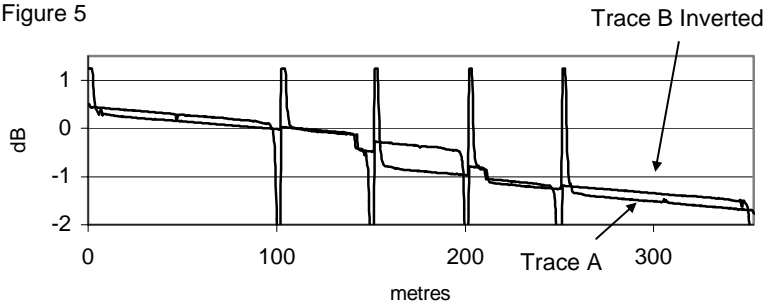
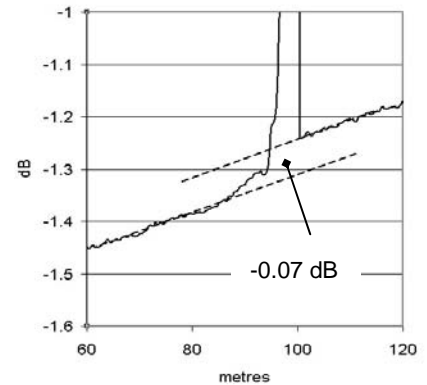


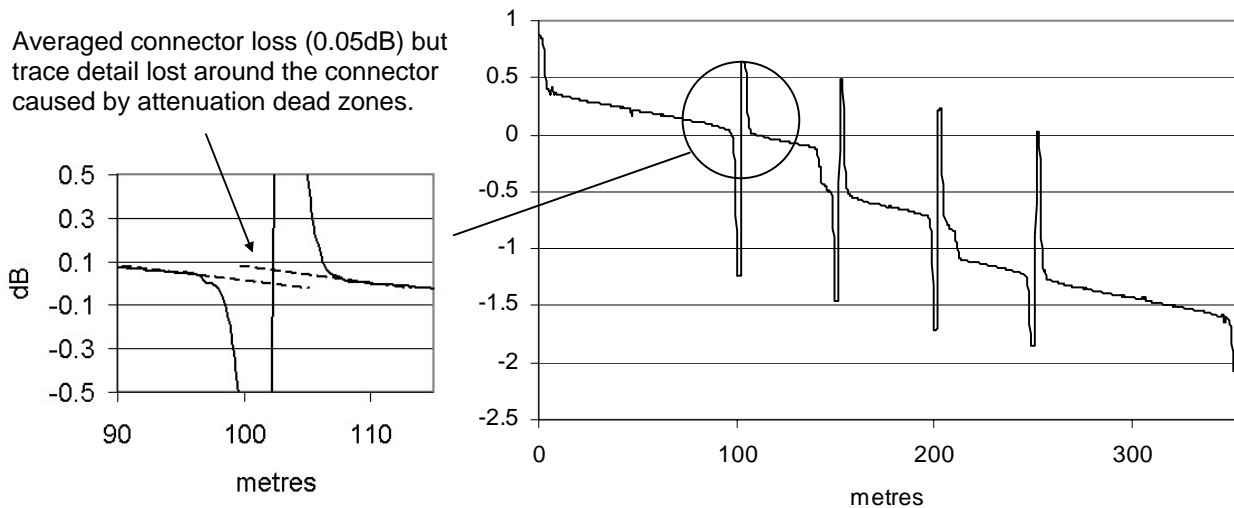
Figure 4



Although the connector and other event losses are successfully averaged the trace around every connector is obscured for a length equivalent to twice the attenuation (non-reflective) dead zone that is typically several metres. In LAN situations this can be a significant proportion of the FUT and in an area where statistically there is a high risk of faults such as breaks and tight bends.

Figure 6

Averaged connector loss (0.05dB) but trace detail lost around the connector caused by attenuation dead zones.



Resulting bi-directional trace of the LAN fiber loop shown in Figure 1. (Conventional process)

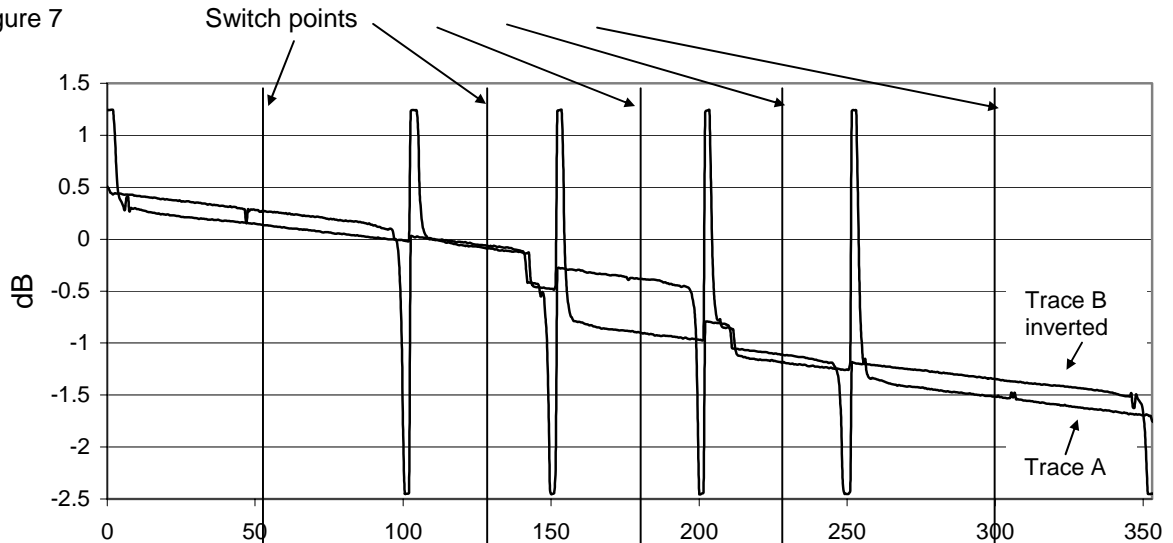
An Improved Processing Method

In the process of measuring the initial traces used in this bi-directional measurement the OTDR has gathered information right up to the connector interface in both directions and this can be used to construct a better bi-directional trace by the following method.

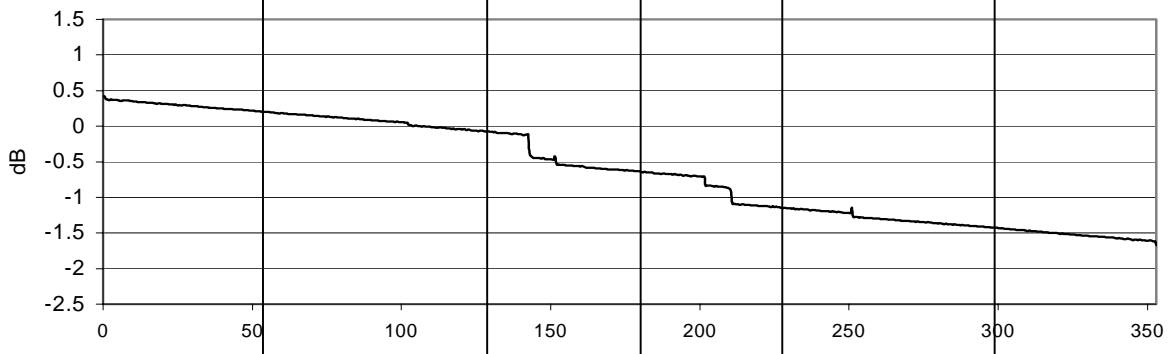
The two traces A and B are measured in the same way. Trace B is reversed and by using a simple correlation technique shifted to obtain the best alignment of the leading edges of the connector peaks. This removes any error caused by the reported 'zero' distance not aligning with the start of the fiber. Where a peak does not correlate with that measured in the reverse direction it indicates that there is a break close to that connector and its exact position computed. This is described more fully later. Trace B is then inverted as shown in Figure 7.

A point, the "switch point" is selected within every fiber segment of the trace. It need not be the mid-point but should be clear of any dead zone or events such as splices or bends. Simple detection algorithms may be used to select a suitable point. In the example below, the mid-point (50%) is the default choice but it is moved to the 40% or 60% distance points if the data quality (peak to peak variation) is better at one of these other positions. (The third switch point below is shifted to avoid a small ghost reflection.) The mean power between the two traces is computed at these points and the offset of each trace from that mean.

Figure 7



Trace used	B	A	B	A	B	A	B	A	B	A
------------	---	---	---	---	---	---	---	---	---	---



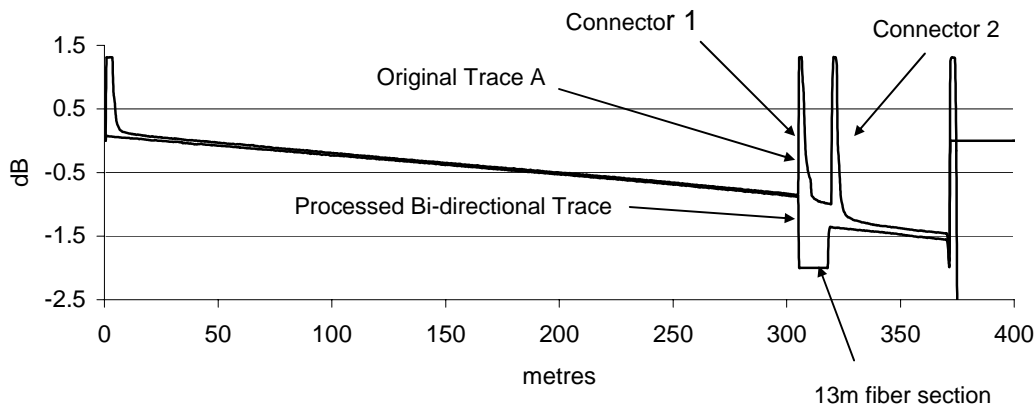
Resulting bi-directional trace of the LAN fiber loop shown in Figure 1. (Improved process)

Construction of the bi-directional trace comprises selecting the data from the segment portion between the connector and the switch point from Trace A or B, whichever is not obscured by dead zone, and shifting it by the appropriate offset towards the switch point mean. The resulting trace is shown in the lower section of Figure 7. The loss across every connector is therefore averaged and none of the trace is obscured by reflection and dead zone corruption.

Ghosts reflections may show on the bi-directional trace as positive or negative peaks, or may disappear completely, depending on their position relative to the switch points. However, by examining the original traces and the processed trace, ghosts are very easily identified.

There are limitations to this technique. The most important is that any fiber segment must be longer than twice the event dead zone of the OTDR. Segments shorter than this must be identified by the analysis software and appropriately marked. The loss across these short segments is still accurately averaged and the length is measured. Figure 7 shows two connectors, 13m apart, in a 370m length of fiber. The total loss across both connectors and the 13m fiber is averaged in the processed trace. The exact position of both connectors is measured from the correlation result and displayed by artificially setting the trace to a default (arbitrary) value -2dB . This indicates that there is no valid information available for the fiber between the two connectors. The method can therefore measure events that are very close together and is only limited by the sampling resolution of the OTDR.

Figure 7



A second limitation is that losses within a segment such as the tight bend shown in Figure 2 are not averaged but will be shown as in one of the original traces. This is generally not a large error since bends, by their nature, comprise the same fiber both sides of the loss and are represented accurately in both directions. Note that no bi-directional trace technique will reliably show the worse case loss of an event.

Conclusion

Bi-directional OTDR measurements are a useful way of averaging losses measured in fiber links. Conventional processing may be used to give averaged loss results but an unacceptable amount of the fiber is obscured in short links such as those in LANs. The alternative method described here averages connector losses and effectively displays all of the fiber by removing reflection and dead zones. It is easily automated and is particularly suited for use in duplex links with a loop-back fiber.

References

- [1] FOTP ANSI/TIA/EIA-455-8 Measurement of Splice or Connector Loss and Reflectance using an OTDR.
- [2] DIVITA, P. and U. ROSSI. 1980. The Backscattering Technique: its field of applicability in fibre diagnostic and attenuation measurements. *Optical and Quantum Electronics* 11(17):17-22.
- [3] DERICKSON, D. *Fiber Optic Test and Measurement*. Chapter 11 Section 11.4.2

An improved method for the distributed measurement of the chromatic dispersion of an optical fiber using a wavelength tunable OTDR

S. G. Murdoch¹, D. A. Svendsen²

¹ Department of Physics, University of Auckland, Private Bag 92019, Auckland, New Zealand (e-mail: s.murdoch@auckland.ac.nz).

² Photon Kinetics (UK) Ltd, Carpenter House, Broad Quay, Bath BA1 1UD, United Kingdom (e-mail: david.svendsen@pkinetics.com).

Abstract—In this paper, we present an improved distributed measurement of the chromatic dispersion of an optical fiber, which is based on the analysis of a set of bi-directional optical time domain reflectometer (OTDR) traces collected over the wavelength range of interest. The method uses the known mode field diameter and chromatic dispersion of a reference fiber to reduce the significance of the approximations made in the technique and hence improve upon previous methods. The validity of the approximations is verified via a numerical simulation and experimental measured results are given for both step-index and dispersion shifted fibers. Our results show that this technique is well adapted to the distributed chromatic dispersion measurement requirements of an optical fiber factory.

I. INTRODUCTION

Optical time domain reflectometer (OTDR) measurements are an important part of the process of qualifying an optical fiber for loss and imperfections, and it is useful to be able to use such measurements for estimating other parameters. A particularly convenient method of measuring the distributed chromatic dispersion of an optical fiber using bi-directional OTDR measurements was developed some years ago [1,2]. This method involves measuring the bi-directional OTDR trace of the fiber under test at a number of discrete wavelengths, and computing the distributed chromatic dispersion of the fiber by making a number of plausible approximations. The aim of the study reported here is to reduce the number of approximations and to test the validity of those remaining on which the technique rests. Previous implementations of this technique have required knowledge of the refractive index profile of the fiber under test to calculate its distributed chromatic dispersion. The implementation reported here uses a reference fiber of the same fiber type as the fiber under test, and of known mode field

diameter and chromatic dispersion. This allows the distributed chromatic dispersion of the test fiber to be measured without requiring any additional knowledge of the characteristics of the test fiber.

To validate this method, we have constructed a wavelength tunable OTDR which we use to measure the distributed mode field diameter and distributed chromatic dispersion, of both step-index and dispersion-shifted fibers. Numerical simulation of the detailed properties of the guided mode, allows us to place an upper bound of the error of these measurements.

II. THEORY

A. Distributed mode field diameter.

The first step in deriving an expression for the distributed chromatic dispersion from OTDR measurements is to express the Petermann II mode field diameter d [3] as a function of position z along the length of the fiber. This is obtained from standard expressions for the backscatter power detected by the OTDR, P_R [4,5], the backscatter fraction [5], and the bi-directional method [1,2,6], and results in:

$$d(z) = d(0) \cdot 10^{-P'_R(z)/20} A, \quad (1)$$

$$\text{and } A = \frac{n(0) \Omega(0)}{n(z) \Omega(z)}, \quad (1b)$$

where $P'_R(z) = P_{R1}(z) + P_{R2}(z) - P_{R1}(0) - P_{R2}(0)$, and $\Omega(z)$ encapsulates the details of the interaction of the guided mode with the refractive index profile and the Rayleigh scattering that generates the backscatter. This expression for the distributed mode field diameter of the fiber cannot be measured experimentally, as we have no

way of determining the distributed value of $\Omega(z)$. If the guided mode is Gaussian and the Rayleigh scattering is uniformly distributed then $\Omega(z) = 1$ for all z , and since $n(z) \approx n(0)$, $A \approx 1$. Thus, since the guided modes of most fibers of interest are close to Gaussian and the scattering is almost uniformly distributed, we can approximate the distributed mode field diameter of the fiber with:

$$d_{OTDR}(z) = d(0) \cdot 10^{-P'_R(z)/20} \quad (2)$$

This approximate distributed mode field diameter can be easily measured from a pair of bi-directional OTDR traces (to obtain $P'_R(z)$), and a standard mode field diameter measurement at the start of the fiber (to obtain $d(0)$). To avoid having to make this discrete mode field diameter measurement for each new fiber under test, a reference fiber, of the same fiber type, and known mode field diameter, can be connected between the fiber under test and the OTDR [2].

B. Distributed chromatic dispersion.

The second step in obtaining the distributed chromatic dispersion is to use the variation of the Peterman II mode field diameter with wavelength [3]. The total chromatic dispersion of an optical fiber is given by the sum of its material, waveguide, and profile dispersions. The waveguide dispersion of the fiber can be written as a function of its mode field diameter, and the derivative of its mode field diameter with wavelength [2]:

$$D_w(\lambda, z) = \frac{2\lambda}{\pi^2 c n d^2(\lambda, z)} \left(1 - \frac{2\lambda}{d(\lambda, z)} \frac{\partial d}{\partial \lambda}(\lambda, z) \right) \quad (3)$$

This means we can obtain a distributed measure of the waveguide dispersion of a fiber from a set of distributed mode field diameter traces collected over the wavelength range of interest. If we know the integrated chromatic dispersion of the reference fiber, and assume that the variation of the chromatic dispersion along the length of the fiber is solely due to the variation of the waveguide dispersion, we can write the total distributed chromatic dispersion of the fiber under test as:

$$D_{FUT}(\lambda, z) = D_w(\lambda, z) + D_{Ref}(\lambda) - \frac{1}{L_R} \int_0^{L_R} D_w(\lambda, z) dz \quad (4)$$

where $D_{Ref}(\lambda)$ is the integrated chromatic dispersion of the reference fiber, and $D_w(\lambda, z)$ is the waveguide dispersion calculated using expression (3). The final term of expression (4) is the mean waveguide dispersion of the reference fiber (length L_R). This method differs from the previous approaches to the problem which have required knowledge of the refractive index profile of the fiber to estimate the material and profile dispersions [1,2]. Using the above method requires only a measurement of the integrated chromatic dispersion of the reference fiber.

The validity of these approximations relies on the uniformity of the material and profile dispersion along the length of the fiber under test, and the identical composition of the test and reference fibers. To our knowledge the validity of these approximations, and the approximations required to reduce expression (1) to expression (2) have never been reported. Thus, in order to test the accuracy of the above theory for both step-index and dispersion shifted fibers, we have implemented a full numerical simulation of the modal properties of the fiber, starting from the scattering and dispersion properties of the refractive index profile of the fiber.

C. Numerical simulation of the distributed chromatic dispersion measurement

Using our numerical simulation and computing the actual value of A for a range of wavelengths, we find that for a step-index fiber with a $\pm 5\%$ variation in its index-step and core diameter the maximum error in the measured mode field diameter due to the assumption that $A \approx 1$ does not exceed $\pm 0.5\%$. Then, using expressions (3) and (4), we calculate the distributed chromatic dispersion, and find that the maximum error of the distributed chromatic dispersion measurement is ± 0.3 ps/nm/km for the $\pm 5\%$ variations in the index-step and core diameter.

A similar simulation for a Germanium-doped ring-type dispersion-shifted fiber, with a zero-dispersion wavelength of around 1500nm, reveals a significant variation in parameter A . This results in a maximum error in the mode field diameter measurement of $\pm 3\%$ for $\pm 5\%$ variations in the profile width, and dopant concentration. The maximum error in the distributed chromatic dispersion in this case is ± 0.4 ps/nm/km which is little more than for the step index fiber, despite the much larger variation in A . Figure 1 shows a typical simulation of OTDR traces used in this study, where the profile width of the test fiber varies linearly from 95% to 105% of the profile width of the reference fiber, and the dopant concentration of the test fiber varies

sinusoidally with a 10km period from 95% to 105% of that of the reference fiber. The close agreement between the actual chromatic dispersion of the fiber, and the chromatic dispersion measured via the bi-directional OTDR technique can be readily seen.

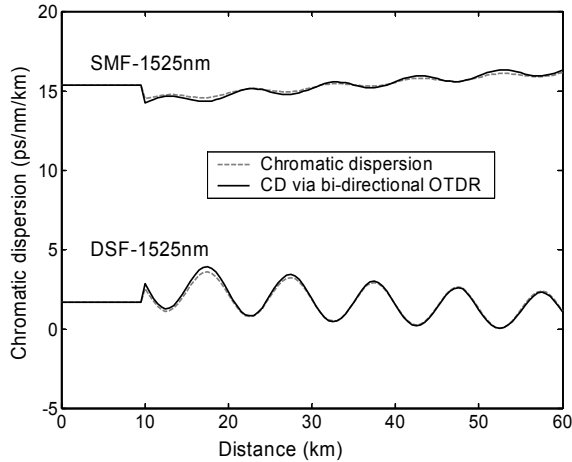


Figure 1. Distributed chromatic dispersion obtained by simulation. The simulated fiber consists of a 10km reference fiber attached to a 50km test fiber. The width of the refractive index profile of the test fiber varies linearly from 95% to 105% of the width of the profile of the reference fiber. The dopant concentration of the test fiber varies sinusoidally with a 10km period from 95% to 105% of the dopant concentration of the reference fiber.

III. EXPERIMENTAL SETUP.

Our wavelength tunable OTDR consists of a standard mainframe OTDR into which we have integrated an external cavity tunable laser. The bi-directional OTDR measurements are made in the configurations shown in Figure 2.

IV. EXPERIMENTAL RESULTS.

We now present the results of our measurements of the distributed mode field diameter, and distributed chromatic dispersion, of step-index and dispersion shifted fibers. For both sets of measurements we use a reference fiber of the same fiber type as the test fiber connected between the OTDR and the test fiber. The mode diameter at the start of the reference fiber was measured using the VAFF technique[7], and the integrated chromatic dispersion of the reference fiber was measured using the modulation phase shift technique[8]. These are the only external measurements we require for our distributed mode field diameter and chromatic dispersion measurements.

For both the step-index and dispersion shifted setups we perform two sets of measurements, the first with the reference and test fibers connected inside-end to inside-end, as shown in Figure 2a, the second with the two

fibers flipped (connected outside-end to outside-end) as shown in Figure 2b. Any difference between these two measurements can be attributed to the measurement error of the OTDR. This gives us a simple method to estimate the experimental accuracy of the technique.

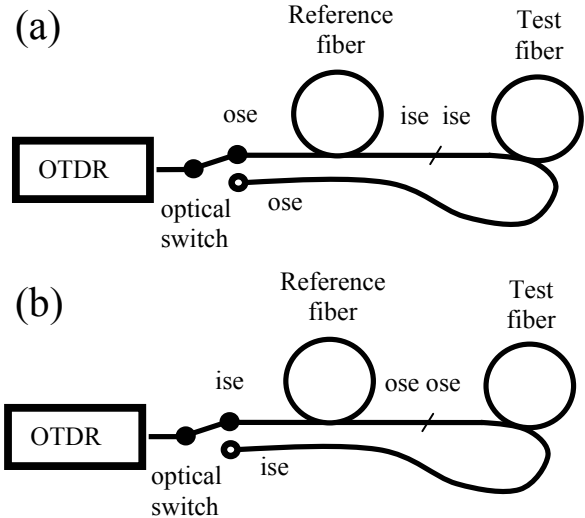


Figure 2. bi-directional OTDR measurement setup, showing the reference and test fibers attached (a) inside-end (ise) to inside-end, and (b) outside-end (ose) to outside-end.

A. Step-index fiber results.

Our step-index setup consists of a 12.8km reference fiber (fiber A), spliced to a 51.5km fiber under test (fiber B). We measure five pairs of bi-directional OTDR traces with center wavelengths of 1595.7, 1568.5, 1541.0, 1513.1, and 1484.7nm.

From our distributed mode field diameter measurements we calculate the distributed chromatic dispersion of the fiber at the three center wavelengths using the procedure outlined in section II. The results are shown in Figure 3. The solid traces correspond to the fiber setup of Figure 2a, and the dashed traces to the setup of Figure 2b with both reference and test fibers flipped. The difference between these two sets of measurements never exceeds 0.1ps/nm/km.

This experimental error and the error due to the theoretical approximations necessary to calculate the distributed chromatic dispersion (see section II), will add in quadrature. This means that, for step-index fiber with $\pm 5\%$ variations in its core diameter and index-step, the total error in our distributed chromatic dispersion measurement will not exceed ± 0.32 ps/nm/km.

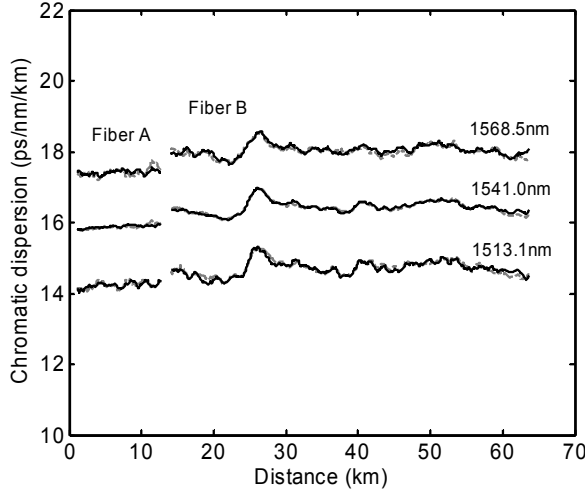


Figure 3. OTDR distributed chromatic dispersion measurements of the step-index fiber setup.

B. Dispersion shifted fiber results.

Our dispersion-shifted setup consists of an 11.5km reference fiber (fiber C), spliced to a 24.5km fiber under test (fiber D). We measure six pairs of bi-directional OTDR traces with center wavelengths of 1595.7, 1568.5, 1541.0, 1513.1, 1484.7, and 1456.8nm.

From these distributed mode field diameter measurements, we calculate the distributed chromatic dispersion of the fiber using exactly the same procedure as we used for the step-index fiber. The results are shown in Figure 4. The solid traces correspond to the fiber setup of Figure 2a, and the dashed traces to the setup of Figure 2b with both reference and test fibers flipped. The difference between these two sets of measurements never exceeds 0.1ps/nm/km.

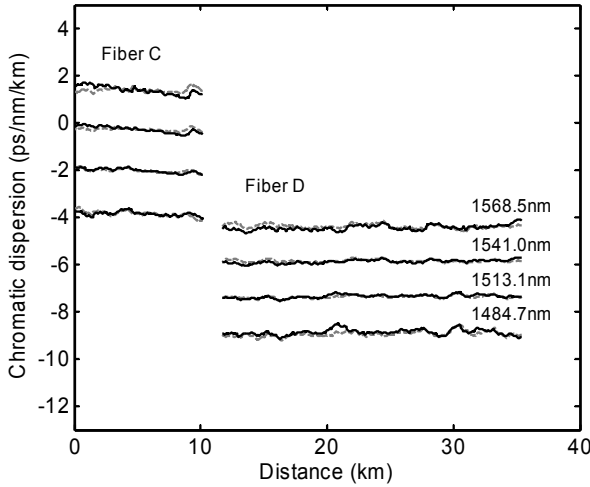


Figure 4. OTDR distributed chromatic dispersion measurements of the dispersion-shifted fiber setup.

From Figure 4 we can see that the chromatic dispersion of the two fibers differ significantly. This implies that the two fiber profiles are not identical as required. The numerical simulations indicate that the test and reference fiber profiles differ by $\sim 10\%$ which gives rise to an error in the difference of the chromatic dispersion measurements of fiber C and D of ± 1 ps/nm/km. The error in the relative accuracy of the chromatic dispersion of fiber D is unaffected by any difference between the reference and test fibers. Assuming a possible $\pm 5\%$ variation in the refractive index profile along the length of the fiber, the relative accuracy of our measurement of the distributed chromatic dispersion of fiber D will be ± 0.4 ps/nm/km, taking both experimental error and the approximation of expression (2) into account.

V. CONCLUSION.

The method presented here improves upon previous methods of obtaining distributed chromatic dispersion from bi-directional OTDR measurements by replacing some approximations with measurements made on a reference fiber. In an optical fiber factory where much information is available about the properties and tolerances of the fiber under test, we believe that this technique can provide usefully accurate measurements of distributed chromatic dispersion.

REFERENCES

- [1] K. Nakajima, M. Ohashi, M. Tateda, "Chromatic dispersion distribution measurement along a single-mode optical fiber", *J. Lightwave Technol.*, Vol. 15, pp. 1095-1101, Jul. 1997.
- [2] A. Rossaro, M. Schiano, T. Tambosso, D.D'Alessandro, "Spatially resolved chromatic dispersion measurements by a bi-directional OTDR technique", *IEEE J. Selected topics in Quant. Electron.*, Vol. 7, pp. 475-483, May 2001.
- [3] K. Peterman, "Constraints for fundamental-mode spot size for broadband dispersion-compensated single-mode fibres", *Electron. Lett.*, Vol. 19, pp. 712-714, 1983.
- [4] D. Derrickson, *Fiber Optic Test and Measurement*. New Jersey: Prentice Hall, 1997.
- [5] A. Hartog, M. Gold, "On the theory of backscattering in single-mode optical fibers", *J. Lightwave Technol.*, Vol. 2, pp. 76-82, Apr. 1984.
- [6] P. DiVita, U. Rossi, "Backscattering measurements in optical fibers: separation of power decay from imperfect contribution", *Electron. Lett.*, Vol. 15, pp. 467-469, 1979.
- [7] J.M.Dick, R.A.Modavis, J.G.Racki, R.A.Westwig, "Automated-mode radius measurement using the variable aperture method in the far field" *Tech. Dig. Conf. Opt. Fiber Commun.* (New Orleans, LA), paper WB3, 1984.
- [8] L.G.Cohen, "Comparison of single-mode fiber dispersion measurement techniques", *J. Lightwave Technol.*, Vol 3, pp. 958-966, Oct. 1985.

Inter-Comparison of Chromatic Dispersion Reference Fibre Measurements: Results of Euromet Project 666

J. Morel, Swiss Federal Office of Metrology and Accreditation (metas)

Lindenweg 50, 3003 Bern-Wabern, Switzerland
Phone: +41 31 32 33 350, E-mail: Jacques.morel@metas.ch

Abstract

The results of the inter-comparison of chromatic dispersion measurements, which was performed in the frame of EUROMET Project 666, are discussed. The applied measurement techniques are explained and the consistency between the reported values and their uncertainties is analysed.

Introduction

The calibration of the chromatic dispersion properties of singlemode fibres is of critical importance for a proper optimisation of high-bitrate, long-haul optical fibre communication systems. Although some analysis of the commonly used calibration techniques and some inter-comparisons were already performed in the past [1], [2], no large scale inter-laboratory comparisons that could be used as an effective basis for the Mutual Recognition Agreements (MRA) [3] between the National Metrology Institutes (NMI) existed at this time. The aim of this project was to perform a comparison of chromatic dispersion measurements that were carried out on four of the most commonly used fibre types, namely G652, G653, G655-TeraLight and G655-Leaf. Five NMIs [6] participated to this inter-comparison, which was also registered as a supplementary comparison within the MRA (EUROMET.PR-S1) and will serve as a basis for the review of the claimed Calibration and Measurement Capabilities (CMC) of each NMI. METAS acted as pilot laboratory for this comparison.

Measurement technique

Each laboratory performed the chromatic dispersion measurements by using a phase shift technique. The measurement setup used at METAS is for example shown in Fig. (1).

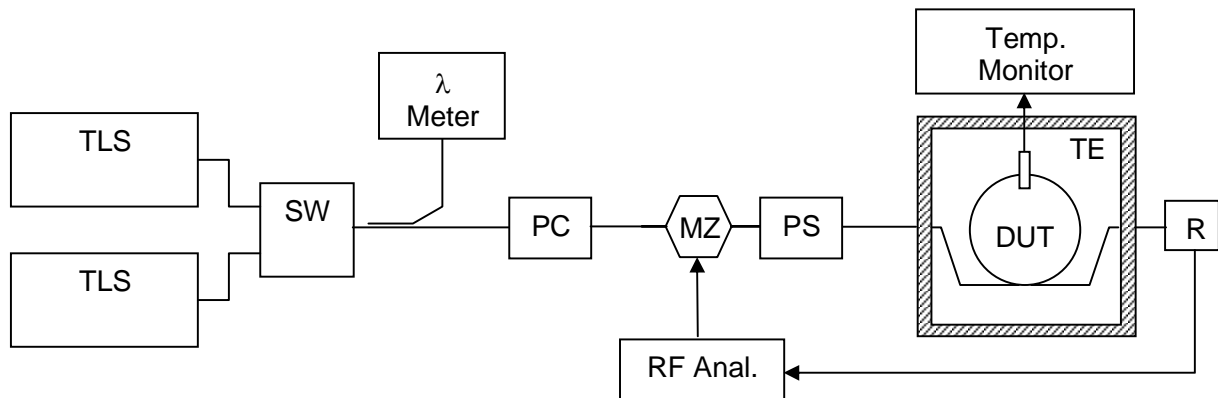


Fig. (1). Measurement setup used at METAS for the chromatic dispersion measurements. TLS: tunable Laser Sources, SW: optical switch, PC: Polarisation controller, MZ: Mach Zehnder Modulator, PS: Polarisation scrambler, DUT: Device Under Test, R: optical receiver. TE: passively Temperature controlled Enclosure.

The total chromatic dispersion D (ps/nm) was then obtained by measuring the phase shift $\Phi(\lambda)$ between the RF modulation and the signal detected at the output of the DUT, namely

$$D(\lambda) = \frac{d\tau(\lambda)}{d\lambda} = \frac{1}{2\pi \cdot f_m} \cdot \frac{d\phi(\lambda)}{d\lambda}, \quad (1)$$

where $\tau(\lambda)$ was the group delay and f_m was the RF modulation frequency. The group delay function was fitted by using one of the commonly used Sellmeier polynomial functions, depending on the fibre type and on the wavelength range, or by applying more dedicated functions, when proved that they would significantly improve the quality of the fit. Most of the laboratories performed a curve fitting over a broad wavelength range of about 100 nm and used the fitting functions as specified in [4]. One laboratory also used a parabolic fitting function for all fibres, but by successively analysing narrow spectral windows.

Uncertainty budget

Each participating laboratory was asked to calculate his specific uncertainty budget, based on a list of the most important influence factors that should be considered [4]. Despite of the fact that all laboratories used very similar measurement systems, very large differences of the reported uncertainties were observed. For example, a ratio larger than 40 was calculated between the largest and the smallest reported uncertainty for the calibration of the G652 reference fibre at 1550 nm.

Reference fibres

Each Reference fibre consisted of a reel of a singlemode fibre with a length comprised between 10 km and 20 km. The fibre was mounted in a metal case and was protected against large temperature deviations with a thick layer of dense foam rubber. A sensor was mounted in the centre of the reel and was used for the monitoring of temperature and humidity during the chromatic dispersion measurements. The reference fibres were prepared and calibrated at METAS and were then sequentially circulated among the laboratories. Two re-verifications of the reference fibres were performed during the inter-comparison and showed no significant drifts of the chromatic dispersion values.

Results and analysis

The measurement results were compared by calculating the deviation between the dispersion values reported by each laboratory and the arithmetic mean, according to Eq. (2), namely

$$\Delta D_i = D_i - \frac{1}{n} \cdot \sum_{i=1}^n D_i, \quad (2)$$

where n was the number of participants and i was the index of the laboratory. The uncertainty of the deviation of each point was then given by [5]

$$u_{\Delta D_i} = \sqrt{u_{D_{mean}}^2 + \left(1 - \frac{2}{n}\right) \cdot u_{D_i}^2} \quad (3)$$

Where $u_{D_{mean}}$ was the uncertainty of the arithmetic mean, and u_{D_i} was the claimed dispersion uncertainty.

The results reported by one laboratory systematically showed large discrepancies compared to the others. These data haven't been considered for the calculation of the mean value and aren't discussed here. The analysis of the calibration results of the G655-Leaf reference fibre are shown in Fig. (2). The deviation values $D - D_{mean}$ were found to be well within their corresponding uncertainties, which proved a good consistency between the results given by each participant.

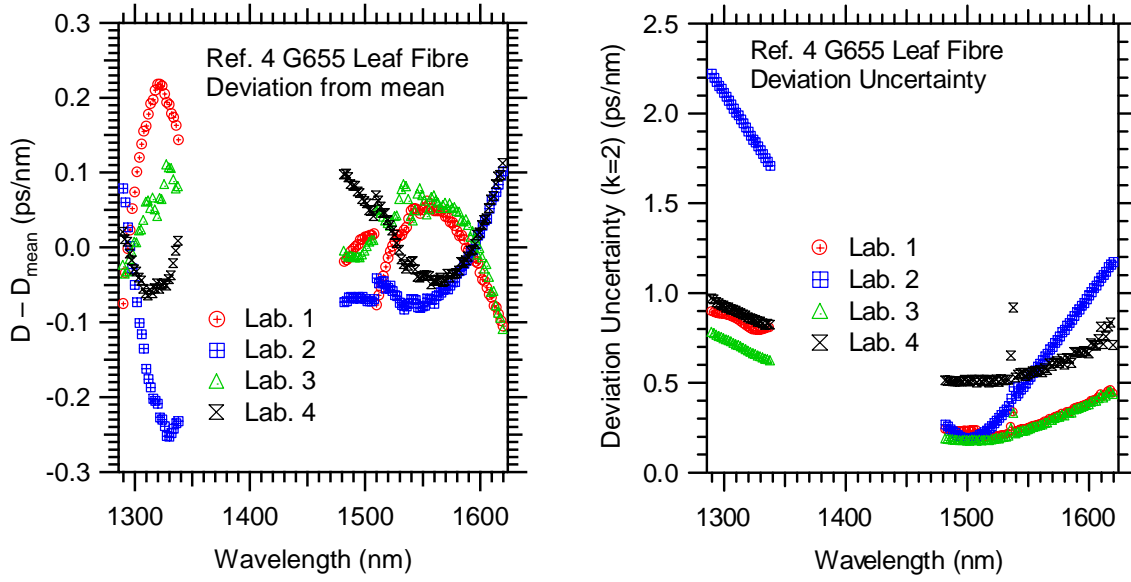


Fig. (2). (Upper): Deviation of the chromatic dispersion to the mean value measured by each laboratory. (Lower): Uncertainty of the deviation ($k=2$).

A closer analysis showed a significant spread of the uncertainties reported by the different participants, which made the determination of the uncertainty of the mean value and thus the estimation of the uncertainty of the deviation more difficult. Depending on how $u_{D_{mean}}$ was calculated, one extreme overestimated uncertainty u_{D_i} may lead, for example, to a large value of the uncertainty of the deviation, and thus to a too optimistic image of the consistency between the calibration results of the participants. For that reason, $u_{D_{mean}}$ was calculated by using two different methods. The first one was to estimate $u_{D_{mean}}$ from the reported dispersion uncertainties; the second one was to calculate $u_{D_{mean}}$ as the standard deviation of the reported dispersion values. The analysis of the calibration results of the four reference fibres using these two methods demonstrated a very good agreement between the participants. Some small discrepancies were observed by one laboratory for a few measurement points. The histograms of the deviations of all the measurements performed by all laboratories are shown for each reference fibre in Fig. (3). The distributions didn't show any noticeable systematic offsets and had a rather good symmetrical shape.

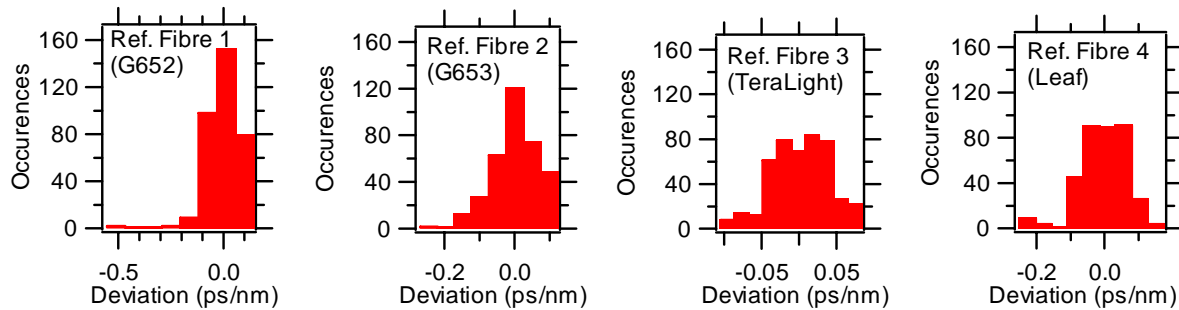


Fig. (3). Histogram of the deviations of all chromatic dispersion measurements performed by the four laboratories for each reference fibre.

The calibration of the zero dispersion wavelength λ_o and of the dispersion slope S_o were achieved by means of a phase shift measurement performed around λ_o , and by applying a specific curve fit to the measured data. CSIC performed a subsequent calibration of λ_o , by using the four-wave mixing (FWM) technique. The results were compared using the same technique as previously described for the

chromatic dispersion. The deviations of λ_0 and S_0 to their respective mean values are shown in Fig. (4) for the G655-Leaf reference fibre.

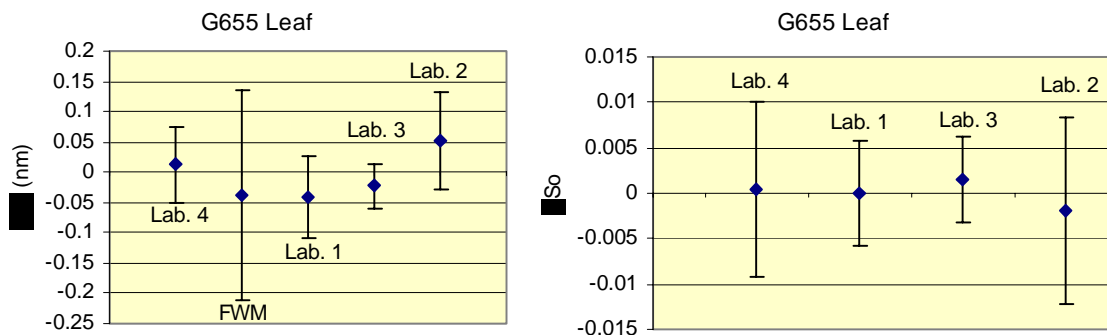


Fig. (4). Histogram of the deviations of all the chromatic dispersion measurements performed by the four laboratories for each reference fibre.

A very good consistency was found between the results provided by the four participants. The deviation values $\Delta\lambda_0$ and ΔS_0 were well within their corresponding uncertainties. The same observations were made for all, but the G653 and G655-TeraLight reference fibres, where two other laboratories underestimated the uncertainty of λ_0 and of S_0 .

Conclusions

The inter-comparison of the calibration of the chromatic dispersion of four different types of singlemode fibres showed a very good consistency between all participating laboratories but one, where larger discrepancies were found. A large spread in the reported dispersion uncertainties was observed, which made the consistency analysis more complicated. A detailed evaluation of the calibration results showed that one of the four laboratories slightly underestimated the dispersion uncertainty for a few measurement points and that the three other laboratories gave somewhat overestimated uncertainties, especially in the 1280 nm – 1340 nm wavelength domain. The calibration of the zero dispersion wavelength and of the dispersion slope showed a good consistency between the participants. These results provide a good basis for the review of the future CMC entries on chromatic dispersions.

Acknowledgments

This work was only possible with the collaboration of all the participating laboratories. Many thanks to M. Wicks (NPL), Pedro Corredra (CSIC), T. Dennis (NIST) and H. Ludwigsen (HUT).

References

- [1] Franzen, D. L. et al., "Accurate Measurement of the Zero-Dispersion Wavelength in Optical Fibers", *J. of Research of the NIST*, (May 01, 1997).
- [2] COST 265, "Measurement Techniques for Active and Passive Fibres to support Telecommunication Standards"
- [3] "Mutual recognition of national measurement standards and of calibration and measurement certificates issued by national metrology institutes", BIPM, Paris, 14 October 1999.
- [4] J. Morel, "Technical protocol EUROMET Project 666, Inter-comparison of Chromatic Dispersion Reference Fibres", (2003).
- [5] K. Beissner, "On a measure of consistency in comparison measurements", *Metrologia*, **39**, pp. 59-63 (2002).
- [6] Participating NMIS: "Instituto de Fisica Aplicada" (CSIC), Spain; "Helsinki University of Technology" (HUT), Finland; "National Physics Laboratory" (NPL), United Kingdom; "National Institute of Standards" (NIST), United States; "Swiss Federal Office of Metrology and Accreditation" (METAS), Switzerland.

Generalized Interferometric Method for Accurate Match with DGD Measurements and Comparison Against Standard References

Normand Cyr

EXFO Electro-Optical Engineering, 400 Godin Ave, Vanier, Québec, Canada, G1M 2K2.
email: normand.cyr@exfo.com, ncyr@total.net

Abstract: We summarize the key points of the Generalized Interferometric Method (GINTY), and we point out the basically exact match between the PMD value retrieved from GINTY and a measurable value deduced from DGD measurement over a finite wavelength range. Given this match, it should now be possible to develop standard references for GINTY-based analyzers to be tested against; two main approaches are suggested.

1. Introduction

The traditional analysis (TINTY) [1] that is applied in the interferometric PMD-measurement method has basic limitations which arise from the underlying models of the interferogram [2-7]. Stringent assumptions restrict the application domain where this analysis remains, at least in principle, mathematically exact. Notably, the formula that links PMD to the rms-width of the interferogram is based on the assumptions that the device under test (DUT) is an ideal random-mode-coupled device of infinite coupling ratio, that PMD is much larger than the source coherence time, and that the interferogram is a statistical average over all possible devices having the same conceptual PMD value. Given these assumptions of TINTY,

- the conceptual, *never observed* interferogram assumed by the formula is a Gaussian curve, but it is not specified by how much the result is biased whenever the actual interferogram deviates from the Gaussian shape, e.g. in the case of mixed mode-coupling [8] for instance.
- The relation between the rms-width of the *observable* interferograms and the actual rms-DGD, in the finite wavelength range of an actual measurement, has been left unspecified.

Among common sources of concern resulting from these shortcomings, let's mention:

- the inability to establish standard references for TINTY-based analyzers to be tested against.
- systematic discrepancies between the displayed PMD value and the rms-DGD deduced from DGD measurements, in addition to large deviations observed in round-robin intercomparisons.
- difficulties when comes the time to evaluate the overall uncertainty, because, in particular, fluctuations in time of the displayed PMD value cannot be considered as faithfully representative of the fluctuations of the DUT itself, and neither can be ascribed to instrument instability or noise.

The Generalized Interferometric analysis (GINTY) [9-11] addresses these concerns and offers a practical solution which is valid whatever the coupling regime and the shape or wavelength range of the actual spectrum at the output of the DUT. The theoretical framework has been described in [9]. In the present article, we focus on the basically exact match between i) the PMD value returned by GINTY, and ii) a rigorously defined measurable quantity, DGD_{RMS} , that can be deduced from DGD measurements over a finite wavelength range (c.f. section 2., definition (2)). And as a natural consequence, we also discuss how this can lead to the development of a standard reference material (SRM) for Interferometric analyzers to be tested against, and to consistently successful intercomparisons.

The key points of GINTY are summarized in section 2 (the underlying theory can be found in [9]). In section 3, we describe a simulated result that illustrates the basically exact match between the PMD value retrieved from GINTY and DGD_{RMS} deduced from the actual DGD curve of the DUT (experimental results will be shown in the oral presentation). In section 4, we discuss an aspect of DGD measurements and data processing (i.e. computing DGD_{RMS}) that must be taken care of in order to achieve a successful comparison. In section 5, we make suggestions as how it should be suitable to proceed in order to develop standard references for GINTY-based analyzers.

2. GINTY: Outline of Key Points

- PMD is deduced from both the auto- and cross-correlation interferograms as

$$\text{Measured_PMD} = \text{DGD}_{\text{RMS}} = \sqrt{\frac{3}{2} (\sigma_x^2 - \sigma_0^2)} \quad (1)$$

where σ_0 and σ_x are the rms-widths (square root of second moment) of the auto- and cross-correlation *mean-square* envelopes (MS-envelopes), respectively. "Mean-square" here refers to averaging over I/O-SOPs *only*, i.e. an actually achievable average. It does not refer to the unachievable average over all possible DUTs with a same conceptual PMD value, nor does it refers to any smoothing of the envelopes.

- Both the auto- and cross-correlation interferograms are measured separately to obtain both rms-widths needed in (1). A setup as shown in Fig. 1 provides the means to retrieve both interferograms simultaneously. They are obtained via the sum and difference of the two interferograms observed along orthogonal polarization axes (this can be considered as the definition of the auto- and cross-correlation interferograms to which (1) refers).
- Polarization scrambling (continuous or scan-to-scan) is performed both at the input and output (I/O-SOP scrambling), and PMD is deduced from the MS-envelopes as stated above, not as the average of single I/O-SOP values. As an efficient alternative to random scrambling, the MS-envelope can be obtained by averaging the squared envelopes observed with only nine I/O-SOPs. This nine-state Mueller set consists of three analyzer-axes forming a right-angled trihedron, for each of three input-SOPs also forming a right-angled trihedron.
- The relation between the actual DGD curve and the measured PMD as given by (1) is,

$$\text{DGD}_{\text{RMS}}^2 = \int_{\nu} w_0^2(\nu) \text{DGD}^2(\nu) / \int_{\nu} w_0^2(\nu) \quad (2)$$

where $w_0(\nu)$ is a *user-selectable* window, equal to the Fourier transform (FT) of the *effective* auto-correlation interferogram; if no normalization of the spectra is performed, the "natural" $w_0(\nu)$ is the physical spectrum at the output of the DUT, i.e. $w_0(\nu) = S_0(\nu)$. But since $S_0(\nu)$ is known via FT of the auto-correlation interferogram, one has the freedom to specify his own averaging window, via normalization of the spectra (equivalent to spectrum normalization in the fixed-analyzer method [7,11]); through respective application of forward and inverse FT, the spectra are multiplied by $w_0(\nu)/S_0(\nu)$ and the new, effective interferograms are retrieved.

Applying the method as described above, (1) and (2) remain valid for DUTs showing any type of mode-coupling or any interferogram shape, including the no-coupling case, 1, 2,... N-segment concatenations, random or not, even with add-drop filters inserted in the path, etc., with no theoretical restriction regarding the output-spectrum width, smoothness or overall shape. Because simply, such restrictions have been removed at the start from the underlying theory.

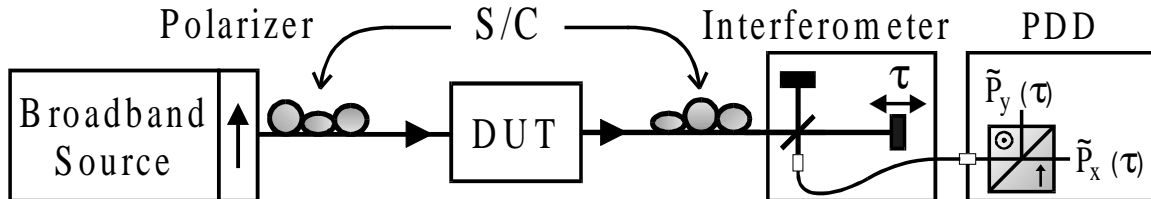


Fig. 1. A GINTY setup. Auto- and cross-correlation interferograms are obtained separately via the sum and difference of two interferograms observed along orthogonal polarization axes. PDD: Polarization Diversity Detector. S/C: I/O Polarization Scramblers or Controllers; scrambling can be performed continuously while scanning.

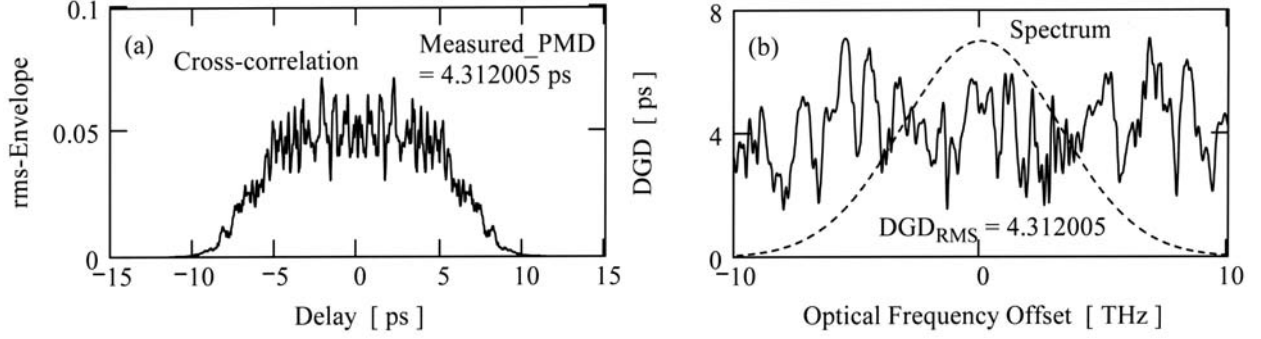


Fig. 2. Simulation - Mixed coupling device. Example of a flattened interferogram. (a) Cross-correlation RMS-Envelope. (b) DGD curve (solid) and output spectrum (dashed).

3. Simulation - Example of a Flattened Interferogram

The simulated device is a concatenation of 60 segments with random DGDs and axes, with two intertwined segments ($k = 20$ and $k = 40$) whose DGDs (4.3067 ps and 1.4356 ps) are much larger than the average DGD of the other segments (0.2448 ps). A Gaussian output-spectrum with $\sigma_A = 50.00$ fs is used, where σ_A is the RMS-width of the auto-correlation envelope, giving $\text{FWHM} = 7.496$ THz (60.07 nm @ 1550 nm). See [9] for details about the simulations. The computed $\text{DGD}(\nu)$ and cross-correlation rms-envelope are shown in Fig. 2. DGD_{RMS} calculated according to (2) is 4.312005 ps, and application of (1) to the MS-envelope gives the same result, with a residual difference $\Delta = 1.0 \times 10^{-8}$ ps (rounding and finite sampling error).

The purpose of this example is to illustrate the mathematical exactness of (1) and (2), with an interferogram that deviates significantly from a gaussian shape. But simply, such match is obtained whatever the concatenation or the selected spectrum.

In contrast, the formula of TINTY, i.e. $\text{PMD}_T = \sqrt{3/4} \sigma$ [1,4], where σ is the RMS-width of the cross-correlation envelope (*not squared*), here gives $\text{PMD}_T = 3.5772$ ps, off-target by 17 %. Somewhat flattened interferograms similar to the one shown in Fig. 2a are frequently observed. They are representative of either mixed coupling or moderate coupling-ratios. What has to be pointed out is the following: the bias of TINTY with respect to the actual DGD_{RMS} in the finite range of the measurement, as seen here, is not a manifestation of, and cannot be ascribed to the zero-mean Gisin uncertainty. It is a systematic bias, an "interferogram-shape bias", because the conditions are outside the assumptions and validity range of TINTY, even if the interferogram may appear as bell-shaped enough to satisfy the gaussian assumption.

On the other hand, GINTY simply gives the actual DGD_{RMS} , as it is within the finite measurement range, with no bias, with no assumption on coupling, interferogram shape, spectrum width or smoothness. Nothing more can be achieved in practice, but at least this can be achieved, i.e. measuring correctly the only thing that is actually measurable.

4. DGD Measurement: The Sampling and Reconstruction Aspect

4.1 The Question of Discrete Wavelength Values vs Continuous Average

Physically speaking, the PMD value measured through the Interferometric method is a continuous average, i.e. DGD_{RMS} as given by (2). Mother Nature performs the integral for us, all wavelengths within the averaging window contribute to the result, there is no "wavelength step". On

the other hand, some DGD measurement techniques or instruments (but not all, see below) basically measure DGD at only a limited number of discrete wavelength values, sometimes separated by quite a large step. If the averaging is performed over this limited number of points, the result may depend significantly on the specific choice of the discrete wavelength values. Thus, a first question arise: how do we reliably obtain an average that is identical to the continuous average (2) for all practical purposes, independently of the DGD measurement setup or initial choice of the discrete wavelength values. Moreover, since any optical measurement is performed with some given resolution bandwidth (RBW), an accurate match is ensured only if the two measurements have the same effective RBW. If RBW is not taken into account or is let unspecified, "unexplained" discrepancies may arise just from there, i.e. unmatched RBWs.

The fundamental answer to the above questions is obvious: explicitly or implicitly, the DGD curve must be effectively reconstructed from the raw data, with a known RBW and a small enough step (smaller than RBW). According to the sampling theorem, such reconstruction is not only achievable, but is also safe and faithfully representative of the true signal whenever the basic rules of sampling are applied. Thus, the general solution comes down to a careful application of sampling and reconstruction rules. These rules, as they shall be applied to optical measurements (something vs optical frequency) in order to ensure optimal and reliable results, in the same way as they are systematically applied to time signals (e.g. audio), are described in [12]. In short, the golden rule is: *the initial sampling step must be safely smaller than the RBW*.

Before going into more details, we must distinguish different DGD measurement setups. We limit our discussion to the Reference Test Method (RTM), i.e. the Stokes Parameters Evaluation [13-14]. The RTM can be performed with the following types of setup:

- Type-1. Broadband Source (BBS) + Polarimetric Interferometer
- Type-2. Tunable Laser or BBS-tunable filter + Polarimeter
 - a. swept-wavelength system
 - b. step-stop-measure system

Type-1 and Type-2a setups do not basically lead to the above mention difficulties. In the following section, we discuss why they don't and how to ensure that they don't.

4.2 The Basically Suitable Setups: Type-1 and Type-2a

In the case of type-1 setups, the question of discrete wavelength values is irrelevant, because raw data (interferograms) are sampled in the delay-domain. There is no finite step in the optical frequency domain, nor an equivalent. All wavelengths contribute to the interferograms, information about all wavelengths is contained in the raw data. On the other hand, what exists and must be small enough, or matched with the GINTY measurement, is the effective RBW given by $1/\Delta\tau$, where $\Delta\tau$ is the effective delay-travel of the interferometer. In short: the interferograms must not extend outside the delay-travel, a well-known condition that can be checked easily.

Type-2a setups also retrieve the raw data with an known effective RBW safely larger than the initial sampling step, "by design". Because, assuming that the system is indeed designed correctly, the sampling rate of the time-signals observed with a swept-wavelength system is set safely larger than the overall bandwidth of the electronics that precedes the sampling device. This single condition ensures a correctly performed raw sampling in all cases, such that continuous curves can be faithfully reconstructed. Furthermore, one is then entitled to further process the sampled signals with full confidence, as filtering afterward to obtain a larger effective RBW and resampling with a larger or smaller step, safe from any aliasing artifact and free from folded-back noise and unforeseen spurious "tones" [12,15,16].

More details about good sampling practices and calculation of DGD_{RMS} using swept-wavelength systems shall be discussed in a dedicated paper. On the other hand, it is straightforward and easy to explain through a single sentence in the case of swept-delay systems: a perfect match of the RBWs is obtained "all-naturally" by using the same *effective* delay-travel as the one used in the GINTY measurement (note: *it does not mean* that the interferometers must have the same physical travel. The *effective* delay-travel can be set at any value smaller than the physical travel of the interferometer. At the simplest, it consists in "throwing away" or setting to zero the non-useful data (noise) that have been sampled outside of the selected effective delay-travel).

4.3 The Problematic Case of Type-2b Setups

Step-stop systems may be problematic for this application. There is a number of reasons, but the mother of all potential difficulties is a poorly controlled RBW that is also typically far too small with respect to the raw sampling step, so that the primary rule of sampling and reconstructing is violated at the start. Noise and artifacts that fold back via aliasing [12,15,16] may impair the faithful reconstruction of the continuous curve. All right, it still may be o.k. or "not so bad" in a significant number of cases, but the reliability is not basically ensured, and moreover, cannot be assessed from the sampled data. Contrary to a swept-wavelength system, the RBW of a step-stop system is irremediably determined by the physical laser linewidth, and to complicate matters further, lasers with linewidths as small as a few kHz are often used; it is indeed most suitable when used in a swept-system since the effective RBW at sampling is then determined solely by the bandwidth of the electronics. But with such a small linewidth, the only way for a type-2b setup to be consistently reliable for the present application is to increase the physical laser linewidth, via some form of so-called coherence control for example. If not, discrepancies are almost guaranteed. Also, the resulting effective lineshape shall be clean and stable, and the effective linewidth accurately known. If so, all the said potential problems vanish.

5. Development of Standard Reference Material: Suggested Approaches

It comes naturally to the mind that it should now be possible to develop some standard reference material (SRM) for GINTY-based interferometric PMD-analyzers. Two general approaches are suggested and briefly commented below. In all cases, it is assumed that the SRM is a stable device, i.e. that the DGD curve is stable enough for the variations of DGD_{RMS} , within some specified averaging windows, to be negligibly small with respect to measurement uncertainty.

5.1 Approach 1: The specified DGD-Curve Approach

In this approach, the user is given a file which contains the DGD curve of the SRM. The discrete DGD values, observed *with a known RBW* over some large wavelength range, are stored in the file with an optical frequency step safely smaller than the specified RBW. Then, as discussed in section 4., a continuous DGD curve can be reconstructed by the user with as much point as he see fit, even when it is not necessary. To be more precise regarding RBW, what shall be specified for a truly perfect match is the effective lineshape of the measurement, or equivalently the shape of the effective delay-filter (FT of the lineshape, see [12]). Then the exact same delay-filter can be applied to the interferograms observed with GINTY.

Advantages: The user can select any averaging window that is encompassed within the range where the DGD curve is known. On the other hand, a comparison can also be performed without spectrum normalization, allowing cheaper interferometers to be used (c.f. 5.2). He can perform the GINTY measurement using different sources with different center wavelengths or different spectral widths. In order to compare to the reference, all he has to do is to compute DGD_{RMS} from the DGD curve using the spectrum measured at the output of the DUT as the window.

Disadvantages: Some users may not like it because they must compute DGD_{RMS} . Also, it may appear more difficult for the provider of the SRM to certify the accuracy of a full DGD curve than the accuracy of a single PMD value observed with a fixed averaging window (approach 2), so the SRM may be more costly. However, let's point out that noisy DGD curves as well as a number of difficulties and unexplained features encountered in the past may simply vanish if a suitable DGD measurement setup is used along the lines pointed out in section 4, ensuring a known lineshape and RBW, and a raw sampling step safely smaller than RBW.

5.2 Approach 2: The Specified PMD Approach

The PMD value of the SRM is specified, i.e. the value of DGD_{RMS} within one or a few given, fixed averaging window $w_0(v)$ ("standard windows"). But, as a matter of fact, this approach does not require the knowledge of the DGD curve. Indeed, the provider can elect to measure the PMD of the SRM using GINTY, selecting the standard $w_0(v)$ as the averaging window.

Advantages: Many users may prefer the conceptual simplicity of testing their PMD-analyzer against a single reference PMD value. Also, it may be a cheaper solution, as far as the cost of the SRM is concerned, because easier for the provider to certify a single PMD value.

Disadvantages: No free choice of the averaging windows. Spectrum normalization is required unless the physical output spectrum is made to match the standard window. So, forget it whenever spectrum normalization is simply not implemented or cannot be implemented as an option in the PMD-analyzer. Normalization implies that the spectra are retrieved cleanly, which requires an interferometer that includes a reference laser for "linearization" of the scan. In short, the interferometer must be used as a Fourier transform spectrometer. Typically, such interferometer is somewhat more costly than an interferometer which can only display the envelope.

6. References:

- [1] Polarization-Mode Dispersion Measurement for Single-Mode Optical Fibers by Interferometry, TIA/EIA-455-124 (FOTP-124), ITU-T Rec. G.650.2 and IEC 60793-1-48.
- [2] N. Gisin, J. P. Von der Weid, and J. P. Pellaux, "Polarization mode dispersion of short and long single-mode fibers," J. Lightwave Technol., vol. 9, pp. 821–827, 1991.
- [3] N. Gisin, R. Passy, and J. P. Von der Weid, "Definitions and measurements of polarization mode dispersion: Interferometric versus fixed analyzer methods," J. Lightwave Technol., vol. 6, pp. 730–732, 1994.
- [4] B. L. Heffner, "Influence of optical source characteristics on the measurement of polarization-mode dispersion of highly mode-coupled fibers," Opt. Lett., vol. 21, pp. 113–115, 1996.
- [5] G. J. Foschini and C. D. Poole, "Statistical theory of polarization dispersion in single mode fibers," J. Lightwave Technol., vol. 9, pp. 1439–1456, 1991.
- [6] N. Gisin, "Solutions of the dynamical equation for polarization dispersion," Opt. Commun., vol. 86, pp. 371–373, 1991.
- [7] C. D. Poole, and D. L. Favin, "Polarization-mode dispersion measurements based on transmission spectra through a polarizer," J. Lightwave Technol., vol. 12, pp. 917–929, 1994.
- [8] C. J. Mackechnie, S. P. Ferretti, A. J. Barlow, "Inadequacies of interferometric measurements of PMD as defined by FOTP-124," Conference Digest of the 6th Optical Fibre Measurement Conference (OFMC'01), Cambridge, United Kingdom, September 2001, pp. 141-144.
- [9] N. Cyr, "Polarization-Mode Dispersion Measurement: Generalization of the Interferometric Method to Any Coupling Regime", J. Lightwave Technol., vol. 22, pp.794–805, March 2004.
- [10] Polarization-Mode Dispersion Measurement for Single-Mode Optical Fibers by Interferometry, TIA-455-124-A (Rev. of TIA/EIA-455-124)
- [11] Polarization-Mode Dispersion Measurement for Single-Mode Optical Fibers by the Fixed Analyzer Method, TIA/EIA-455-113 (FOTP-113), ITU-T Rec. G.650.2 and IEC 60793-1-48.
- [12] N.Cyr, F.Babin, B.Ruchet, A.Girard, "Optical Sampling-Step and Effective Resolution-Bandwidth: a Fundamental Aspect of Component Testing", Asia Pacific Optical and Wireless Communication Conference (APOC'2002), Shanghai, China, October 2002, Proceedings of SPIE Vol. 4906, Session 10, invited paper 4906-17.
- [13] N. Cyr, A. Girard, G. W. Schinn, "Stokes Parameter Analysis Method, The Consolidated Test Method for PMD Measurements," in Technical Proceedings of 15th National Fiber Optic Engineers Conference (NFOEC'99), Chicago, Illinois, September 1999, Vol. II, p. 280.
- [14] Polarization-Mode Dispersion Measurement for Single-Mode Optical Fibers by Stokes Parameter Evaluation, FOTP-122A - (ANSI/TIA-455-122-A-02); Measurement methods and test procedures - Polarization mode dispersion, IEC 60793-1-48 Ed 1.0: Optical Fibres.
- [15] N. Cyr, M.Leclerc, B. Ruchet, "PMD measurements in multipath components: The single waveplate example", in Applications of Photonics Technology 5, Proceedings of SPIE Vol. 4833 (Photonics North 2002), pp. 1061-1068.
- [16] P.A. Williams, J. D. Kofler, "Measurement and Mitigation of Multiple-Reflection Effects on the Differential Group Delay Spectrum of Optical Components," Tech. Digest, Symposium on Optical Fiber Measurements (SOFM 2002), Sep 24-26, 2002, Boulder, CO, NIST Special Publication 988, pp. 173-176.

Study of variation of the Laplacian parameter of DGD time derivative with fiber length using measured DGD data

Pradeep Kumar Kondamuri¹, Christopher Allen¹, and Douglas L. Richards²

¹Lightwave Communication Systems Laboratory
Information and Telecommunications Technology Center (ITTC)
The University of Kansas, Lawrence, Kansas 66045

²Sprint Corporation, Overland Park, Kansas

Abstract

Temporal and spectral DGD measurements were made on different combinations of three 95-km fibers within a slotted-core, direct-buried, standard single-mode fiber-optic cable over long time periods to characterize DGD variability. From this data we observed that DGD varies slowly over time but rapidly over wavelength. We also observed that the DGD variation with time becomes more rapid for longer length fibers. The DGD time derivative data obtained from the measured DGD data showed good agreement with a Laplacian distribution. We observed that the Laplacian parameter, which dictates the Laplacian pdf of DGD time derivative, seems to converge to a lower value as the fiber length is increased. This observation, which needs further verification, if true, would greatly simplify the system outage analysis due to first-order PMD on long-haul optical fiber links.

Introduction

In spite of the recent telecom bubble, statistics show that the net traffic growth (combined Internet, data and voice traffic) remains at the same level as it was three years ago and network capacity is being exhausted at the same rate as it was during the pre-bubble time [2]. To cope up with the demand for network capacity, major carriers are looking at increasing the transmission speeds. Polarization-mode dispersion (PMD) may be a major impediment for network operators seeking to increase the per channel data rate on long-haul fiber-optic links. While there are PMD challenges facing carriers at 10 Gb/s, these challenges are not as severe as originally feared. A marked improvement in the PMD tolerance of 10 Gb/s long-reach receivers will likely satisfy most length demands, obviating the need for PMD mitigation. However, transmission speeds of 40 Gb/s and beyond will most likely require some form of PMD mitigation in long-haul applications. To ensure signal quality on their fiber at such higher rates, network engineers must anticipate the impact of PMD on various fiber routes. A solid understanding of PMD-induced system outages will help engineers and researchers to develop new and cost-efficient mitigation alternatives to maintain high network reliability.

The availability of PMD data measured over long time periods on installed, buried fibers is limited. In this paper we present differential group delay (DGD) data measured over long time periods and simplified first-order PMD outage analysis based on measured data for buried, standard single-mode fiber.

Measurement setup

Measurements of instantaneous DGD were made on different combinations of three 95-km fibers (1, 2, and 3) within a slotted-core, direct-buried, standard single-mode fiber-optic cable made available by Sprint. The combinations of fibers used are three individual fibers (1, 2, 3, each ~95 km), three 2-fiber concatenations (1-2, 2-3, 1-3, each ~190 km) and one 3-fiber concatenation (1-2-3, ~285 km). A polarization analyzer employing the Jones-Matrix-Eigenanalysis (JME) method was used for measurements. The specifications of measurements on the three individual fibers and some results from the analysis of measured data were reported in our previous paper [3]. For measurements on 2-fiber concatenations two EDFAs were used along the link; one post-amplifier and one in-line amplifier in between the two fibers. For measurements on 3-fiber concatenation five EDFAs were used along the link; one post-amplifier and four in-line amplifiers after every ~47.5 km of fiber except for the last 95 km. For all the concatenated fiber combinations measurements were made at wavelengths from 1535 nm to 1565 nm with a spectral resolution of 0.1 nm (about 12.5 GHz) and were repeated every 23 minutes.

Measurements were carried on for 18 days on 1-2 concatenation (Aug. 22, 2002 - Sept. 9, 2002), for 21 days on 2-3 concatenation (Aug. 1, 2002 - Aug. 22, 2002), for 16 days on 1-3 concatenation (Sept. 27, 2002 - Oct. 13, 2002) and for 34 days on 1-2-3 concatenation (April 13, 2004 - May 17, 2004). Over the 34 days 2,127 measurements were made on 1-2-3 concatenation across 300 discrete wavelengths representing 638,100 measured DGD values. The corresponding number of measured DGD values for 2-fiber concatenations are 339,000 for 1-2, 394,200 for 2-3, and 306,000 for 1-3.

Plots of DGD vs. wavelength and time

Figures 1, 2, 3, and 4 show in a color-coded format normalized DGD data (i.e., $\text{DGD}/\text{Mean DGD}$) measured on the three 2-fiber concatenations and the 3-fiber concatenation, respectively. From the plots it is evident that the DGD varies significantly with wavelength and relatively high-DGD events are spectrally localized. A comparison of the above-mentioned plots with the corresponding plots for individual fibers reported in [3] shows that the variation of DGD with time is more rapid on concatenated fibers than on individual fibers.

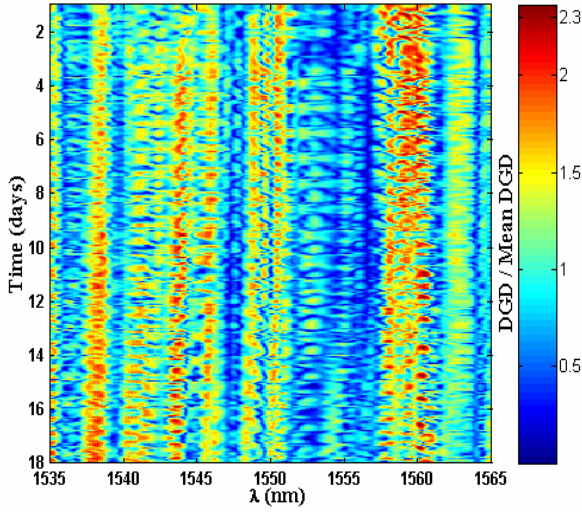


Figure 1. Measured, normalized DGD vs. wavelength and time for 1-2 fiber concatenation (18 days of data).

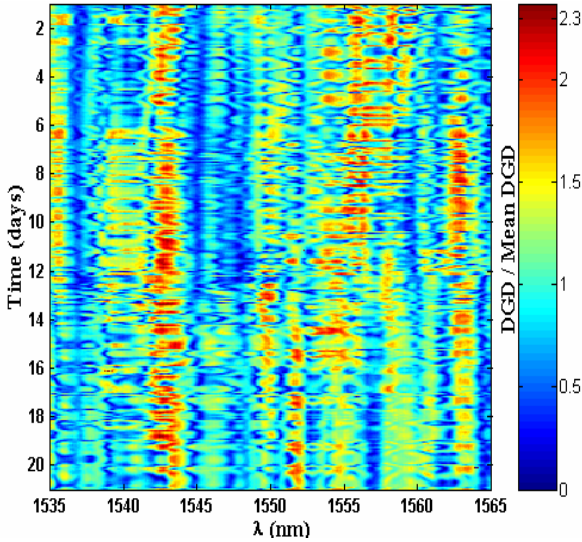


Figure 2. Measured, normalized DGD vs. wavelength and time for 2-3 fiber concatenation (21 days of data).

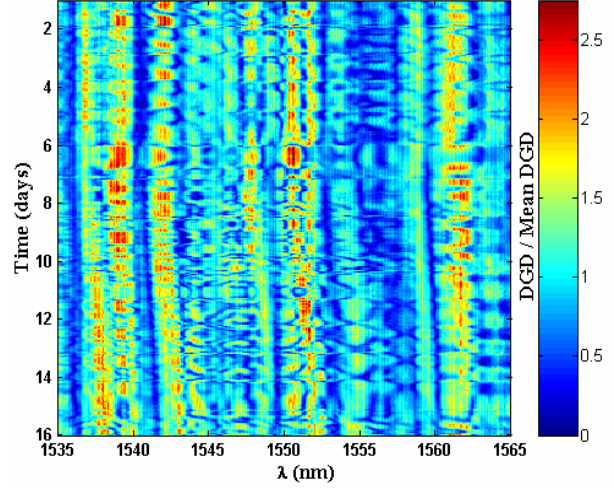


Figure 3. Measured, normalized DGD vs. wavelength and time for 1-3 fiber concatenation (16 days of data).

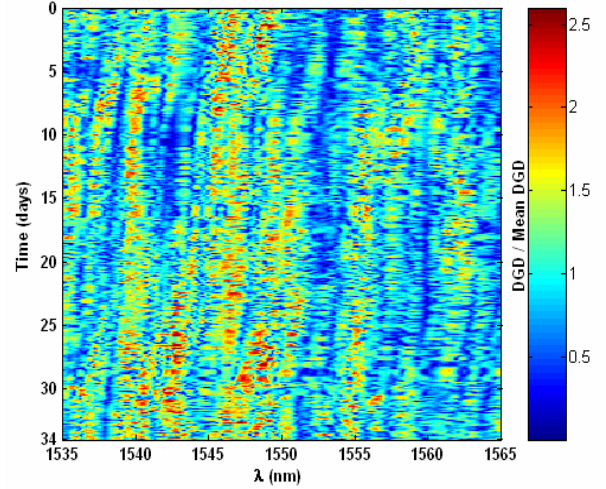


Figure 4. Measured, normalized DGD vs. wavelength and time for 1-2-3 fiber concatenation (34 days of data).

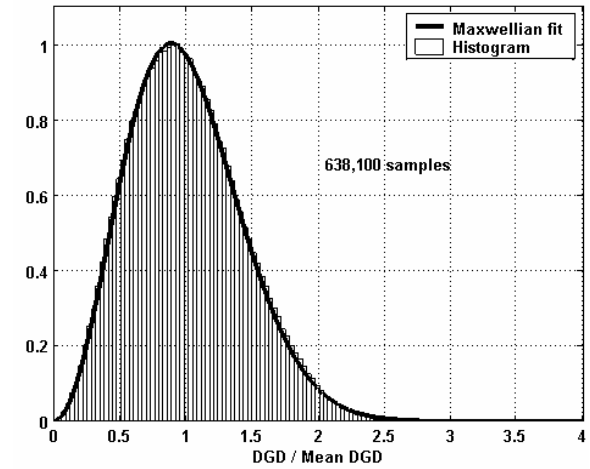


Figure 5. Histogram of measured, normalized DGD data for 1-2-3 fiber concatenation (34 days of data).

A histogram of the measured, normalized DGD data on 1-2-3 fiber concatenation, shown in figure 5, is seen to have shape consistent with a Maxwellian distribution as expected. A curve representing a Maxwellian distribution for a 1-ps mean DGD is also plotted for comparison. Also, we observed that the histograms of measured DGD data on the other combinations of the three fibers were in good agreement with the Maxwellian pdf (plots not shown here).

The pdf of DGD time derivative

Caponi et al. [1] defined a first-order PMD outage as an event in which a given threshold value of DGD ($\Delta\tau_{th}$) is exceeded. They showed that the mean outage rate, R_{out} (defined as the mean number of outage events per unit time with units of events/year), is found using [1]

$$R_{out} = \frac{1}{2} f_{\tau}(\Delta\tau_{th}) \int_{-\infty}^{\infty} f_{\tau'}(\Delta\tau') |\Delta\tau'| d\Delta\tau' \quad (1)$$

where $\Delta\tau'$ is the time derivative of DGD, $f_{\tau}(\cdot)$ is the pdf of $\Delta\tau'$ and $f_{\tau'}(\cdot)$ is the Maxwellian pdf of DGD. In [1] and [3], where predictions of R_{out} based on measurements on different buried links were reported, the integral in (1) was evaluated numerically from measured data. However, we observed [4] that $\Delta\tau'$ has a Laplacian pdf of the form

$$f_{\tau'}(\Delta\tau') = \frac{\alpha}{2} e^{-\alpha|\Delta\tau'|} \quad (2)$$

where $\alpha = \frac{\sqrt{2}}{\sigma}$ and is the Laplacian parameter with units of hours/picosecond and σ is the standard deviation of $\Delta\tau'$. Using the Laplacian pdf of $\Delta\tau'$, we reported [4] the following closed-form expression for R_{out} , which depends only on mean DGD and α .

$$R_{out} = \frac{1}{2\alpha} f_{\tau}(\Delta\tau_{th}) \quad (3)$$

To verify the Laplacian nature of $\Delta\tau'$, histograms of $\Delta\tau'$ were obtained from measured DGD data on all fiber combinations mentioned earlier. Figures 6, 7, and 8 show the $\Delta\tau'$ histograms obtained using measured DGD data on fiber 1, 2-3 fiber concatenation and 1-2-3 fiber concatenation respectively. For comparison, curves representing Laplacian distribution with different values for α , are also shown in the figures. It can be observed from the figures that the $\Delta\tau'$ histograms are in good agreement with the Laplacian distribution. Similar histograms were obtained for the data on the other fiber combinations (plots not shown here) and they also showed good agreement with the Laplacian distribution.

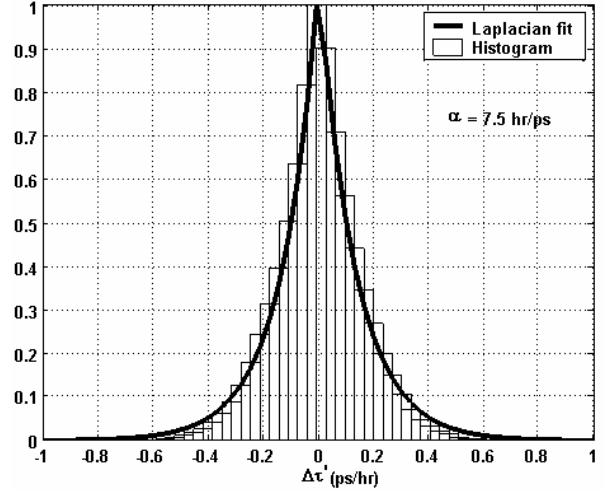


Figure 6. Histogram of measured $\Delta\tau'$ data from fiber 1 and its Laplacian fit.

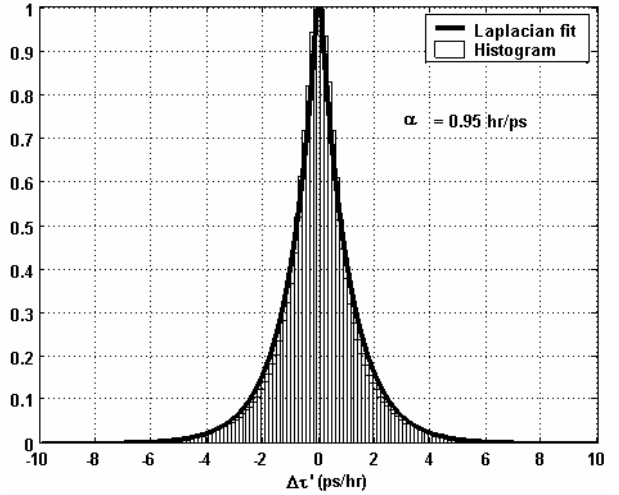


Figure 7. Histogram of measured $\Delta\tau'$ data from 2-3 fiber concatenation and its Laplacian fit.

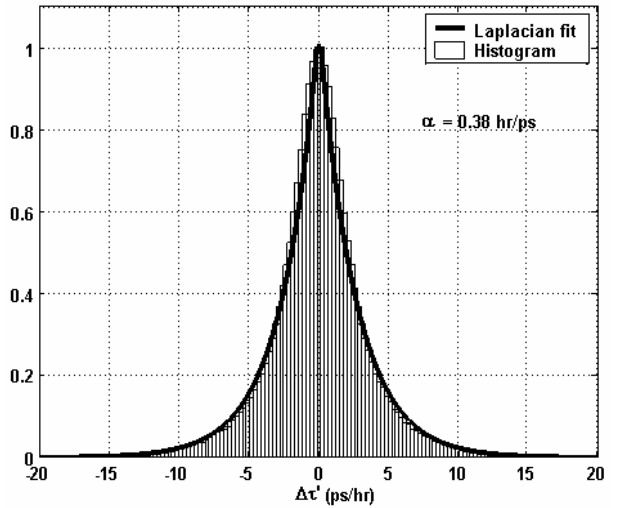


Figure 8. Histogram of measured $\Delta\tau'$ data from 1-2-3 fiber concatenation and its Laplacian fit.

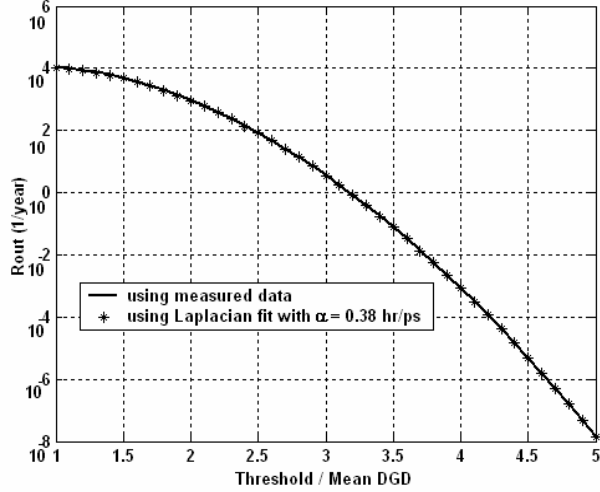


Figure 9. Comparison of R_{out} values on 1-2-3 fiber concatenation calculated using (1) and (3).

A comparison of R_{out} values calculated using (1) and (3) for 1-2-3 concatenation is shown figure 9. Excellent agreement between both sets of R_{out} values is evident from the figure. Similar agreement between the values calculated using (1) and those calculated using (3) was observed for other fiber combinations also (plots not shown here).

Variation of the Laplacian parameter (α) with fiber length

The Laplacian parameter (α) values for all of the fiber combinations mentioned earlier are shown in table 1. From the values in table 1, it can be observed that the Laplacian parameter decreased by an order of magnitude for concatenated fibers (longer lengths) compared to individual fibers (shorter lengths). But the decrease in the Laplacian parameter from the 2-fiber concatenations to the 3-fiber concatenation is less significant. This appears to indicate that the Laplacian parameter is converging to a value as the fiber length is increased. However, the validity of this observation must be further verified, possibly using modeling. If such a behavior is in fact true, then this would be extremely useful for network engineers in predicting the first-order PMD outage rates on long-haul optical fiber links.

Table 1. Laplacian parameter (α) values for different fiber combinations studied

	Individual fibers (~95 km)			2-fiber concatenations (~190 km)			3-fiber concatenation (~285 km)
Fiber combination	1	2	3	1-2	2-3	1-3	1-2-3
Laplacian parameter α (hr/ps)	7.5	4.25	10.9	0.6	0.95	0.7	0.38

Conclusions

We have measured DGD over long time periods on different combinations of three 95-km fibers within a slotted-core, direct-buried, standard single-mode fiber-optic cable. From these measurements we observed that DGD varies slowly over time but rapidly over wavelength or frequency. However, we also observed that the temporal variation becomes more rapid for longer length fibers.

Using the measured data we were able to verify the Laplacian nature of DGD time derivative and the closed-form expression for predicting first-order PMD outage rates that we reported in [4]. We observed that the Laplacian parameter, which dictates the Laplacian pdf of DGD time derivative, seems to converge as the fiber length is increased. This observation, which needs further verification, if true, would greatly simplify the system outage analysis due to first-order PMD on long-haul optical fiber links.

Acknowledgements

This work was funded by Sprint Corporation Company, L. P. and NSF grant ECS-0116213.

References

1. R. Caponi, B. Ripsati, A. Rossaro, and M. Schiano, "WDM system impairments due to highly correlated PMD spectra of buried optical cables," *Electronics Letters*, 38(14), pp. 737-738, 2002.
2. L.E. Nelson, M. Karlsson, and D.Q. Chowdhury, "Guest editorial, Special issue on polarization-mode dispersion," *Journal of Lightwave Technology*, 22(4), pp. 951-952, 2004.
3. C. Allen, P.K. Kondamuri, D.L. Richards, and D.C. Hague, "Analysis and comparison of measured DGD data on buried single-mode fibers", *Symposium on Optical Fiber Measurements, NIST conference, USA*, pp. 195-198, Sept. 2002.
4. P.K. Kondamuri, C. Allen, D.L. Richards "Laplacian pdf of DGD time derivative and application to predicting PMD-induced outage rates," *Electronics Letters*, 40(8), pp. 503-504, 2004.

The long-term distribution of differential group delay in a recirculating loop

Hai Xu¹, Brian S. Marks^{1, 2}, John Zweck³, Li Yan¹, Curtis R. Menyuk¹,
and Gary M. Carter^{1, 2}

¹ *Department of Computer Science and Electrical Engineering, University of Maryland Baltimore County,
1000 Hilltop Circle, Baltimore, MD 21250*

² *Laboratory for Physical Sciences, 8050 Greenmead Drive, College Park, MD 20740*

³ *Department of Mathematics and Statistics, University of Maryland Baltimore County.*

I. Introduction

It is well known that the distribution of differential group delay (DGD) in a straight-line optical fiber transmission system is a Maxwellian when the fiber realization drifts ergodically and the fiber is statistically homogeneous [1]. However, in a recirculating loop system, a common test-bed in laboratories to study long-haul optical transmission, the periodicity of the fiber path induces different polarization-dependent behavior from that of a straight-line system [2, 3]. To break this periodicity, the loop-synchronous polarization scrambling was developed, whereby the signal undergoes a random polarization rotation each round trip [3]. If the DGD per round trip is constant, the DGD distribution in a loop with such scrambling will be a Maxwellian, similar to the DGD distribution in a uniform straight-line system. However, because of the inevitable drift of the loop fiber birefringence, the DGD per round trip varies over time. Consequently, the DGD distributions in recirculating loops are not Maxwellian, as has been shown both experimentally and theoretically [4, 5]. To our knowledge, there has been no published measurement result to date for the DGD distributions in a loop system from non-ergodic drift to ergodic drift.

In this work, we provide an analytical formula for the DGD distribution after multiple round trips in a loop when the fiber drifts ergodically. Experimentally, we measured the DGD distribution in a 107 km loop system for 6.5 days, during which the fiber drift was nearly ergodic. After nearly ergodic fiber drift, the DGD distribution is very close to the analytical formula. However, over shorter time intervals, the fiber does not drift ergodically, and the DGD distribution strongly depends on the choice of time interval over which the measurements were taken. In comparison to our previous experimental work [4], we shortened the time for one DGD measurement from 16 seconds to 180 ms thus making the measurement uncertainty induced by the fiber drift negligible. As a result, the overall measurement uncertainties were greatly reduced.

II. Theoretical model of ergodic drift in a loop

For a recirculating loop with loop-synchronous polarization scrambling with ergodic fiber drift, the DGD distribution, $F_N(x)$, after N round trips was given and numerically evaluated in [5] by

$$F_N(x) = \int_0^\infty f_N(x; \tau) f_1(\tau) d\tau \quad (1)$$

Here, $f_1(\tau)$ is the distribution of the DGD in one round trip, which is Maxwellian with mean $\langle \tau \rangle$ if the fiber drift is ergodic. Also, $f_N(x; \tau)$ is the distribution of the DGD, x , after N round trips, given that the round trip DGD is τ . Since f_N is close to Maxwellian when $N \gg 1$, in this case we can evaluate the integral to obtain the closed-form analytical expression

$$F_N(x) = \left(1024 x^2 / \pi^4 \langle \tau_N \rangle^3 \right) K_0(8x / \pi \langle \tau_N \rangle), \quad (2)$$

where K_0 is the zeroth order modified Bessel function of the second kind, and $\langle \tau_N \rangle = \sqrt{8N/3\pi} \langle \tau \rangle$ is the mean DGD after N round trips.

III. Experimental setup

As shown in Fig. 1, our recirculating loop consists of four spans of 25-km-dispersion-shifted fiber and two spans of 3.5-km-single-mode fiber. The details of the loop were described in [4]. We used a loop-synchronous lithium-niobate (LiNbO₃) polarization scrambler (PS) to randomly rotate the polarization state of the signal once per round trip. We then measured the DGD after each round trip of the loop using the Jones matrix eigenanalysis (JME) technique [6].

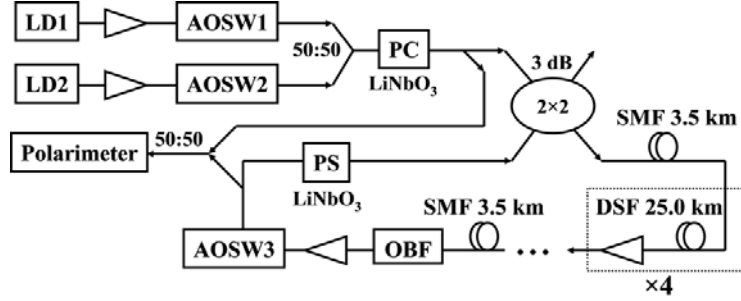


Fig. 1. Experimental setup

We require the DGD measurements to be as fast as possible so that the loop does not drift significantly during a single set of measurements. Therefore, in comparison to [4], we modified the transmitter to shorten the DGD measurement time. Two continuous wave signals at 1551.0 ± 0.04 nm were generated from two laser diodes. These two signals were sent into the loop one at a time, using two acoustic-optic switches. Each wavelength was transmitted for 30 ms — longer than the propagation time over 50 round trips. Every 60 ms, we varied the input polarization states using another LiNbO₃ polarization controller PC. Different input polarization states were widely separated on the Poincaré sphere. Consequently, over each 180 ms, we launched 2 wavelengths each at 3 different polarization states. From the input and output polarization states in these 6 combinations, we calculated the DGD using the JME for all 50 round trips in 180 ms.

Both the input and output polarization states were measured by a real-time polarimeter (Adaptif A1000), with a sampling rate of 100 kHz, corresponding to 50 samples per round trip. We averaged these 50 samples to obtain the Stokes vector for one round trip. The sampling window of the polarimeter was 240 ms. In the first 180 ms, the DGD values after all 50 round trips were measured. In the remaining 60 ms, the wavelengths and input polarization states were the same as those in the first 60 ms. We computed the difference between the Stokes vectors measured in the last 60 ms and those in the first 60 ms, and we call the angle between these two vectors the *noise angle* [4], which is a measure of the uncertainty of the Stokes vector.

Every 10 seconds, the loop-synchronous polarization scrambler PS was set to randomly choose a new set of rotations and one sample of DGD was measured for each round trip. For 6.5 days we repeated this process continuously and collected 55 000 samples of DGD.

IV. Experimental results and discussion

Fig. 2a shows the distribution of the noise angle at the first and the 50th round trip, collected from 55 000 DGD measurements in 6.5 days. For each DGD measurement, we used the corresponding measured noise angle to simulate the uncertainty in that DGD value as follows. We perturbed the measured Stokes vector to a random point on a circle, the center and radius of

which are the measured Stokes vector and noise angle. Then we re-calculated the DGD using the perturbed Stokes vector, and the difference from the measured DGD is called the *DGD deviation*. For each DGD measurement, we obtained 50 values of the DGD deviation by repeating this perturbation. In Fig. 2b we show the probability that the DGD deviation exceeds certain value at the first and the 50th round trip from 55 000×50 samples. Fig. 2b show the extent to which the DGD values are affected by the uncertainties of the Stokes vectors in our JME measurement.

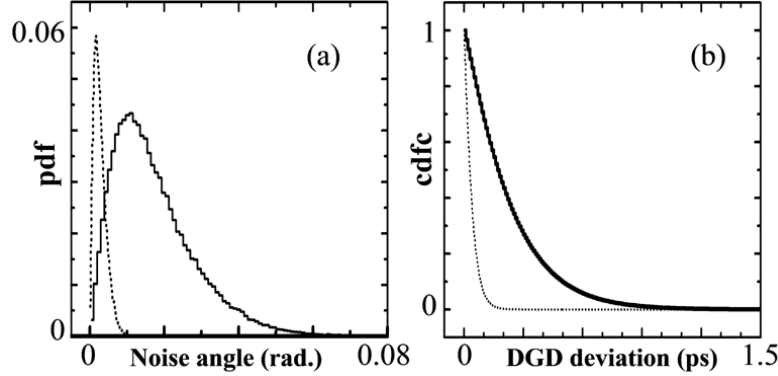


Fig. 2. (a) Probability density function (pdf) of noise angle after one (dotted line) and 50 round trips (solid line). (b) Probability of the DGD deviation larger than certain value for one (dotted line) and 50 round trips (solid line).

The mean and the standard deviation of the DGD deviation are 0.04 ps and 0.04 ps after one round trip. These values increase to 0.23 ps and 0.26 ps after 50 round trips due to a larger amount of Stokes noise at longer propagation distance. In comparison to our previous experiment [4], we reduced the measurement uncertainties by a factor of two by shortening the measurement time to 180 ms. In such a short measurement time, the influence of the fiber drift is insignificant, and the uncertainty is mostly caused by the optical noise in the system, particularly at longer distances. As shown in our previous simulation study [7], for the JME method the effects of high-order polarization-mode dispersion and polarization dependent loss on the DGD measurement are much less than the Stokes noise.

In Fig. 3, we show the distribution of DGD over different time intervals for one (left column) and 50 round trips (right column). The three distributions in Figs. 3a and 3a' are from DGDs measured over three hours: hours 11–14, 48–51, and 91–94. The three distributions in Figs. 3b and 3b' are measured over two days: days 0–2, 2–4, and 4–6. The distributions in Figs. 3c and 3c' are from the entire 6.5 days, together with the Maxwellian fits. In addition, in Fig. 3c', the distribution obtained using the analytical formula in Eq. (2) is shown with a dotted line. These fits have the same mean DGD values as the measured results. There are 1 060, 16 940, and 55 000 DGD samples in the three-hour, two-day, and 6.5-day distributions, respectively.

As shown in Fig. 3a, over three-hour time intervals, the DGD per round trip cannot be treated as a constant value because the fiber can drift significantly. Consequently the DGD distribution at the 50th round trip can be very different from a Maxwellian, as shown in Fig. 3a'. On the other hand, a three-hour drift is far from ergodic. As a result, the DGD distribution depends on the time interval over which the measurements were taken. The fiber drift over two-day intervals is still not ergodic, and the DGD distribution varies for different two-day intervals, as shown in Figs. 3b and 3b'. However, the variation is less than in the three-hour distributions. As the measurement time interval increases, at the first round trip the distribution becomes closer to a Maxwellian, and at the 50th round trip, the distribution becomes closer to the analytical expression of Eq. (2). After 6.5 days, as shown in Figs. 3c and 3c', the DGD distribution in one

round trip is nearly Maxwellian, indicating a nearly ergodic drift. The DGD distribution at the 50th round trip agrees well with the analytical expression of Eq. (2). For a loop system with ergodic fiber drift, the Maxwellian distribution underestimates the probability of both small and large DGD.

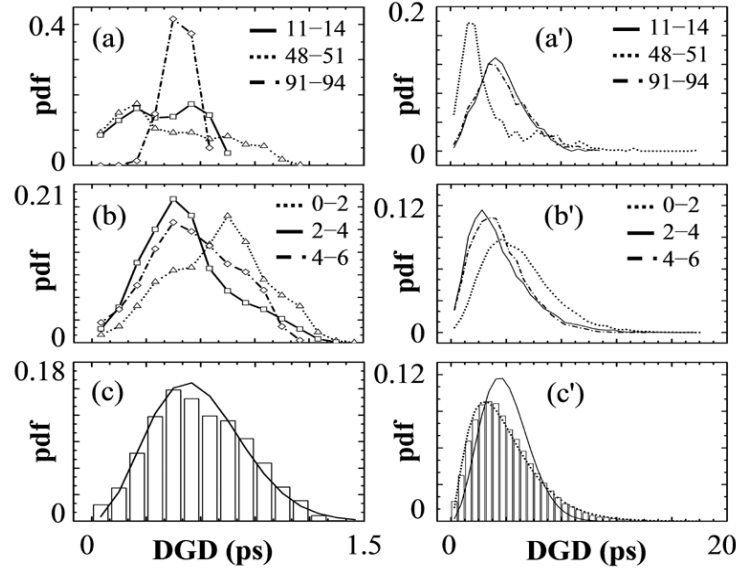


Fig. 3. (a, a') The DGD distribution measured at the first (a) and 50th round trip (a') over 3 hours, with the starting and ending time shown in the insets with units of hours; (b, b') The DGD distribution measured at the first (b) and 50th round trip (b') over 2 days, with the starting and ending time shown in the insets with units of days; (c, c') bar: The DGD distribution measured at the first (c) and 50th round trip (c') in 6.5 days, solid line: Maxwellian fit, dotted line: analytical expression in Eq. (2). In (a) and (b), the center of each histogram bin is marked.

V. Conclusion

We present an analytical formula for the DGD distribution after many round trips in a recirculating loop with loop-synchronous scrambling when the loop fiber drifts ergodically. Our DGD measurements over 6.5 days agree with this formula. When the loop fiber drifts only partially, the DGD distribution varies from measurement window to measurement window.

References:

1. G. J. Foschini and C. D. Poole, "Statistical theory of polarization dispersion in single mode fibers", *J. Lightwave Technol.* **9**, pp. 1439–1456, (1991).
2. Y. Sun, I. T. Lima, H. Jiao, J. Wen, H. Xu, H. Erefej, G. M. Carter, and C. R. Menyuk, "Study of system performance in a 107-km dispersion-managed recirculating loop due to polarization effects", *Photon. Technol. Lett.* **13**, pp. 966–968, (2001).
3. Q. Yu, L.-S. Yan, S. Lee, Y. Xie, and A. E. Willner, "Loop-synchronous polarization scrambling technique for simulating polarization effects using recirculating fiber loops", *J. Lightwave Technol.* **21**, pp. 1593–1600, (2003).
4. H. Xu, H. Jiao, L. Yan, and G. M. Carter, "Measurement of differential group delay in a recirculating loop," *OFC'2004*, Los Angeles, CA, Feb. 2004, paper FA6.
5. E. Corbel, "Concerns about emulation of polarization effects in a recirculating loop", *ECOC'2003*, Rimini, Italy, Sep. 2003, paper Mo3.7.4.
6. B. L. Heffner, "Automated measurement of polarization mode dispersion using Jones matrix eigenanalysis", *Photon. Technol. Lett.* **4**, pp. 1066–1069, (1992).
7. H. Xu, B. S. Marks, L. Yan, C. R. Menyuk, and G. M. Carter, "A comparison of measurement techniques for differential group delay in a long-haul optical system", *OFC'2004*, Los Angeles, CA, Feb. 2004, paper FI4.

Experience in reflectometry and PMD measurements for WAN in Costa Rica

Prof. Luis D. Marin-Naranjo M.Sc.

University of Costa Rica – Photonics and Laser Laboratory LAFTLA – Electrical Engineering School – Engineering Department

Phone 506 207 4700 Fax 506 207 4139 E-mail: lmarin@eie.ucr.ac.cr

Abstract: Costarrican local carrier (ICE) began to install optical fiber links in Costa Rica in 1989. One task at LAFTLA (Laboratorio de Fotonica y Tecnologia Laser) was to measure and advice to ICE engineering staff for precise PMD measurements and to develop good practices procedures. We present how we did that task and what problems we faced.

1. Introduction

Costa Rica is a country in Central America that began installing optical fibers for Telco and Datacom WAN in 1989 under the management of the local public carrier called ICE (for Instituto Costarricense de Electricidad). At University of Costa Rica (UCR) our job in this field began a little bit before in 1988 in education and training. In 2000 we started a program in Photonics and Laser and that resulted in LAFTLA (Laboratorio de Fotonica y Tecnologia Laser in Spanish), that means Photonics and Laser Technology Laboratory. Our first goal was to work for local industry in areas related to light and optical parameters. As a third world country we do not develop technology but we need to understand and apply standards for day to day jobs trying to get quality. So we developing not only an education and training program in applied optics but also we are developing measurements and metrology services in the field. Because optical fibers communications are important now, we present our experiences in the particular field of reflectometry and PMD measurements. ICE requested to us to improve and perform the local standards in order to prepare the links to upgrade to DWDM this year.

2. LAFTLA and country overview

LAFTLA is a technical program that belongs to Electrical Engineering School, University of Costa Rica as a program developed into the research program of Instituto de Investigaciones en Ingeniería - INNI (Engineering Research Institute of University of Costa Rica). We get funds from the university, self-funding by the courses and services we offer and some donations. Intel for example donated last year two 30 W Nd:YAG Lasers for material processing. We have the basic equipment and physical space, and are in process to ISO 17025 for metrology.

The main company that uses fiber optics in Costa Rica in telecommunications is ICE (Instituto Costarricense de Electricidad). It is a governmental company owner of WAN rings under SDH technology (currently has links at 622 Mbps and 2.5 Gbps) for Telco and Datacom mainly at 1 310 nm. ICE has the monopoly of cellular links and subscriber telephony. Also is the local company for international links with optical submarine cables. Right now Costa Rica has 2 submarine accesses, one in the Atlantic Ocean from MAYA and one in the Pacific Ocean from ARCOS. ICE has been training personnel since 1990 but in simple optical fiber systems of second generation. The whole country has optical fiber cable and Central America will be link via land with optical networks this year. ICE also uses OPGW system along the country for power system control and communications.

3. Project Border to Border

ICE is in process to install 32 wavelengths DWDM system around the country and also is testing FSO links in San Jose. For DWDM the project is call Border to Border from Nicaragua to Panama. The equipment will have the basic optical and network elements to transmit 32 λ as final capacity but must be formed with the essentials to start with 12 λ .

The optical frequencies must follow the ITU-T grid, Rec. G.692 item 6.1.5 and table A.1/G.692. The capacity will begin with 32 wavelengths at 2,5 Gbps and grow to 10 Gbps in the future. The project will use only standard single mode fiber **ITU-T G.652**.

The proposal now already in process includes a series of links around the country following routes indicated in the figure 1.



Figure 1. Situation of the country for the project Border to Border

Figure 2 show the 2 steps North and South of the country.

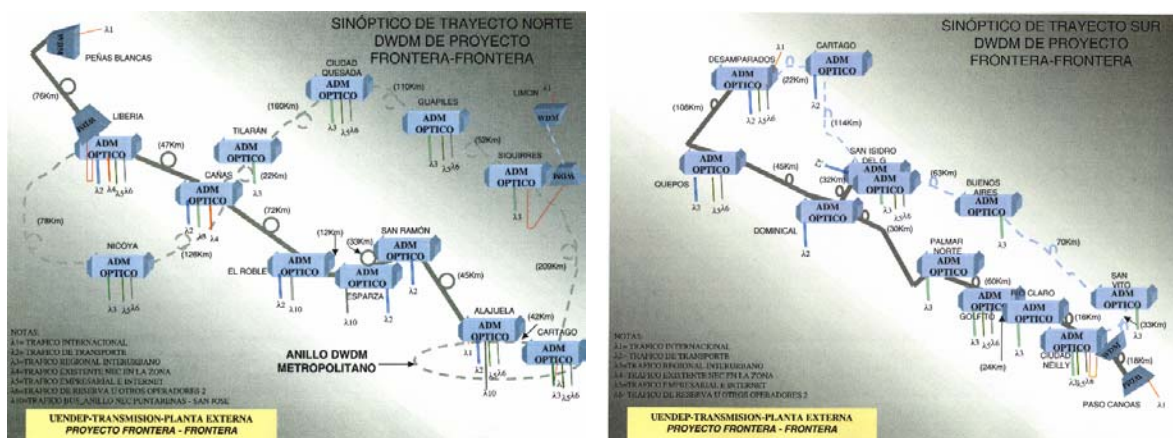


Figure 2. North and south links for Project Border to Border. Layout of links in the country

As indicate it will use OADM, optical amplifier and alternative routes for management. In order to organize the management ICE requested us to help the staff GRM (Management of Network and Maintenance) with the reflectometry and PMD measurements.

A general procedure was developed in order to follow the bid proposal which includes optical testing with equipment offers and perform measurements of optical properties already in place. These measurements include attenuation, dispersion and PMD (Polarization Mode Dispersion). The last is required in order to investigate if fibers already installed can manage 10 Gbps. The amount of optical fiber cable is approximate 3 000 km around the country. The proposal bid proposal included the conditions for PMD for cabled optical fibers, which must be less than $0.5 \text{ ps/Km}^{1/2}$. This allows a transmission length limited by PMD of 400 km for STM-64.

4. Measurements procedures and results developed for PMD at ICE

As part of LAFTLA advice to ICE we developed joint with ICE staff the procedure to measure PMD which was a new test never done before. We develop a single method using a mini OTDR Agilent 6000B to get the real length as real as possible. Here we found something really interesting.

ICE staff had been doing reflectometry for years without precise index of refraction, that mean they used the default OTDR index with different fiber brands. We investigate and obtained the general effective index for Corning SMF 28 at 1310 nm is 1,4675 and for 1 550 nm 1,4681. For fiber LG for 1 310 nm is 1,4676 and for 1 550 nm is 1,4682. They were using 1,4575 and other by default. After then the whole personnel is using the right indexes. I found myself with my OTDR Agilent the following measurements in a link Sur-Desamparados, around 3 029 meters for 1 561 nm $n=1,47110$, at 1 561 with $n=1,46810$ and with the real $n=1,4681$. The difference was dropping the 20 meters loop a difference form 3 009 meters to 3 015 meters, that is in a short span a difference of 6 meters.

We measured the optical fiber network in Costa Rica from border to border at 1 550 nm with our Agilent mini OTDR and we got the real distance and reflectometry parameters in all links which are now already updated for ICE by using the real index of refraction, . - With that we generated a table for the following PMD measurements.

The following procedure then was developed for the EXFO equipment FTB-300/FTB-400, PMD module FTB-5500 and Polarized light model FSL-110.

1. To know the right distance using the data from LAFTLA measurements.
2. Introduce file name in setup, threshold and maximum acceptable range on a single or multiple measurement.
3. Introduce fiber ID, comments, strong coupling and total distance.
4. Set up in remote the polarized light with respective patch cord.
5. Measure with FTB-300/FTB-400.

Recommendations:

Select always coupling mode in strong

Measure with OTDR with the right indices the span, to give the real distance to PMD analyzer.

Clean and verify patch cords

Confirm connections

Do not move patch cords during measurement

In case of doubt repeat the procedure.

This is temporal dispersion

Table 1. Proposed requisites for digital rate (with probability of 99,994% that loss is less 1 dB) were:

Rate (Gbps)	Max PMD (ps)	PMD coefficient $\text{ps}/(\text{km})^{1/2}$ for 400 km
2,5	40	$\leq 2,0$
10	10	$\leq 0,5$
20	5	$\leq 0,25$
40	2,5	$\leq 0,125$

Threshold for 2,5 Gbps delay of PMD 10 ps – measurements must be less than that value.

Table 2. Some examples of PMD measurements in real links in Costa Rica.

Place and connector	Span (km)	Delay PMD (ps)	Coefficient PMD (ps/ $\sqrt{\text{km}}$)	Date
Llano Grande – Guardia 55	12,493	0,06	0,016	12/7/02
Nicoya – Santa Barbara 18	25,920	1,68	0,330	13/7/02
Peñas Blancas – La Cruz 07	19,308	1,27	0,290	12/7/02
Filadelfia - Guardia 30	15,022	0,07	0,018	20/7/02
Liberia – Cañas 61	51,250	2,21	0,309	20/7/02

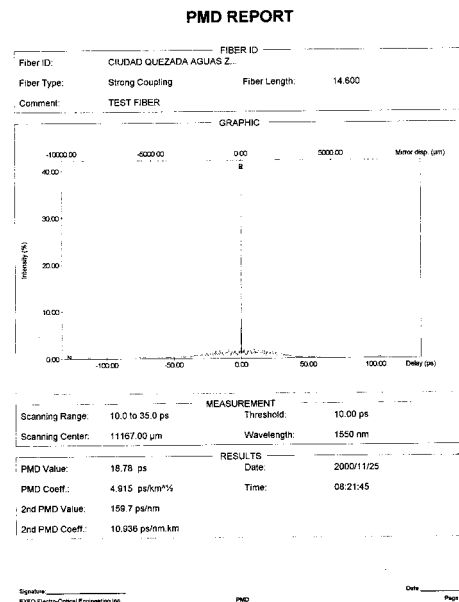


Figure 3 Sample of print report for PMD using EXFO platform

Conclusions

We condense in these lines the main result of our job of 6 months and the following report. The first result was to establish the use of real index of refraction in reflectometry instead of the default index. The whole outside plant in Costa Rica was re measured in the following months after this report. With the data the PMD reports were done with the EXFO platform and we developed the procedures for PMD measurements and taught it to ICE staff following the EXFO manual. The results were as we hoped, and some results produce that some optical cables in bad conditions or regular dispersion, not useful for 10 Gbps, were changed or repaired for the next future. The main idea was to obtain a neutral results from the University of Costa Rica, not from the local optical fibers suppliers, in order to certify the real status of the fiber for DWDM and the immigration to 1 550 nm. So many tasks of maintenance were undertaken in the next 2 years up to now with the interpretation of the high PMD coefficient in several spans.

References

1. Luis D. Marin –Naranjo, *PMD and reflectometry in ICE WAN*, UEN DEPT, ICE , project report LAFTLA – UCR, San Jose, Costa Rica, November 2002.
2. Agilent Technologies, *Lightwave Test and Measurements*, 2002 Catalog
3. EXFO, *Lightwave Test and Measurements*, 2002

Locating High PMD Sections of an Overhead Cable using Polarization-OTDR

A.B. Conibear (1), F.J. Visser (2), F. Audet (3), R. Salmi (4) and A.W.R. Leitch (5)

1 : University of Port Elizabeth, P.O. Box 1600, Port Elizabeth, 6000, South Africa. Ann.Conibear@upe.ac.za

2 : Telkom S.A. visserfj@telkom.co.za, 3 : EXFO francis.audet@exfo.com, 4 : EXFO redha.salmi@exfo.com,

5: University of Port Elizabeth. Andrew.Leitch@upe.ac.za

Abstract— High Polarization Mode Dispersion (PMD) values pose an obstacle to the upgrading of links for higher transmission rates. Polarization Optical Time Domain Reflectometry (P-OTDR) measurements give an indication of the specific fiber sections that cause the high PMD values, allowing an informed decision to be taken regarding the upgrading of a link. In this work P-OTDR measurements are used to indicate the fiber sections potentially giving rise to high PMD in an overhead optic fiber cable in the Eastern Cape, South Africa. Verification of the P-OTDR predictions is done by cutting out the sections flagged as being high PMD contributors, and measuring actual PMD values.

I Introduction

Polarization-mode dispersion (PMD) is a serious limitation in modern optical communication systems. The upgrading of existing fiber links for higher data transmission rates is challenging, since in some cases, the cables were deployed before PMD was even measured by fiber manufacturers. In such links, high PMD values are not uncommon, and there is often significant variability in the PMD within a given cable, and along the length of an individual fiber. There is a considerable time and cost saving incentive for identifying specific fiber sections that are the chief PMD contributors, with a view to re-routing or replacing only the problematic sections when upgrading a link. Polarization-Optical Time-Domain Reflectometry (P-OTDR) offers the possibility, not of giving a quantitative distributed PMD measurement, but of indicating sections that are likely to be the main PMD contributors. In this work, such predictions are made for an overhead optical fiber cable, and the predictions tested by interferometric PMD measurements.

The concept of P-OTDR was introduced over twenty years ago by Rogers [1], who described an OTDR sensitive to the state of polarization (SOP) of the backscattered signal. The simplest P-OTDR consists of an OTDR, in which a polarizer is introduced in the return path, just prior to the detector. This technique can be used to measure the local birefringence, and there has recently been heightened interest in variants of this approach to estimate distributed PMD [2-4].

Each of these proposed techniques requires that the P-OTDR have sufficient spatial resolution to register the evolution of the states of polarization (SOP) as the light propagates down the fiber.

The SOP of the light transmitted through a fiber, when plotted on the Poincaré sphere, is known to rotate about the birefringence axis at a rate that depends on the local birefringence of the fiber. The beat length, L_b , is the distance travelled in the fiber for which the SOP makes one complete revolution about the birefringence axis on the Poincaré sphere. The beat length is defined by

$$L_b = \frac{\lambda}{\beta c} \quad (1)$$

where λ is the wavelength of light, β is the local birefringence of the fiber and c is the speed of light. The fiber birefringence places requirements on the resolution of a P-OTDR if it is to measure variations in the backscattered SOP. For example, a birefringence of 1 ps/km corresponds to $L_b = 5$ m. If such a fiber were measured with a P-OTDR and if the fiber birefringence were purely linear, the backscattering signature would oscillate with a period of $L_b/2$, in this case 5 m, since the light travels forward and backward in the fiber. Accordingly, a P-OTDR would need a spatial resolution of roughly 1 m (or less) in order to discriminate the oscillations, requiring optical pulses of 10 nsec or less. Typical OTDR instruments do not have a large useful dynamic range with such a high spatial resolution, and the requirements on the OTDR performance become even more stringent for fibers having a higher birefringence. Consequently, these techniques are normally limited to low birefringence fibers, and are unsuitable for the application we are considering.

In the next section, we will more specifically outline the parameters that a P-OTDR system should measure in order to detect high PMD sections, before describing the system of Huttner et. al [5] which addresses these requirements.

II Distributed PMD measurements

PMD itself is a global phenomenon generated by the local birefringence along the fiber. We have already outlined the relationship between the local

birefringence, and the beat length of the backscattered SOP. It is to be noted however, that the birefringence axis itself changes along the fiber, and this change is represented by the so-called coupling length, h . This is defined as the length of fiber for which the spatial correlation of $\vec{\beta}(z)$ decreases by $1/e^2$.

The PMD of a fiber depends on two characteristics: the birefringence β , which determines the difference in the time of flight of the polarization modes, and then secondly, the mode coupling at sites where the local birefringence changes, causing an exchange of energy between polarization modes. There are thus two characteristic lengths that need to be considered, namely the beat length and the coupling length which are related to the PMD through the following approximation:

$$PMD = \frac{\lambda}{L_b c} \sqrt{\ell h} \quad (2)$$

where ℓ is the length of the fiber. One assumes that ℓ is long compared to both the beat length and the coupling length. Older fibers with high PMD values tend to have long coupling lengths, while fibers with good PMD values have a combination of long beat lengths and short coupling lengths.

Using equations 1 and 2 it is possible to evaluate the minimum β needed to generate a PMD of 1 ps in a 1-km fiber link for different h . It can be seen that an unrealistically high birefringence (>6 ps/km) is required for $h < 25$ m. It is therefore expected that most fiber segments having a PMD coefficient above $1 \text{ ps}/(\text{km})^{1/2}$ will correspond to cases where h is long (> 50 m). Consequently, the detection of a long h value should be sufficient to identify the high-PMD sections of the fiber.

III The Principle of P-OTDR

The approach taken by Huttner et al [5], and applied in the EXFO instrument used in this study, is to measure the degree of polarization (DOP) of the backscattered pulse. The DOP statistics give insight into the beat length, and most importantly, the coupling length h .

The experimental set-up is shown in Fig.1. The detector is preceded by a rotating quarter-wave plate, and a polarizer. By taking four different P-OTDR traces, with an appropriate orientation for the quarter-wave plate and the polarizer for each trace, it is possible to obtain a fully polarimetric measurement of the SOP evolution against distance. There are naturally constraints imposed by the system resolution, which will be discussed later in this section. The rest of the P-OTDR consists of a standard OTDR where we will denote the spatial resolution of the instrument L_p . The only modification is the replacement of the broad linewidth Fabry-Perot laser with a DFB

laser. This is because for a broad linewidth source, the SOP of the each spectral component evolves differently as it propagates down the fiber. This will cause an effective depolarisation of the transmitted and backscattered light.

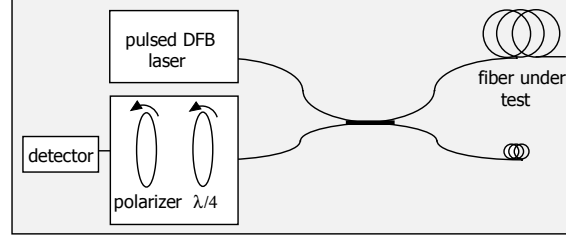


Fig.1: Optical configuration of the P-OTDR used for the experiments

The degree of polarization (DOP) of the backscattered signal should remain close to unity when the P-OTDR resolution is less than the backscattering beat length, that is for $L_p < L_b/2$. A high DOP thus serves to identify low PMD fibers. The coupling length is immaterial, since the PMD does not accumulate rapidly because of the low birefringence.

The SOP that is detected is an average over the OTDR pulse in the fiber, and so when the P-OTDR pulses are of the order of the backscattering beat length, there is some fading in the oscillations that leads to a decrease in the measured DOP. This so-called temporal depolarization is dependent on the local birefringence only and is not affected by the accumulated PMD. For a very long pulse, the backscattered DOP will tend toward $1/3$ rather than zero [6].

The other factor to be considered is the relationship between the P-OTDR resolution, and the coupling length. Two cases are possible- firstly that the birefringence axis varies rapidly on the scale of the OTDR pulse, corresponding to short coupling length. For this case of $L_p \gg h$, the light in the pulse is totally depolarised, and the backscattered DOP is $1/3$. This corresponds to intermediate PMD values. The birefringence may even be relatively high, but because there is frequent exchange of energy between the polarization modes, the PMD does not accumulate rapidly.

The second case is when $h \gg L_p \gg L_b/2$. Here the birefringence axis does not change along the pulse, but because of the small beat length, the SOP changes rapidly. The measured DOP depends on the angle between the SOP and the local birefringence axis. The average DOP registered at the detector changes slowly, governed by the rate at which the birefringence axis

changes. It is not sufficient to know the DOP then, in order to find fiber sections with high PMD. The correlation length of the DOP, represented by H_{DOP} , is defined as the distance over which the spatial correlation of the DOP decreases by $1/e^2$. A high value of the parameter H_{DOP} is a good indicator of a long coupling length, and the primary requirement for a high PMD section.

In summary, a consistently high DOP would indicate a low PMD section. Sections with low average DOP where the DOP is rapidly oscillating are likely to have intermediate PMD, while the high PMD sections are characterised by slowly changing DOP, or equivalently, large H_{DOP} .

IV Link characterisation

Measurements were carried out on a 66.4 km aerial cable deployed in the Eastern Cape Region, South Africa.

Table 1: Fiber PMD and suitability for 10 Gb/s

Fiber	PMD (ps)	Usable for 10 Gb/s
37	7.639	
38	19.444	
39	12.434	
40	3.681	Yes
41	8.382	
42	8.777	
43	8.215	
44	15.690	
45	2.497	Yes
46	28.079	
47	9.500	

■ <7 ps, □ from 7 to 10 ps, and ■ >10 ps

Table 1 gives the PMD values measured by an interferometric technique with an EXFO FTB-5500B PMD analyser (GINTY, as per the recent standard [7] and described in [8]). These values were measured several months before the P-OTDR measurements. There is also an indication given of the suitability of each fiber for 10 Gb/s transmission, (medium shading being acceptable, the light sections indicating caution, and the dark not acceptable for 10 Gb/s). These limits are set conservatively since they are based on interferometric PMD measurements, using only one input/ output SOP configuration. Only fibers 40 and 45 would be suitable for 10 Gb/s transmission.

A typical interferogram for a high PMD fiber, in this case fiber 38 with a PMD of 19.4 ps is shown in figure 2.

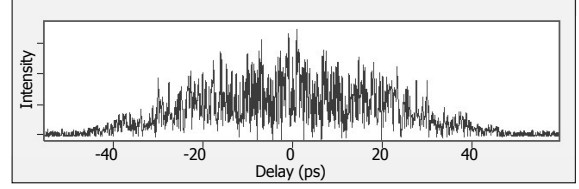


Fig. 2 Interferogram for fiber 38 with PMD 19.4 ps

Measurements were done using an EXFO 1100 P-OTDR to determine whether the PMD was uniformly high in the cable, or whether specific sections were responsible. A representative P-OTDR trace for fiber 38 is shown in Figure 3, where the dots in greyscale below the trace flag particular segments based on their DOP statistics.

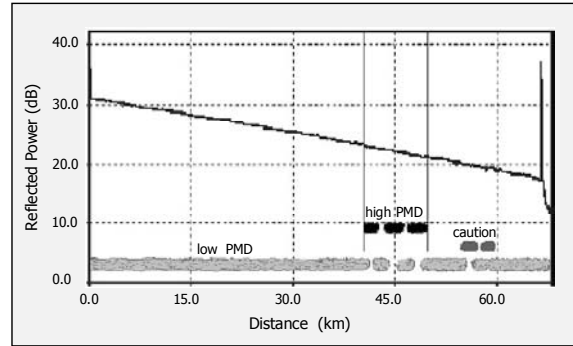


Fig. 3 P-OTDR trace for fiber 38

Table 2 summarises the specific regions in each of the 11 fibers that were flagged by P-OTDR. The actual resolution of the instrument is 500m, but the fibers are summarised in 3 km segments for simplicity.

Table 2: Regions flagged as having high PMD

Fibre	Distance from point A in km																			
	0	3	6	9	12	15	18	21	24	27	30	33	36	39	42	45	48	51	54	57
37																				
38																				
39																				
40																				
41																				
42																				
43																				
44																				
45																				
46																				
47																				

Probability of section being a high PMD contributor:
 ■ low, □ borderline ■ high

It is to be noted that in general caution should be exercised in using P-OTDR with aerial cables, since they are particularly sensitive to environmental effects. In this

case however, strong evidence was gained from the DOP statistics for a localised section of high PMD.

V. Verification of P-OTDR predictions

Verification of the predictions focuses on fibers 37 to 40. In fibers 38 and 39, the portion of the link responsible for the high PMD values appears to be a section between 40.6 and 49.6 km. The positions were taken from OTDR splice events. The strategy for verifying the P-OTDR measurements was to re-measure the link PMD, to cut the fibers, and measure the PMD of the 9.0 km section for each. Fiber sections in fibers 37 and 40 were expected to have low PMD and 38 and 39 high PMD. Fiber sections from 37 and 39 were then swapped and spliced into the link, similarly fibers 38 and 40. The new link PMD values were measured, with the expectation that the two previously unacceptable fibers 38 and 39 would be significantly improved. The fibers were then re-cut and restored to their individual configuration and the PMD measured. The results of this process carried out in April 2004 are given in Table 3 below.

Table 3: *Fibers 37 to 40 PMD values*

Fiber	PMD values (ps)			
	Link pre-swap	9.0 km section	Link swapped	Link restored
37	8.30	1.70	11.40	8.07
38	17.07	18.53	2.92	16.64
39	13.57	7.22	9.91	12.22
40	2.97	2.66	16.73	*

* Not available

Firstly, it is evident that the sets of PMD values are comparable with those in Table 1, both prior to swapping, and after restoration. Considering the PMD for the flagged section, it is seen that the high PMD predictions for fibers 38 and 39 are confirmed, with this section constituting 14% of the total length, but accounting for essentially all of the PMD in the case of 38, and of the order of 50% in the case of fiber 39. The fact that the PMD of the fiber section for fiber 38 is more than the link PMD measured a few hours earlier is not cause for concern given the variability of PMD. Fiber sections from 37 and 40 have significantly lower PMD values, as predicted, although in the case of 40, this section still accounts for most of the PMD, since the rest of the link is very low.

The link PMD values after fiber swapping show fibers 38 and 39 having significantly lower PMD values, while the two previously low fibers inherit the high PMD of the sections spliced into these links.

Restoration of the fibers returns the PMD to levels comparable with the initial measurements.

VI. Conclusions

While it is true that high PMD values in a fiber link can be a result of accumulated PMD along the entire link, the results presented in this work demonstrate that the primary contribution may be from a localised region. In such cases there is a considerable time- and cost-saving incentive for identifying the sections of a link that are the main contributors, with a view to replacing or re-routing only the problematic sections when upgrading the link for higher data rates. P-OTDR measurements accurately identified the sections of fiber that were the main contributors. While it should be noted that P-OTDR data require careful interpretation, the technique is nonetheless potentially extremely useful in assessing the PMD characteristics of deployed fiber links.

VII Acknowledgements

The authors would like to thank Mr Chris Nel of Lambda Test Equipment, the South African agent for EXFO, for his assistance in arranging the loan of the 1100 P-OTDR, and with the field trials. The financial support of THRIP, the NRF, Telkom S.A., Aberdare Fibre-Optic Cables, and Corning Optical Fiber is gratefully acknowledged.

VII. References

- [1] A. J. Rogers, "Polarization-optical time domain reflectometry: A technique for the measurement of field distributions", *Appl. Opt.*, vol.20, pp.1060-1074, 1981
- [2] F. Corsi, A. Galtarossa, L. Palmieri, "Beat length characterization based on backscattering analysis in randomly perturbed single-mode fibers", *J. Lightwave Tech.*, vol. 17, pp. 1172-1178, 1999
- [3] H. Sunnerud, B.-E. Olsson, P. A. Andrekson, "Measurement of polarization mode dispersion accumulation along installed optical fibers", *IEEE Photonic Tech. Letters*, vol. 11, pp. 860-862, 1999
- [4] M. Wulpart, A. J. Rogers, P. Megret, M. Blondel, "Fully-distributed polarization properties of an optical fiber using the backscattering technique", *Applications of Photonic Tech. (Photonics North 2000)*, SPIE 4087, pp. 396-404, 2000
- [5] B. Huttner, B. Gisin and N. Gisin, "Distributed PMD Measurement with a Polarization-OTDR in optical fibers", *J. Lightwave Tech*, vol 17, 1843-1848, 1999
- [6] M.O. van Deventer, "Polarization Properties of Raleigh backscattering in single-mode fibers", *J. Lightwave Tech*, vol. 11, pp. 1985-1989, 1993
- [7] FOTP 124A, TIA 455-124-A, annex A.2, (2004) 40.
- [8] N. Cyr, "Polarization Mode Dispersion Measurement: Generalization of the Interferometric Measurement to any Coupling regime", *J. Lightwave Tech*, vol. 22, pp 794-805, 2004

Effects of polarization-mode dispersion on four-wave mixing efficiency

M. González-Herráez, J. Pelayo, P. Corredera, M. L. Hernanz,
J. A. Méndez, S. Martín-Lopez and A. Carrasco
Instituto de Física Aplicada, CSIC. Serrano 144, 28006 Madrid. Spain

A physical model for the simulation of four-wave mixing in the presence of PMD is proposed and its consistency with real data is discussed. Some measurements of FWM efficiency in fibers with high PMD confirm the behaviour predicted theoretically.

1 Introduction

In the last years, four-wave mixing has been successfully used to measure the chromatic dispersion distribution along the fiber [1, 2, 3, 4]. Most of the methods for chromatic dispersion mapping along the fiber are based on the widespread assumption that the polarization states of the FWM pumps keep aligned along the fiber. This assumption is not valid in the presence of polarization-mode dispersion. Our aim is to explore how PMD affects the resolution of these mapping techniques.

2 Theory

We start by obtaining the growth equation of FWM for any arbitrary polarization state of the pumps. We consider the case of two low-power pumps propagating along the fiber. We assume that there is no pump depletion associated to the nonlinear process, and that only linear attenuation and random polarization evolution affects the two pumps. Since the power of the pump waves is low, we also neglect self-phase and cross-phase modulation phenomena. We start by obtaining the nonlinear electronic polarization vector induced in the medium by means of the tensor product $\mathbf{P}_{NL} = \chi^{(3)} : \mathbf{E}\mathbf{E}\mathbf{E}$. In the case of an isotropic medium, only three elements of the tensor $\chi^{(3)}$ are nonzero, and using the Born-Oppenheimer approximation, only one element ($\chi_{1111}^{(3)}$, for instance) is enough to describe the third-order interaction. To describe the FWM process, we keep the terms with frequency $f_s = 2f_1 - f_2$. We obtain the propagation equation of the Stokes wave in terms of the amplitude vectors $\mathbf{A}_i = (A_{ix} \ A_{iy})^T$:

$$\frac{\partial}{\partial z} \mathbf{A}_s = -\frac{\alpha}{2} \mathbf{A}_s + \left[(i\gamma \mathbf{A}_1 \cdot \mathbf{A}_2^*) \mathbf{A}_1 + \gamma \frac{1}{3} (\mathbf{A}_1 \cdot \sigma_3 \mathbf{A}_2^*) \sigma_2 \mathbf{A}_1 \right] \exp(i\Delta\beta z) \quad (1)$$

where σ_2 and σ_3 are the standard Pauli matrices defined as:

$$\sigma_2 = \begin{pmatrix} 0 & 1 \\ 1 & 0 \end{pmatrix} \quad \sigma_3 = \begin{pmatrix} 0 & -i \\ i & 0 \end{pmatrix} \quad (2)$$

and \cdot denotes the scalar product. The amplitudes of the waves have been defined so that $P_i = |A_i|^2$. We now assume that, since the two pump wavelengths are very close in wavelength, the evolution of the states of polarization keeps their relative alignment within the diffusion length (i.e. the length after which the probability density function of the state of polarization (SOP) can be considered

uniformly distributed in the Poincaré sphere). In the usual nearly phase-matched case, we can also assume that the diffusion length is much smaller than the inverse of the phase mismatch. With these assumptions, we can average the previous equation over all the possible states in the Poincaré sphere:

$$\frac{\partial}{\partial z} \mathbf{A}_s = -\frac{\alpha}{2} \mathbf{A}_s + i\gamma \frac{8}{9} (\mathbf{A}_1 \cdot \mathbf{A}_2^*) \mathbf{A}_1 \exp(i\Delta\beta z) \quad (3)$$

where \cdot denotes scalar product. From this point, it can be easily demonstrated that for fibers with low PMD (i.e. random but parallel evolution of the polarization states), the FWM efficiency is proportional to $|\mathbf{A}_1(z=0) \cdot \mathbf{A}_2^*(z=0)|^2$, which is in agreement with the well-known result that the FWM efficiency is zero when the input states of the waves are perpendicular. Note that a final factor $\gamma_e = (8/9)\gamma$ has been obtained. This factor 8/9 makes this equation consistent with the well-known model of Manakov solitons [5].

3 Numerical modelling

In order to investigate the effect of polarization-mode dispersion (PMD) on fiber four-wave mixing it is convenient to construct a numerical model of the fiber so that simulation results can be obtained in a simple fashion. We have developed a split-step model of the fiber, suitable for obtaining valid conclusions about the behaviour of the nonlinear effect in the presence of PMD. Our numerical model of the fiber is depicted in figure 1. The basic idea is to model the fiber as a cascade of

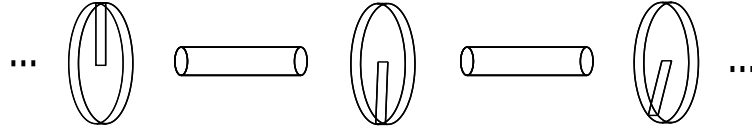


Figure 1: Modelling of polarization and nonlinear evolution in the fiber

waveplates [6] with pieces of ideal fiber inserted between them. By using this model, all the changes in the polarization state take place in the waveplates, while all the nonlinear processes take place in the pieces of fiber. Only linear birefringence is considered in the plates. Thus, the effect of a single waveplate is modeled through the use of a Jones matrix of the form $\mathbf{M}_i = \mathbf{Q}_i^{-1} \mathbf{D}_i \mathbf{Q}_i$ where \mathbf{Q}_i and \mathbf{D}_i stand for:

$$\mathbf{Q}_i = \begin{pmatrix} \cos \theta_i & \sin \theta_i \\ -\sin \theta_i & \cos \theta_i \end{pmatrix} \quad (4)$$

$$\mathbf{D}_i = \begin{pmatrix} \exp(-j\Delta\tau_i\omega/2) & 0 \\ 0 & \exp(j\Delta\tau_i\omega/2) \end{pmatrix} \quad (5)$$

The orientation of the waveplates (θ_i) is considered to follow a uniform distribution in the interval $[0, 2\pi]$, while the delay of the individual plates ($\Delta\tau_i$) follows a maxwellian distribution. The delays of the plates are fitted so that the differential group delay (DGD) of the whole structure is the desired one. The mean DGD of the structure can be estimated using the following expression:

$$\langle \Delta\tau \rangle = \sqrt{\frac{8}{3\pi}} \sqrt{\sum_{i=1}^N \Delta\tau_i^2} \quad (6)$$

where $\Delta\tau_i$ is the individual delay of each plate. The total length of one period (waveplate and piece of fiber) is called the rotation length (L_R).

We did our tests on a fiber with a length of 10 km, a linear attenuation coefficient of 0.2 dB/km and a nonlinear coefficient $\gamma = 2.3 \text{ W}^{-1}\text{km}^{-1}$. The rotation length L_R was set to 100 m.

Other rotation lengths were tested (1-500 m), and no significant deviations were obtained in the mean results. We understand this by noting that the main source of non-ideality in this problem is the relative misalignment between the SOPs of the pump waves. Since the two pump waves are very close in wavelength, they tend to keep their relative alignment in a length scale which is much larger than the correlation length of the fiber. To achieve some relatively general results, we perform averaging of the results obtained. Typically, we average the results 100-1000 times. The power of the two input waves in the tests shown is 1 mW.

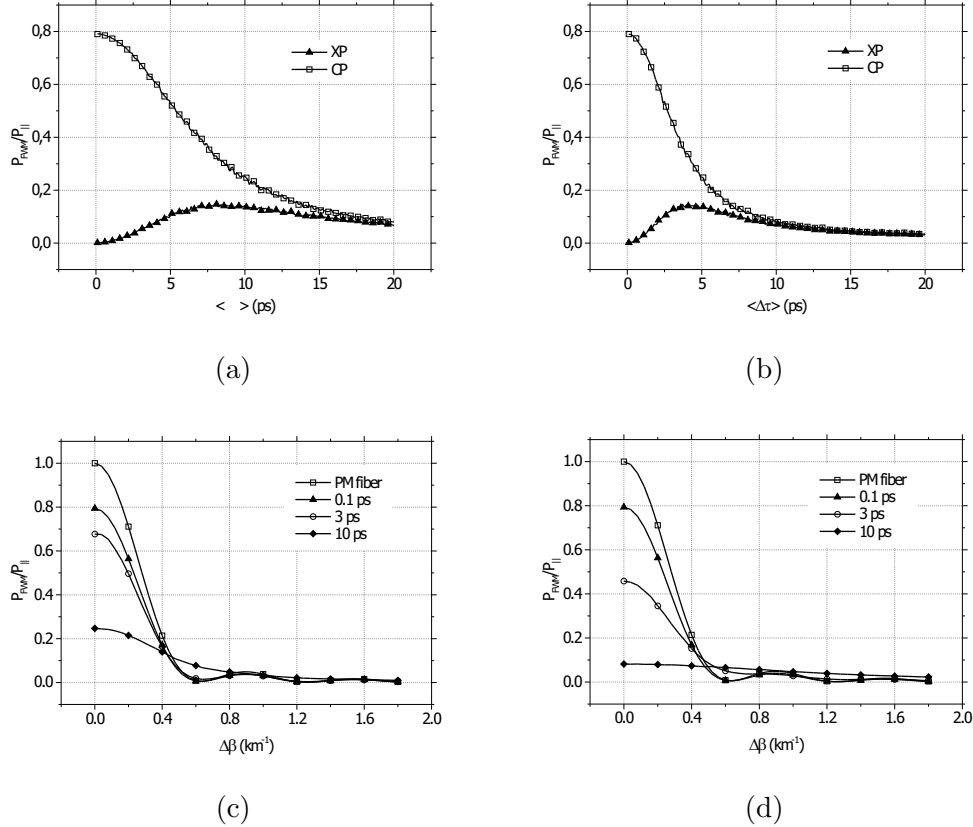


Figure 2: (a) and (b) Normalized FWM efficiency for parallel (CP) and crossed (XP) polarizations and $\Delta\beta = 0$, with 0.5 and 1 nm pump separation respectively. (c) and (d) Spectral shape of the FWM efficiency as a function of the phase mismatch, for a 0.5 and 1 nm pump separation respectively. The case of linear polarizations preserved along the fiber (PM case) is also shown for comparison

Some of the results can be seen in figure 2. Figures 2a and 2b represent the mean power of the Stokes wave at the fiber output, considering perfect phase matching ($\Delta\beta = 0$). In figure 2b we can see that as the total DGD of the fiber grows, the relative input states of polarization become less relevant, and finally converge to the same result. In both cases, (parallel and crossed input SOPs) it can be seen that for very large DGDs the power of the four-wave mixing decays to zero. This happens because the states of polarization of the two waves become increasingly independent as the DGD grows. Hence, in the case of complete independence of the two SOPs, the average of the scalar product in equation 3 is zero. Figures 2(c) and 2(d) shows how the random evolution of the polarization states of the waves causes a vast change in the spectral behaviour of the four-wave mixing effect. As the DGD of the fiber grows, the phase matching condition due to chromatic dispersion is less relevant and the existence of random phase matchings due to random polarization evolution tends to broaden the previous restrictive condition. In both figures it can be seen that

the impact of PMD is higher as the two pumps are more separate in wavelength. It is clear that the validity of the scalar model of FWM is limited to a certain wavelength detuning between the FWM pumps. Since the resolution of all the chromatic dispersion mapping methods is inversely proportional to the wavelength separation between the FWM pumps, it is clear that PMD poses a limit to the achievable resolution given by these techniques.

4 Experimental results

We perform measurements of FWM efficiency using the setup described in [3]. Two tunable lasers (acting as FWM pumps) are swept over the λ_0 region of the fiber. The output FWM is recorded by use of an optical spectrum analyzer. A feedback routine ensures that the power of the lasers is kept constant throughout all the acquisition process. The polarization of the two pumps is controlled so that it can be set parallel or crossed at the input of the fiber under test. In our case, the fiber under test is a 7-km long dispersion-shifted fiber with a PMD of nearly 2 ps. Figure 3 shows the experimental results obtained for this fiber. Note that for increasing wavelength separation among the FWM pumps, the results with parallel and crossed input SOPs become more indistinguishable, in agreement with the results of the model.

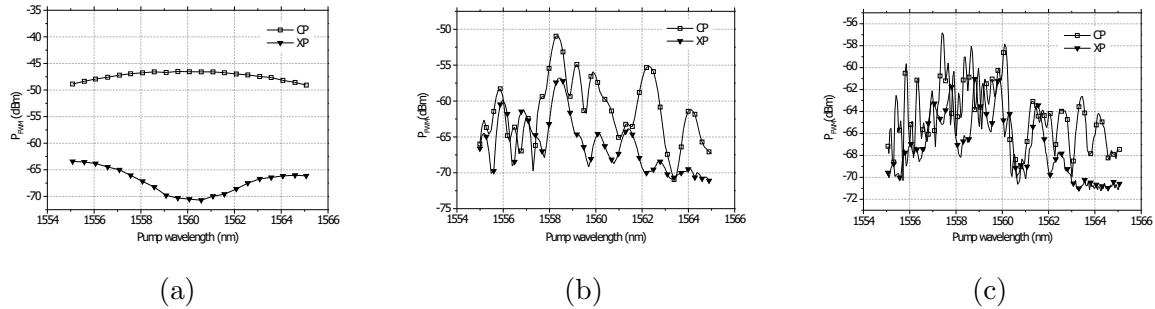


Figure 3: Measured FWM efficiency with parallel and crossed input SOPs: (a) $\Delta\lambda = 1$ nm, (b) $\Delta\lambda = 5$ nm y (c) $\Delta\lambda = 8$ nm

5 Conclusions

We have developed a physical model for the simulation of four-wave mixing in the presence of PMD. The results of this model are in good qualitative agreement with experimental observations. Further work should enable us to examine from this model the resolution limits imposed by PMD on the existing chromatic dispersion mapping techniques based on four-wave mixing.

References

- [1] L. F. Mollenauer, P. V. Mamyshev, and M. J. Neubelt, *Opt. Lett.* **21** 1724-1726 (1996).
- [2] I. Brener, P. P. Mitra, D. D. Lee, D. J. Thomson and D. L. Philen, *Opt. Lett.* **23**, 1520-1522 (1998).
- [3] M. Gonzalez-Herraez, P. Corredera, M. L. Hernanz and J. A. Mendez, *Opt. Lett.* **27**, 1546-1548 (2002)
- [4] M. Gonzalez-Herraez, L. Thevenaz and Ph. Robert, *Opt. Lett.* **28** 2210-2212 (2003)
- [5] Y. Chen and H. A. Haus, *Opt. Lett.* **25** 290 (2000)
- [6] C. D. Poole and D. L. Favin, *J. Lightwave Technol.* **12** 917 (1994)

Calibration of a Polarisation Rotator, to Launch Defined Polarisation States

David Ives, National Physical Laboratory,
Teddington, Middlesex, United Kingdom, TW11 0LW.

Abstract: Polarisation rotators are used to set defined launch polarisation states in systems designed to measure the polarisation properties of optical fibre and optical fibre components. In order to predictably set polarisation states the properties of the control elements must be well known. This paper describes the calibration of a polarisation rotator based on three rotating optical elements: a linear polariser, a quarter wave plate and a half wave plate. The calibrated polarisation rotator was used to reliably set polarisation states.

1. Introduction

The measurement of polarisation properties of optical fibre systems and components often requires the setting of a number of defined polarisation states, for example the four-state method for measuring polarisation dependent loss^[1]. This is achieved using a polarisation controller or polarisation rotator that for repeatability is often based on free space optical wave plates. Previously with uncalibrated polarisation rotators the settings required to launch a defined polarisation state have been found by iteration. In order to improve the polarisation setting it is first necessary to calibrate the elements within the polarisation rotator.

2. Measurements

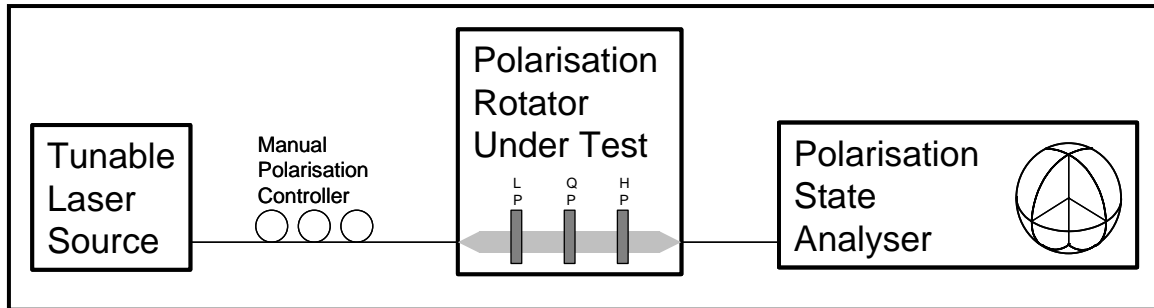


Figure 1, Experimental set up.

The polarisation rotator under test was placed between a tunable laser source and a calibrated polarisation state analyser^[2], as shown in Figure 1. The polarisation rotator is connected such that the light propagates through the linear polariser first, thence the quarter and half wave plates. The linear polarising element was set to a nominal azimuth of 0° and fixed in this position. This defines the datum angle for all the other measurements. The manual polarisation controller is adjusted to align the input polarisation state with the linear polariser, within the polarisation rotator, to give maximum signal transmission.

The polarisation state received at the polarisation state analyser is recorded as the quarter wave plate is rotated in steps through 360° . The recorded loci of the polarisation state on the surface of the Poincaré sphere is analysed as described in section 3 to obtain the retardance of the wave plate and the angular offset between the nominal azimuth and the actual azimuth of the wave plate. The quarter wave plate is set such that its actual azimuth is 0° , i.e. that its birefringence

axis is aligned with the linear polariser. The polarisation state received at the polarisation state analyser is recorded as the half wave plate is rotated in steps through 360°. Figure 2 shows the measured loci of the polarisation state on the surface of the Poincaré sphere as the quarter wave plate or the half wave plate is rotated along with the fitted loci, see section 3.

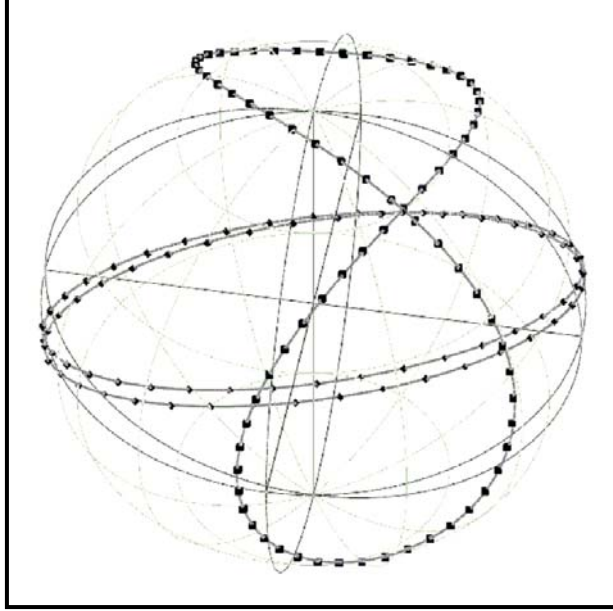


Figure 2, The measured and fitted evolution of the output polarisation state as the quarter wave plate (squares) or half wave plate (diamonds) is rotated through 360°.

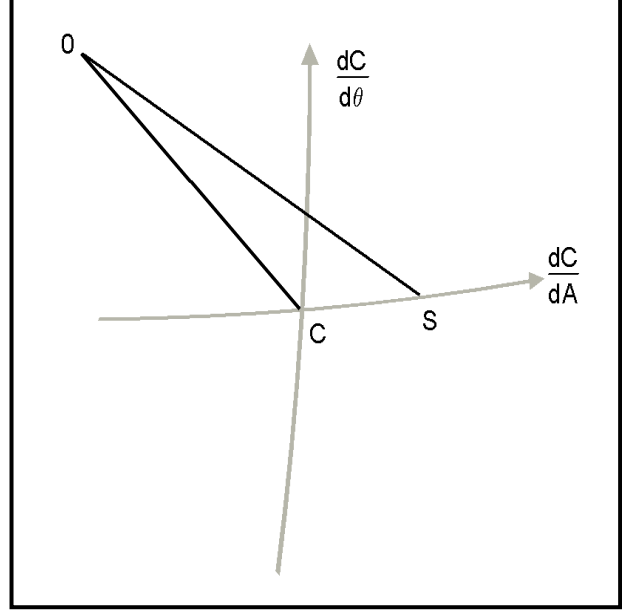


Figure 3, Relationship between the measured point S, the closest point C on the curve and the origin O of the Poincaré sphere.

3. Calculations

The loci of the polarisation vector on the surface of the sphere can be described by a curve $C(\{X_0, X_1, X_2, X_3, X_4\}, \theta)$, see for example[3], which is a function of the wave plate azimuth θ and the fixed coefficients X_0 to X_4 .

$$C(X, \theta) = \begin{bmatrix} \cos(X_0) & -\sin(X_0) & 0 \\ \sin(X_0) & \cos(X_0) & 0 \\ 0 & 0 & 1 \end{bmatrix} \begin{bmatrix} \cos(X_1) & 0 & -\sin(X_1) \\ 0 & 1 & 0 \\ \sin(X_1) & 0 & \cos(X_1) \end{bmatrix} \begin{bmatrix} 1 & 0 & 0 \\ 0 & \cos(X_2) & -\sin(X_2) \\ 0 & \sin(X_2) & \cos(X_2) \end{bmatrix} \begin{bmatrix} \cos(2\theta) & -\sin(2\theta) & 0 \\ \sin(2\theta) & \cos(2\theta) & 0 \\ 0 & 0 & 1 \end{bmatrix} \begin{bmatrix} 1 & 0 & 0 \\ 0 & \cos(X_3) & -\sin(X_3) \\ 0 & \sin(X_3) & \cos(X_3) \end{bmatrix} \begin{bmatrix} \cos(2\theta) & \sin(2\theta) & 0 \\ -\sin(2\theta) & \cos(2\theta) & 0 \\ 0 & 0 & 1 \end{bmatrix} \begin{pmatrix} \cos(X_4) \\ 0 \\ \sin(X_4) \end{pmatrix} \quad (1)$$

where the fixed coefficients X_0, X_1, X_2 describe a three axis rotation as the polarisation states are transformed in the fibre pigtail, X_3 describes the retardance of the element being rotated and X_4 the circular component of the light input to the retarding element.

In order to estimate the retardance of the plate the curve coefficients are optimised to fit the measured data. In order to optimise these coefficients an error between the measured point and the curve is required. In Figure 3 the deviation of the measured point S from the curve C with a

sign dependent as to whether the measured point S is to the left or right of the curve is used as the error deviation. For a point on the curve C and a measured point S the great arc joining these points has an axis along $C \times S$. Such that the vector pointing along the great arc dC/dA is

$$\frac{dC}{dA} = C \times (C \times S) \quad (2)$$

The vector pointing along the curve is $dC/d\theta$. The curve is closest to the measured point S when the vector pointing along the curve is at right angles to the vector pointing along the great arc linking C and S. This occurs when

$$\frac{dC}{dA} \cdot \frac{dC}{d\theta} = 0 \quad (3)$$

which allows for a simple iteration to find θ and hence C. The angular deviation of the measured point S from the curve C is then calculated as

$$\delta C = (C \times S) \cdot \frac{dC}{d\theta} \left| \frac{d\theta}{dC} \right| \quad (4)$$

where the final terms provide the sign information. Given this error deviation we can perform a non-linear least squares fit to optimise the curve coefficients, X_0 to X_4 . We first need good guess values for X_0 to X_4 . X_0 and X_1 are obtained by visual alignment of the cross of the curve with that of the measured data, X_2 is adjusted to align the axis of the line passing through the extreme and the cross of the curve with that of the measured data, X_3 is adjusted to match the extreme of the curve with that of the measured data and X_4 is set to zero. The non-linear least squares fit is then formulated by calculating numerically the design matrix A,

$$A = \begin{bmatrix} \frac{\partial \delta C_1}{\partial X_0} & \frac{\partial \delta C_1}{\partial X_1} & \frac{\partial \delta C_1}{\partial X_2} & \frac{\partial \delta C_1}{\partial X_3} & \frac{\partial \delta C_1}{\partial X_4} \\ \frac{\partial \delta C_2}{\partial X_0} & \frac{\partial \delta C_2}{\partial X_1} & \frac{\partial \delta C_2}{\partial X_2} & \frac{\partial \delta C_2}{\partial X_3} & \frac{\partial \delta C_2}{\partial X_4} \\ \vdots & \vdots & \vdots & \vdots & \vdots \\ \frac{\partial \delta C_n}{\partial X_0} & \frac{\partial \delta C_n}{\partial X_1} & \frac{\partial \delta C_n}{\partial X_2} & \frac{\partial \delta C_n}{\partial X_3} & \frac{\partial \delta C_n}{\partial X_4} \end{bmatrix} \quad (5)$$

where δC_i is the angular deviation of the i^{th} point from the guessed curve. The estimated correction, δX , are calculated from

$$\delta X = [A^T A]^{-1} [A^T \delta C] \quad (6)$$

and used to update the guessed curve coefficients, X. The process is iterated with the new corrected X values replacing the original guesses until δX converges to zero.

The optimum parameter θ , for each measured point is found for the optimum coefficients X and this allows the offset angle of the first point and the apparent angular step to be estimated. The offset angle gives the azimuth difference between the angle of the linear retardance axis of the first measured point and the linear component of the input polarised light.

It is only possible to find the retardance of the wave plates within an offset of $2n\pi$. In the case of the half wave plate this effectively gives an ambiguity as to whether the plate is just less or just more than a half wave plate coupled with an ambiguity of the direction of the fast axis.

4. Results and Uncertainties

For the polarisation rotator under test the following results and uncertainties were found, where the uncertainties shown are the 95% confidence intervals.

Wave Plate	Retardance	Azimuth Offset
Quarter Wave Plate (2 nd position)	1.606 ± 0.008 rad ($=0.2556 \pm 0.0013 \lambda$)	-1.576 ± 0.010 rad ($= -90.3 \pm 0.6^\circ$)
Half Wave Plate (3 rd position)	3.109 ± 0.008 rad ($= 0.4948 \pm 0.0013 \lambda$)	-0.0245 ± 0.025 rad ($= -1.4 \pm 1.4^\circ$)

The uncertainties of the retardance measurement come from the following contributions; the residuals of the polarisation state fitting, the calibration of the polarisation state analyser, the drift of the fibre pigtail during the course of the measurement, the temperature coefficient of the polarisation rotator, the wavelength uncertainty and the wavelength dependence of the polarisation rotator, and the repeatability of the measurements. The largest contribution comes from the calibration of the polarisation state analyser. The uncertainties of the azimuth offset measurement include the contributions above for the retardance measurement and also a contribution due to the setting of the zero azimuth of the previous retarding elements.

5. Conclusions

This paper has described a method to calibrate the elements within a polarisation rotator. The calibrated polarisation rotator can thence be used to set two defined polarisation states immediately after the half wave plate. These test states can then be used to calculate the rotation matrix relating to the fibre pigtail allowing the polarisation states at the output of the fibre pigtail to be predictably set. The maximum deviation of the final set states at the end of the fibre pigtail from the required state was 0.037 rad. This is within the uncertainty of the polarisation state analyser of ± 0.06 rad (95% confidence interval).

6. Acknowledgements

We gratefully acknowledge the financial support of the UK Department of Trade and Industry (National Measurement System Directorate). © Crown Copyright 2004. Reproduced by permission of the Controller of HMSO. Extracts from this report may be reproduced provided the source is acknowledged and the extract is not taken out of context

References

- [1] R. M. CRAIG, "Accurate Spectral Characterization of Polarization-Dependent Loss" *J of Light. Tech.*, **Vol 21 No 2**, February 2003, pp 432 – 437.
- [2] D. J. IVES, "Calibration of a Polarisation State Analyser for Polarisation Mode Dispersion Measurements", *4th Optical Fibre Measurement Conference Digest, NPL UK*, (October 1997).
- [3] H. G. JERRARD, "Modern description of polarized light: matrix methods", *Optics and Laser Tech.*, Dec 1982, pp 309-319.

Extraction of orthogonal incident state of polarization spectra using Mueller matrix approach

Éric Desfonds^α, Kirill Pimenov^α and Trevor J. Hall^β

^αMetroPhotonics Inc., 1887 St. Joseph Boulevard, Ottawa, Ontario, K1C 7J2, Canada

^βUniversity of Ottawa, 800 King Edward Avenue, Ottawa, Ontario, K1N 6N5, Canada

eric.desfonds@metro Photonics.com

ABSTRACT

Novel algorithms based upon Mueller matrix terms are presented herein. These allow the recovery of the spectra of incident TE and TM orthogonal states of polarization, which yield polarization-dependent frequency shifts and other parameters of interest. This solution involves little computational efforts and has significantly improved the testing capacity and capabilities of the Test and Measurement group of MetroPhotonics Inc.

1. INTRODUCTION

MetroPhotonics Inc. DWDM photonic integrated circuits fabricated using InP involves many design trade-offs. The inherent birefringence of such single-mode planar lightwave circuits (PLC) entails a large sensitivity to the incident state-of-polarization and polarization compensation requires accurate characterization.

While typical measurements techniques, such as polarization-maintaining (PM) fiber use or polarization scrambler, may yield satisfactory results, they require longer test times and typically yield less accurate results. We present a new approach where Mueller matrix terms are used to extract the actual spectrum of the TE and TM incident state of polarization (SoP).

2. STATE OF POLARIZATION SIMULATION

Techniques based upon Mueller matrix terms to extract polarization-dependent loss (PDL) information over large wavelength range have been developed(1). Mueller calculus can be used to further explore a device under test's (DUT's) performance.

For each step of the fabrication process flow the orthogonal TE and TM spectrum are often preferred to the extremes of insertion loss. These allow further exploration of issues by investigating shape factor variations or polarization-dependent frequency (PDF) shifts.

Two analysis approaches were used to extract the TE and TM spectrum. The first is based on the sampling of different incident SoPs, or corresponding Stokes vectors, laid out upon the Poincaré sphere. For each of these, the corresponding spectrum is simulated using Mueller matrix terms.

The second approach exploits the orthogonal nature of the TE and TM modes. Mueller matrix terms are analyzed to find the most orthogonal pair of incident Stokes vectors, from which the spectral response of different incident SoPs could be expressed as linear combinations. Two of these numerical approaches were evaluated. The first looks for the pair of orthogonal incident Stokes vectors which yields the largest normalized difference in spectra. The second examines the whole surface of the Poincaré sphere mapping it to a single system of equations, which is solved by using simple eigenvectors and eigenvalues matrix diagonalization techniques.

3. POINCARÉ SPHERE SAMPLING

Sampling the Poincaré sphere corresponds to changing the incident Stokes vector \vec{S} or SoP while evaluating the resulting spectrum, as seen in Equation 1:

$$T_0 = m_{00}S_0 + m_{01}S_1 + m_{02}S_2 + m_{03}S_3 \quad (1)$$

Keeping $S_0 = 1$, ensures only the DUT insertion loss is evaluated, while keeping the norm of the remaining Stokes vector terms equal to 1 ensures all sampling occurs upon the surface of the Poincaré sphere.

Sufficient sampling can be obtained by the combined action of incident linearly polarized light, the Mueller matrix of a quarter-waveplate, $M_{\frac{\lambda_0}{4}}(\alpha)$, and of a half-waveplate, $M_{\frac{\lambda_0}{2}}(\beta)$ as shown in Equation 2, where α and β represent the angle of the fast axis of the corresponding waveplates.

$$\vec{S} = \begin{bmatrix} S_0 \\ S_1 \\ S_2 \\ S_3 \end{bmatrix} = M_{\frac{\lambda_0}{2}}(\beta) M_{\frac{\lambda_0}{4}}(\alpha) \begin{bmatrix} 1 \\ 1 \\ 0 \\ 0 \end{bmatrix} \quad (2)$$

Figure 1. Coverage of Poincaré sphere

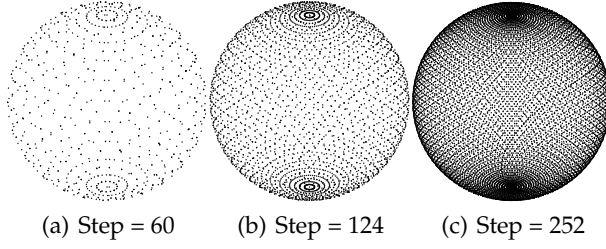
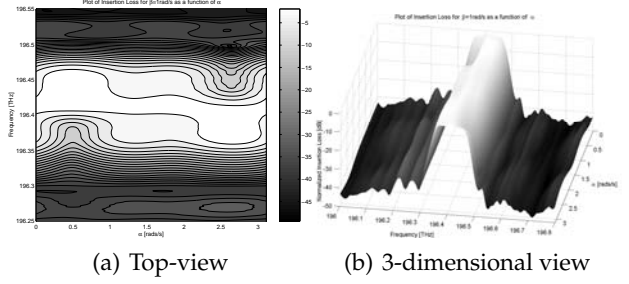


Figure 2. Spectrum for $\beta = 1\text{rad/s}$



which can be expanded to Equation 3:

$$\vec{S} = \begin{bmatrix} 1 \\ \cos^2(2\alpha) \cos(4\beta) + \cos(2\alpha) \sin(2\alpha) \sin(4\beta) \\ \cos^2(2\alpha) \sin(4\beta) - \cos(2\alpha) \sin(2\alpha) \cos(4\beta) \\ -\sin(2\alpha) \end{bmatrix} \quad (3)$$

The T_0 term found in Equation 1 can thus be expressed as a function of the α and β angles, as follows:

$$T_0 = m_{00} + m_{01}S_1(\alpha, \beta) + m_{02}S_2(\alpha, \beta) + m_{03}S_3(\alpha, \beta) \quad (4)$$

The overall variation in spectrum becomes less significant as the number of steps for α and β is increased. A trade-off between simulation-time and accuracy of the end results must be taken into consideration. Figure 1 shows the increase in sampling point density on the Poincaré sphere for different steps.

3.1. State of polarization simulation results

Varying the (α, β) angle pair allows different criterion meant to extract the spectrum corresponding to the TE and TM incident SoPs to be evaluated.

Figure 2 shows the transmission spectra for a polarization-uncompensated DUT, which explains the large variation in insertion loss and centre frequency.

3.2. Extreme centre frequency criterion

Given enough computation time, a large number of spectra can be analyzed for any given parameter. One such parameter is the centre frequency, f_c . Careful design of the polarization compensator aims to minimize any variation of the filter shape and centre frequency for all possible incident SoPs (2). For each

(α, β) angle pair, the f_c of the corresponding simulated spectrum is evaluated and the angle pair yielding extremes of f_c are termed the SoP_1 and SoP_2 spectrum. The subtraction of the two extreme f_c yields the worst-case PDF value.

A DUT having no polarization compensator is expected to have clearly defined extremes of centre frequency. Issues have been noticed when using this criterion with polarization compensated DUTs, yielding ambiguous results in some cases (large PDL or PDF, for example). The resulting pair of Stokes vectors could not be guaranteed to represent orthogonal incident SoPs; a solution based solely on raw measurement data and parameter-independent numerical analysis seemed more appropriate.

4. NUMERICAL SOLUTIONS

As discussed above, new methods aimed at isolating the SoP_1 or SoP_2 incident Stokes vectors were required. This section details those implemented.

4.1. Normalized difference criterion

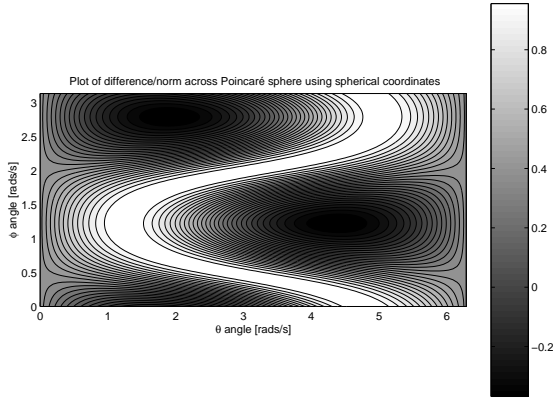
By only sampling half of the Poincaré sphere and comparing opposite orthogonal SoPs, a new criterion focused on comparing the spectrum of the orthogonal incident Stokes vectors SoP_1 and SoP_2 could be evaluated. A normalized difference equation can be used to compare different orthogonal SoPs pairs, with no need for any parameter definition.

Let f_1 be the resulting spectrum for the incident Stokes vector SoP_1 , and f_2 for SoP_2 , defined as follows:

$$\begin{aligned} f_1 &= m_{00}S_0 + (m_{01}S_1 + m_{02}S_2 + m_{03}S_3) \\ f_2 &= m_{00}S_0 - (m_{01}S_1 + m_{02}S_2 + m_{03}S_3) \end{aligned} \quad (5)$$

For each of the (α, β) angle pairs the normalized difference between the f_1 and f_2 functions, is defined as follows:

Figure 3. Mercator projection of normalized difference



$$\xi(\alpha, \beta) = 1 - \frac{\sum_{\lambda} (f_{1(\alpha, \beta)}(\lambda) - f_{2(\alpha, \beta)}(\lambda))^2}{\sqrt{\sum_{\lambda} (f_{1(\alpha, \beta)}^2(\lambda) f_{2(\alpha, \beta)}^2(\lambda))}} \quad (6)$$

For Equation 6, the larger the difference between the f_1 and f_2 spectrum across the desired wavelength range, the smaller the value of ξ . By tracking which sampled (α, β) angle yields the smallest value of ξ , the corresponding incident SoP_1 and SoP_2 Stokes vector pair is isolated as the TE and TM most likely candidate.

Figure 3 shows the resulting projection of the normalized difference parameter (over the whole sphere) for a polarization-uncompensated DUT. An S-shape plateau can be seen, which reaches a value of $\xi = 1$, which corresponds to an equal mix of TE and TM, as expected since linear combinations using the two extreme orthogonal SoPs are expected to appropriately recreate all incident Stokes vectors.

This new criterion and analysis approach offers many advantages, namely parameter definition are entirely avoided, the SoP_1 and SoP_2 incident Stokes vectors are orthogonal by definition and, in consequence, a unique unambiguous solution is found.

4.2. Numerical most orthogonal analysis

The normalized difference criterion still requires thousands of incident Stokes vectors to be sampled which involve large computational efforts. The technique described in (1) uses a quadratic equation to find the extremes of insertion loss on an individual wavelength-basis, which are found to be orthogonal on the Poincaré sphere.

Expanding upon this approach and the normalized difference criterion described in Section 4.1, the most orthogonal numerical analysis approach aims to take into account the whole spectrum to extract the orthogonal spectra for SoP_1 and SoP_2 .

This new analysis approach takes into account all Mueller matrix terms acquired, instead of only the main filter lobe. The same solution as for the normalized difference criterion is obtained, since this new approach is analogous to using an infinitely dense sampling grid upon the Poincaré sphere.

The $m_{00}(\lambda)$ S_0 terms were removed from Equation 5, yielding the following:

$$\begin{aligned} f'_1 &= (m_{01}S_1 + m_{02}S_2 + m_{03}S_3) \\ f'_2 &= -(m_{01}S_1 + m_{02}S_2 + m_{03}S_3) \end{aligned} \quad (7)$$

The vector, $[S_1 \ S_2 \ S_3]$, which maximizes the difference between the $f'_1(\lambda)$ and $f'_2(\lambda)$ equations must be isolated. A simple way to define this optimization problem is to define:

$$\psi = \left(\sum_{\lambda} (f'_1(\lambda) - f'_2(\lambda))^2 \right) \rightarrow \max \quad (8)$$

Since $f'_1(\lambda) \equiv -f'_2(\lambda)$ and using the following notation $M_{ij} \equiv \sum_{\lambda} (m_{0i}(\lambda) m_{0j}(\lambda))$ we can rewrite Equation 8 in a matrix form as follows:

$$\begin{aligned} \psi &= \begin{bmatrix} S_1 \\ S_2 \\ S_3 \end{bmatrix}^T \begin{bmatrix} M_{11} & M_{12} & M_{13} \\ M_{21} & M_{22} & M_{23} \\ M_{31} & M_{32} & M_{33} \end{bmatrix} \begin{bmatrix} S_1 \\ S_2 \\ S_3 \end{bmatrix} \\ &= \vec{S}^T \mathbf{M} \vec{S} \end{aligned} \quad (9)$$

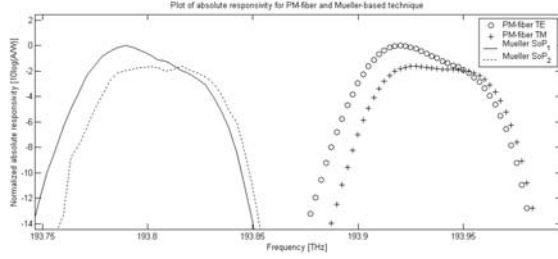
where the \mathbf{M} matrix is a symmetric real matrix, since $M_{ij} = M_{ji}$.

The solution of Equation 8 is given by the normalized eigenvector, X_i , of matrix \mathbf{M} having the largest eigenvalue, μ_i , which can be found using the Jacobi method. To prove this, recall that eigenvectors and eigenvalues of a 3×3 matrix are nontrivial solutions to the equation $\mathbf{M} \vec{X}_i = \mu_i \vec{X}_i$, where $i = 1, 2$ or 3 .

Any Stokes vector can be expanded as $\vec{S} = aX_1 + bX_2 + cX_3$, where $(a^2 + b^2 + c^2) = 1$. This allows us to rewrite Equation 8 as:

$$\begin{aligned} \psi &= \vec{S}^T \mathbf{M} \vec{S} \rightarrow \max \\ &= a^2 \mu_1 + b^2 \mu_2 + c^2 \mu_3 \rightarrow \max \end{aligned} \quad (10)$$

Figure 4. SoP_1 and SoP_2 and TE and TM spectrum



We maximize ψ by only using the eigenvector with the largest eigenvalue, $\max(\mu_1, \mu_2, \mu_3)$. The eigenvector, \vec{S}_i , with the largest eigenvalue, μ_i , maximizes the difference in the orthogonal spectra. The eigenvector, \vec{S}_i , can be assigned to the SoP_1 Stokes vector, while its opposite, $-\vec{S}_i$, can be assigned to the SoP_2 Stokes vector.

This optimization problem is reduced to the diagonalization of a 3 by 3 symmetrical quadratic form. This approach yields a single solution with very little computational efforts. From simulating thousands of incident Stokes vectors on the Poincaré sphere, we now can obtain the same result after only a few simple mathematical operations.

5. STATE OF POLARIZATION-SIMULATION ENGINE CONCLUSIONS

No Mercator-type plots can be created for the most orthogonal numerical analysis approach, as seen in Figure 3. It was found to correlate very well with the normalized difference approach when enough samples were taken upon the surface of the Poincaré sphere. For these reasons and comparison with other available measurement techniques, this analysis technique has become the *de facto* technique for all T&M production-oriented measurements.

Comparison with PM fiber measurements

Direct comparison of PM-fiber measurements is one of the most obvious technique used to compare the TE and TM modes spectra to the ones obtained from Mueller matrix terms. Figure 4 shows absolute responsivity measurement results of one channel of a SurePath MonitorTM obtained from extracted Mueller matrix terms and PM-fiber measurements.

These Mueller matrix based measurements show some residual 60Hz noise found in an early responsivity test station setup. Correlation of passband

widths, absolute responsivity and passband shapes further gave credence to the different criterion used.

Routinely performed measurements continue to confirm the efficiency of this approach, for example, the slope of Pdf as a function of channel number is highly repeatable as it is due to the geometric shape of the polarization compensator (2), as obtained by this technique.

6. CONCLUSIONS AND FUTURE WORK

These analysis tools allowed the extraction of the TE and TM spectra from the DUT Mueller matrix terms and the decommissioning of all production PM-fiber based test stations, yielding highly increased testing capacity, repeatability and accuracy.

Equipment suppliers, such as dBm Optics Inc. are now offering approximation of the Pdf or polarization dependent bandwidth variation obtained by using the "all-states" approach or a four state approach (3). On-going projects include the potential integration of the numerical most orthogonal algorithm in the firmware of different measurement tools.

This novel approach to recover the TE and TM incident SoP spectrum has allowed the Test and Measurement group of MetroPhotonics Inc. to largely increase its testing capacity of the high-channel count SurePathTM portfolio and provide accurate results for internal design activities and for external device calibration of insertion loss and absolute responsivity.

References

- [1] D. Favin, B. M. Nyman, and G. M. Wolter, "System and method for measuring polarization dependent loss," United States of America Patent 5,371,597, December 6, 1994.
- [2] J.-J. He, E. S. Koteles, B. Lamontagne, L. Erickson, A. Delage, and M. Davies, "Integrated polarization compensator for WDM waveguide demultiplexer," *IEEE Photonics Technology Letters*, vol. 1., pp. 224–226, 1999.
- [3] W. Swann, S. Dyer, and R. Craig, "Four-state measurement method for polarization dependent wavelength shift," in *Technical Digest: Symposium on Optical Fiber Measurement*, NIST Special Publication 988. Boulder, Colorado, United States of America: National Institute of Standards and Technology, Sept. 24–26, 2002, pp. 125–128.

Detailed polarization properties comparison for three completely different species of highly birefringent fibers

M. Wegmuller, M. Legré, N. Gisin

GAP-Optique, University of Geneva, Rue de l'Ecole-de-Médecine 20, CH-1211 Genève 4, Switzerland

K.P. Hansen, T.P. Hansen, C. Jakobsen

Crystal Fibre A/S, Blokken 84, DK-3460 Birkerød, Denmark

Abstract: We present a detailed experimental investigation for four different fiber samples: a standard PANDA fiber, two index-guiding nonlinear photonic crystal fibers, and an air-core photonic bandgap fiber. Although all fibers exhibit large birefringence, their polarization properties are found to be quite different. Most surprisingly, the principle states of polarization strongly vary with wavelength for the photonic bandgap fiber, indicating the presence of polarization mode coupling.

I. Introduction

During the last years, the appearance of microstructured or photonic crystal fibers (PCFs) have given a real boost to the field of fiber optics. Their popularity is mainly due to the huge versatility of these fibers that can be tailored for specific applications such as supercontinuum generation, frequency comb generation, or high energy pulse delivery. PCFs can also be made extremely birefringent due to the larger index contrast between silica and air. Beatlengths that are an order of magnitude smaller than what can be achieved in standard PM fibers have been demonstrated [1]. Even if not introduced intentionally, PCFs - especially small core area fibers where the slightest asymmetry already introduces a large difference between the polarization modes - often possess a considerable amount of birefringence [2]. Recently, we also found large birefringence for an air-guiding bandgap fiber.

Large birefringence therefore seems widely spread in single-mode microstructured fibers in general, and it is consequently important to gain a better knowledge of the polarization properties of these fibers. To obtain a more general picture, we also include a standard PM fiber in our analysis.

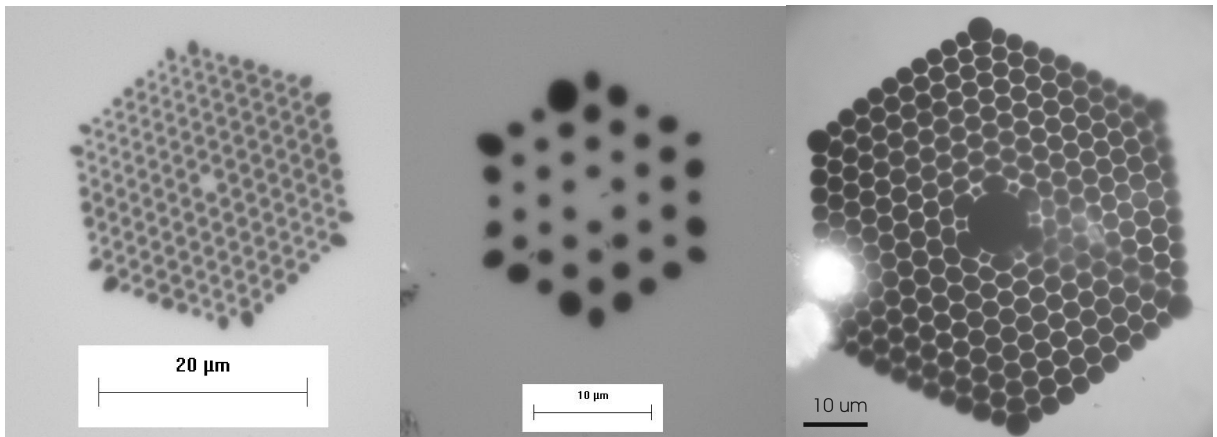


Fig.1: The analyzed microstructured fibers: 2μm core PCF, 3.5μm core PCF, and air-guiding bandgap fiber

II. General characteristics of the fiber samples

The four tested fiber samples are two index guiding PCF (NL-2.0-740, NL-3.5.975), an air-guiding bandgap fiber (AIR-10-1550), all from Crystal Fibre A/S, and a standard Panda fiber from Fujikura (SM.15-P-8/125-UV/UV400 PANDA). The lengths of the characterized samples were 20m (2um core PCF), 5m (3.5um core PCF), 50m (bandgap), and 3m (Panda). Especially for the bandgap fiber, it is important to use not too short a sample as otherwise non-guided and surface modes would still be present at the fiber exit. The bandgap of the 50m long sample analyzed here ranges from 1450 - 1565nm, with a loss below 0.09dB/m. The cross-sections of the three microstructured fibers are shown in Fig.1. The core diameter of the PCF fibers (2 and 3.5um, respectively) are much smaller than those of the bandgap (9.3um) and Panda (8um) fibers. No intentional asymmetry was introduced, so that the birefringence represents today's state-of-the-art production possibilities.

fiber sample	Lb [mm]	β [ps/m]	B [ps/m]	B/ β
Panda	4.2	1.23	1.36	1.1
2um core PCF	8.7	0.60	0.24	0.4
3.5um core PCF	31	0.17	0.21	1.3
bandgap	11	0.47	0.70	1.5

Table 1: beatlength, phase delay $\beta = \lambda / cLb$, group delay, and their ratio, at 1550nm

III. Beatlength and DGD

First, we measured the beatlength to characterize the (phase) birefringence of the fiber samples. This is readily done by using a POFDR method [3], which is ideally suited for the task as it is a non-destructive method with sufficient spatial resolution (0.9mm for a 10m range) to extract the small beatlengths associated with large birefringence. The measurement method is very solid as it has been thoroughly crosschecked [4] by comparison with other measurement methods on several test fiber samples.

The beatlengths at the operating wavelength of the POFDR, 1550nm, are summarized in table 1. As can be seen, all fibers are strongly birefringent with beatlengths below 0.03m (typical SMF fibers have >20m beatlength). As expected for similar asymmetry, the 2um core PCF has a larger birefringence than the 3.5um core PCF. Following the same argumentation, the bandgap fiber, with a large core diameter of 9.3um, seems to possess more asymmetry as it exhibits a similar beatlength than the 2um core PCF. Note also that whereas for the Panda and the PCF fibers, clearly distinctive peaks appear in the spectrum of the backreflected signal power, this is not the case for the bandgap fiber. There, a spectrum similar to those obtained for standard fibers [3] with polarization mode coupling is found. This is surprising for a fiber with large birefringence. However, when looking at the evolution of the output polarization state with wavelength (Fig.2), one indeed finds that the principle states are strongly wavelength dependent. This suggests the presence of polarization mode coupling in the bandgap fiber.

The differential group delay (DGD) of the three fibers was measured using the standard JME method. The corresponding group delays normalized to fiber length are given in table1 for 1550nm, along with the ratio of group to phase delay B/ β . The ratio is close to 1 for the Panda fiber, but amounts to 0.38 and 1.27 for the 2um core and 3.5um core PCF, respectively, and to 1.49 for the bandgap fiber. Differences between phase and group delay are typically found for fibers where form birefringence is more important than stress birefringence [4]. This result

therefore suggests that the microstructured fibers possess little asymmetric stress. It is also interesting to see that although the phase delays for the two PCFs are quite different, their group delays $B \equiv |\partial\beta_{rad}/\partial\omega| = |\beta - \lambda\partial\beta/\partial\lambda|$ are almost equal.

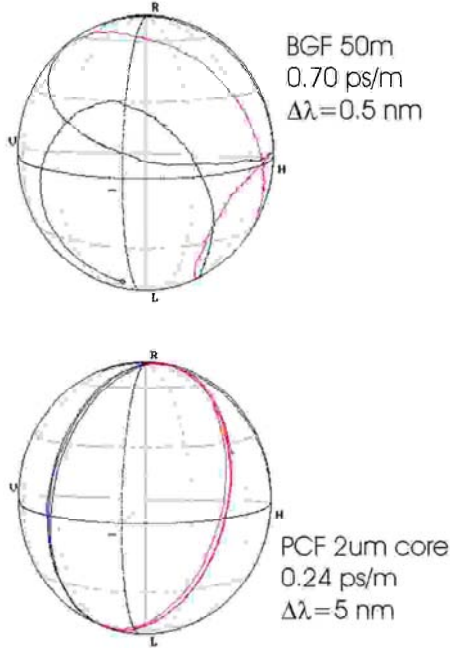


Fig.2: evolution of the output polarization state with wavelength for the bandgap (top) and 2μm core PCF (bottom)

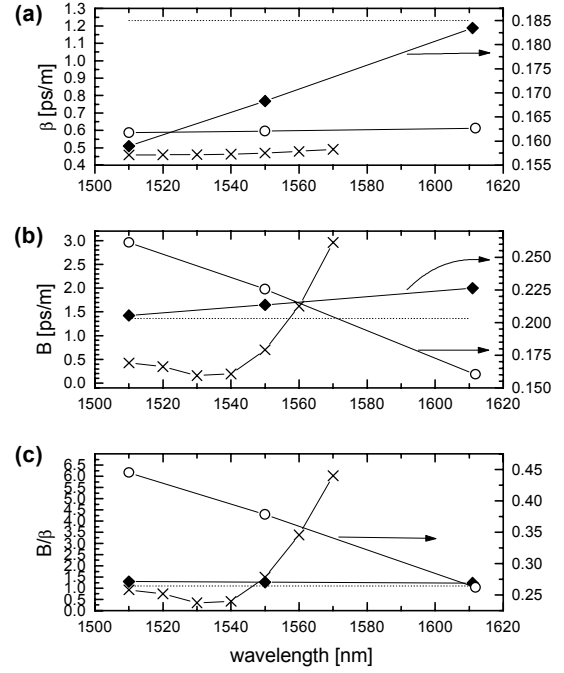


Fig.3: phase delay (a), group delay (b), and their ratio (c) for the 4 fiber samples. dotted: Panda, circles: PCF 2μm, diamonds: PCF 3.5μm, crosses: bandgap

With the JME method, one conveniently obtains the DGD as a function of wavelength. Whereas DGD is essentially not wavelength dependent in a Panda fiber, it is found to strongly vary for the three microstructured fibers. As shown in Fig.3b, although the two PCFs have a similar DGD at 1550nm, one decreases with wavelength whereas the other one increases. For the bandgap fiber, an even more exotic behavior is found. As the figure shows, the DGD slowly decreases to a minimum of 0.04ps/m at 1535nm, and then strongly increases while approaching the upper band-edge located at ~1595nm. The DGD curve was found to be very reproducible even after long time periods (2 months), and we believe that detailed numerical modeling is required to explain this result.

With the DGD strongly varying for both PCFs and bandgap fiber, it is of interest to look at the wavelength dependence of the phase delay as well, and to check whether the B/β ratio varies. As the POFDR at hand works at 1550 nm only, another way of beatlength extraction has to be used. We infer the total phase delay at a given wavelength from the one at 1550nm (obtained from the beatlength measurement) and the measured relative dephasing between the two wavelengths [2]. The corresponding results are given in Fig.3a, along with the B/β ratios (Fig.3c). As can be seen, the phase delay increases with wavelength for all fibers with exception of the Panda fiber where it is essentially constant. For PCF, other experiments and numerical predictions qualitatively agree with our findings. In all microstructured fibers, the phase to group delay ratio is found to vary with wavelength (especially for the bandgap fiber), and can be very different from 1. Consequently, both phase and group birefringence should be carefully measured in these fibers.

fiber sample	K_T [rad/K/m]	K_T/β_{rad} [1/K]	K_τ [fs/K/m]	K_τ/B [1/K]
Panda	-2.06	$-1370 \cdot 10^{-6}$	-1.78	$-1310 \cdot 10^{-6}$
2um core PCF	0.012	$17 \cdot 10^{-6}$	0.03	$117 \cdot 10^{-6}$
bandgap	-0.007	$-12 \cdot 10^{-6}$	-0.1	$-266 \cdot 10^{-6}$

Table 2: temperature sensitivities of the phase and the group delay at 1550nm (1517nm for bandgap). Note that the sign of K_T is not measured, but simply chosen equal the (measured) sign of K_τ

IV. Temperature dependence

Besides the polarization properties themselves, it is also of interest to investigate their dependence on external perturbations such as temperature or stress. The microstructured fibers, made from one solid material only, should be much less sensitive (i.e. more robust) to temperature changes than standard PM fibers due to the absence of the stress contribution. Microstructured fibers are therefore good candidates for (temperature independent) polarimetric pressure sensors [5].

We investigated the temperature dependence of the phase and group delay by putting the fiber into a temperature controlled water bath. The corresponding results are summarized in table2, where we use the common description of $K_T \equiv \partial\beta_{rad}/\partial T$ for the phase change with temperature and $K_\tau \equiv \partial B/\partial T$ for the temperature sensitivity of the DGD. The 3.5um core PCF was not analyzed as due to its lower birefringence and short length, the temperature sensitivities are expected to be too low to be measurable. The results in table2 demonstrate that the PCF and bandgap fiber are indeed much less temperature dependent than the Panda fiber. Even when normalized with the overall phase difference β_{rad} to account for the differences in phase birefringence among the samples, K_T is about 100 times smaller in the microstructured fibers with respect to the Panda. A similar but less pronounced difference is found for the temperature sensitivity of the group delay, K_τ . Note also that the DGD decreases with temperature for the Panda and bandgap fibers, whereas it grows for the 2 um core PCF.

V. Conclusions

We have measured the wavelength and temperature dependence of the phase and group delays for four highly birefringent fiber samples, including PCFs and an air-guiding photonic bandgap fiber. All microstructured fibers showed a qualitatively different polarization behavior than a standard Panda fiber. Ratios of group to phase delays that are both strongly wavelength dependent and different from 1 are found, along with a good temperature stability.

Acknowledgments: We would like to thank the Swiss OFES (COST P11) and EXFO Inc., Quebec, for financial support.

References

- [1] A.Ortigosa-Blanch et al, Highly birefringent photonic crystal fibers, *Opt. Lett.* **25** (18) 1325-1327, 2000
- [2] M.Wegmuller et al, Experimental investigation of wavelength and temperature dependence of phase and group birefringence in photonic crystal fibers, *accepted for ICTON/ESPC 2004*, July 4-8, Wroclaw, Poland, 2004
- [3] M.Wegmuller et al, Distributed beatlength measurement in single-mode fibers with Optical Frequency-Domain Reflectometry, *J. Lightwave Tech.* **20** 828-835, 2002
- [4] M.Legré et al, Investigation of the ratio between phase and group birefringence in optical single-mode fibers, *J. Lightwave Tech.* **21** 3374-3378, 2003
- [5] T.Nasilowski et al, Birefringent photonic crystal fiber as a multi-parameter sensor, *Symp. IEEE/LEOS Benelux Chapter, Enschede, Netherlands*, 29-32, 2003

Determination of the Phase and Group Birefringence of Single-Mode Optical Fibers based on the Twist

Matthieu Legré, Mark Wegmuller, Nicolas Gisin

Group of Applied Physics, University of Geneva,
20 rue de l'Ecole-de- Medecine, CH-1205 Genève, Switzerland.

Abstract: A novel method for the measurement of the phase and group birefringence is described. The method is based on the evolution of the differential group delay as function of the twist applied on the fiber. It gives the birefringence values for zero twist for fibers within the beatlength range of 5mm-1m. The technique is very simple and found advantageous for the study of special fibers like PCF.

I. INTRODUCTION

In the small length regime (no polarization coupling), the polarization properties of single-mode optical fibers are completely defined by the phase and group birefringences, whereas for long fibers, the description has to be completed by introduction of a coupling length parameter. In the following, we will focus on short fibers only, where arbitrary polarization modes coupling is negligible.

Generally, the phase birefringence ($\delta\beta$) is represented by the beatlength ($L_b=2\pi/\delta\beta$), which is the length interval over which the polarization describes a full circle on the Poincaré sphere. The group birefringence ($d(\delta\beta)/d\omega=\delta\beta'$) is characterized by the DGD (differential group delay). It is frequently assume, that there is a simple relation between the phase and group birefringence:

$$DGD = \frac{\lambda}{c \cdot L_b} \quad (1)$$

DGD is expressed in s/m, λ is the center wavelength of the spectrum, and c is the light velocity in vacuum.

For standard telecom fibers, relation (1) holds well. But it has been shown in [1] that this is not the case for other fibers. Ratios between group birefringence and the phase delay ($\delta\beta'/\omega$) found in the literature or measured by us cover a range from 0.3 to 3. The ratio is close to 1 for fibers with birefringence due to stress (like panda fibers), whereas it can take different values (depending of the wavelength) for fibers with birefringence due to geometry.

Recent fibers like PCF (photonic crystal fiber), bandgap fibers, or even heavily doped erbium fibers, are generally birefringent because of geometrical defects during the manufacturing. As a consequence, it is important to have tools that allow to measure the phase *and* group birefringence. Moreover, as it has been demonstrated in [2], a residual twist can, for certain measurement techniques, falsify the extracted beatlength. Our method is able to determine the intrinsic phase and group birefringences, i.e. the birefringence when the fiber is not subjected to twist.

II. BASIC IDEA AND PRINCIPLE OF OPERATION

It is well known that twisting a fiber induces circular birefringence on it [3]. Then its polarization properties change, leading to elliptical or even circular principal states for the case of very large twist. Because of the induced polarization mode coupling and additional circular birefringence, both phase and group delays change with the twist rate. Siddiqui *et al.* have shown in [4] that the DGD varies with the twist rate as:

$$DGD = \frac{\delta\beta_l \cdot \delta\beta'_l + (g\gamma - 2\gamma) \cdot g'\gamma}{\sqrt{\delta\beta_l^2 + (g\gamma - 2\gamma)^2}} \quad (2)$$

with $\delta\beta_l$ the linear intrinsic phase birefringence of the fiber (i.e. the phase birefringence for zero twist), $\delta\beta'_l$ the linear intrinsic group birefringence (DGD for zero twist), γ the twist rate (in turns/m), g the elasto-optic coefficient (the circular birefringence induced by twisting equals $g\gamma$), and $g' = dg/d\omega$. The idea of our technique is to measure the DGD for different twist rate and to fit the data with equation (2) to determine the parameters $\delta\beta_l$ and $\delta\beta'_l$.

The implementation of the measurement is very simple (see figure 1). We have to be able to measure the DGD of the FUT (fiber under test) and to induce a regular twist on the fiber. We will see later that the precision and the sensitivity of the DGD measurement device is important for the quality of the beatlength extraction but also for the range of beatlengths we can determine with it. To allow the rotation of the left connector in the adapter, its key has been removed. The first part of the measurement consists in measuring the DGD of the FUT at a fixed wavelength for different values of the twist rate. Once the data have been collected, we fit them with equation (2). Notice that no special conditions have been imposed on the fit parameters except that g has to be close to the range 0.14-0.16 because there are the typical values that have been measured for silica optical fibers. However, in order for the fitting algorithm to work properly, reasonable initial values have to be chosen.

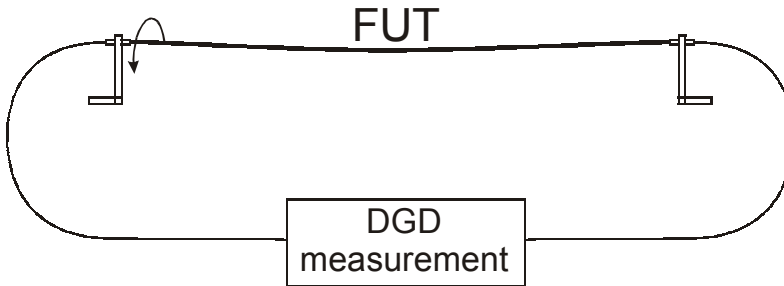


Figure 1: Diagram of the set-up. A connector key has been removed to allow the rotation of the fiber under test.

III. RESULTS AND EVALUTATION OF THE METHOD

In order to evaluate the performance of the measurement technique, we have tested it on several different fibers. The eight fibers we have studied are numbered for easy identification and their characteristics are summarized in table 1. Fibers 1 and 2 have elliptical core, fiber 3 is a panda fiber, fiber 4 has elliptical cladding, fibers 5 and 6 are erbium doped fiber samples with quite large asymmetries, and fibers 7 and 8 are PCFs with hexagonal hole symmetry (hole diameter: 0.9 and 0.8 μm , core diameter: 3.5 and 2.0 μm , respectively).

#	remarks	a (μm)	b (μm)	Δ	measured Lb (mm)			δ (%)
					twist	P-OFDR	pressure	
1	e-core	1.65	1.43	0.05	559	596	570	4.1
2	e-core	7.51	2.4	0.008	54	57	55	3.4
3	panda	4.1	4.06	0.005		3.96		
4	e-cladding	140*	70*	-	8.4	8.1		3.5
5	e-core, Er doped	2	1.82	0.02	524	537		2.4
6	e-core, Er doped	2.16	1.69	0.02	162	166		2.4
7	PCF	1.8	-	-	30	30.7		1.2
8	PCF	1	-	-	7.9	8.5		7.3

Table 1: Results of beatlength measurements for the eight investigated fibers, using the ‘twist’ method presented here, and two alternative methods (‘P-OFDR’[5], ‘pressure’[6]). δ gives the relative deviation of our method from the mean beatlength found with the alternative methods. a , b : major and minor axis (radius) of the core or cladding. Δ : refractive index difference.

Figure 2 shows the results obtained for fiber 1. The DGD changes strongly with the twist rate for small twists, whereas the evolution is slower for larger twist rates. To be more precise, the fiber is turned by one turn (or even less) between two data points for small twist rates, whereas it is turned by 20 turns or more in the wings to speed up the measurement. Our DGD measurement apparatus is based on Jones Matrix Eigenanalysis (JME). The minimum DGD value measurable with our JME device is $\sim 5\text{fs}$. Therefore all data points corresponding to a global DGD under 7fs have been removed from the curve to not falsify the fit. Also, from equation (2) it can be seen that for large twist values the linear phase birefringence ($\delta\beta_i$) has only a small influence on the DGD. Consequently, it is better to only fit the central peak, giving the solid line in figure 2. As we can see, this fit corresponds very well to the measured data even in the wings (thin line in figure 2). From the fitting parameters, an intrinsic (i.e. twistless) beatlength of 559mm is obtained for this fiber.

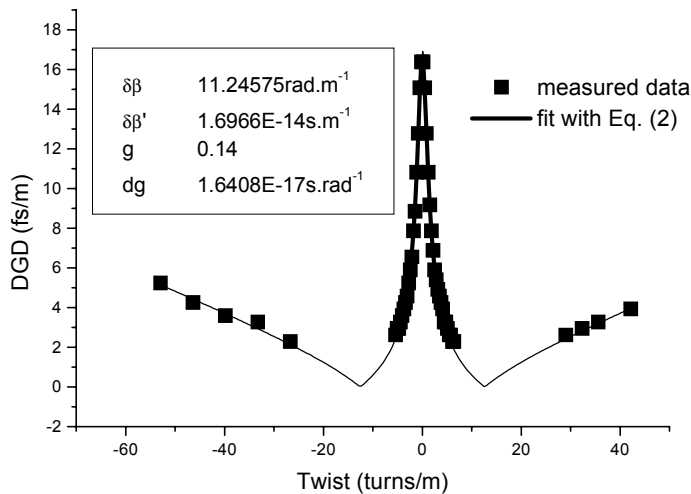


Figure 2: Experimental results for fiber 1. Square points: measured DGD as a function of the twist rate. Line: fit of the central peak with Eq 2. The fit parameters $\delta\beta$ and $\delta\beta'$ are the phase and group birefringence of the fiber in the absence of twist.

The precision of our technique depends essentially on the quality of the DGD measurement. We have verified that the reproducibility of the measurement is good. Changing the twist back to a value slightly above zero – where the DGD values are large and change strongly as a function of twist - typically results in deviations of the measured overall delay of about a femtosecond or less, and consequently one finds the same fit values. Moreover, we have to pay attention to the additional DGD coming from the lead fibers in figure 1. In our experiment,

their total length is around 6m, corresponding to an additional *DGD* of ~ 2 fs. With simulations we have estimated that it introduces an error on our measured values of 4% in the case of fiber 1 (which is the worst studied case because the total *DGD* of the fiber sample is the smallest) and $< 2\%$ for all other fibers. The error would of course be larger for total *DGD* values of the FUT closer to the *DGD* of the lead fibers.

However, we can not measure all fibers with this technique. The maximum measurable beatlength is determined by the minimal “twistless” *DGD* we can work with (the sensitivity of our JME device is ~ 5 fs then we need a “twistless” *DGD* value over 20fs to measure enough data points for the fit) and by a “reasonable” length of sample (because of stability reasons, *DGD* measurement is precise for maximum length of ~ 4 -5m). Those values limit the maximum measured beatlength to 1m. The minimum beatlength measurable is fixed by the maximum twist rate supported by fibers (typ. ~ 70 -80 tr/m). This value gives a minimum for the beatlength of ~ 5 mm.

For further verification, we have compared our technique with two standard methods for L_b extraction. The first one is a coherent, polarization-sensitive reflection measurement (P-OFDR), described in detail in [5]. As can be seen from table 1, the results of the P-OFDR and the “twist” method typically agree to within 3.5% for the fibers analyzed (except for fiber 8). The error for fiber 8 is larger because we have used a long sample (20m) compared to the others (~ 4 m) -so the quality of *DGD* measurement is worse-, and the measured beatlength is smaller, leading to larger relative errors. The second method works in transmission and consists of analyzing the power through crossed polarizers as a function of the distance at which coupling between the two polarization modes is introduced by pressing on the fiber [6]. We again obtained a beatlength agreeing reasonably with the previously obtained values (see table 1).

IV. CONCLUSIONS

We have presented a novel method for determination of phase and group birefringence. The two main advantages are first its simple implementation (we just measure *DGD*), and that it provides the extraction of intrinsic (“twistless”) birefringence parameters (remember that residual twist changes the measured values of phase and group birefringence). The ‘twist’-method works in a precise and reproducible way for fibers with beatlengths of 5mm-1m.

Acknowledgements: Financial support from EXFO Inc (Vanier, Canada) are acknowledged.

References

- 1- “Investigation of the ratio between phase and group birefringence in optical single-mode fibers”, M. Legre, M. Wegmuller, and N. Gisin, *J. Lightwave Tech.*, **21**, pp. 3374-3378 (2003)
- 2- “Circular birefringence in optical fibers: influence on local beatlength extraction from reflectometric fixed analyzer data”, M. Wegmuller, M. Legre, and N. Gisin, OFMC01 Cambridge, 131 (2001)
- 3- “Polarization optics of twisted single-mode fibers”, R. Ulrich and A. Simon, *Appl. Opt.*, **18**, pp. 2241-2251 (1979)
- 4- “Theoretical analysis and measurement of effects of fiber twist on polarization mode dispersion of optical fibers”, R. E. Schuh, E. S. R. Sikora, N. G. Walker, A. S. Siddiqui, L. M. Gleeson and D. H. O. Bebbington, *Electron. Lett.*, **31**, pp. 1772-1773 (1995)
- 5- “Local birefringence measurements in single-mode fibers with coherent optical frequency-domain reflectometry”, B. Huttner, J. Reecht, N. Gisin, R. Passy, and J. P. Von der Weid, *IEEE Photon. Technol. Lett.*, **10**, pp. 1458-1460 (1998)
- 6- “Precision measurement of modal birefringence of highly birefringent fibres by periodic lateral force”, K. Takada, J. Noda, and R. Ulrich, *Appl. Opt.*, **24**, pp. 4387-4391 (1985).

An Improved Lyot Fibre Depolariser

M. Matar¹, I.M. Bassett¹, B. Gordon², J.H. Haywood¹, A. Michie¹

¹Australian Photonics CRC, Optical Fibre Technology Centre
University of Sydney, NSW, Australia

Tel: +61 02 9351 1985, Fax: +61 02 9351 1911

m.matar@oftc.usyd.edu.au

²Cochlear Ltd 14 Mars Rd Lane Cove, NSW, Australia

Abstract: An improved fibre Lyot depolariser is proposed and demonstrated. The improvement results from adding a third section to the standard 2-section Lyot. Experimental work to compare the performance of a 2-section Lyot and a 3-section Lyot depolariser is also presented. Residual degree of polarisation is found to be as low as 0.09% (-30.5dB).

Introduction: Depolarised light is essential for many applications, especially those that involve the detection of small variations of light. This is because the state of polarisation in most fibres and fibre optic components is influenced by birefringence resulting from random vibrations and environmental temperature fluctuations. The polarisation fluctuations may be translated into intensity fluctuations, which then becomes noise in the detected signal. Depolarised light is unaffected by these random fluctuations, except in the presence of polarisation dependent loss (PDL), and thus is useful in maintaining low noise levels.

There are many methods that have been developed to produce depolarised light in an optical fibre context [1] [2] [3]; the most common method is the use of the fibre Lyot depolariser. This method works by causing the polarisation state to vary rapidly with wavelength. At any precise wavelength, the light is perfectly polarised, however on average over a sufficient range of wavelengths the output light appears unpolarised. A standard fibre Lyot depolariser consists of two highly linearly birefringent (hi-bi) fibre sections, with a length ratio of 2:1 with their principal axes aligned at 45° with respect to each other. The choice of a 45° angle between the first (L_0) and second (L_1) section is to allow the input light to have any state of polarisation [4] (any at all, not just linear, and also any degree of polarisation).

Many mathematical analyses have been developed to predict the performance of the fibre Lyot depolariser [4] [5] [6]. These analyses involve making many approximations, often neglecting the effect of angle misalignment between the sections. It is nearly impossible to manufacture a depolariser such that the first (L_0) and second (L_1) sections are aligned at exactly 45°. If L_1 is slightly misaligned, it will result in a residual polarisation. However, a small misalignment can be remedied by adding a third section (L_2) that is aligned at approximately $\pm 45^\circ$ with the L_1 . In other words a 3-section Lyot depolariser is built by splicing two sections, L_0 and L_1 at 45°, and a third section L_2 spliced at $\pm 45^\circ$ to L_1 , with the length ratio of 4:2:1. The function of the third section is to correct for small misalignment of the splices. If the first two sections do not achieve depolarisation, it will be achieved by the third.

Experiment & Results: The experimental set-up, shown in Fig. 1, was used to directly compare the residual degree of polarisation of a 2-section depolariser and a 3-section Lyot depolariser. The light source is an ASE source, which has a peak power at 1530nm and FWHM= 6nm; its spectrum is shown in Fig. 2. A commercial polarisation maintaining (PM) fibre was used for the fabrication of the depolarisers. A cut-off wavelength of $\lambda_c=1360\text{nm}$ and the beat length of $L_b= 3.2\text{mm}$ at 1550nm were measured for this particular fibre.

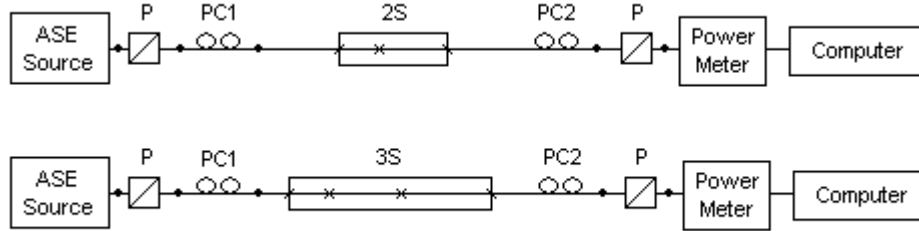


Fig. 1 *Experimental set-up for comparing the performance of a 2-section (2S) and a 3-section (3S) Lyot depolariser.*

Components: P: polariser; 2S: 2-section Lyot depolariser; 3S: 3-section Lyot depolariser; PC1: polarisation controller; PC2 polarisation controller 2

Splices and connectors:

- × 45° PM splice
- ✓ Singlemode to PM splice
- ∖ PM to singlemode splice
- Standard singlemode connector or splice

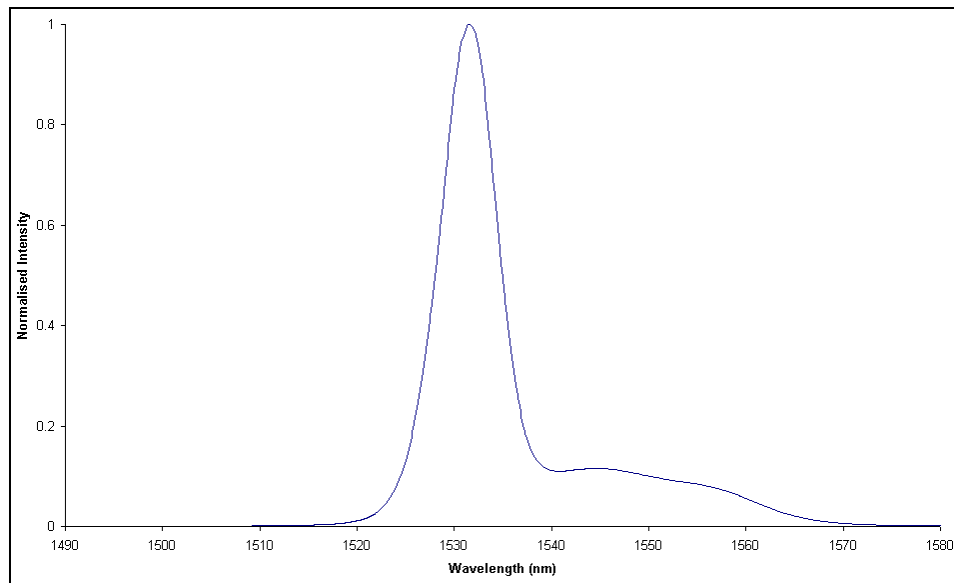


Fig. 2 *Measured ASE spectrum.*

For the fabrication of the 2-section and 3-section Lyot depolariser, L_0 has to be much longer than the beat length of the fibre. The broader and smoother the source

spectrum, the shorter L_0 needs to be. As we know the source spectrum, $G(k)$, the accuracy attainable as a function of L_0 can be calculated for perfect 45° alignment for a 1-section Lyot depolariser [5]

$$DOP = \frac{\left| \int dk |G(k)|^2 e^{i\mu k} \right|}{\int dk |G(k)|^2} \quad (1)$$

Where μ is equal to the free space wavelength, λ_m , multiplied by the number of beat lengths in L_0 .

$$\mu = \frac{\lambda_m L_0}{L_b} \quad (2)$$

It is clear from Fig. 3, for the residual degree of polarisation to be small, L_0 needs to be greater than about 2.2m. The lengths of L_0 , L_1 , and L_2 were taken as 2.5m, 5m, and 10m, respectively. It is also clear from Fig. 3 that the simulated result using (1) agrees with the experimental results. The small discrepancy is due to the input polarisation not being perfectly 45° to X-axis of L_0 . This illustrates the difficulty of angular alignment.

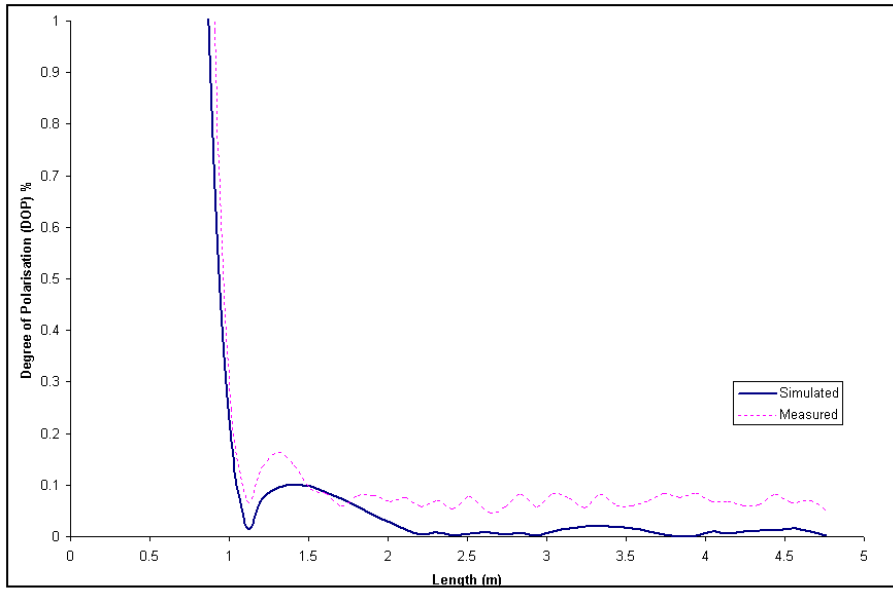


Fig. 3 *Residual degree of polarisation with respect to length for a 1-section Lyot Depolariser.*

Light from the ASE source is launched into a polariser. This is done so that the input signal used is fully polarised. The input polarisation state was arbitrarily selected by adjusting the polarisation controller 1. The polarisation controller 2 was scanned through all possible polarisation states in order to determine the upper and lower intensity values. Measurements were taken and recorded by a desktop computer. DOP was calculated from [4]

$$DOP = \frac{I_{\max} - I_{\min}}{I_{\max} + I_{\min}} \quad (3)$$

Where I_{\max} and I_{\min} are the upper and lower intensity values for all possible states of polarisation at the output.

Table 1. shows the residual degree of polarisation for a 2-section and 3-section Lyot depolariser. It was found that a 3-section is less sensitive to the input polarisation angle compared to a 2-section Lyot depolariser. A residual DOP better than 0.61% could be achieved at the output when the input polarisation is launched parallel to the X-axis of L_0 (0° worst case scenario).

Input Polarisation Angle	Residual Degree of Polarisation (%)	
	2-section	3-section
0° (worst Case)	3.6	0.61
45° (Best Case)	0.15	0.09

Table 1. Results of the Comparison between 2-section and 3-section Lyot depolariser

Conclusion: In summary, an improved Lyot depolariser has been proposed and demonstrated. The experiments show that a 3-section outperformed the 2-section Lyot depolariser. The reduction of the sensitivity to the input polarisation was also examined experimentally. The advantages are: (i) The device is less sensitive to input polarisation (ii) Less sensitive to angle misalignment (iii) Low DOP (iv) Reduction in the costs of production by reducing the required degree of precision in construction.

References

- [1] Shen, B.P and Lin, C.: ‘ Passive fibre depolariser based on incoherent cascaded fibre-rings’, Electron. Lett., 1998, Vol. 34, No. 18, pp.1777- 1778
- [2] Takada, K., Okamoto, K and Noda, J.: ‘ New Fiber-Optic Depolarizer’, J. Lightwave Technol., 1986, Vol. LT-4, No. 2, pp. 213-219.
- [3] Noe, R., Rehage, M., Harizi, C. and Ricken, R.: ‘ Depolariser based on acousto-optical TE-TM converters for suppression of polarisation holeburning in long haul EDFA links’, Electron. Lett., 1994, Vol. 30, No. 18, pp.1500- 1501
- [4] Bohm, K., Petermann, K. and Weidel, E.: ‘ Performance of Lyot Depolarizers with Birefringent Single-Mode Fibers’, J. Lightwave Technol., Mar 1983, Vol. LT -1, No. 1, pp. 71-74.
- [5] Burns, W.K.: ‘ Degree of Polarisation in the Lyot Depolariser’, J. Lightwave Technol., Sept 1983, Vol. LT -1, No. 3, pp. 475-478.
- [6] Takada, K., Chida, L., Noda, J.: ‘ New Diagrammatical method for calculation of fiber-optic Lyot Depolarizer performance’, J. Opt. Soc. Amer., 1988, Vol.5, No. 11, pp. 1905-1917.
- [7] Born, M. and Wolf E.: ‘ Principles of Optics’, 6th Edition, Pergaman Press, 1980, pp. 30-36.

Measurement issues in Microwave Photonics

José Capmany, Daniel Pastor, Beatriz Ortega and Salvador Sales

Optical Communications Group

IMCO2 Research Institute

Universidad Politécnica de Valencia

jcapmany@com.upv.es

Abstract

Microwave Photonics is a recent field of application where optical technologies can be used advantageously to solve limitations encountered in the transmission and processing of radiofrequency signals. Measurement techniques are needed to evaluate the quality of Microwave Photonic devices, subsystems and systems in order to assess their performance. This paper presents and reviews some of the most important approaches developed for different applications in this field.

1) Introduction

The exploitation of the unique properties that photonic devices and systems bring to the generation, transport, processing and detection of microwave and millimeter wave signals has been a subject of constant active research over the last 25 years and has crystallized in the new discipline known as Microwave Photonics [1].

Microwave Photonics has found a wide range applications including:

- a) Optical Processing of Microwave and millimetre wave signals [2]
- b) Radio over fiber transmission and antenna remoting/beamforming systems [3-6]
- c) Millimetre wave generation [1]

While others are currently on the line of sight, such as label extraction in subcarrier multiplexed optical label swapping networks. In any of the former applications devices, subsystems and systems are required to meet particular performance criteria and therefore measurement techniques and systems are essential and have been developed to carry out these tasks.

The purpose of this paper is twofold. On one hand it pursues to give the reader specialised in measurement systems and techniques an introduction to the performance criteria required in each of the main Microwave Photonic application fields and in other hand it aims to provide a summary and review of the main measurement techniques employed for measuring these parameters. Since b), and c) have similar requirements we shall address them jointly.

2) Measurement techniques and parameters for Photonic signal processing of microwave signals

This approach involves the use of photonics technology and especially fiber and integrated photonic devices and circuits to perform signal processing tasks of microwave signals conveyed by an optical carrier directly in the optical domain. This approach is shown in the upper part of figure 1. The RF to optical conversion is achieved by direct (or externally) modulating a laser. The RF signal is the conveyed by an optical carrier and the composite signal is fed to a photonic circuit that samples the signal in the time domain,, weights the samples and combines them using optical delay lines and other photonic elements. At the output/s the resulting signal/s are optical to RF converted by means of an/various optical receiver/s. Depending on whether the delays are longer or shorter than the optical coherence length one deals with incoherent or coherent filters .A rich variety of configurations either in finite or infinite (recirculating) impulse response configuration have been proposed and experimentally demonstrated [2]. In any case, the filter performance is given by a series of parameters such as: Resonance bandwidth (Q factor), free spectral range, main resonance to secondary sidelobe ratio, in-band group delay, insertion losses and noise figure.

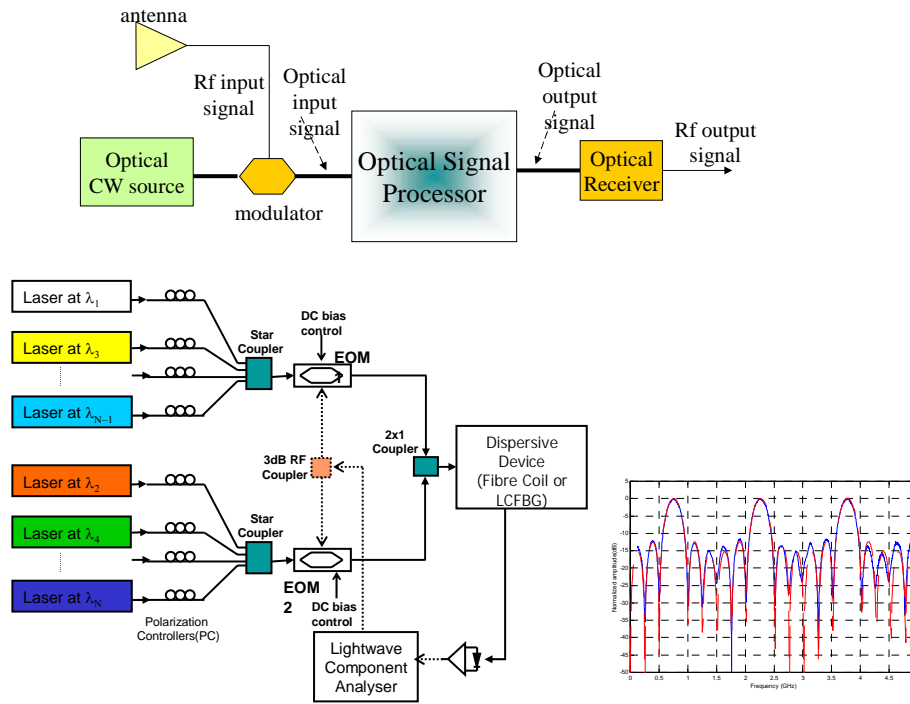


Figure 1

The definition of the above parameter is similar to that of typical microwave filters. The most suitable characterization of the filter is obtained by measuring its vectorial radiofrequency transfer function. This is obtained by a Lightwave Component Analyser (LCA) formed by the combination of a vectorial RF analyser with an/or various optical transmitter/s and a broadband optical receiver. The LCA operates using the small signal concept, i.e an RF tone with small amplitude compared to the applied electric bias signal modulates the optical transmitter and propagates through the filter. The RF signal is recovered after the photodetector and its amplitude and phase is compared to that of the modulating tone. The frequency of the modulation signal is

swept across the spectrum of interest. The measurement yields the filter transfer function from which most of the above parameters can be obtained. . A prior calibration of the RF connections between the vectorial analyser and the optical transmitter/receiver is required in order to subtract its effect on the overall response. The lower part of figure 1 shows for instance the measurement setup for an incoherent Microwave signal processor composed of a modulated array of lasers follower by a dispersive fiber which acts as a wavelength selective delay line. The laser wavelengths are adjusted so the incremental delay suffered by each lightwave carrier is constant.

There are important differences if coherent or incoherent filters are to be measured. While the second are very robust to environmental conditions, the former have to be measured in a completely controlled environment free from mechanical and temperature variations. Polarization has to be controlled in both cases. Other degrading effects such as noise figure and phase to amplitude noise conversion can also be measured. For further information the reader is referred to [2] and the references therein.

3) Measurement techniques and parameters for Radio over fiber systems

Radio over fiber (RoF) systems have multiple applications such as the distribution of CATV signals, antenna remoting and cellular/mobile communication systems and antenna beamforming for phased-arrays.

A RoF link comprises all the hardware elements needed to modulate a RF signal onto an optical carrier, the optical transmission medium and the hardware required to recover the RF subcarrier from the optical carrier [3]. Figure 2 shows the layout of a typical RoF system.

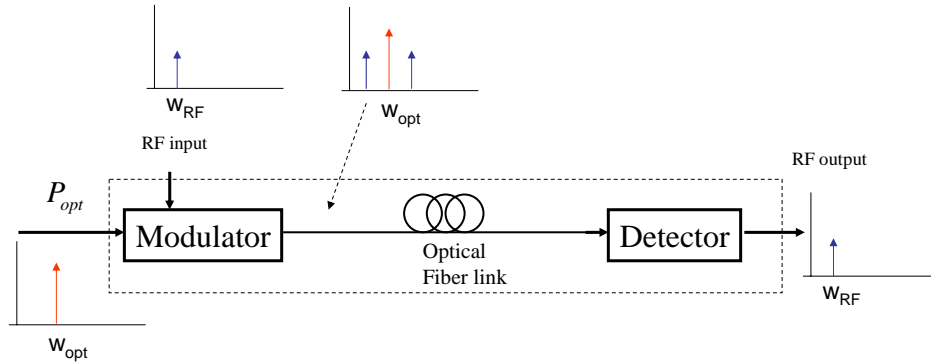


Figure 2

The main parameters which characterize a RoF system and which need to be measured are the link gain, the noise figure and the dynamic range. Also, the possible impact of the fiber link chromatic distortion needs to be measured in certain cases. The link gain is defined as the quotient between the output RF power from the link and the input RF

power injected to the link. In general, if S_{MD} and S_D represent the slope efficiencies of the source to fiber and photodetector (in W/A and A/W) respectively and Z_{MD} , Z_D their impedances, then the link gain is given by:

$$g = S_{MD}^2 S_D^2 \frac{Z_D}{Z_{MD}} \quad (1)$$

Particular expressions of the above can be specialised for direct and externally modulated links. The link gain is usually in between -40 and 10 dB. One straightforward procedure to measure the link gain is using the lightwave component analyser configuration described in the prior section. Using the calibration procedure that was indicated will yield the direct value of the link gain from the measured trace. The upper part of figure 3 illustrates the setup.

The Noise Figure (NF) is defined as:

$$NF = 10 \log \left[\frac{\bar{N}_{out}}{gKT} \right] \quad (2)$$

Where \bar{N}_{out} stands for the total noise spectral density at the link output, k is the Boltzman constant and $T=290^\circ\text{K}$. NF has little relevance in CATV applications but it is critical for instance in antenna remoting applications. Once the link gain is known or measured, the obtention of NF requires the measurement of the noise spectral density at the output of the system. This can again be done in a straightforward way by placing an RF spectrum analyser at the receiver output, measuring the noise power over a bandwidth region and then dividing by the bandwidth expressed in Hz (lower part of figure 3). In general noise figures of un-amplified optical links range from 24 to 50 dB.

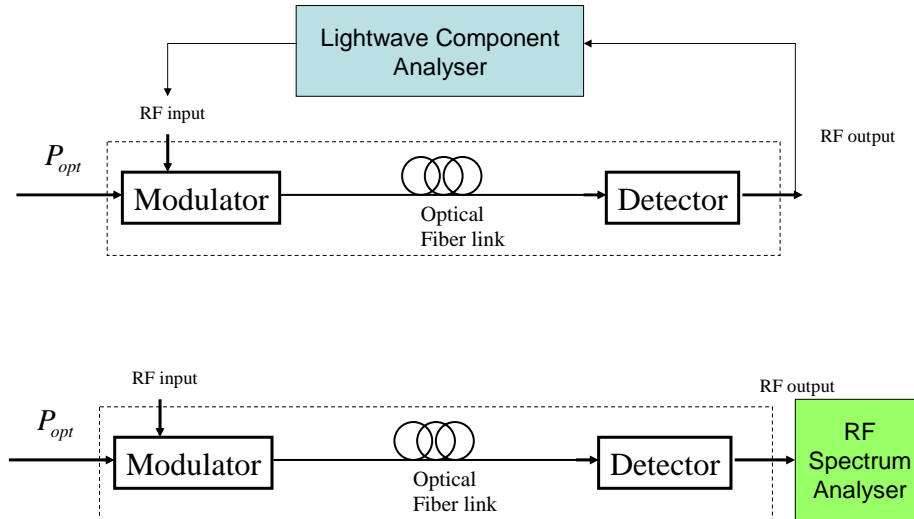


Figure 3

The link dynamic range, also known as intermodulation free or IM-free Dynamic range or simply DR is also a very important parameter, especially for RoF systems where multiple Rf frequencies are simultaneously present and also for millimetre wave generation techniques based in nonlinear effects in optical and optoelectronic devices. In CATV industry for instance the effect of intermodulation is specified and measured through the Composite Triple Beat (CTB) and Composite Second Order (CSO) parameters. Their definitions and main measurement techniques are quite well established and the interested reader is referred to [4] for a comprehensive review. In other RoF applications, the DR is defined as the maximum difference between the noise floor and the fundamental output which produces distortion terms of equal amplitude to the noise floor. The Noise floor will depend on the instantaneous bandwidth which varies by application. Therefore DR measurements are given over a 1 Hz noise bandwidth and are then scaled to the receiver instantaneous bandwidth, where the scaling exponent depends on the order of the dominant distortion.

For instance in several RoF applications such as Antenna remoting, millimetre wave generation and microwave mixing the second order intermodulation terms can be discarded and the lowest in-band distortion is due to third order. In such cases the DR scales as $B^{2/3}$. In this case the DR is referred to as the Spurious Free Dynamic Range or SFDR. For instance, figure 4 shows a schematic diagram of an RoF link generating third order intermodulation and also the typical measurement curve for the computation of the SFDR.

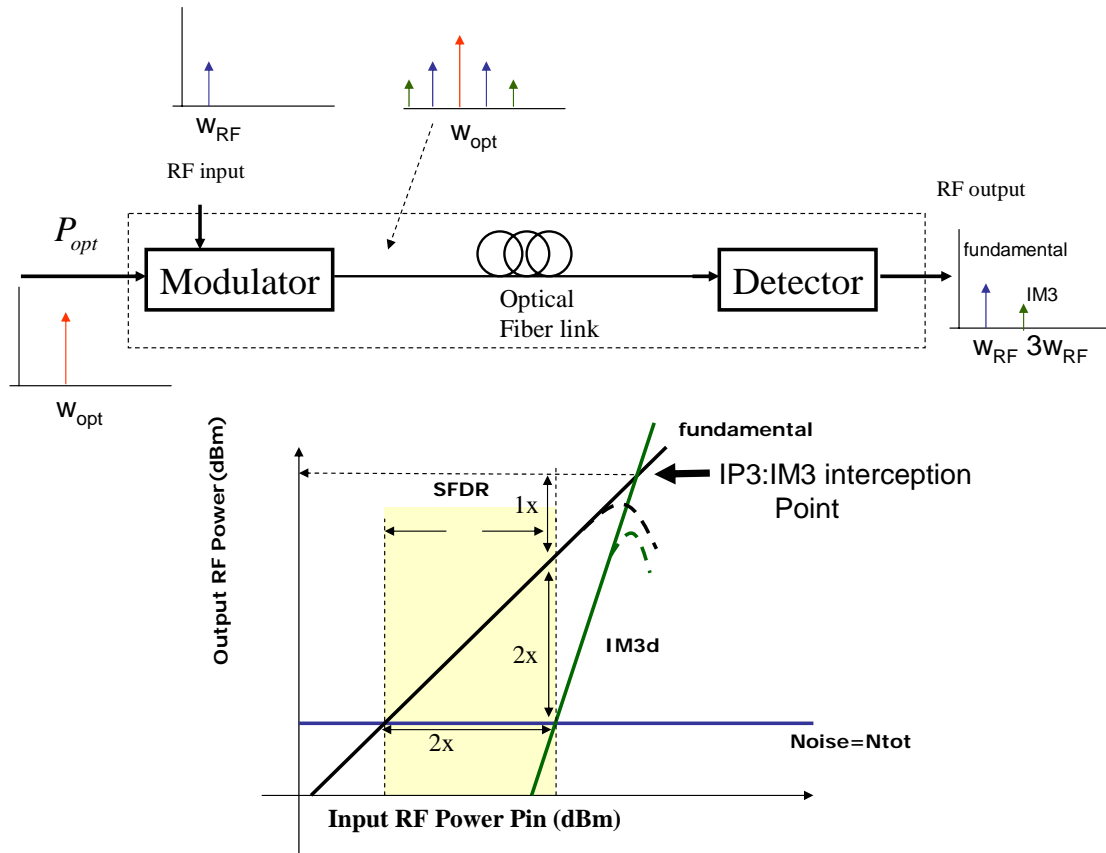


Figure 4

The measurement of the SFDR involves three stages. First of all, the noise spectral density of the RoF link must be determined. This can be achieved by means of an RF spectrum analyser placed at the detector output. The second stage implies the measurement of the RF output power versus the RF input power for the transmitted

fundamental tone. Again the output RF power can be determined by means of a RF spectrum analyser. Finally the RF output power of the third order intermodulation product must be measured against the RF power of the input fundamental tone (again with a RF spectrum analyser). The SFDR is given by the input RF power margin comprised between the crossing of the fundamental tone RF output power with the system noise and the crossing of the IM₃ tone RF output power with the system noise as shown in the lower part of figure 4. Typical SFDR or DR values must range above 100 dB.Hz^{2/3}.

The effect of chromatic dispersion must be measured in typical double sideband (DSB) RoF systems to guarantee that the impact of the carrier suppression effect (CSE) does not limit the systems performance. Using a LCA to test the RoF transfer function is the usual procedure to characterize the effect of fiber chromatic dispersion in a RoF link.

4) Recent developments

Most of the measurement techniques described and proposed so far rely on the access to the RF signal once detected by the lightwave receiver. Novel techniques using nonlinear optics have been recently proposed [7] where the advantage of conventional approach, based on fast photodetection and analysis of the generated photocurrent via electronics means, is replaced by a nonlinear interaction of the system under test with a quasimonochromatic source followed by an optical spectrum measurement. These novel techniques bring the advantage of an all-optical measurement and the potential of a much larger bandwidth than electronic alternatives.

5) Summary and conclusions

In this paper we have presented and reviewed some of the most important performance parameters and measurement approaches developed for different Microwave Photonic applications. We have concentrated mainly in Signal Processing and Signal Transmission applications and described techniques based on the analysis of the detected RF signal. Novel techniques very recently proposed based on the use of nonlinear optics have also been pointed out..

References

- [1] A. Seeds, 'Microwave Photonics', IEEE MTT, vol 50, pp. 877-887 (2002).
- [2] J. Capmany, D. Pastor, B. Ortega and S. Sales, 'Discrete time Optical Processing of Microwave Signals', IEEE JLT (invited paper), to be published, (2004).
- [3] C.H. Cox, 'Gain and noise figure in analogue fiber-optic links', Proc. IEE Pt. J. vol 139, pp. 238-242, (1992)
- [4] N.J. Frigo, M. Phillips and G. Bodeep, 'Clipping distortions in lightwave CTAV systems: Models, simulations and measurements', IEEE JLT, vol 11, pp. 138-146, (1993).
- [5] C.H. Cox, et al., 'Techniques and performance of intensity-modulation direct-detection analog optical links', IEEE MTT, vol 45, pp. 1375-1383, (1997).
- [6] K.I. Kitayama, 'Ultimate performance of optical DSB signal-based millimetre-wave fiber-radio systems: effect of laser phase noise', IEEE JLT, vol. 17, pp. 1774-1781, (1999).
- [7] C. Dorrer and D.N. Maywar, 'RF spectrum analysis of optical signals using nonlinear optics', IEEE JLT, vol 22, pp.266-274, (2004).

Applications of Metrology for Optical Coherence Tomography

Thomas E. Milner, Nate J. Kemp, Christopher G. Rylander, and Digant P. Davé
Department of Biomedical Engineering
The University of Texas at Austin

Abstract: Optical coherence tomography (OCT) is a novel technique that has recently emerged as a promising biomedical imaging modality in ophthalmology, cardiology, oncology and a number of other medical disciplines. Basic contrast mechanism for OCT is gradient in refractive index of tissue constituents. Additional contrast mechanisms include Doppler, polarization and phase-sensitive imaging modalities. Applications of metrology include high-resolution spectrum analyzers for spectral domain OCT instrumentation development and characterization of refractive index of tissue constituents.

1. Introduction: Metrology or the science of measurement is recognized as an essential component for industrial development and exchange of scientific information in the modern world[1]. Measurement standards allow quantitative comparison and hence meaningful interpretation of experimental results which are independent of the investigators, location of the laboratory or time of measurement. Without national and international measurement standards, much of the industrial development over the last century that has improved the quality of life for countless millions in the United States and abroad would have been substantially impeded or impossible.

Recently, many observers have suggested that the biomedical sciences and associated engineering disciplines will become increasingly important as we enter the 21st century[2]. Indeed a casual examination of subject matter reported in leading scientific journals reveals the increasing level of activity in the biomedical sciences and associated engineering fields. Although the biological sciences began by primarily cataloguing and classifying living organisms with subject matter being more qualitative in nature, modern biomedical sciences have become increasingly more exact and quantitative. The large variation observed in living organisms at the cell, organ, species, and environmental levels has often precluded quantitative investigations without extensive use of statistical analysis. A number of fundamental advances have transformed the biomedical sciences. Important advances include unraveling the genetic code[3], understanding of protein structure and function[4], and working-out the kinetics of chemical reaction pathways associated with cell metabolism[5]. Many of these fundamental advances have made extensive use of principles and ideas in the traditional physical sciences and engineering disciplines. Important in this transformation is the development of analytical instrumentation that can be applied to study living systems.

Optical techniques provide a number of important advantages for studying living systems. First, because light can be directed onto and collected from living systems without mechanical contact, in vitro and in vivo studies of live organisms can be completed with little or negligible disruption. Second, because the wavelength of visible light ($0.5\ \mu\text{m}$) is more than an order of magnitude smaller than the diameter ($10\ \mu\text{m}$) of most cells, light imaging systems can be applied to resolve subcellular constituents and cell boundaries. Third, because the bandwidth of light is exceedingly large ($10^{12}\ \text{Hz}$), the potential to engineer light systems to record the spatial and structural complexity inherent in living systems appears feasible. Fourth, because substantial resources from governmental agencies and private investors have been directed to the development of photonic components and equipment for telecommunications and related applications, development costs required to investigate novel applications of light in the biomedical sciences is reduced.

A principal problem encountered when using light to study living systems is reduced penetration of light due to optical scattering that originates in spatial variation of the refractive index in tissue. When light enters a tissue, optical scattering gives rise to an infinite distribution of photon paths with substantial variation in pathlength and time of flight. Optical coherence tomography (OCT) is a novel technique that allows recording depth-resolved reflectivity images of a tissue specimen[6]. Because the technique can record images rapidly and non-invasively, OCT has emerged as a promising biomedical imaging modality in ophthalmology[7], cardiology[8], oncology[9] and a number of other medical disciplines. Purpose of this report is to review various contrast mechanisms that have been exploited in OCT and present applications of metrology for further development of OCT. The paper is organized by first presenting a brief background and description of OCT. A discussion of basic contrast mechanisms includes Doppler[10], polarization[11, 12] and phase-sensitive OCT[13]. Metrology applications are discussed in the context of instrument development and refractive index characterization of tissue specimens.

2. Optical Coherence Tomography: Optical Coherence Tomography (OCT) has emerged as a promising technique for high resolution cross-sectional imaging of tissue specimens. Application of OCT to clinical and biomedical imaging problems is expanding rapidly and is expected to continue to increase in coming years. OCT instrumentation uses a spatially coherent and spectrally broadband light source in a two-beam interferometer (e.g., Michelson) with the reflector in the sample path replaced by the tissue specimen under study. Depth ranging in the tissue specimen is possible because interference fringes are detected only for coherent backscattered photons that have an optical path-length matching the reference-target distance to within the source coherence length ($L_c=5-10\ \mu\text{m}$). As optical path-length in the reference path is varied over a specified range, detected interference fringe intensity is mapped to the tissue specimen's backscattering profile in depth (A-scan). Coherence length of the source light determines axial resolution ($L_c=5-10\ \mu\text{m}$) of an OCT system while numerical aperture of the focusing optics determines lateral resolution. Consecutive A-scans acquired laterally across the tissue specimen allow reconstruction of two-dimensional and three-dimensional tomographic images.

2A. Doppler OCT: Doppler OCT combines laser Doppler flowmetry with optical coherence tomography (OCT) to obtain high resolution tomographic images of static and moving constituents in highly scattering biological specimens. Doppler OCT uses the apparent shift (Δf_D) in frequency of light scattered from a moving constituent according to,

$$\Delta f_D = \frac{1}{2\pi}(\mathbf{k}_s - \mathbf{k}_i) \cdot \mathbf{v} \quad (1)$$

where, \mathbf{k}_i and \mathbf{k}_s are wave vectors of incoming and scattered light respectively, and \mathbf{v} is the velocity vector of moving particles. When light backscattered from a moving constituent interferes with the reference beam, beating at the Doppler frequency occurs. With knowledge of the angle between the scattering vector ($\mathbf{k}_s - \mathbf{k}_i$) and the velocity (\mathbf{v}), measurement of the Doppler frequency shift (Δf_D) allows determination of particle velocity at discrete spatial locations in a turbid specimen.

The rodent mesentery model is used to demonstrate the potential of Doppler OCT for in vivo imaging of vascular blood flow in different organs. After a loop of small intestine was exposed through an abdominal incision to allow access to the mesenteric vasculature, in vivo blood flow in both veins and arteries was imaged using Doppler OCT (Figure 1). Two vessel-like circular structures are evident in

the structural image (Figure 1A). Velocity images of blood flow moving in opposite directions, as determined by the sign of the Doppler shift (Δf_D) are shown in Figures 1B and C, respectively. Here static structures ($v=0$) in the mesentery appear dark, while blood flow in both veins and arteries appears as lighter shades.



Figure 1: Doppler OCT images of *in vivo* rodent mesentery blood flow. OCT structural image (A), with white and black representing high (80 dB) and low (0 dB) backscattered light intensities, respectively. ODT velocity image of blood flow in artery (B), white and black represent high (4000 $\mu\text{m/s}$) and zero velocity, respectively. Velocity image of blood flow in veins (C), white and black represent high (1000 $\mu\text{m/s}$) and zero velocity, respectively.

2B. Polarization Sensitive OCT: Polarization sensitive optical coherence tomography (PS-OCT)

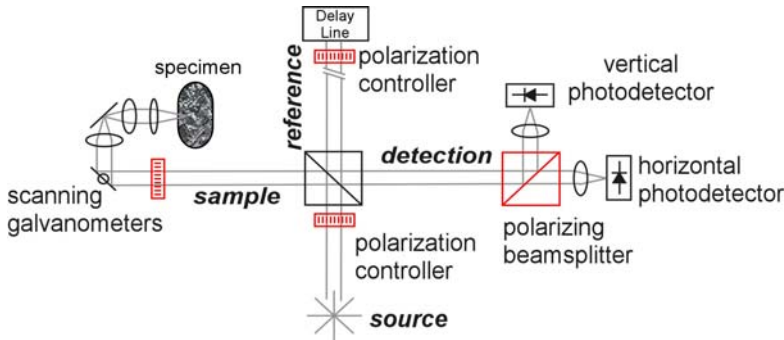


Figure 2: Instrumentation for PS-OCT is similar to OCT with additional polarization control elements (red).

combines the depth-ranging features of OCT with polarimetric detection to record the depth-resolved normalized Stokes parameters $[S_Q(z), S_U(z), S_V(z)]$ of light backscattered from a tissue specimen.

PS-OCT instrumentation (Figure 2) is similar to that used in OCT with the addition of polarization control elements in source, sample, and reference paths. In the detection path, photo-detectors measure light intensities of horizontal and vertical polarization modes.

Digital signal processing of the detected double-side-band modulated signals provides demodulated horizontal $[\tilde{I}_h(z)]$ and vertical $[\tilde{I}_v(z)]$ interference fringe amplitudes and relative phase $[\phi_{v-h}(z)]$ between horizontal and vertical polarization components. Depth-resolved normalized Stokes parameters $[S_Q(z), S_U(z), S_V(z)]$ of light backscattered from tissue are determined directly from $|\tilde{I}_h(z)|$, $|\tilde{I}_v(z)|$ and $\phi_{v-h}(z)$,

$$S_Q(z) = \frac{|\tilde{I}_h(z)|^2 - |\tilde{I}_v(z)|^2}{|\tilde{I}_h(z)|^2 + |\tilde{I}_v(z)|^2} \quad S_U(z) = \frac{2|\tilde{I}_h(z)||\tilde{I}_v(z)|\cos(\phi_{v-h}(z))}{|\tilde{I}_h(z)|^2 + |\tilde{I}_v(z)|^2} \quad S_V(z) = \frac{2|\tilde{I}_h(z)||\tilde{I}_v(z)|\sin(\phi_{v-h}(z))}{|\tilde{I}_h(z)|^2 + |\tilde{I}_v(z)|^2} \quad (2)$$

PS-OCT images were recorded from both eyes of two healthy, 6 kg, 4-year-old, female rhesus primates. All experimental procedures involving primates were approved by the University of Texas at Austin IACUC (protocol #02032203) and conform to all USDA, NIH, and ARVO guidelines for animal welfare. The primates were anesthetized with a combination of ketamine (10mg/kg) and xylazine (0.25 mg/kg) given intramuscularly. Anesthesia depth was monitored and maintained by a certified veterinary technologist. Pupils were dilated using one drop of 1% cyclopentolate and one

drop of 1% tropicamide. The primate's head was gently secured to a goniometer in the prone position using a custom-made mask. One drop of 10% methylcellulose was placed in the eye to be imaged and a contact lens was placed on the cornea to prevent dehydration and render the eye slightly myopic. Eyelids were held open with an infant speculum. The eye was manipulated with an 11mm diameter Thornton fixation ring to place the aiming beam directly onto the optic nerve head.

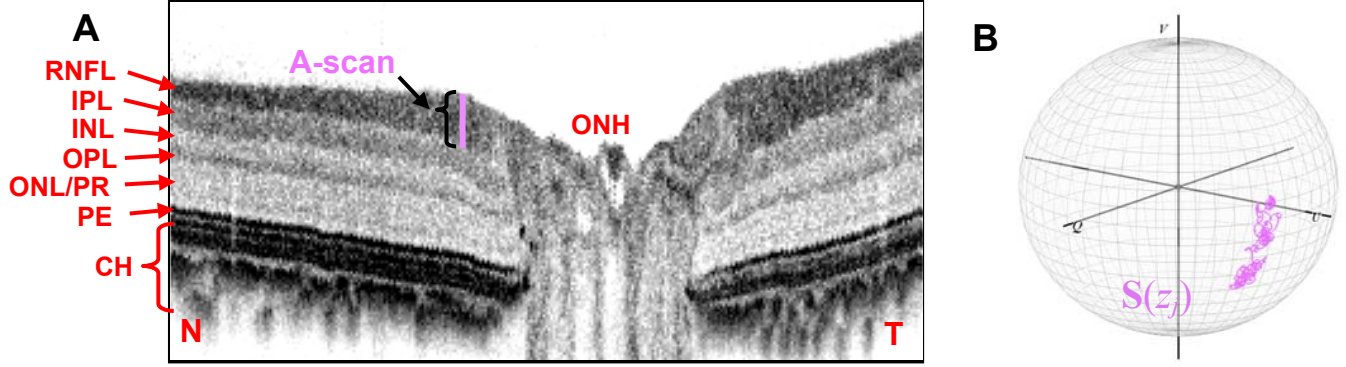


Figure 3: **A.** PS-OCT B-scan image of in vivo primate retina (“N” is nasal and “T” is temporal; ONH: optic nerve head; RNFL: retinal nerve fiber layer; IPL: inner plexiform layer; INL: inner nuclear layer; OPL: outer plexiform layer; ONL/PR: outer nuclear layer and photoreceptors; PE: pigment epithelium; CH: choroid; image dimension is 1mm deep by 4mm wide). **B.** Depth-resolved polarization data $[S(z)]$ (purple) plotted on the Poincaré sphere for PS-OCT A-scan location denoted by purple line in **A**.

Depth-resolved normalized Stokes vectors $[S(z)]$ resemble a circular polarization arc on the Poincaré sphere (Figure 3B). Measurement of RNFL thickness and phase retardation may be used to determine birefringence (Δn).

2C. Phase-Sensitive OCT: We have developed a fiber-based phase-sensitive system as a differential phase-contrast optical coherence microscope (DPC-OCM) for high resolution quantitative phase-contrast imaging of cells. The fiber-based DPC-OCM provides flexibility in interrogating a variety of samples and is well suited for biomedical applications requiring in vivo imaging.

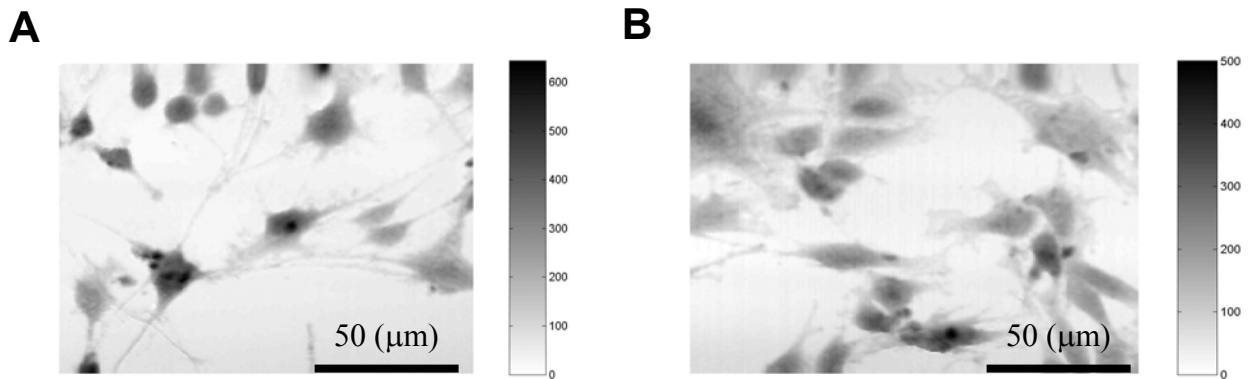


Figure 4: Quantitative DPC-OCM images of **A.** human skeletal muscle cells; and **B.** human kidney cancer cells. Grayscale on right of each image is optical pathlength in nanometers.

DPC-OCM images of human skeletal muscle and kidney cancer cells give optical pathlength through the cells in nanometers. DPC-OCM is capable of recording quantitative phase-contrast images of

individual cells with subcellular resolution. Because the DPC-OCM can record transient changes in the optical path length (OPL), the system may be used to record quantitative OPL alterations in cells in response to chemical and photothermal stimuli. A fiber-based DPC-OCM has the potential to improve *in vivo* imaging of epithelial tissues for a variety of clinical diagnostics and monitoring applications.

3. Metrology for OCT: Inasmuch as Optical Coherence Tomography (OCT) is a relatively recent imaging modality, a number of opportunities are recognized for applying metrology to accelerate the industrial development and the exchange of scientific information related to this field. Applications of metrology in OCT are generally divided into two areas: instrumentation and specimen characterization. Metrological applications related to OCT instrument development are compatible with the historic mission of NIST and relate to providing reference data or standards that can be utilized by investigators engaged in instrument development. Alternatively, metrological applications related to specimen characterization is a relatively new undertaking and will require careful definition of objectives that can be sharpened through active dialogue among people in the biomedical and traditional engineering disciplines as well as the physical and life sciences.

3A. Spectral Domain OCT: With few exceptions, the central component in an OCT system is a two-beam Michelson interferometer. Interference fringes formed between light reflected from the reference path and backscattered from the tissue specimen may be detected in temporal or spectral domains. Although to date most clinical applications of OCT have utilized time-domain detection, signal-to-noise ratio is substantially increased using spectral-domain detection[14]. Two distinct spectral-domain detection approaches have been recognized. In one approach, interference fringes formed between broadband light reflected from a reference path and tissue specimen are detected by a conventional grating spectrometer[15]. In a second approach, a narrowband tunable laser source is utilized with an optical frequency that is swept in time[16]. Because linewidth of tunable laser sources may be extremely narrow (MHz), the usable bandwidth of systems utilizing the second approach is substantially broader (10^6 resolvable cells) than that provided by a conventional grating spectrometer (10^3 resolvable cells). The broader bandwidth available in the second approach using a tunable laser source allows encoding additional information (e.g., polarization or spatial) into the optical spectral domain. Utilization of the additional bandwidth available in systems using a narrowband tunable laser source requires a high resolution optical spectrum analyzer that can provide calibrated spectral data for each scan. Although optical spectrum analyzers incorporating HCN gas cells with sub-picometer resolution combined with tunable laser sources are available for telecommunication applications in the 1.5-1.6 μm spectral range, similar instrumentation does not exist at shorter wavelengths for optical coherence tomography. For example, a calibrated optical spectrum analyzer with sub-picometer resolution combined with a narrowband tunable laser source covering spectral regions less than 1.5 μm would find important applications in optical coherence tomography.

3B. Refractive Index Characterization: Images of tissue recorded using optical coherence tomography represent depth-resolved reflectivity of light backscattered from tissue. Amplitude of light backscattered from tissue is proportional to the depth gradient (d/dz) in the refractive index distribution $[n(\mathbf{r})]$. Inasmuch as forward- and back-scattering properties of tissue may be derived from $n(\mathbf{r})$, availability of reference data giving the frequency-dependent refractive index $[n_i(\nu)]$ of specific biochemical constituents that comprise cells and tissues would benefit both the interpretation and exchange of scientific information related to OCT. Moreover, determining $n_i(\nu)$ may allow distinguishing quantitatively between material- and form-dependent dispersion effects.

When discussing the refractive index of tissues we distinguish between a mean-squared value ($\overline{n^2}$) and the frequency-dependent refractive index $[n_i(\nu)]$ of specific biochemical constituents. Mean-squared value is related to refractive index $[n_i(\nu)]$ of specific biochemical constituents by[17],

$$\overline{n^2} = \sum_i f_i \cdot n_i^2(\nu) \quad (2)$$

where f_i is the volume fraction of the i 'th constituent. Although data exists for refractive index of tissues and specific proteins, values are sparse and generally unreliable. Not only are data of important constituents sparse, variation with pressure and temperature have not been investigated. Characterization of $n_i(\nu, T, p)$ is required to interpret optical pathlength changes in tissues associated with diagnostic techniques that result in transient temperature or pressure changes.

3C. Tissue Form Birefringence: Birefringence in tissues originates in the anisotropic distribution of refractive index of specific constituents. In contrast to molecular birefringence found in common optical materials such as quartz and calcite, form birefringence results from the anisotropic shape of specific tissue constituents. Theory of form birefringence was first formulated by O. Weiner in 1912. Following Weiner's original derivation, Oldenbourg[18] derived an expression (Eq. 3) for the effective dielectric constant ($\epsilon_x = n_x^2$) of a protein with dielectric constant $\epsilon_2 = n_2^2$ surrounded by a fluid with refractive index $\epsilon_1 = n_1^2$

$$n_x^2 = n_1^2 + \frac{f(n_2^2 - n_1^2)}{1 + (1-f) \cdot \frac{(n_2^2 - n_1^2)}{n_1^2} \cdot A_x} \quad (3)$$

A_x is a depolarizing factor that depends on the alignment of the protein to the external field, and f is volume fraction of the protein. Birefringence (Δn) is determined by computing refractive index for particles aligned parallel (n_{\parallel}) and perpendicular (n_{\perp}) to the external field with corresponding depolarizing factors (A_{\parallel} and A_{\perp}). Oldenbourg applied Eq. 3 and experimental data to estimate refractive index of DNA parallel ($n_{\parallel} = 1.575$) and perpendicular ($n_{\perp} = 1.737$) to the long axis at $\lambda = 633$ nm.

Reference data for birefringence of specific protein constituents in solution is important to interpret measured values of phase retardation using PS-OCT. For example in the retinal nerve fiber layer birefringence is due primarily to neurotubules. Values of retinal nerve fiber layer phase retardation measured using PS-OCT can be better interpreted if reference data for n_{\parallel} and n_{\perp} were available. Similar arguments apply for obtaining reference data for refractive indices of collagen - the primary constituent of fibrous connective tissues.

4. Summary and Conclusions: Optical coherence tomography (OCT) is an emerging imaging modality that may be used to provide Doppler, polarization and phase contrast. Moreover, advances in OCT instrumentation will likely incorporate photonic technologies developed in telecommunications and related fields. Application of metrology to instrumentation and specimen characterization can substantially improve the engineering and science of OCT. Development of calibrated optical

spectrum analyzers with sub-picometer resolution combined with a narrowband tunable laser source covering visible and near-infrared spectral ranges (500-1500 nm) can benefit optical coherence tomography. Reference data for the refractive index $[n_i(\nu)]$ and birefringence $[\Delta n]$ of specific biochemical constituents (e.g., DNA, microtubules, collagen fibrils) would have tremendous value in clarifying interpretation of OCT data and advancing novel clinical applications of the methodology.

References

- [1] D. Kind, Quinn, T., "Metrology: Quo Vadis?," *IEEE Transactions on Instrumentation and Measurement*, vol. 44, pp. 85-89, 1995.
- [2] W. R. Hendee, "Informatics at the National Institutes of Health: a call to action," *Journal of the American Medical Informatics Association*, vol. 6, pp. 267-271, 1999.
- [3] I. C. Gerling, Solomon, S.S., and Breyer-Ash, M., "Genomes, transcriptions, and proteomes: molecular medicine and its impact on medical practice," *Archives of Internal Medicine*, vol. 163, pp. 190-198, 2003.
- [4] D. R. Richter, and Beck-Sickinger, A.G., "Expressed Protein Ligation. Method and Applications," *European Journal of Biochemistry*, vol. 271, pp. 663-677, 2004.
- [5] B. E. Kemp, Mitchelhill, K. I., Stapleton, D., Mitchell, B.J., Chen, Z.P., Witters, L.A., "Dealing with Energy Demand: the AMP-activated kinase protein kinase," *Trends in Biochemical Sciences*, vol. 24, pp. 22-25, 1999.
- [6] D. Huang, E. A. Swanson, C. P. Lin, J. S. Schuman, W. G. Stinson, W. Chang, M. R. Hee, T. Flotte, K. Gregory, C. A. Puliafito, and J. G. Fujimoto, "Optical Coherence Tomography," *Science*, vol. 254, pp. 1178-1181, 1991.
- [7] W. Drexler, H. Sattmann, B. Herrmann, T. H. Ko, M. Stur, A. Unterhuber, C. Scholda, O. Findl, M. Wirtitsch, J. G. Fujimoto, and A. F. Fercher, "Enhanced visualization of macular pathology with the use of ultrahigh-resolution optical coherence tomography," *Archives of Ophthalmology*, vol. 121, pp. 695-706, 2003.
- [8] G. J. Tearney, Yabushita, H., Houser, S.L., Aretz, H.T., Jang, I.K., Schelendorf, K.H., Kauffman, C.R., Shishkov, M., Halpern, E.F., Bouma, B.E., "Quantification of Macrophage Content in Artherosclerotic Plaques by Optical Coherence Tomography," *Circulation*, vol. 107, pp. 113-119, 2003.
- [9] J. Strasswimmer, Pierce, M.C., Park, B.H., Neel, V., and deBoer, J.F., "Polarization-sensitive Optical Coherence Tomography on Invasive Basal Cell Carcinoma," *Journal of Biomedical Optics*, vol. 9, pp. 292-298, 2004.
- [10] Z. Chen, Milner, T.E., Shrinivas, S., Wang, X., Lalekafzali, A. van Gemert, M., Nelson, J.S., "Noninvasive imaging of in vivo blood flow velocity using optical Doppler tomography," *Optics Letters*, vol. 22, pp. 1119-1121, 1998.
- [11] J. F. de Boer and T. E. Milner, "Review of polarization sensitive optical coherence tomography and Stokes vector determination," *Journal of Biomedical Optics*, vol. Accepted, 2002.
- [12] J. F. de Boer, T. E. Milner, and J. S. Nelson, "Determination of the depth-resolved Stokes parameters of light backscattered from turbid media using Polarization Sensitive Optical Coherence Tomography," *Optics Letters*, vol. 24, pp. 300-302, 1999.
- [13] C. G. Rylander, Dave, D.P., Akkin, T., Milner, T.E., Diller, K. R., Welch, A.J., "Quantitative phase contrast imaging of cells with phase-sensitive optical coherence tomography," *Optics Letters*, vol. 29, pp. 1509-1511, 2004.

- [14] J. F. de Boer, Cense, B., Park, B. H., Pierce, M. C., Tearney, G.J., Bouma, B.E., "Improved signal-to-noise ratio in spectral domain compared with time-domain optical coherence tomography," *Optics Letters*, vol. 28, pp. 2067-2069, 2003.
- [15] S. H. Yun, Tearney, G.J, Bouma, B.E., Park, B.H., de Boer, J.F., "High speed Spectral Domain Optical Coherence tomography at 1.3 micron wavelength," *Optics Express*, vol. 11, 2003.
- [16] S. H. Yun, Tearney, G.J, de Boer, J.F., Iftimia, N., and Bouma, B.E., "High-speed optical frequency domain imaging," *Optics Express*, vol. 11, 2003.
- [17] C. J. F. Bottcher, *Theory of Electric Polarization*, vol. 1, 2nd ed. Amsterdam: Elsevier North-Holland Biomedical Press, 1973.
- [18] R. Oldenbourg and T. Ruiz, "Birefringence of macromolecules: Wiener's theory revisited, with applications to DNA and tobacco mosaic virus," *Biophysical Journal*, vol. 56, pp. 195-205, 1989.

High-power nonlinearity of optical fiber power meters

Igor Vayshenker, Ralph Swafford*, and Shao Yang

National Institute of Standards and Technology, 325 Broadway, Boulder, CO 80305

*OZ Optics Ltd., 219 Westbrook Rd., Carp, Ontario, K0A 1L0 OZ Optics, Canada

Abstract

We have developed a system for measuring the nonlinearity of optical fiber power meters at a maximum power of 2 W. This system is based on the triplet superposition method. This system provides an accurate determination of nonlinearity of optical power meters by means of correction factors at different powers.

1. Introduction

Most users of optical power meters assume that the meter output reading is directly proportional to the optical input power. This proportionality property is called linearity, and the departure from this direct proportionality is defined as nonlinearity. Optical power meter nonlinearity is defined as the relative difference between the response at an arbitrary power and the response at the reference power:¹

$$\Delta_{NL}(P;P_c) = \frac{R(P)}{R(P_c)} - 1, \quad (1)$$

where $R(P)=V/P$ is the response of the meter at optical power P , the subscript c indicates the calibration point, and V is the meter output reading.

While the calibration gives the true input power from the power meter output reading at the calibration point, the measurement of nonlinearity and range discontinuity, together with calibration, provides this input-output relationship at any power within the entire dynamic range of the optical power meter.

1.1. Correction factor for nonlinearity and range discontinuity

The true input power P is obtained from the power meter reading V by

$$P = \frac{V}{F_c \cdot CF}, \quad (2)$$

where $F_c = V_c/P_c$ is the calibration factor, and

$$\begin{aligned}
CF &= \frac{a_1[c]}{a_1[m]} \times \frac{1 + \sum_{k=2}^n b_k[c] V_c^{k-1}}{1 + \sum_{k=2}^n b_k[m] V^{k-1}} \\
&= \frac{a_1[c]}{a_1[m]} [1 + \Delta_{NL}(V;0) - \Delta_{NL}(V_c;0)],
\end{aligned} \tag{3}$$

where CF is a correction factor due to nonlinearity and range discontinuity, m is a number that corresponds to a specific range of an optical power meter, a_k and b_k are coefficients. b_k is determined by measurement of nonlinearity, $a_1[c]$ is determined by calibration and $a_1[m]$ by range discontinuity. Consequently, each range of a power meter has its own correction factor. The degree of the polynomial n depends on the value of the data's standard deviation.

2. Measurement system and results

We have based the operation of our system on the triplet superposition method,²⁻⁶ which relies on the principle that, for a linear power meter, the sum of meter outputs corresponding to inputs from two individual beams should equal the output when the two beams are combined and incident on the meter at the same time. The measurement system is depicted in Figure 1 and described below.

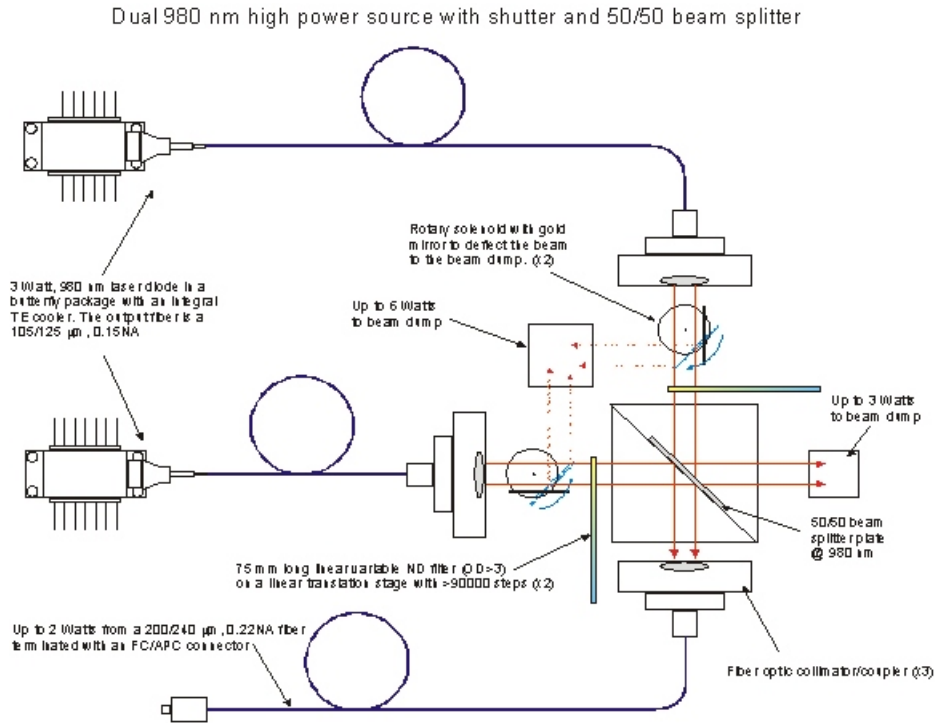


Figure 1. Measurement system.

Each source is a 980 nm laser diode in a butterfly package with an integrated thermoelectric (TE) cooler, monitor photodiode, and thermistor. The laser pigtail's core/cladding size is 105/125 μm with a numerical aperture (NA) of 0.15. The laser diode is driven in a constant-power mode with a high-power laser driver, that contains an adjustable current limit and a laser enable feature. The temperature is held constant at 23°C by the TE cooler control module.

The output fiber of the first laser diode is aligned to a high-power collimator that produces a beam diameter of approximately 6 mm. This beam then propagates through a high-power optical shutter. The shutter is a rotary solenoid with a mirror-mounted offset onto the shaft. For safety reasons, the beam is blocked when the shutter is in the "OFF" position and is sent to a beam dump. When the shutter is activated, the mirror is removed from the optical path and enables the beam to pass through.

The beam then passes through a linear, variable neutral density filter that is 75 mm in length. The filter is variable from 0 to approximately 30 dB at 980 nm. The filter is mounted on a linear translation stage and is driven by a servo motor/encoder combination. The translation stage has its travel limit set at each end by a limit switch. The total beam travel is approximately 60 mm with a step count of >90,000. The translation stage is controlled through an RS232 port. The beam then enters the 50/50 beam splitter plate where half of the light is propagated to a second beam dump. The remaining light proceeds to the high-power output lens and gets coupled into a 200/240 μm fiber with a NA of 0.22.

The second laser transmits, via an identical system, through the 50/50 beam splitter plate at 90° perpendicular to the beam of the first laser. The second laser's beam is then coupled with the first laser beam into the 200/240 μm fiber with the NA of 0.22. The output of each laser at the tip of the 200/240 μm fiber is set at 1 W. The fiber is routed to the outside of the case via a 3 mm stainless-steel armored cable (for safety) and is terminated with an FC/APC connector.

The measurements are performed by taking sets of three power readings from the test power meter: (1) shutter 1 is open and shutter 2 is closed, (2) shutter 1 is closed and shutter 2 is open, and (3) both shutters are open. This sequence is then repeated at different powers.

To measure the range discontinuity (offsets between range or scale settings), readings are taken at the lower power end of each range and compared to the readings on the higher power region of the next lower range (if any) at a constant power. The calculated correction factors result from the meter nonlinearity within each range, combined with the range discontinuity.

Figure 2 depicts correction factors obtained on a high-power optical fiber power meter at 980 nm. Each data group represents a separate power range setting of the meter. The total nonlinearity of this power meter is approximately 3.5 % for powers from several milliwatts to several watts.

3. Conclusion

We have designed and built a nonlinearity system that allows us to obtain correction factors for optical fiber power meters at a maximum power of 2 W at 980 nm. This system is an important tool to characterize optical fiber power meters at high powers. Similar nonlinearity systems could be built at other telecommunication wavelengths: 1310, 1480 and 1550 nm.

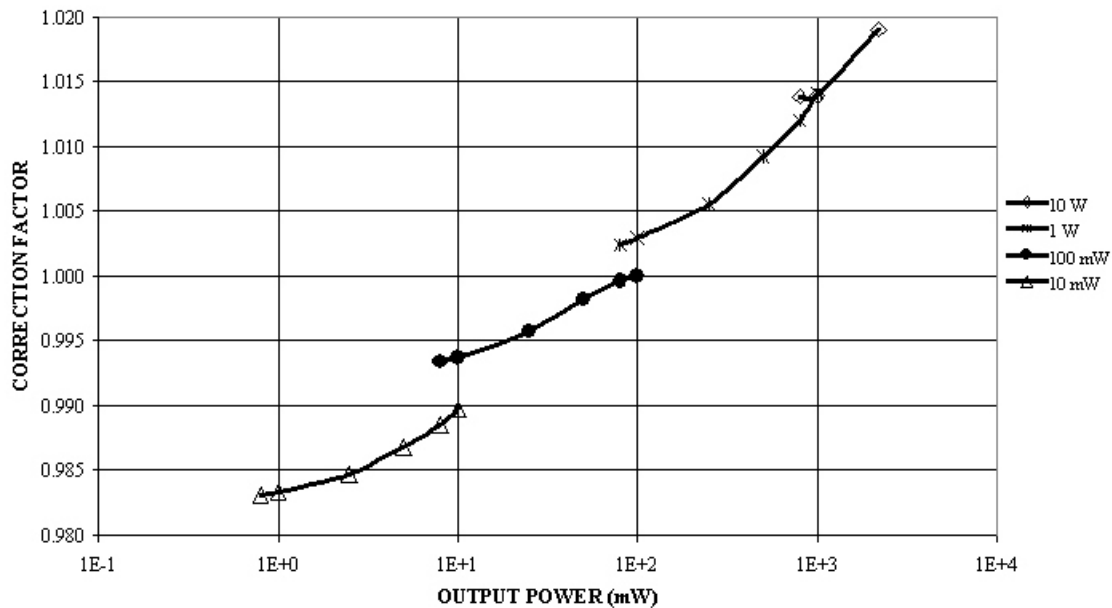


Figure 2. Correction factor vs. incident power at 980 nm.

References

1. International standard, IEC 61315, *Calibration of fibre optic power meters, Ed. 1.0*, International Electrotechnical Commission, Geneva, Switzerland, 1995.
2. S. Yang, I. Vayshenker, X. Li, and T.R. Scott, "Optical detector nonlinearity: a comparison of five methods," Digest, Conf. Precision Electromagnetic Measurements, pp. 455-456, June-July 1994.
3. S. Yang, I. Vayshenker, X. Li, M. Zander and T.R. Scott, "Optical detector nonlinearity: Simulation," Natl. Inst. Stand. Technol. Technical Note 1376, May 19, 1995.
4. I. Vayshenker, S. Yang, X. Li, and T.R. Scott, "Automated measurement of nonlinearity of optical fiber power meters," Proc. SPIE, Vol. 2550, pp. 12-19, San Diego, CA, July 11-12, 1995.
5. I. Vayshenker, S. Yang, X. Li, and T.R. Scott, "Nonlinearity of optical power meters," Natl. Inst. Stand. Technol. Spec. Publ. 905, 101-104; 1996.
6. I. Vayshenker, S. Yang, X. Li, T. R. Scott, and C. L. Cromer, "Optical Fiber Power Meter Nonlinearity Calibrations at NIST," NIST Special Publication 250-56, 2000.

CHARACTERIZATION OF A HIGH POWER AND HIGH ACCURACY INTEGRATING SPHERE RADIOMETER FOR FIBER APPLICATIONS.

P. Corredera, M. L. Hernanz, M. González-Herraez, S. Martín-López and A. Carrasco-Sanz.
Instituto de Física Aplicada (CSIC), Serrano 144, 28006. MADRID, SPAIN. pcorredera@ifa.cetef.csic.es

Abstract: This paper describes the calibration of a high power and high accuracy transfer standard based on an integrating sphere radiometer to be used for power levels ranging from -40 dBm to +30 dBm. The integrating sphere radiometer has been calibrated in the spectral range of 1250 nm to 1650 nm, using an electrically calibrated pyroelectric radiometer and four tuneable laser diodes. The total uncertainty obtained is lower than $\pm 1.4\%$ for these wavelength and power ranges.

Introduction

In the present, optical fiber power meters need to be calibrated at all telecommunication transmission bands (O, E, S, C, L and U). Moreover, due to the appearance of high power fibre lasers for Raman pumping, there is a strong requirement of better accuracy in the measurement of absolute powers in fibres at levels from 0.5 W to 10 W. Accurate characterization of the absolute power in the fiber is also required for a good measurement and control of the nonlinear parameters of the optical fiber.

Since 1996 the Instituto de Física Aplicada (IFA-CSIC-Madrid) has been working on the development of integrating sphere radiometers (ISR) as transfer standards for calibration of optical fibre power meters^(1,2).

Integrating sphere radiometers are interesting for high-power applications because they avoid modal and polarization problems, they are inherently attenuating and the spectral response is smooth and wide since no accessory optics are used in the design⁽³⁾. This paper presents the calibration of an ISR over the 1250 to 1650 nm wavelength range, and the evaluation of its long term calibration stability. We extend the results and estimate the uncertainties for +30 dBm optical power, based on linearity measurements of the InGaAs detector used in the ISR.

Integrating sphere radiometer design and characterization.

Figure 1 shows the integrating sphere radiometer used in this work. This radiometer is composed of a 3 mm diameter InGaAs detector coupled to a 2-inch SPECTRALON® integrating sphere. The sphere has three ports with 90° orientation between each other. One of these ports is an auxiliary port used for complementary characterization and usually closed by a light trap. The others input and output ports are 3 mm diameter. Due to the non-linear behaviour observed in InGaAs detectors with overfilled illumination⁽⁴⁾, as is normally the case of the output port of an integrating sphere, an additional 2 mm diameter aperture has been placed just in front of the detector surface in order to produce underfilled illumination.

We measure the linearity of the InGaAs detector and aperture, over the full range of the detector signals using the stimuli addition method. The signal of the detector and aperture is close to the signal of the ISR multiplied by 200. The total nonlinearity correction is calculated as the product of all individual factors, obtained in steps of 3 dB, from the calibrated level to the test level. In the same way, the total uncertainty of the nonlinearity correction is the square root of the quadratic sum of all these individual uncertainties. Figure 2 shows the nonlinearity correction factor and their uncertainty. In the upper axis of this figure, the equivalent power level

in the ISR obtained with the 1550 spectral responsivity value is represented. The saturation level observed for this radiometer is +30 dBm (6 mA in the photodiode response).

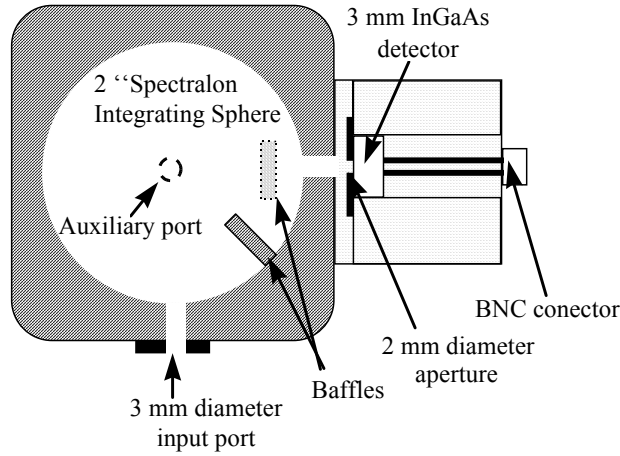


Figure 1: Integrating sphere radiometer.

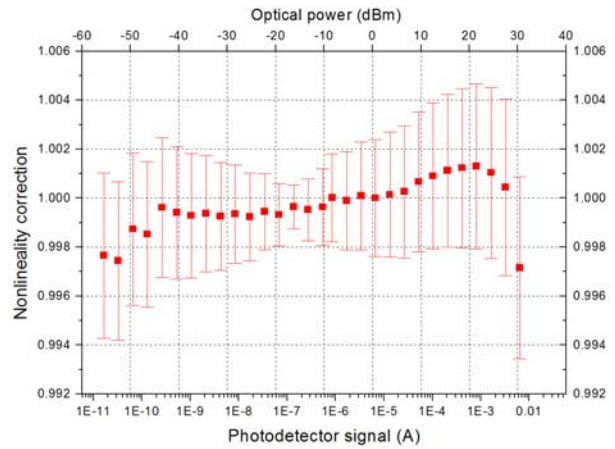


Figure 2: Nonlinearity correction of the InGaAs detector at 1550 nm. The upper axis is the equivalent optical power in the ISR.

Spectra responsivity calibration

The spectral responsivity calibration of ISR has been performed by direct comparison with an Electrically Calibrated Pyroelectric Radiometer (ECPR)⁽⁵⁾.

The calibration system used is very similar of the setup used in reference /2/. The output power of the laser diode is collimated by a microscope objective into the ISR and the ECPR as figure 3 shows. Four tuneable laser diodes (Photonetics), covering from 1250 to 1650 nm are used as sources with high spectral purity. The main characteristics of these lasers are: output power over 5 mW with a relative power stability of 0.1% over 1 hour, 100 kHz linewidth (full-width-half-maximum) and the absolute wavelength calibration of 0.02 nm.

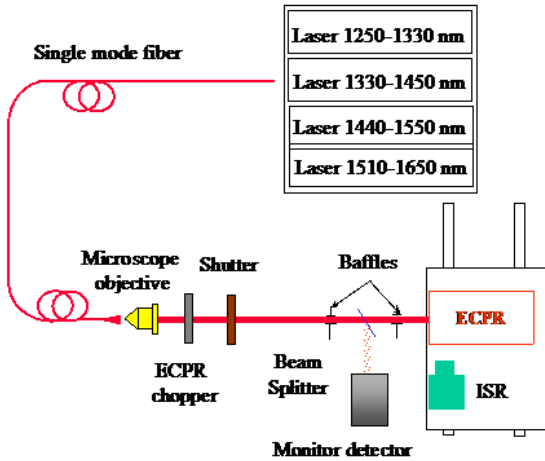


Figure 3: Experimental setup used for absolute calibration.

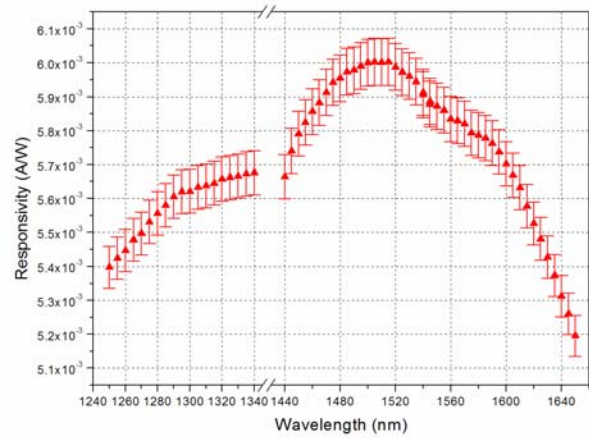


Figure 4: Spectral responsivity of integrated sphere radiometer.

The beam was prepared by coupling the tuneable laser diode to a 2-meter-long single-mode optical fiber with a core diameter of 9 μm . The beam spot was within 1.3 ± 0.2 mm at $1/e^2$ irradiance diameter. An aperture of 3 mm diameter was used on from of the ECPR in order to

minimize the scattered light. 1 mW optical power was used for all the measured wavelengths and controlled by the monitor detector. The figure 4 shows the spectral responsivity and their uncertainty ($k=2$) obtained as result of the described process.

Inconsistencies in the results of the spectral responsivity has been found from 1340 to 1440 nm wavelengths as figure 5 shows. The relative spectral responsivity depths coincide with absorption lines of water. For this reason it is impossible to use this type of radiometer in this spectral region. The effect shown in figure 5 is enhanced due to the narrow linewidth of the lasers used. Unfortunately, this spectral region is specially important for Raman pumping in the S-band (1460-1530 nm).

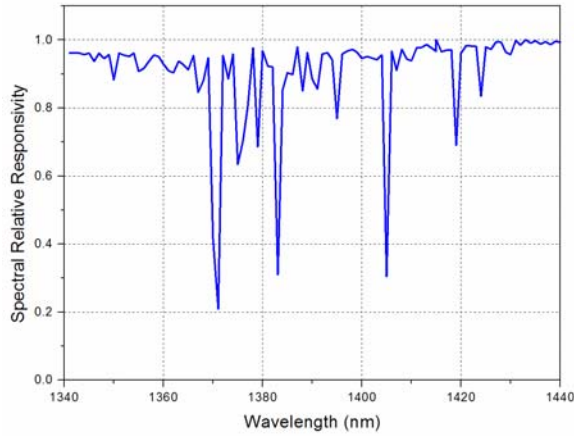


Figure 5: Spectral relative responsivity of the radiometer in the water vapour absorption region.

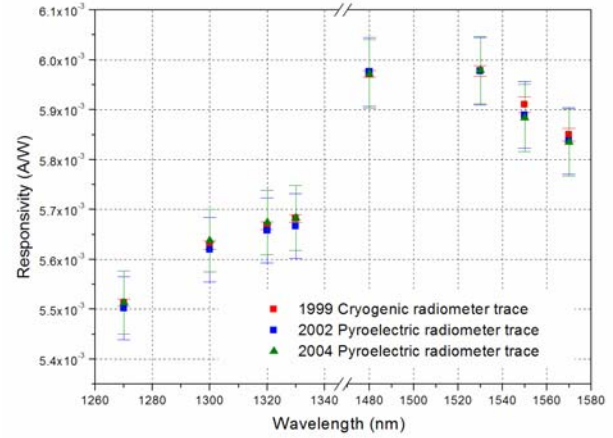


Figure 6: Long term stability of integrating sphere radiometer.

The contributions of the different sources of error to the final calibration uncertainty of the radiometer is summarized in table 1. Two uncertainty sources are interesting to remark: the linearity of the detector, that enables us to extend the calibration data from 0 dBm to +30 dBm, and the long time stability of the responsivity.

Table 1: Uncertainties in the calibration of the integrating sphere radiometer with the ECPR.

Error source	Uncertainty type	Value (%)
ECPR calibration constant	B	0.96
ECPR power measurement	A	0.05
ECPR power resolution	B	0.02
ECPR wavelength flatness	B	0.50
ISR photocurrent measurement	A	0.05
ISR photocurrent resolution	B	0.03
Picoamperimeter gain calibration	B	0.05
Picoamperimeter drift	B	0.04
Spatial uniformity	B	0.30
Temperature factor	B	0.20
Aperture correction	B	0.12
Long temp stability	B	0.50
Linearity (0 dBm to 30 dBm)	B	0.50
Relative combined standard uncertainty ($k=2$)		1.35

We have studied the long term stability of the spectral responsivity of this ISR from 1999 to 2004. We have two different calibration data to be compared: the 1999 set are referred to a cryogenic radiometer^(2,6) (CRI), and the 2002 and 2004 data are referred to the ECPR. Table 2 and figure 6 show the responsivity results obtained along these years. The differences compared with CRI data are lower than $\pm 0.5\%$. This result confirms that the long time stability of this radiometer is within the ECPR uncertainty.

Table 2: Long time stability responsivity for the ISR.

λ (nm)	1999 CRI		2002 ECPR		2004 ECPR		Relative difference	
	R(λ) (A/W)	U (k=2) (A/W)	R(λ) (A/W)	U (k=2) (A/W)	R(λ) (A/W)	U (k=2) (A/W)	2002/1999 (%)	2004/1999 (%)
1270.00	5.513E-03	7.260E-06	5.502E-03	6.309E-05	5.513E-03	6.309E-05	-0.20	0.01
1300.00	5.629E-03	8.640E-06	5.619E-03	6.443E-05	5.638E-03	6.240E-05	-0.17	0.16
1320.00	5.668E-03	7.660E-06	5.658E-03	6.487E-05	5.674E-03	6.487E-05	-0.18	0.10
1330.00	5.682E-03	7.600E-06	5.667E-03	6.497E-05	5.683E-03	6.497E-05	-0.27	0.02
1480.00	5.972E-03	6.620E-06	5.976E-03	6.852E-05	5.972E-03	6.847E-05	0.07	0.00
1530.00	5.978E-03	1.042E-05	5.977E-03	6.768E-05	5.979E-03	6.768E-05	-0.01	0.01
1550.00	5.910E-03	1.562E-05	5.890E-03	6.704E-05	5.884E-03	6.746E-05	-0.34	-0.45
1570.00	5.850E-03	1.248E-05	5.838E-03	6.644E-05	5.834E-03	6.690E-05	-0.21	-0.27

Conclusions

We have characterized an integrating sphere radiometer based on an InGaAs 3 mm diameter detector and 2-inch SPECTRALON® sphere.

The complete calibration of the ISR in the O, E, S, C, L and U band has been realised using four tuneable lasers diodes and an Electrically Calibrated Pyroelectric Radiometer. By employing the linearity factor of the detector, it is possible to extend the calibration of the radiometer up to +30 dBm with an estimated uncertainty lower than $\pm 1.4\%$ (k=2) in this spectral range.

As drawback, we found the impossibility of using the ISR in the E-band (specifically in the range from 1340 to 1440 nm) due to water vapour absorptions.

Acknowledgements

This work was supported by Spanish Commission Interministerial de Ciencia y Tecnologia, projects TIC2000-02005&TIC2003-01867 and by Comunidad Autónoma de Madrid through project 07T/0041/2003.

References

- /1/ P. Corredera, J. Campos, M. L. Hernanz, J. L. Fontecha, A. Pons y A. Corróns. *Metrologia* **35**, 273-277 (1998).
- /2/ P. Corredera, M. L. Hernanz, J. Campos, A. Corróns, A. Pons y J.L. Fontecha. *Metrologia* **37**, 513-516 (2000).
- /3/ D. H. Nettleton, in *New developments and applications in optical radiometry*, Bristol, Techno House, 93-97 (1989).
- /4/ P. Corredera, M. L. Hernanz, M. González-Herráez and J. Campos. *Metrologia*, **40**, 150-153 (2003)
- /5/ W. M. Doyle, B. C. McIntosh and J. Geist. *Optical Engineering* **15**, 541-548 (1976).
- /6/ Foukal P.V., Hoyt C., Kocchling H. and Miller P. J. *Appl. Opt.* **29**, 983-993.

Insertion Loss Measurement of Low Loss Fiber Optic Splices

NEMI Fiber Optic Splice Improvement Project

L. Wesson, Aurora; P. Arrowsmith and R. Suurmann, Celestica; D. Gignac, Nortel Networks;
S. Pradhan, Sanmina-SCI; J. Garren, Solectron; T. Watanabe, Sumitomo Electric; and E. Mies, Vytran

ABSTRACT

Results from a National Electronics Manufacturing Initiative (NEMI) project, formed to improve aspects of fiber optic fusion splicing, are reported. The focus of this paper is ultra low loss splicing for telecommunications product assembly, with typical loss of <0.05 dB per splice for standard SMF-SMF. A detailed review of available industry standards, relevant to splice loss acceptance criteria and loss test procedures, revealed the standards are generally inadequate for low loss splicing. Various project participants using different equipment and procedures performed fiber preparation, splicing, splicer loss estimation, and actual loss measurements. An industry standard gage repeatability and reproducibility (GR&R) analysis was used to compare the data. Loss measurement set-ups based on a cutback method for dissimilar fiber (SMF-EDF) splices showed significant directionality in some cases, and root cause was identified using a round robin approach. Several of the methods evaluated will form the basis for a new loss measurement standard for low-loss and dissimilar fiber splices.

INTRODUCTION

For many Optoelectronic manufacturing (OEM) applications, such as EDFA assembly, the ability to fabricate low loss fusion splices is critical for proper function of the optical circuit. Splice loss requirements of less than 0.05 dB are common. While the interdependence of the factors that cause variability in splice loss have been reported [1-3], at these very low loss requirements, the measurement uncertainty can be a significant problem in determining whether or not a splice is acceptable. Because it is usually not possible or practical to perform actual splice loss measurements during production builds, it is typically necessary to rely on the loss estimation provided by the splicer. To assess the accuracy of splice loss estimators at these low loss levels, a measurement system must be capable of repeatability and reproducibility (R&R) value of $\pm 10\%$ of the range, or ± 0.005 dB. Further measurement uncertainty arises in dissimilar fiber splices, where directionality can be observed.

The practical aspects of how to achieve repeatable measurements for low-loss similar and dissimilar fiber splices were the main drivers for forming a National Electronics Manufacturing Initiative (NEMI) member project in mid-2002. A comprehensive review and gap analysis of industry standards relating to splice loss acceptance and test methods revealed that most of these standards were developed for outside plant (field) splicing applications, where loss ranges of over 0.30 dB can be acceptable. [4] While TIA 455-34A [5] comes closest towards addressing the needs for a precision loss measurement method, there are important omissions for OEM splicing, e.g. measurement methods for splicing dissimilar fibers, such as SMF to EDF. The objectives of the NEMI project are to assess the repeatability of different measurement methods and set-ups, and to incorporate the best practices in draft standards for adoption by the appropriate industry organizations. Use of common test methods will enable comparison of splice losses and splicing equipment between vendors and users, and potentially lead to improvement in the accuracy of loss estimators and better splice yield for low loss applications.

EXPERIMENTAL METHODOLOGY

Gage R&R Test Method

To quantify and compare the capability of current splice loss test methods, a gage repeatability and reproducibility (GR&R) study [6] was conducted on several optical test system using various loss ranges and fiber types. This investigation required the production of 5-10 splices for a given process range. Each splice was measured three times, using 1-3 operators in a random order, resulting in 3-9 measurements per splice. The spliced fiber was moved between each measurement to introduce any additional variation that would normally occur during the splice. This data was then used to determine the measurement R&R by calculating the 99% spread of this distribution, taking into account both the equipment and appraiser variation represented by each data set. The measurement spread divided by the measurement range (either the actual range or a defined process or tolerance range) gives the gage R&R. The measurement system should ideally provide a percent R&R-value of $\leq 10\%$ for acceptable discrimination, 10-30% for marginal and $>30\%$ GR&R for poor. [6]

Loss Measurement Methods

Techniques commonly used to measure splice loss include an optical power source and meter, or an optical time domain reflectometer (OTDR). There are many variations possible when using a power source and meter, but in general they fall into one of two categories: the in-line method, Figure 1, where the fiber ends remain fixed throughout the entire testing process, or the "cutback" method, Figure 2, where the connection to the power meter is changed during the measurement. For this paper we refer to the cutback method as the Bare Fiber Adaptor (BFA) method, in reference to the need for connecting a free fiber end into the power meter detector. Both methods begin with setting up a reference fiber, then

measuring the splice loss compared to the reference. If the fiber under test has significant loss, compensation must be included. The test methods used in this study, summarized in Table 1, were further divided between those that accommodate similar and dissimilar fibers. Dissimilar fibers typically have different mode field diameters (MFD), which can result in significant contribution to the splice loss, according to Equation 1 [7, 8].

$$\text{Loss(dB)} = -20 \log \left(\frac{2 * \text{MFD}_1 * \text{MFD}_2}{\text{MFD}_1^2 + \text{MFD}_2^2} \right) \quad (1)$$

There are several setup variations that may make both the in-line and BFA methods more repeatable. These include using cladding mode strippers (per TIA 455-34A), external isolators and securing fibers to prevent unnecessary movement. Within the BFA measurements, distinction was also made between systems that incorporated an integrating sphere (IS), which ideally removes any measurement dependence on how the fiber is coupled to the detector.

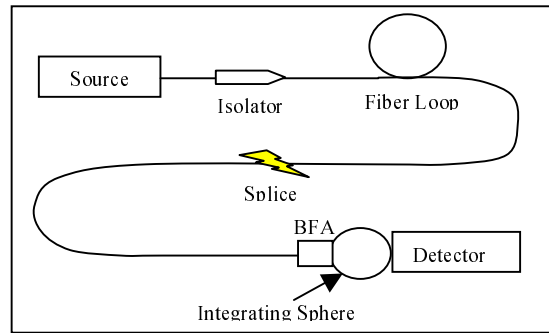


Figure 1. In-line method (I) for similar fibers (BFA and IS optional)

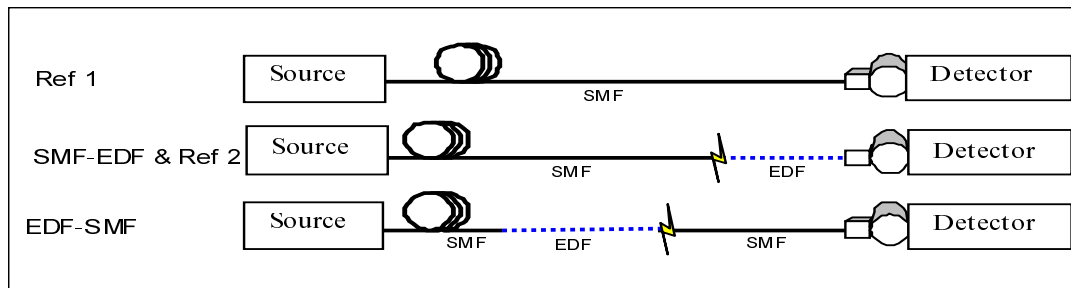


Figure 2. BFA method (B) setup for measuring dissimilar fibers in two directions (SMF and EDF shown)

Table 1. Splice loss measurement methods

Loss Test Method	Fiber Type(s)	Procedure	Attributes
In-line (I)	Similar	See Fig. 1. Initial setup consists of a reference fiber between an optical source and a power meter. The system is allowed to stabilize, the meter's wavelength is matched to the source and the meter referenced. The fiber is cut and spliced back together, with the new power meter reading representing the splice loss. [9]	Fiber ends at source and detector remain fixed throughout. BFA not required.
Bare Fiber Adapter (BFA) "cut-back" (B)	Similar or dissimilar	See Fig. 2. Fiber end at the power meter is prepared and inserted into the BFA. The BFA is inserted into the detector or integrating sphere and the power meter referenced (1st stage). Next, the fiber is removed from the BFA. A piece of test fiber cut, prepared at one end and inserted into the BFA. The other end of the test fiber is spliced to the reference fiber. The new reading on the meter indicates the splice loss (or the combined splice and fiber losses). A second length of test fiber may be added to enable measurement in the other direction (3rd stage).	Different splices required to make measurements in each direction. Absorption correction required if test fiber has non-negligible loss. Integrating sphere recommended.
OTDR (O)	Similar (not evaluated for dissimilar)	Use of an OTDR for fusion splice evaluation is described in Telcordia GR-765-CORE and in detail in TIA/EIA fiber optic test procedures (FOTP) 455-8 and 455-59. [10, 11]	OTDR is continuously self-referencing so the long term stability of the optical source is irrelevant. Long fiber lengths required.
Directional BFA (D)	Dissimilar	Modified BFA method, based on Fig. 2, for each direction. The splice section remains intact. For details see Appendix C of Ref. 4.	Measurement of same splice in each direction enables a paired comparison assessment of directionality.
BFA with add-on (A)	Dissimilar	See Fig. 2, 3rd stage. The system is referenced with the test fiber, a length of reference fiber (with negligible loss) is spliced on and the loss measurement made.	Single loss direction only, e.g. test-to-reference fiber. Absorption correction not required.
Inserted section (S)	Dissimilar	Start as In-line method, Fig. 1. The fiber is cut 1-2 m from end, a length of test fiber is spliced in and the measurement made.	Fiber ends remain fixed. Two splices, each direction, measured in aggregate.

RESULTS AND DISCUSSION

Gage R&R for Similar Fiber Splices

Test setups representing the In-line, BFA and OTDR methods were compared amongst different participants (users), using the Gage R&R stability and repeatability metrics. Table 2 provides a summary of the results for the lowest loss range investigated (0-0.05 dB). Based on the % R&R data, only 5 of the 9 methods were able to meet the 10% threshold and obtain a rating of “adequate”. The addition of stability results further degraded the performance with only two of the methods meeting the 10% threshold. Significant levels of variation were seen across and within each test method. For example, even within the in-line test method, results varied by a factor of three or more, with %R&R variations from 2.4% to 16.1%. Similar results are shown for the BFA method. Group B-3 obtained a very high value, which is indicative of a faulty gage.

The results of the study indicate that many of the commonly used methods for assessing optical power loss need careful implementation and assessment to achieve trustworthy and meaningful results. Also, the data did not suggest that any one method (in-line, BFA, OTDR) was consistently superior. Possibly, factors such as splice and test equipment, testing environment, and whether or not an isolator is used, play a bigger role than anticipated. These findings further emphasize the need for standards that describe the practical aspects of low loss splice testing in more detail.

Table 2. Gage R&R test results for standard SMF similar fiber splices (two-sided values). The setups are described in Table 1.

Setup-User	R&R (dB)	% R&R (%)	Stability (dB)	% R&R + Stability (%)
I-1	0.0012	2.4	0.0034	7.2
I-2	0.0026	5.3	0.0028	7.7
I-3	0.0054	10.9	0.0100	22.8
I-4	0.0080	16.1	0.0472	95.8
B-1	0.0154	30.7	0.008	34.6
B-2	0.0036	7.2	0.006	14.0
B-3	0.0769	153.8	---	---
B-4	0.0052	10.3	0.010	22.5
O-1	0.0190	38.1	---	38.1

Table 3. Gage R&R results for SMF-EDF splice loss measurements at 1310nm (two-sided). Values for each direction are combined.

Test Method	Test Setup	Max GR&R (%)	Min GR&R (%)	Avg. GR&R (%)
D	B-1	8.8	7.8	8.3
D	B-3	4.5	3.0	3.7
B	B-4	1.5	0.9	1.2
D	B-4	1.6	1.5	1.6
D	B-5	3.0	1.5	2.2
D (EDF2)	B-5	3.0	0.0	1.5
D	B-6	4.6	3.4	4.0

Gage R&R for Dissimilar Fiber Splices

The two BFA-cutback methods (methods B and D, Table 1) were assessed using gage R&R for EDF to SMF fiber splices. The values shown in Table 3, based on a typical loss process range (tolerance) of 0.2 dB for SMF-EDF, indicate both methods have acceptable measurement repeatability for this range of interest. The contribution to the variation from stability (not shown in Table 3), would approximately double the R&R values (cf. Table 2).

Effect of Measurement Direction and Other Variables

The purpose of investigating the loss measurement of dissimilar fiber splices was to evaluate the performance of different user test setups and to determine whether splice losses are significantly different depending on the direction in which they are measured. The BFA-cutback method has the advantage of enabling the splice loss to be measured in the forward and reverse directions for dissimilar fibers, e.g. when the fibers have mismatched MFDs, as for SMF-EDF splices. Theory predicts there should be no directionality dependence for pure Gaussian mode propagation, as given by Equation 1. Although directional dependence of the loss is not expected, to our knowledge this has not been experimentally verified. Since a proposed standard method would need to accommodate any directional dependence, this issue was addressed in the methods.

Since EDF exhibits optical non-linearity and loss measurement instability in the gain region at 1550 nm, 1310 nm was used to obtain more precise measurements. Results obtained with the various set-ups based on the two BFA-cutback methods are shown in Figure 3. The divergence of the data sets indicates that some users observed significant measurement directionality, well above the measurement standard deviation.

Although the source of the directionality may be the fiber combination, the splice and/or the test set-up, a clue was revealed by ranking the data by the difference in loss for each direction. There was complete separation between set-ups that utilized an integrating sphere and those that did not. One user made measurements with and without fiber loops and did not observe any significant difference in directionality. Since the directionality finding was unexpected, the cause was investigated by means of a round-robin study, whereby splices made by several users are measured on all the various set-ups.

Round-Robin Study

The round-robin was performed with four users, all of whom made measurements in each direction on sets of SMF-EDF splices prepared with two types of EDF (method D). The directional results (Figure 4) show that test users B-3 and B-4 obtained high directionality ($>\pm 0.05$ dB). There is no significant directionality dependence associated with the fiber type, the splice preparation or the splice sample. This leads to the conclusion that the measurement set-up is the source of the directionality, and the effect correlates with absence of the integrating sphere.

The loss values measured in the round-robin were also compared by averaging the two directional values for each splice. The good agreement (within 0.05 dB) between different users further supports that the observed directionality is a measurement artifact, and not a physical loss difference. The good agreement of average losses across measurement set-ups also points to the possibility of standardizing on a “bi-directional average” method for specifying dissimilar fiber splice loss, as an alternative to using an integrating sphere.

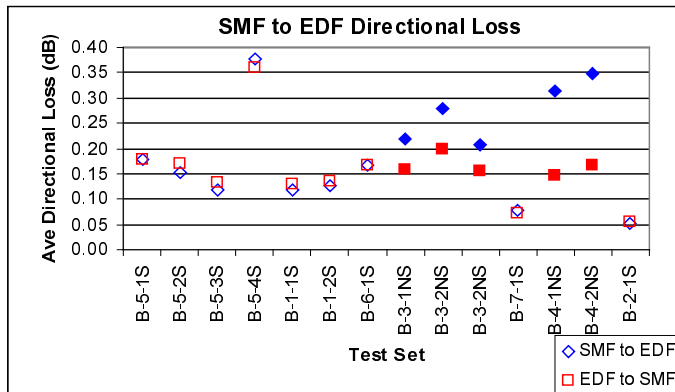


Figure 3. Loss data for SMF-EDF splices, measured in each direction at 1310 (method B and D). Set-ups B-3 and B-4 are without integrating sphere (NS).

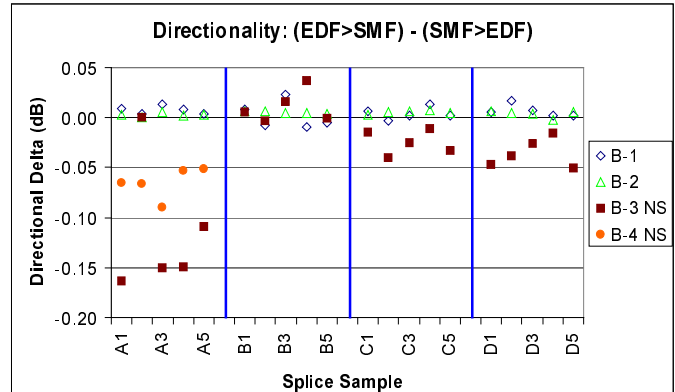


Figure 4. Round-robin directional data for SMF-EDF splices, at 1310 nm. A-D are fiber combinations and B-1 to B-4 user test set-ups.

Field Intensity Distribution Measurement

Far field intensity measurements for both the erbium doped fibers, as well as standard SMF, showed that at high angles of incidence, both of the EDF fibers have a significantly broader far field pattern compared to standard SMF. [4] This is as expected, given that the MFD of the erbium fibers at 1310 nm is 5.0 μm , versus 9.2 μm for SMF. (The more tightly guided the mode within the fiber, the greater the expansion exiting the fiber.) (See Ref. 12 for a detailed treatment.)

The differences in the far field patterns between EDF and SMF point to an explanation for the observance of directional splice losses with non-integrating sphere measurement systems. The purpose of the integrating sphere is to collect a constant fraction of the light emitted from the end of the fiber, regardless of angular input to the sphere (and other optical properties), and couple this to the detector. If an integrating sphere is not used, it is possible that some of the power radiating at large angles from the end of the fiber is “lost”, either because it simply “missed” the detector, or because the detector has reduced sensitivity to off-axis light. Because splice loss measurements involve the detection of very small change in power, even very subtle differences in collection efficiency between fiber types can significantly influence the measurement results.

If a detector system were unable to collect power at high output angles, say $>12^\circ$, the reference power reading exiting EDF would be lower than actual. If SMF is then spliced on to the EDF, and a reference power reading exiting the SMF is then taken, the “lost” power from the EDF reference would now be collected, and the apparent loss of the splice would therefore be lower than actual. This was indeed the case for the non-integrating sphere measurement systems used in this study. The apparent loss was lower when splicing EDF into SMF. This also explains why the “bi-directional average” splice losses were in good agreement between all measurement systems, even when high directionality was observed. This is because any power that is “lost” when measuring in one direction, is identically “gained” when measuring in the other. When averaged, this adds nothing to the actual loss.

Verification of Test Methods for Dissimilar Fiber Combinations

The BFA add-on (A), directional (D) and inserted section (S) are suitable loss measurement methods for dissimilar fiber splices and these were further evaluated using fiber types with substantially different MFD from standard SMF. The results

are shown in Table 4. Here the precision (defined as measurement error divided by the average loss for the data set) is based on the tolerance method because the splice loss varied widely for the different fiber types and users. Loss values for method S were halved to give the average loss per splice. The methods have acceptable repeatability (<5%) and they are candidates for inclusion in the proposed new standard.

Table 4. Loss values for various fiber combinations and user set-ups for three methods. HNA (High NA) and LEAF refer to different types of fiber. PDL and Pwr are the polarization dependent loss and power modes of the test equipment.

Method	Fiber Combination	Wavelength (nm)	User	# Parts/ Appraisers	Avg Loss (dB)	GR&R +/-Error (dB)	Relative +/-Error (%)
A	EDF1-SMF	1550	B	10/2	0.1163	0.0072	6.2
A	EDF2-SMF	1550	B	10/2	0.1988	0.0068	3.4
A	EDF2-SMF(PDL)	1550	B	5/1	0.2445	0.0033	1.4
A	EDF2-SMF(Pwr)	1550	B	5/1	0.2355	0.0038	1.6
D	HNA-SMF	1310	B	6/1	0.2504	0.0067	2.7
	SMF-HNA				0.2534	0.0057	2.3
D	LEAF-SMF	1550	B	5/1	0.1285	0.0074	5.8
	SMF-LEAF				0.1239	0.0050	4.1
S	SMF-HNA-SMF	1310	B	10/1	0.2384	0.0189	7.9
S	SMF-HNA-SMF	1550	B	10/1	0.2452	0.0059	2.4
S	SMF-HNA-SMF	1310	D	10/1	0.7006	0.0016	0.2
S	SMF-HNA-SMF	1550	D	10/1	0.5914	0.0018	0.3
S	SMF-LEAF-SMF	1550	B	10/1	0.1017	0.0042	4.1
S	SMF-LEAF-SMF	1550	D	10/1	0.1126	0.0019	1.7
S	SMF-HNA-SMF	1310	F	10/1	0.6060	0.0050	0.8
S	SMF-LEAF-SMF	1550	F	10/1	0.1275	0.0050	3.9

CONCLUSIONS

A review of currently available standards related to optical fiber splicing and splice loss measurements revealed that they do not adequately address the very low splice loss specifications and dissimilar fiber splicing requirements of today's typical optoelectronic manufacturing applications. An industry-wide gage R&R study confirmed that many of the commonly used methods for measuring optical power loss need careful implementation and assessment to achieve trustworthy and meaningful results. These findings emphasize the need for standards that describe the practical aspects of low loss splice testing in more detail. The gage R&R analysis was found to be a useful way of qualifying and comparing these measurement methods and is recommended as a means for verifying measurement capability.

A round-robin measurement comparison of EDF-SMF fiber splices showed that the directionality that can often be observed in these measurements is primarily a measurement artifact and not a true directional loss difference. The use of an integrating sphere, and/or a bi-directional average splice loss method is required for accurate results.

The description of the loss test methods for both absorbing and non-absorbing dissimilar fiber splices will form the basis of the draft specification to be developed in collaboration with interested standards organizations.

Acknowledgements

Project members acknowledge the assistance of D. Godlewski of NEMI. We thank the TIA for the generous donation of sets of standards for review, Sumitomo Electric and StockerYale for donating fiber, and JDS Uniphase for loan of test equipment.

REFERENCES

1. Zamzow, B. and Takasu, K., "Fusion Splicing of Fiber Optic Components – How to Minimize Rework", Proc. of the IPC SMTA Council APEX 2002 Technical Conference, S09-1 (2002)
2. Zamzow, B. and Takasu, K., "Splicing Loss Control and Assembly Yield Management", SMTA-IMAPS Joint Conference on Telecom Hardware Solutions (2002)
3. Corning application note: Single Fiber Fusion Splicing, AN103, September 2001
4. Proc. IPC-APEX, paper S35-2-1, February 2004
5. TIA/EIA 455-34A: Interconnection Device Insertion Loss Test (Oct 1995, reaffirmed May 2002)
6. Measurement Systems Analysis: Reference Manual. Automotive Industry Action Group (1998)
7. Kilmer, J., "Optical Fiber Mode Field Diameter Specification - Statistical Analysis of Predicted Splice Loss", in Proc. SPIE, Fiber Optics Reliability; Benign and Adverse Environments II, 992 (1988)
8. Mynbaev, D. and Scheiner, L. *Fiber-Optic Communications Technology*, p. 249, Prentice Hall, 2001. ISBN 0-13-962069-9
9. Derickson, D., *Fiber Optic Test and Measurement*, ISBN 0-13-534330
10. TIA/EIA 455-8, Measurement of splice or connector loss and reflection using an OTDR
11. TIA/EIA 455-59, OTDR Measurement of Fiber Point Defects
12. Ghatak A. and Thyagarajan K. *Introduction to Fiber Optics*, Cambridge University Press. ISBN 0-521-57785-3

Quantum Cryptography in Optical Networks and Supporting Metrology

R. J. Runser¹, P. Toliver¹, S. McNown², T. E. Chapuran¹, M. S. Goodman¹, J. Jackel¹, R. J. Hughes³,
J. E. Nordholt³, C. G. Peterson³, K. Tyagi³, P. Hiskett³, K. McCabe³

(1) Telcordia Technologies, 331 Newman Springs Rd., Red Bank, NJ 07701

Tel: (301) 688-1841; Fax: (301) 931-2591; rrunser@telcordia.com

(2) Laboratory for Telecommunication Sciences, Adelphi, MD 20783

(3) Los Alamos National Laboratory, Los Alamos, NM 87545

Introduction

While the need to provide security has long been a critical driver for the design and architecture of government networks, it is also becoming increasingly important to provide secure networking for commercial services over today's infrastructure. Supporting electronic financial transactions, virtual private networks (VPNs), and virtual local area networks (VLANs) over a shared network are some of the key drivers for security on today's large service provider and carrier networks. These services today typically depend on cryptographic algorithms which rely on mathematical or computational complexity for providing security. The conditional security guarantees of these "classical" cryptographic methods are predicated on specific assumptions related to future advances in both mathematical techniques and computation. However, the difficulty in predicting future breakthroughs in mathematical methods and computation may limit the applicability of today's cryptographic techniques to future security needs.

Quantum cryptography (QC) has recently emerged as a candidate for providing security based on the fundamental laws of physics rather than algorithmic complexity [1]. Quantum key distribution (QKD), a subset of QC, has recently emerged as a potential near term application of these new security techniques. QKD provides a secure means to transmit cryptographic keys for symmetric classical cryptography. The inherent ability of QKD to provide the end users a built-in capability to detect the presence of an eavesdropper makes it ideal for protecting the transfer of cryptographic keys which provide today's security foundation. QKD is beginning to approach the threshold of commercial feasibility. Several companies throughout the world are already advertising the availability of QKD appliances [2]. These systems are designed to operate over dedicated point-to-point dark optical fiber links. Although there are likely to be important applications that can utilize QKD in these dedicated environments, compatibility with the overall optical networking infrastructure would allow deploying fiber-based QKD on a wider scale. This paper identifies the issues associated with deploying QKD systems on existing fiber networks and the prospects for multiplexing quantum channels onto fiber links carrying classical optical communications wavelengths generated by commercial DWDM systems. The metrology for qualifying fiber links for QKD in these environments is critically important for understanding the scalability of QKD and more generally the applicability of quantum cryptography to today's fiber infrastructure.

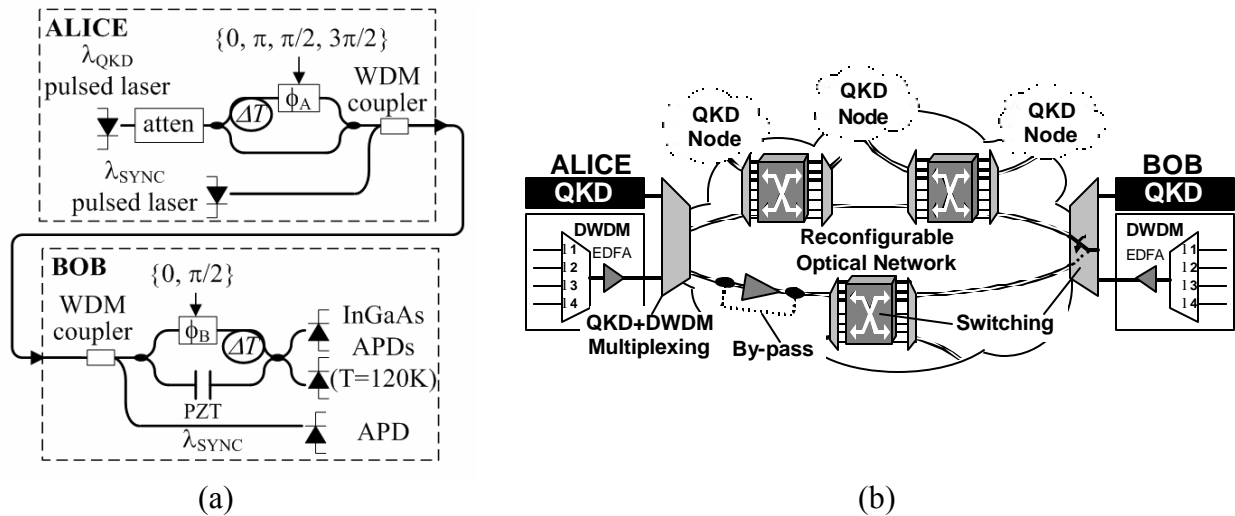


Fig. 1 (a) phase-based BB84 QKD fiber optic system architecture; (b) implementation of QKD systems on reconfigurable optical networks with classical DWDM bearer channels

QKD System Overview and Architecture

Although there are many different approaches for implementing fiber-based QKD, a typical configuration uses the BB84 protocol [3] implemented in the phase basis as described in Fig 1(a) [4]. In this approach, single photons at Alice (sender) pass through a Mach-Zehnder interferometer containing a fixed time delay, ΔT , and a phase modulator, \mathbf{f}_A , in one of the arms. The phase is modulated with one of four different states depending on whether Alice's secret random bit is a 0, $\mathbf{f}_A = \{0, \pi/2\}$, or 1, $\mathbf{f}_A = \{\pi, 3\pi/2\}$, and on her random choice of non-orthogonal basis state $\{0, 3\pi/2\}$ and $\{\pi/2, \pi\}$. Bob uses a similar interferometer and time delay to perform measurements on the photons he receives from Alice and randomly chooses between basis states by setting $\mathbf{f}_B = 0$ or $\pi/2$. He assigns a bit value, 0 or 1, according to which of the two APD detectors fires. In an ideal system, Alice and Bob will unambiguously agree on the bases used for the transmission and detection when the phase difference, $(\mathbf{f}_A - \mathbf{f}_B)$, is 0 or π , which occurs with 50% probability. Alice and Bob perform an authenticated public discussion to determine which bits were unambiguously measured by simply exchanging the basis that was used. The possible states for 0 and 1 are non-orthogonal, so exchanging the basis does not reveal the value of the bit. In order to account for realistic imperfections (whether they are intrinsic to the system or created by an eavesdropper), two additional post-processing procedures are generally performed—error correction and privacy amplification. For the approach illustrated in Fig. 1(a), the interferometers require phase tracking due to slowly varying thermal conditions at Alice and Bob. An air gap controlled by a piezo-transducer (PZT) is used to provide active stabilization. Additionally, a synchronization pulse at a different wavelength, λ_{sync} , far from the quantum channel, λ_{QKD} , is often used to gate the single photon detectors for reducing detector noise at Bob [4].

Although QKD systems have been demonstrated over a wide variety of point-to-point dedicated fiber links, few experiments [5] have evaluated the potential for adding QKD directly to existing classical DWDM networks. A general architecture for deploying QKD in a multi-user optical network is shown in Fig. 1(b). Wide-band multiplexers are used to combine classical DWDM channels with a quantum channel from Alice's QKD system. These signals are transmitted together over the same fiber infrastructure and are demultiplexed using high isolation filters at Bob. Along the path between Alice and Bob, it is possible to re-route the connection using a transparent optical switch at an intermediate node. Switching may also occur at Bob to facilitate optical protection and restoration in redundant network configurations such as a fiber ring [6]. This reconfigurable network provides the capability to establish cryptographic keys among multiple parties over existing infrastructure. Active elements such as mid-span optical amplifiers require a by-pass path to avoid wavelength selective components and optical noise that could disturb the QKD signal [7]. Although the architecture described in Fig. 1(b) may seem straightforward to implement, many challenges must be overcome to successfully achieve this vision. This presentation will address some of these challenges and demonstrate techniques for achieving interoperability between today's classical communications networks and future QKD systems.

Characterizing Broadband Noise Emission from Classical Systems

In order to combine quantum and classical signals on the same fiber infrastructure, the noise properties of the classical system must be well characterized to avoid interference with the quantum channel at *both* Alice and Bob. In dedicated QKD systems, detector dark counts typically limit system performance under practical experimental conditions. In gated mode, QKD detectors in the telecommunications window exhibit dark count probabilities of $1\text{E-}4$ to $1\text{E-}5$ per gate which is on the order of a few nanoseconds [1]. This implies that the noise generated in the QKD wavelength region by other sources should be limited to less than $1\text{E-}4$ photons per gate at Bob's receiver.

Fig. 2 shows the wideband optical spectrum of potential sources of classical interference in the region of the quantum channel. The average power, typically given in dBm, has been converted to photons/ns to reflect the magnitude of the probability of detecting noise photons within Bob's detector gate interval. On this scale, a typical 0dBm classical channel at 1550nm contains approximately 8×10^6 photons/ns. The full spectrum of a single DFB laser is measured in Fig. 2(a) over the telecommunications window. (Although the peak power at 1550nm was set to 0dBm, it is not resolved in the measurement.) For classical communications, the laser provides an excellent signal to noise ratio (approx. 50 dB). However, the spontaneous emission noise in the 1550nm region is in the hundreds of photons/ns presenting a formidable challenge for multiplexing a QKD channel in or around the carrier. The 67dB dynamic range of the instrument limited the accuracy of measurements below 2 photons/ns. In order to evaluate the noise properties of wavelengths below 1500nm, the 1550nm carrier was suppressed using a notch filter. By reducing the peak power of the carrier, the dynamic range of the measurement was extended to the noise floor (in

this case, $1\text{E-}3$ photons/ns) for wavelengths in the 1300-1500nm region. Note that the spontaneous emission noise from the laser extends down into the 1300nm window albeit at a much reduced average power.

Fig. 2(b) shows the complex spectrum typical of a commercial amplified DWDM system. Four bearer channels modulated with data are clustered close together in the 1550nm region and amplified by an EDFA. A 1510nm supervisory channel, also modulated by the system, is multiplexed with the DWDM traffic. The dynamic range of the instrument limits the accuracy of the measurement. The spurious peaks in the region less than 1500nm were determined to be instrument artifacts. However, when the optical channels from the DWDM system were suppressed by a filter, the spectrum revealed optical noise in the 1300 nm region that was not observed previously. While the specific noise source was not immediately identified, it is likely due to the combination of broadband EDFA noise and the filter architecture used on the DWDM line output.

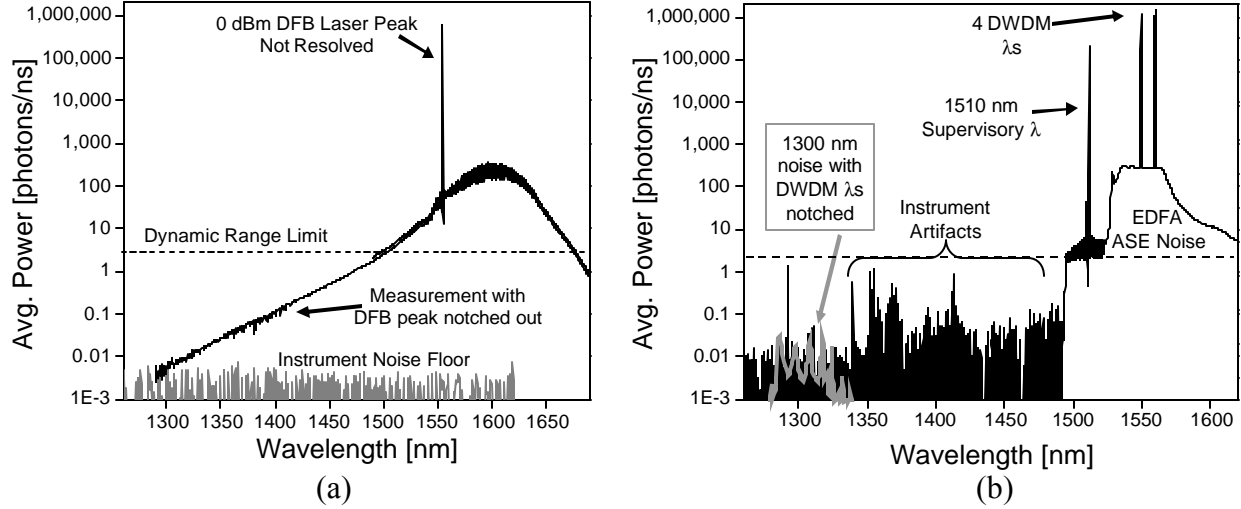


Fig. 2 (a) broadband optical spectrum of a 0dBm DFB laser; (b) broadband optical spectrum of a 4 wavelength DWDM system

To successfully multiplex and demultiplex quantum signals in the presence of classical communications channels, both Alice and Bob must use filters for noise suppression at the transmitter and channel isolation at the receiver. The choice of the quantum wavelength in these scenarios is determined by minimizing the potential sources of classical noise as well as choosing a wavelength in the low loss region of conventional fiber to maximize QKD throughput. In the examples described in Fig. 2, a potential wavelength for the QKD channel is in the 1310nm region. Alice must use a filter to suppress the 1310nm noise from the classical sources prior to multiplexing. In both cases, a simple 1310/1550nm wide-band multiplexer can provide $>30\text{dB}$ suppression at 1310nm to reduce in-band interference to the QKD detector noise limit. Bob, however, has a more stringent requirement for extracting the quantum channel from the classical channels at the receiver. Bob's demultiplexer must provide at least 120dB isolation between the 1310 and 1550nm bands to prevent leakage of the light from the classical channels into the single photon detectors [8].

Experimental Demonstration of QKD and DWDM Transmission over 10 km of Conventional Fiber

To investigate the prospects for implementing QKD over a fiber network shared with classical DWDM systems, the architecture shown in Fig. 3 was experimentally implemented. The QKD system throughput and quantum BER or QBER [1] were evaluated as a function of the DWDM system launch power by varying an optical attenuator at Alice. A 1310nm QKD system similar in design to the BB84 approach but using the simpler B92 protocol [9] was multiplexed with a commercial DWDM system at 1550nm using a thin film, wide-band multiplexer. The average photon per pulse at the output of Alice was set to 0.5 at the input of the band multiplexer. A cascaded filter architecture of high isolation, band demultiplexers was used at Bob to provide $>120\text{dB}$ isolation between the quantum and classical channels. In both filter designs, the filter cut-off was near 1410nm. In the back-to-back configuration ($\ll 1\text{km}$ fiber), an average rate of 500 secret bits/s were transferred between Alice and Bob with a QBER of 3.6% after error correction and privacy amplification. Since there was no dependence on the launch power of the DWDM system, we conclude that the filters provided adequate noise suppression and isolation.

To emulate a networking environment, 10 km of fiber was inserted between Alice and Bob. The QKD throughput in the absence of the DWDM system (atten. = ∞) was reduced to about 200 secret bits/s due to the fiber loss at

1310nm. However, as the DWDM system power was increased, the throughput of the QKD system dropped rapidly and the QBER rose to over 7.5%. Upon careful investigation of the optical spectrum at Bob's 1310nm port, it was discovered that broadband noise was generated in the fiber by the classical DWDM channels. The Initial Key Bits (photon detector clicks) for the 10km experiment shown in Fig. 3 actually increased as the WDM system power increased. Since this effect was not observed in the back-to-back configuration, we have concluded that the noise is the result of nonlinear scattering in the 10km fiber spool. The suspected source of this noise is spontaneous anti-Stokes Raman scattering. Due to the wide-band nature of the Anti-Stokes noise generated by the classical channels, a portion of the noise passes through the passband of the band demultiplexer into the QKD port at Bob's receiver.

To reduce the impact of the scattered light on the QKD system performance, a 1310nm bandpass (BP) filter, centered on the QKD wavelength, was added after the band demultiplexer. As shown in Fig. 3, the BP filter loss reduced the throughput in the 10km configuration to 100 secret bits/s. However, as the DWDM system power was increased to the maximum level (atten. = 0dB), there was no observed degradation in the throughput or the QBER.

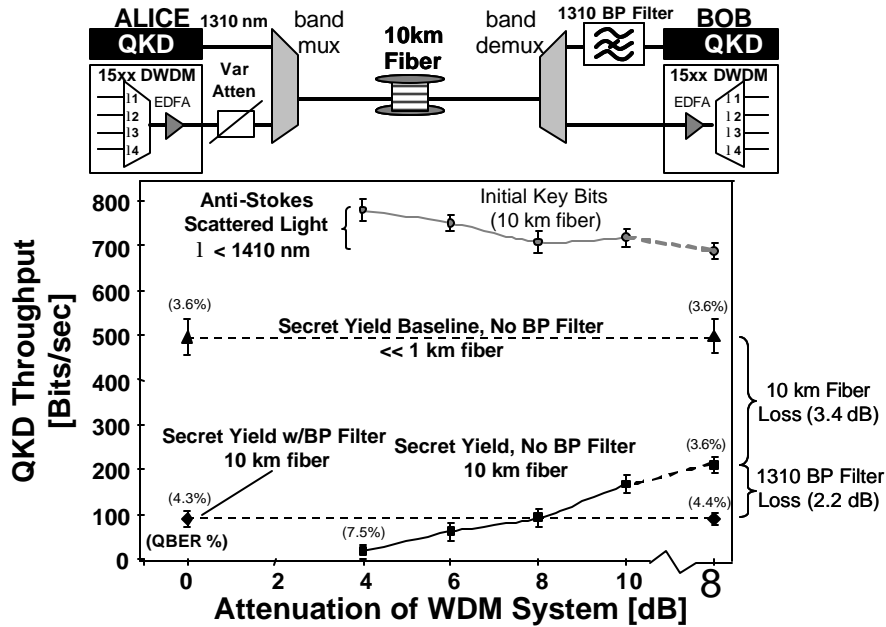


Fig. 3 1310nm QKD system throughput and QBER as a function of the launch attenuation of a 1550nm DWDM system multiplexed onto a shared fiber span.

Conclusions

We have demonstrated the successful transmission of 1310nm QKD signals over a 10km fiber span carrying amplified 1550nm DWDM channels. We have established a filter design and wavelength selection criteria that reduce the impact of noise from classical optical systems while minimizing the effect of broadband Raman scattering on the received QKD signal. This is an important step toward realizing practical QKD systems over installed fiber networks.

References

- [1] N. Gisin, G. Ribordy, W. Tittel, and H. Zbinden, *Rev. Mod. Phys.*, vol. 74, pp. 145–195, 2002.
- [2] See for example: www.magiqtech.com or www.idquantique.com
- [3] C. Bennett, and G. Brassard, *Proc. IEEE Int. Conf. on Comp., Sys., and Sig. Proc.*, Bangalore, India, 1984.
- [4] P. Townsend, P.J. G. Rarity, P.R. Tapster, *Electronics Lett.*, vol. 29, pp. 634–639.
- [5] P. Townsend, *Electronics Letter*, vol. 33, pp. 188–190, 1997.
- [6] P. Toliver, R.J. Runser, T.E. Chapuran, J.L. Jackel, et al., *IEEE Photon. Techn. Lett.*, **15**, pp. 1669–1671 (2003)
- [7] R. Hughes, J. E. Nordholt, M. S. Goodman, *IEEE Commun. Mag.*, to be published.
- [8] M. Goodman, P. Toliver, R.J. Runser, T.E. Chapuran, J. Jackel, R.J. Hughes, et al., *LEOS* 2003.
- [9] R. J. Hughes, G. L. Morgan, and C. G. Peterson, *J. Mod. Optics*, vol. 47, pp. 533–547, 2000.

* We acknowledge the support of Tim Persons at ARDA and Art Goldman and Nnake Nweke at the Laboratory for Telecommunication Sciences for helpful discussions.

Measurement of phase diagrams of optical communication signals using sampled coherent detection

Michael G. Taylor

*Optical Networks Group, Dept. of Electronic & Electrical Engineering, University College London,
Torrington Place, London WC1E 7JE, UK; e-mail: mtaylor@unodos.net*

Abstract A phase diverse coherent detection apparatus is used to obtain a description of an optical signal as an electric field versus time. This information can be displayed as a phase diagram, or used to make diagnostic decisions about the signal.

Introduction

After many years where on-off modulation was the universal mode of imposing digital information on an optical carrier, there has recently been interest in imposing information on the phase of the lightwave. In most experiments differential detection is used to extract the phase information, such as with the binary formats DPSK [1] and RZ-DPSK [2], and the oDQPSK format [3] which imposes information on the inphase and quadrature parts of the carrier. Also it has been suggested recently that new technologies will make coherent detection viable [4-5]. Since studying the power of the optical signal is of limited benefit, to work with these phase-encoded formats a measurement method is needed which delivers the electric field of the optical signal, and which can display a component of the electric field (the inphase or quadrature part) vs. time, and the phase diagram.

In this paper it is shown that sampled coherent detection is an effective way to access and display the electric field vector. This method combines phase and polarisation diverse coherent detection with post-processing of the discrete-time samples to give a mathematical representation of the electric field vs. time within a numerical processor. Sampled coherent detection was introduced in references 4 and 5 as a way of solving some of the issues of transport of dense WDM signals, and it was proposed to use a dedicated numerical processor housed in an ASIC for that application. For the test equipment-type application a burst-mode architecture can be used, where the numerical processor does not have to make calculations in real time. This burst-mode architecture has the advantage that more sophisticated algorithms can be applied and the algorithm being used can be changed by software, at the cost of less than 100% of the samples being processed.

Phase diverse coherent detection

Coherent detection differs from direct detection in that the incoming signal is mixed with a c.w. local oscillator (LO) of near-identical wavelength, and the photocurrent in the detector then corresponds to the beat product of the two lightwaves. Figure 1 shows how the signal is mixed with the LO in a phase/polarisation diverse hybrid, as detailed below. The outputs of the photodetectors are digitised at a sample rate typically higher than the symbol rate of the signal, and the samples taken over an interval of time are stored in memory. A numerical processor calculates the envelope of the signal electric field from the stored samples, and can display the result in the desired way. When the calculations are complete the process is repeated with another observation burst.

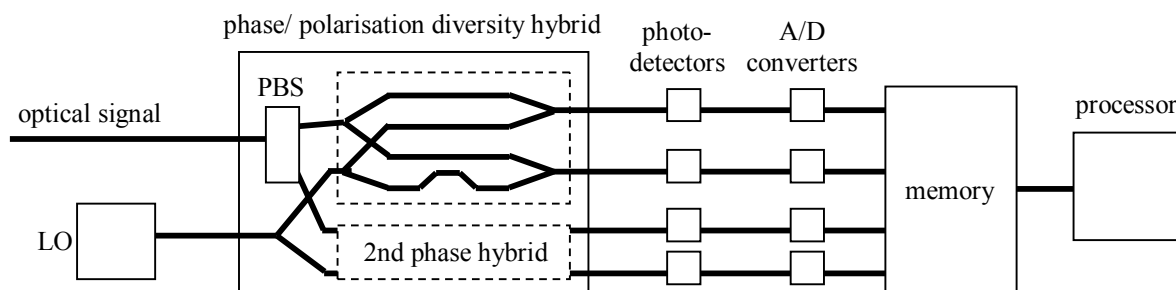


Figure 1 Layout of a sampled coherent detection analyser

The function of a phase diverse hybrid is to combine the signal and LO in (at least) two paths going to separate photodetectors, where the LO has a $\pi/2$ phase shift in one path compared to the other. The information from the two photodetectors delivers the inphase and quadrature parts of the optical signal, whereas with a single coherent detection path only one component of the signal's electric field can be determined. The phase diverse combining stage is indicated in the dotted box of Figure 1.

Because coherent beating only happens when the local oscillator has a similar state of polarisation (SOP) to the signal, and it is not possible to predict the signal's SOP, it is necessary to add polarisation diversity for the coherent detection method to work for all possible signal SOPs. As shown in Figure 1, the signal is separated by a polarisation beamsplitter (PBS) into two orthogonal components, and each of these goes into a separate phase diverse combining stage. The information from the four photodetectors enables the electric field vector for both polarisation components to be calculated.

The phase diverse coherent detection process is described mathematically below. The equations that follow use the outputs of one phase diverse hybrid and assume that the signal is aligned in SOP with the LO in that hybrid. The equations can be extended to take into account the polarisation diverse outputs, in which case the Jones vector is calculated, instead of simply the complex electric field envelope. The electric field of the signal can be written as $\text{Re}[E_s(t)\exp(i(\omega_s t + \phi_s))]$, where $E_s(t)$ is the complex envelope containing the information encoded on the optical signal, ω_s is the angular frequency of the optical carrier, and ϕ_s is the slowly varying phase arising from the phase noise of the carrier. The local oscillator electric field can be written as $\text{Re}[E_{LO} \exp(i(\omega_{LO} t + \phi_{LO}))]$, where E_{LO} is a constant given that the local oscillator is c.w., and ω_{LO} and ϕ_{LO} are the angular frequency and phase of the LO. The electric field of the light arriving at each of the two outputs of the phase diverse hybrid is the sum of the signal and LO fields, as follows

$$\begin{aligned} E_1 &= \text{Re}[E_s(t)\exp(i(\omega_s t + \phi_s)) + E_{LO} \exp(i(\omega_{LO} t + \phi_{LO}))] \\ E_2 &= \text{Re}[E_s(t)\exp(i(\omega_s t + \phi_s)) + iE_{LO} \exp(i(\omega_{LO} t + \phi_{LO}))] \end{aligned}$$

The photodetector responds to the optical power, which is related to the electric field by

$$P_1 = E_1^* E_1 = |E_s(t)|^2 + |E_{LO}|^2 + 2 \text{Re}[E_s(t)E_{LO}^* \exp(i(\omega_s - \omega_{LO})t + \phi_s - \phi_{LO})]$$

$|E_{LO}|^2$ is constant with time, and $|E_s(t)|^2$ is small given that the local oscillator power is much larger than the signal power. We can write the difference between P_1 and its time average as ΔP_1 , and

$$\Delta P_1 = 2 \text{Re}[E_s(t)E_{LO}^* \exp(i(\omega_s - \omega_{LO})t + \phi_s - \phi_{LO})]$$

Alternatively, ΔP_1 can be obtained by differential detection using a 4-port phase diverse combining stage instead of 2-port, and the common mode terms are rejected inherently. Similarly for the second output of the phase diverse hybrid

$$\Delta P_2 = 2 \text{Im}[E_s(t)E_{LO}^* \exp(i(\omega_s - \omega_{LO})t + \phi_s - \phi_{LO})]$$

The electric field envelope of the signal can therefore be constructed within the numerical processor by

$$E_s(t) = \frac{1}{2E_{LO}^*} \exp(-i(\omega_s - \omega_{LO})t - (\phi_s - \phi_{LO})) (\Delta P_1 + i\Delta P_2)$$

To calculate the Jones vector, the top two outputs of the phase/polarisation diverse hybrid in Figure 1 are used to obtain the first element, and the bottom outputs the second element of the Jones vector. The phase of the signal with respect to the LO, $(\omega_s - \omega_{LO})t + \phi_s - \phi_{LO}$, is estimated from the values of $(\Delta P_1 + i\Delta P_2)$ using a method appropriate to the signal modulation format. For example for carrier-suppressed formats a power law function followed by a phase locked loop, or a decision directed phase locked loop, can be used [6].

The sample rate must be high enough to satisfy the Nyquist criterion. The symbol clock can be recovered from the samples using an appropriate algorithm, for example by finding a spectral line in $|E_s(t)|^2$, and then the values of $E_s(t)$ at the symbol centre can be determined by interpolation. A hardware-based clock recovery solution is not needed.

The Jones vector as a function of time constitutes a complete description of the optical signal, from which any signal parameter can be derived. The main limitation on the measurement is that only information within (sampling rate)/2 of the local oscillator is recorded. The use of a pulsed LO has recently been demonstrated as a way to increase the observation bandwidth [7]. An additional limitation is that the A/D conversion process adds some noise, which can be significant for some measurements, but it is possible to apply averaging to reduce the noise.

Polarisation diversity was not employed in the experiments used to generate the data shown in this paper. Only one phase diverse hybrid was used, and the SOP of the signal was matched to the LO using a manual polarisation controller. A real time sampling scope (either a Tektronix TDS6604 or Agilent Infinium 54832B) was used in place of the A/D converters and memory. The data was transferred to a PC after the acquisition was complete to process the samples. The sampling rate was set at the Nyquist rate or higher. The frequency difference between the signal and LO was at most 10% of the symbol rate. In the offline processing the symbol clock was recovered from $|E_s(t)|^2$, and then the values of $E_s(t)$ at the symbol centre estimated by interpolation. To estimate the optical phase a square law function (for BPSK signals) or 4th power law function (for QPSK) was used, followed by smoothing of the open loop phase.

Examples of electric field measurements

The phase diagram is a plot of the quadrature part against the inphase part of the signal, or equivalently a plot of the complex envelope on the complex plane. Figure 2 shows an example of a 10.7 Gb/s BPSK signal at the output of the transmitter and after 90 km of standard singlemode fiber. The sampling rate was 20 GSa/s. In the phase diagrams (Figure 2(a) & (c)) the points in time at the centre of the symbol (when a decision is made) are marked with circles, and the lines between them show the trajectory followed between symbols. The lines appear smooth because multiple points were interpolated between sample times. The corresponding eye diagrams of the inphase (real) component of the electric field are shown in Figure 2(b) & (d). The closure of the eye is due to the chromatic dispersion of the 90 km of fiber. The groupings of the bit centres on arcs of a circle in Figure 2(c) are consistent with chromatic dispersion as the mechanism for eye closure. A different curve would be followed if polarisation mode dispersion or a combination of self phase modulation and chromatic dispersion were responsible for the eye closure, although the eye diagram of Figure 2(d) would look about the same.

Figure 3(a) shows the phase diagram of a 1.6 Gbaud QPSK signal obtained from a dual Mach-Zehnder modulator made in GaAs/AlGaAs, as described in reference 3. The sampling rate was 4 GSa/s. The eye diagrams associated

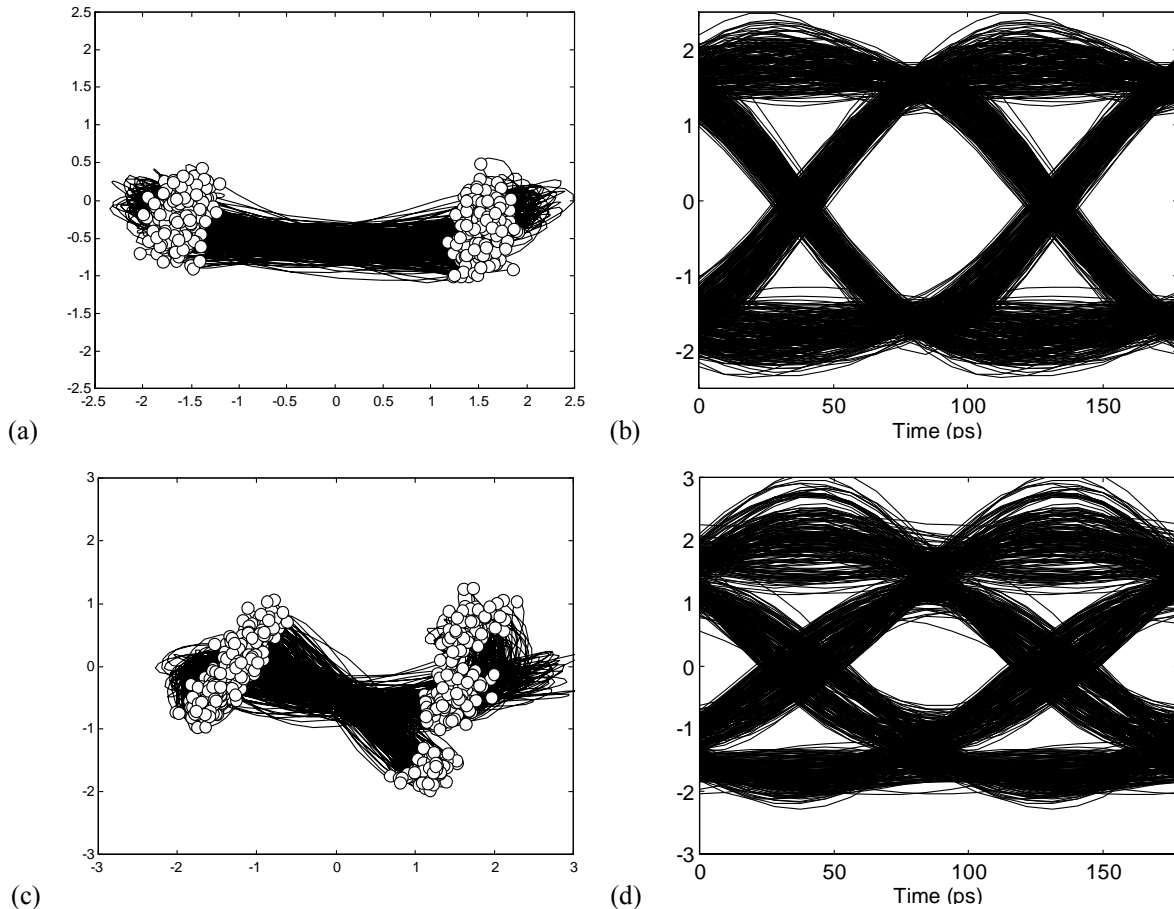


Figure 2 Phase and eye diagrams of 10 Gb/s signal (a) & (b) at transmitter output, and (c) & (d) after 90 km fiber.

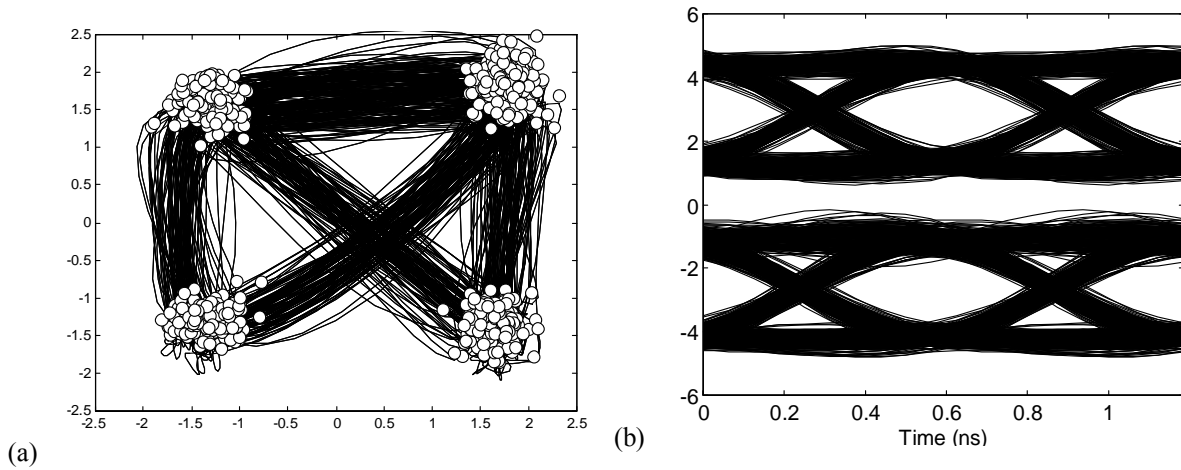


Figure 3 QPSK transmitter output; (a) phase diagram, (b) eye diagrams for the two field components.

with the inphase (real) and quadrature (imaginary) components are shown in Figure 3(b). In the phase diagram shown, one of the transitions between states is clearly missing. This is a result of the way the signals driving the two Mach-Zehnder modulators were derived; one of them is a replica of the other delayed by 15 bits, and a $2^{15}-1$ bit PRBS was used. This set of conditions results in the absence of one of the transitions, and it might be undesirable for some experiments. The phase diagram shows clearly that the transition is missing, but it cannot be seen from the two eye diagrams.

As well as simply displaying the electric field, with the sampled coherent measurement method it is possible to apply sophisticated algorithms to the values of the electric field stored in the processor. It is possible to calculate how much different impairments have impacted the signal. For example, the effects of additive optical noise, cross phase modulation and four wave mixing on a WDM signal have different signatures and could be separately accounted for. This kind of deduction is very hard to make with any other kind of measurement which looks only at the received signal. The processor can also predict what would happen to the signal if it were modified in specified ways. For example, Figure 4 shows what happens to the 10.7 Gb/s signal at the output of the 90 km fiber span if varying amounts of chromatic dispersion compensation are added. The conclusion is that -1580 ps/nm of dispersion provides the best eye opening. Other kinds of transform, such as PMD compensation, could similarly be applied. This approach can be very valuable for field applications given that, unlike this experiment, the reason why the signal is degraded is not known.

Acknowledgements

The author thanks Bookham Technology for the loan of the integrated laser-QPSK modulator, and Agilent and Tektronix for loans of real time sampling oscilloscopes, and S. Wood for assistance with the measurements.

References

1. K. Yonenaga, S. Aisawa, N. Takachio, K. Iwashita, "Reduction of four-wave mixing induced penalty in unequally spaced WDM transmission system by using optical DPSK," IEE Electron. Lett., vol. 32, no. 23, p. 1218-1219, 1996.
2. A.H. Gnauck et al., "2.5 Tb/s (64x42.7 Gb/s) transmission over 40x100 km NZDSF using RZ-DPSK format and all-Raman-amplified spans," OFC 2002, Anaheim, US, paper FC2, 2002.
3. R.A. Griffin et al, "10 Gb/s optical differential quadrature phase shift key (DQPSK) transmission using GaAs/AlGaAs integration," OFC 2002, Anaheim, US, paper FD6, 2002.
4. M. Tseytlin, O. Ritterbush, A. Salamon, "Digital, endless polarization control for polarization multiplexed fiber-optic communications," OFC 2003, Atlanta, US, paper MF83, 2003.
5. M.G. Taylor, "Coherent detection method using DSP for demodulation of signal and subsequent equalization of propagation impairments," IEEE Phot. Tech. Lett., vol. 16, no. 2, 2004.
6. J.G. Proakis, "Digital Communications," McGraw-Hill, 2000.
7. C. Dorrer, J. Leuthold, C.R. Doerr, "Direct measurement of constellation diagrams of optical sources," OFC 2004, Los Angeles, US, paper PDP33, 2004.

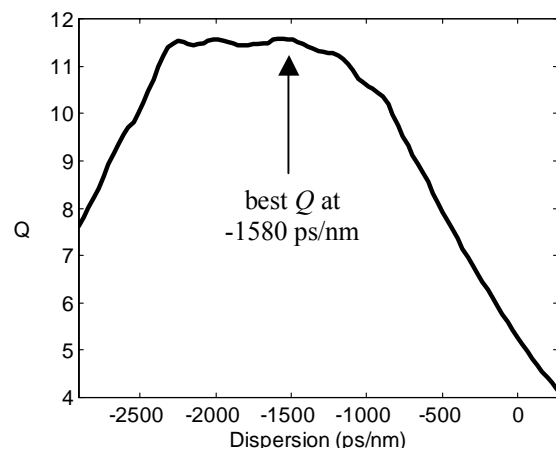


Figure 4 How varying receive end chromatic dispersion impacts signal Q factor

Demonstration of Birefringence in a Bulk Semiconductor Optical Amplifier and its Application to All-Optical Wavelength Conversion

L.Q.Guo and M.J.Connelly

*Optical Communications Research Group
Department of Electronic and Computer Engineering
University of Limerick, Limerick, IRELAND
E-mail: Li-Qiang.Guo@ul.ie*

Abstract --- Birefringence effects in an InGaAsP/InP tensile-strained bulk semiconductor optical amplifier (SOA) are demonstrated. All-optical wavelength conversions based on birefringence induced polarization rotation in SOAs are investigated. It is shown that a bit error rate of $<10^{-9}$ can be achieved and an extinction of $>9\text{dB}$ can be obtained at a bit rate of 2.488Gbit/s with a $2^{31}-1$ non-return-to-zero (NRZ) pseudorandom bit sequence (PRBS).

Index Terms --- Semiconductor optical amplifiers, birefringence, wavelength conversion, polarization rotation, cross polarization modulation.

I INTRODUCTION

ALL-OPTICAL wavelength converters are the key elements in future wavelength division multiplexing (WDM) systems as they can reduce wavelength blocking, provide more flexibility in network management, and offer the possibility of data regeneration [1]. Wavelength converters based on nonlinearities in semiconductor optical amplifiers (SOAs) have been widely investigated in the past few years [2,3]. Wavelength conversion based on cross gain modulation (XGM) in a single SOA has the advantage of simple structure and high conversion efficiency. However, this approach suffers from serious pattern dependence at high bit-rate, strong positive chirping (blue shifted at rising edge and red shifted at falling edge of the pulse), and a degradation of the extinction ratio [4]. Interferometric wavelength converters based on cross phase modulation (XPM) can realize inverted and non-inverted wavelength conversion, and offer an improved extinction ratio. Usually this approach needs two SOAs integrated on a single chip, which makes it more difficult to control the interferometric arrangement (e.g., Mach-Zehnder) [1,5]. Wavelength conversion utilizing four-wave-mixing (FWM) offers strict transparency, including modulation-format and bit-rate transparency, and is capable of multi-wavelength conversions. But it has low conversion efficiency, and needs careful control of the polarization of the input lights [5]. A promising approach of wavelength conversion based on cross-polarization modulation (XPoM) utilizing birefringence effects in SOAs has attracted renewed interest recently, although the

principle of operation had already been demonstrated [6,7]. This approach utilizes the birefringence effects in an SOA, and has great potential to offer inverted and non-inverted wavelength conversions with high extinction ratios.

In this paper, we experimentally present birefringence effects in an InGaAsP/InP tensile-strained bulk SOA, and then investigate all-optical wavelength conversion based on XPoM by utilizing the birefringence effects in SOAs. Both inverted and non-inverted wavelength conversions are demonstrated at a bit rate of 2.488Gbit/s. Inverted wavelength conversion shows better performance, since XGM, which takes place simultaneously with nonlinear polarization rotation, enlarges the effect of inverted wavelength conversion, but reduces the effect on non-inverted case.

II PRINCIPLES OF OPERATION

A polarization resolved amplified spontaneous emission (ASE) spectrum is frequently used to demonstrate the birefringence in SOAs [8]. However, in the spectrum, the periodicities in the ripple for transverse electric (TE) and transverse magnetic (TM) polarizations cannot be obtained precisely enough for one particular wavelength [9], and no exact dispersion relations are known yet.

In this work, the birefringence effects, which lead to polarization rotation in the SOA, are presented in the format of the Poincare sphere [10]. From an experimental point of view, the Poincare sphere is easier to understand and is the best way to display polarization rotation, because the tuning process is visually guided by a moving polarization trace on the sphere. Meanwhile, the Stokes parameters are also given for polarization calculations during the tuning process.

To study the polarization rotation in the SOA, a counter-propagation scheme is used and the experimental setup is depicted in Fig.1. The SOA is a commercially available pigtailed SOA (Kamelian, OPA series), employing a tensile-strained bulk InGaAsP/InP active region. The fiber to fiber gain is 23.4dB at an injection current of 300mA and a wavelength of 1550nm. The polarization sensitivity is less than 0.4dB, and the gain ripple is around 0.25dB. In the experiment, the bias current is 200mA and

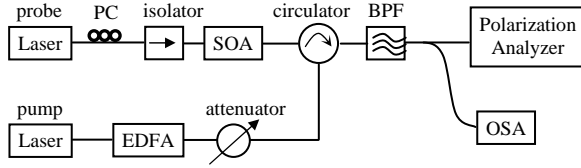


Fig.1. The experimental setup for the study of polarization rotation in the SOA. PC: polarization controller; BPF: band pass filter; OSA: optical spectrum analyzer.

ambient temperature is 20°C. The probe and pump lights are generated from two external cavity lasers, with maximum output of 8.5dBm. The wavelength of the probe and pump light is 1558nm and 1550nm, respectively. The polarization analyzer is from Agilent (model: 8509C), and an HP86142A optical spectrum analyzer (OSA) is used to monitor the output spectrum from the SOA. A band pass filter (1nm) is placed after the circulator to sufficiently suppress the spontaneous noise from the SOA. The power of the probe beam coupled into the SOA is ~ -8dBm. Since the device birefringence is rather sensitive to the input power level, it is necessary to use a relatively low-power probe so that self-induced birefringence by the probe can be ignored, and strong birefringence effects owing to the pump beam dominate inside the SOA [7].

When the pump light is coupled into the SOA, owing to the *TE/TM* asymmetry of the confinement factors, effective refractive indices and carrier distribution of the SOA [11], birefringence effects are induced. Therefore the *TE* and *TM* components of the probe experience different phase shifts, and probe light will change its polarization to be elliptical, circular, or linear depending on the different amount of injected power inside the SOA [12]. These changes are shown in Fig.2, in which the probe light changes its state of polarization (SOP) and traces out a thick solid line on the Poincare sphere as the power of the pump light is increased from -6.5dBm to 8.0dBm. A detailed analysis of this signal-induced birefringence in the SOA can be described by a 2×2 Jones matrix [7]:

$$\begin{pmatrix} E_x^{out} \\ E_y^{out} \end{pmatrix} = J \begin{pmatrix} E_x^{in} \\ E_y^{in} \end{pmatrix} = \begin{pmatrix} j_{11} & j_{12} \\ j_{21} & j_{22} \end{pmatrix} \begin{pmatrix} E_x^{in} \\ E_y^{in} \end{pmatrix} \quad (1)$$

Here x and y are two orthogonal reference axes. For convenience, one can use *TE* and *TM* orientation of the SOA configuration as the reference axes. And by normalizing the element $j_{22}=1$, the element j_{11} can be written as $j_{11} = A \cdot e^{i\Delta\varphi}$, where A and φ represent the gain difference and additional phase shift between *TM* and *TE* components of the probe due to the existence of the pump light. $\Delta\varphi$ is given by:

$$\begin{aligned} \Delta\varphi &= \frac{2\pi L}{\lambda_p} \left[(N_{TM} - N_{TE})_{pump_on} - (N_{TM} - N_{TE})_{pump_off} \right] \\ &= (\varphi_{TM} - \varphi_{TE})_{pump_on} - (\varphi_{TM} - \varphi_{TE})_{pump_off} \end{aligned} \quad (2)$$

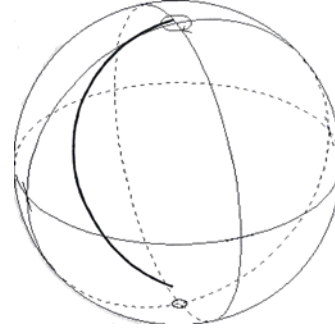


Fig.2. The solid thick line on the Poincare sphere indicates how the probe light change its SOP as the pump light varies between -6.5dBm and 8.0dBm.

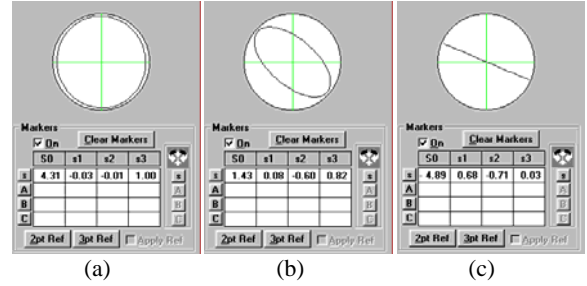


Fig.3. The SOP of the probe light (after passing through the SOA) at different pump light level: (a) absent of pump light, (b) -2.8dBm, (c) 5.9dBm.

and [11]

$$\varphi_{TM/TE} = \frac{2\pi L}{\lambda_p} \left(N_{TM/TE} + \Gamma_{TM/TE} n_p \frac{dN}{dn} \right) + \frac{2\pi L \Gamma_{TM/TE} (n - n_0)}{\lambda_p} \frac{dn}{dn} \quad (3)$$

where L is the cavity length, λ_p is the wavelength of the probe light, $N_{TM/TE}$ is the *TM/TE* effective refractive index averaged along the SOA, $\Gamma_{TM/TE}$ is the confinement factor at the *TM/TE* orientation, n_p is the value of the carrier concentration for zero input power at the bias current used to define the peak gain wavelength, n_0 is the transparency carrier concentration, dN/dn is the changing rate of the refractive index in the active region with carrier concentration.

Fig.3 shows how the probe changes its SOP as the pump power increases. Before entering the SOA, the SOP of the probe light is adjusted by a polarization controller (PC in Fig.1), which makes the SOP of the probe leaving the SOA nearly circularly polarized (see Fig.3(a)) when there is no pump light. When a pump light is coupled into the SOA through a optical coupler and the pump power increases gradually, birefringence effects are induced in the SOA and the circularly polarized probe light will change its SOP to elliptical (with pump power of -2.8dBm shown in Fig.3(b)) and linear (with pump power of 5.9dBm, Fig.3(c)). Therefore, when a polarizer is placed after the SOA (the polarizer was actually placed after BPF during the measurements and is not shown in Fig.1), the phase difference

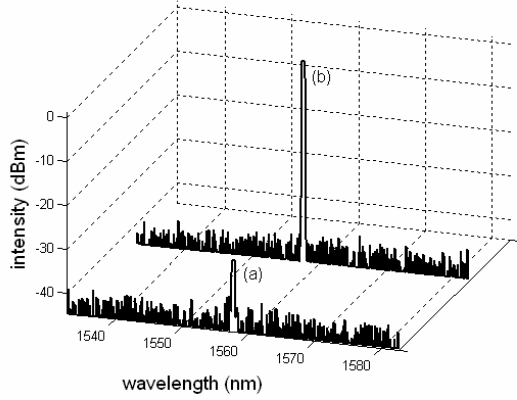


Fig.4. Optical spectra obtained at the output of the polarizer with the (a) absence and (b) presence of the pump light in the SOA.

between the probe's *TE* and *TM* components can be converted to intensity difference, and wavelength conversions can be realized. Fig.4 shows the static wavelength conversion by XPolM for non-inverted case. The spectra are recorded by an HP86142A OSA, and the on/off ration is $>30\text{dB}$.

III EXPERIMENT AND DISCUSSION

The setup for dynamic wavelength conversions by XPolM is depicted in Fig.5. The pump beam is modulated at a bit rate of 2.488Gbit/s with non-return-to-zero (NRZ) pseudorandom bit sequence (PRBS) of length $2^{23}-1$ via a LiNbO₃ Mach-Zehnder modulator. A band pass filter (1nm) is placed after the polarizer to sufficiently suppress the spontaneous noise from the SOA. The SOP of the probe is adjusted by a polarization controller (PC1 in Fig.5), which ensures its SOP orientation to be set at some angle to the *TE* (or *TM*) axis of the SOA. The wavelength of the probe and the pump is 1558nm and 1550nm, respectively; and the power of the probe and the pump coupled into the SOA is $\sim -8\text{dBm}$ and 8dBm , respectively.

To demonstrate the high-speed operation of this wavelength converter, bit-error-rate (BER) measurements are performed at 2.488Gbit/s. Fig.6 shows BER measurements of inverted and non-inverted wavelength conversions, together with back-to-back measurement. It can be seen from Fig.6 that the inverted wavelength conversion leads to a penalty of $\sim 3.0\text{dB}$ at a BER of 10^{-9} . Non-inverted wavelength conversion leads to an additional 0.6dB penalty compared with the inverted case. Inverted conversion shows better performance due to positive contribution from XGM which takes place simultaneous with XPolM in the SOA. No error floor is found up to BER as low as 10^{-12} , which indicates excellent conversion performance. The extinction ratios and power penalties of the converted signals are found to be $3.86\sim 14.50\text{dB}$ and $2.3\sim 3.8\text{dB}$, respectively.

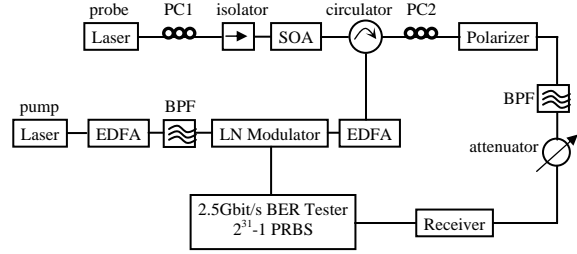


Fig.5. Experimental setup for all-optical wavelength conversion based on XPolM.

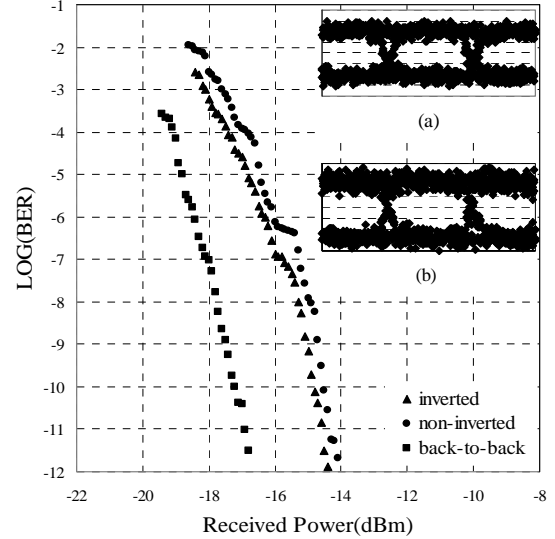


Fig.6. Plot of 2.488Gbit/s BER measurements for inverted and non-inverted wavelength conversions, together with back-to-back measurement. The insets show the corresponding eye diagrams for (a) inverted wavelength conversion, and (b) non-inverted wavelength conversion.

Initially, when there is no attenuation introduced into the system, the Q factor of the converted signal is 27.38 for inverted wavelength conversion, and 19.89 for non-inverted case. The eye diagrams in Fig.6 are measured under the conditions that BERs are optimized around 10^{-9} after introducing a considerable amount of attenuation into the system. An HP8156A optical attenuator in Fig.5 attenuates the converted signal before the BER tester to simulate a telecommunication system in practice. The eye diagram of inverted wavelength conversion presented in the inset(a) in Fig.6 shows an extinction ratio of 5.20 and a Q factor of 6.06; and the eye diagram of non-inverted conversion is presented in the inset(b) in Fig.6, having an extinction ratio of 5.82 and a Q factor of 5.96. The eye diagrams are measured on an HP83480A digital communications analyzer with a 20GHz O/E plug-in module (HP83485A). The time-base of the measurements is 100.0ps/div. The open eyes suggest that there is good potential to operate at even higher bit rate.

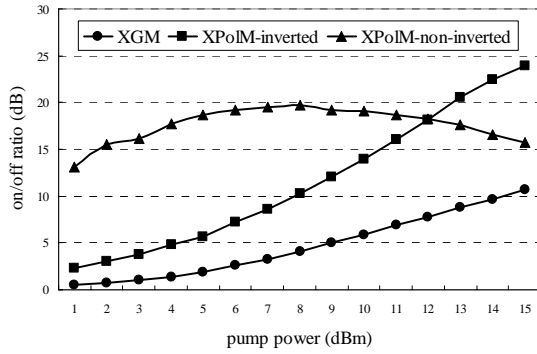


Fig.7. Comparison of on/off ratio between wavelength conversion by XGM, and wavelength conversion by XPolM (inverted and non-inverted conversion) as a function of pump beam power.

Since high-intensity pump light is required to saturate the SOA, XGM takes place simultaneously with XPolM. Therefore when a linearly polarized probe beam is modulated by pump-induced birefringence inside the SOA, not only is the SOP of the probe changed, the intensity of the probe is also modulated by XGM. To fully exploit the co-effect of XGM and XPolM in the converted signal, static modulation by XGM and XPolM with similar setup (both use counter-propagation scheme) were conducted. The experimental results are shown in Fig.7. For the Kamelian SOA used in this work, the saturation output power is ~ 12 dBm. The on/off ratio of the inverted signal by XPolM is increased, while the on/off ratio of the non-inverted signal is decreased when the SOA is being saturated. This can be explained by the fact that XGM enlarges the effect of inverted wavelength conversion, but reduces the effect on non-inverted case. As a result, the slope of the curve for the inverted conversion is increased and sharper than the one for the non-inverted case. Further theoretical analysis and modeling of the co-effect of XGM and XPolM in SOAs are currently under investigation in our research group.

IV CONCLUSION

In this paper, we investigated the birefringence effects in a tensile-strained bulk SOA, and show that all-optical wavelength conversion by XPolM is a simple, fast, and robust mechanism. Error-free wavelength conversion at 2.488 Gbit/s is obtained. No error floors are observed. Although all-optical wavelength conversions in this work were conducted at a bit rate of 2.488 Gbit/s, it should be noticed that by introducing the enhanced gain recovery technique [13], the data rate can exceed 40 Gbit/s [11]. The static co-effect of XGM and XPolM in SOAs is initially studied, and the dynamic effect of XGM in inverted and non-inverted wavelength conversions by XPolM is not yet fully understood, and currently is a research topic in our group.

ACKNOWLEDGEMENT

This work is supported by Science Foundation Ireland Award Investigator 02/IN1/I42.

REFERENCES

- [1] S.J.B.Yoo, "Wavelength conversion technologies for WDM network applications", *J. Lightwave Technol.*, vol.14, pp955, 1996
- [2] M.J.Connelly, *SEMICONDUCTOR OPTICAL AMPLIFIERS*, KLUWER ACADEMIC PUBLISHERS, 2002, Chapter 7, and references therein
- [3] D.Cotter, R.J.Manning, K.J.Blow, A.D.Ellis, A.E.Kelly, D.Neset, I.D.Phillips, A.J.Poustie, and D.C.Rogers, "Nonlinear optics for high-speed digital information processing", *SCIENCE*, vol.286, pp1523, 1999
- [4] J.M.Wiesenfeld, B.Glance, J.S.Perino, and A.H.Gnauck, "Wavelength conversion at 10Gb/s using a semiconductor optical amplifier", *IEEE Photon. Technol. Lett.*, vol.5, pp1300, 1993
- [5] K.L.Hall, E.R.Thoen, and E.P.Ippen, "Nonlinearities in active media", *SEMICONDUCTORS AND SEMIMETALS*, vol.59, p83, 1999
- [6] M.F.C.Stephens, M.Asghari, R.V.Penty, and I.H.White, "Demonstration of ultrafast all-optical wavelength conversion utilizing birefringence in semiconductor optical amplifiers", *IEEE Photon. Technol. Lett.*, vol.9, pp449, 1997
- [7] H.Soto, D.Erasme, and G.Guekos, "Cross-polarization modulation in semiconductor optical amplifiers", *IEEE Photon. Technol. Lett.*, vol.11, pp970, 1999
- [8] S.Diez, C.Schmidt, R.Ludwig, H.G.Weber, P.Doussiere, and T.Ducellier, "Effect of birefringence in a bulk semiconductor optical amplifier on four-wave mixing", *IEEE Photon. Technol. Lett.*, vol.10, pp212, 1998
- [9] G.P.Agrawal and N.K.Dutta, *SEMICONDUCTOR LASERS*, 2nd, VAN NOSTRAND REINHOLD, 1993, Chapter 2
- [10] E.Collett, *POLARIZED LIGHT*, Marcel Dekker, Inc., 1993, Chapter 11
- [11] M.Asghari, I.H.White, and R.V.Penty, "Wavelength conversion using semiconductor optical amplifiers", *J. Lightwave Technol.*, vol.15, pp1181, 1997
- [12] C.S.Wong, and H.K.Tsang, "Polarization-independent wavelength conversion at 10Gb/s using birefringence switching in a semiconductor optical amplifier", *IEEE Photon. Technol. Lett.*, vol.15, pp87, 2003
- [13] R.J.Manning, D.A.O.Davies, D.Cotter, and J.K.Lucek, "Enhanced recovery rates in semiconductor laser amplifiers using optical pumping", *Electron. Lett.*, vol.30, pp787, 1994

Effects of optical coherence and polarization in optical ANA

David A Humphreys National Physical Laboratory, Teddington Middlesex, TW11 0LW, UK

Abstract: Optical Automatic Network Analyzers extend the use of the traditional microwave instrument to measure the modulation response of optoelectronic components such as receivers and transmitters. The issues of linearity, optical coherence and polarization are explored.

Introduction

Microwave Automatic Network Analyzers have been extended to include optical transmitter formed using a CW laser and modulator¹ or directly modulated laser² and high-speed photodiodes as the optical receiver as shown in Figure 1. These instruments are available commercially and are useful to characterize optoelectronic components, such as photodiodes, lasers or modulators, and have also been used to measure certain fiber parameters. The underlying mathematics to use these systems has been formalized^{3,4}.

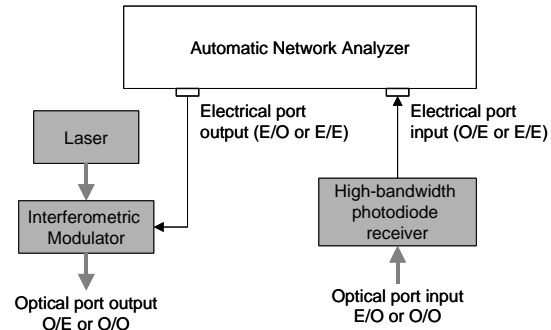


Figure 1 General configuration of an optical ANA

The output from the optical port is an intensity modulated signal $I(t)$ that is proportional to the optical power from the laser. The modulation depth is a function of the amplitude of the RF signal from the ANA. The high-bandwidth photodiode receiver gives a signal voltage that is proportional to the input optical power. Therefore unlike the microwave ANA configuration, where changes in the RF power will be automatically normalized, the laser power must be kept constant as it forms part of the ratio. Unlike a microwave ANA where traceability is through impedance and dimensional measurement, inter-domain characterization (O/E and E/O) requires the vector characterization of a photodiode^{5,6} or modulator and is traceable through optical-impulse/electrical-risetime, current/optical-power RF-power and impedance standards.

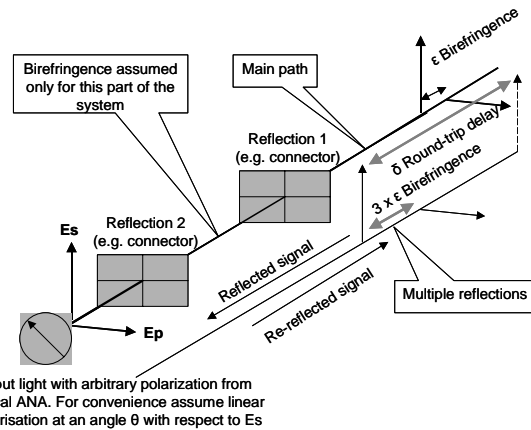


Figure 2 Optical reflections and birefringence in the optical path

Theory

Linearity and superposition are important properties of a measurement system. However, by extending the ANA to modulate an optical carrier there is a problem because the translation from the electrical to the optical domain is inherently nonlinear.

Superposition applies for electric field and current. Under normal operating conditions, a photodiode generates a current that is proportional to the optical intensity. As a consequence, superposition applies to the electrical signals from the photodiode at the input to the ANA. Microwave impedance mismatches between the photodiode and the ANA give rise to multiple reflections of the microwave signal within the system and these can be corrected algebraically.

However, in the optical domain the signal is an amplitude-modulated carrier and therefore superposition applies at the electric field level. Multiple reflections within the optical path will add as the sum of the electric fields provided the overall distance is less than the source coherence length. Also, if the fiber has some birefringence then the polarization states of the main and reflected paths will be different. These issues are illustrated in figure 2. In this diagram, the birefringence has been confined to the fiber between the two reflectors only.

For coherent signals, the photocurrent I_{pd} is proportional to the square of the magnitude of the vector sum of the electric fields for the two polarizations (E_s and E_p). The averaging term occurs because the photodiode bandwidth does not extend to the optical frequencies. If the distance between the reflections is greater than the coherence length of the optical source then the average of the cross-product terms will be zero.

$$I_{pd} \propto \left\langle \left| \sum_i E_{s_i} \right|^2 \right\rangle + \left\langle \left| \sum_i E_{p_i} \right|^2 \right\rangle$$

Eq. 1 Coherent addition of electric fields

$$I_{pd} \propto \left\langle \sum_i |E_{s_i}|^2 \right\rangle + \left\langle \sum_i |E_{p_i}|^2 \right\rangle$$

Eq. 2 Incoherent addition of electric fields

The optical frequency is typically about 200 THz whereas the maximum microwave modulation rate will be <70 GHz and so small changes in the delay, birefringence or optical frequency will cause large phase changes in the optical field of the reflected terms. The system becomes sensitive to changes at the wavelength of the carrier (micron level), rather than at the microwave wavelength (millimeters and longer) because the cross-product terms in $\langle |\Sigma E|^2 \rangle$ are non-zero.

Is the assumption of a monochromatic optical signal realistic? To assess this we need to consider typical components within a measurement system. The optical patch cord used to connect the components for test is likely to be short, a few meters, for operator convenience and the light source commonly used in these systems is a distributed feedback laser (DFB) as these lasers have low relative intensity noise (RIN) and are similar to those used within a telecommunications network. DFB lasers are single-wavelength with a linewidth typically in the MHz range. Unfortunately, this means that the laser also has a coherence length of several meters and so the monochromatic assumption is reasonable.

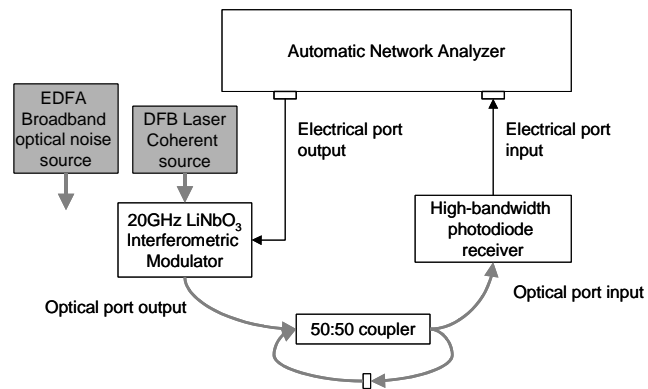


Figure 3 Optical ANA system using a 50:50 coupler in a loop to investigate the optical coherence effect

If the optical bandwidth of the source is increased, for example by using a broad-band noise source, then the average value of the cross-product terms is zero and the system is only sensitive

to changes on the scale of the microwave modulation frequency. However, this means that the optical bandwidth will have to be greater than the highest modulation frequency. A broadband noise source can be used with a Mach-Zehnder modulator because the overall path difference between the two arms is of the order of the optical wavelengths.

Experimental measurement

An optical ANA was formed using a commercial ANA, a 20 GHz modulator and high-speed photodiode (HP83440C). Two different optical sources were used to provide highly coherent (DFB laser) and incoherent (EDFA) light. A 50:50 optical fiber coupler was used in a loop configuration to provide multiply overlaid optical signals. The loop length was measured as 2.41 m. Using an assumed refractive index of 1.46 for the fiber this would give a free spectral range of approximately 85 MHz. Measurements were taken at 201 points over the range 3-19 GHz (80 MHz spacing). The closeness of the frequency point spacing and the loop FSR will result in aliasing.

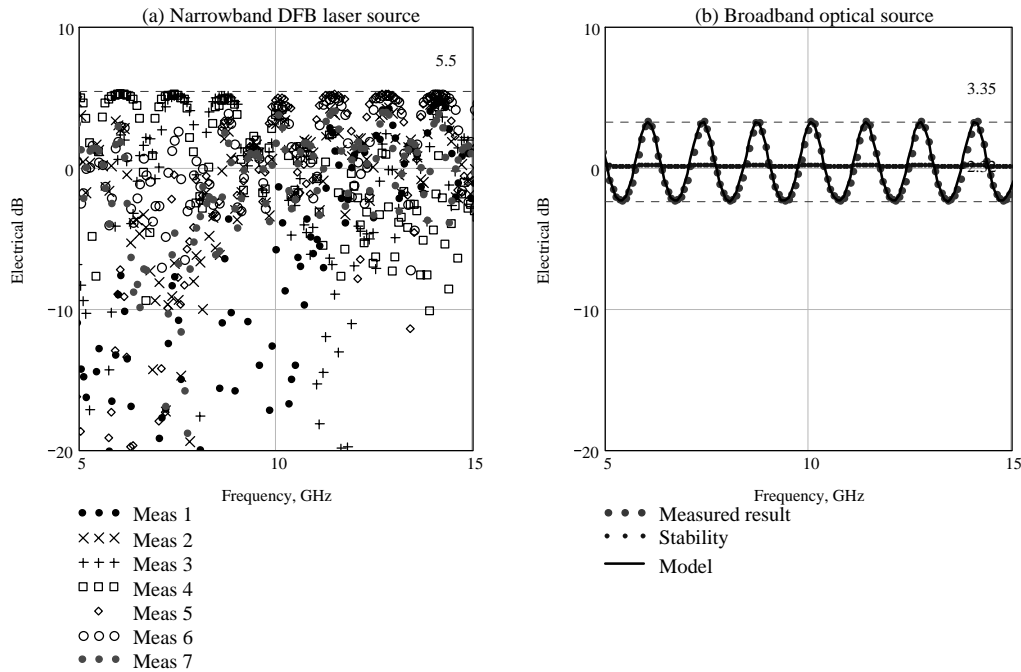


Figure 4 Results measured with the DFB laser (coherent optical source) and the EDFA (broadband optical source)

A normalization signal was measured with the loop disconnected so that the optical power scaling and the frequency responses of the photodiode and modulator could be corrected from the results.

Results

A series of seven measurements were made with the DFB laser (Figure 4a). In between each measurement the optical fiber was perturbed. The instability of the results shows that there is coherent addition of the electric field components. Using the broadband optical source (Figure 4b), the results show good stability and behave according to a simple theoretical model:

$$T(f) = \frac{1}{1 - \theta \cos\left(2\pi f \frac{nL}{c}\right)} \quad \text{Eq. 3}$$

where $T(f)$ is the transmission at a modulation frequency f . L is the loop length, n and c are the refractive index and speed of light respectively. The fraction of the light in the loop is θ . The values of L (2.4135) and θ (0.313) are in reasonable agreement with expectations.

The stability measurement (Figure 4b) was made by calibrating the transmission with the loop connected and measuring the ratio after moving the optical fibers. This confirms that the superposition of optical intensity is occurring rather than superposition of electric fields.

In Figure 5, the model and measured results have been plotted over a smaller frequency range and this shows the effect of aliasing.

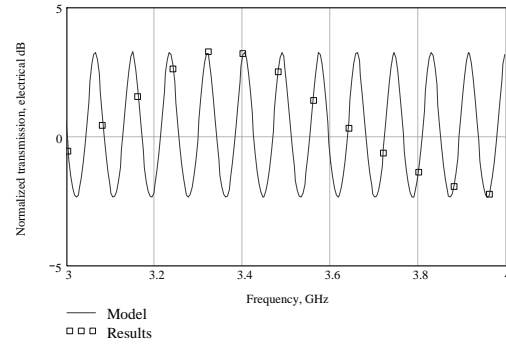


Figure 5 Model and measured results plotted over a 1 GHz range to show the effect of aliasing

Discussion

Coherent addition of optical signals in an optical ANA can cause instability of the measurement results. If the bandwidth of the optical source and transmission bandwidth of the system under test is larger than the maximum modulation frequency then superposition occurs in terms of optical intensity rather than electric field and so the mathematical correction algorithms within the ANA will operate correctly.

Acknowledgements

We gratefully acknowledge the financial support of the UK Department of Trade and Industry, National Measurements Programme. This paper is subject to Crown Copyright, extracts from this report may be reproduced provided the source is acknowledged and the extract is not taken out of context.

References

- ¹ "High-speed lightwave component analysis," Agilent Technologies, Palo Alto, CA, Applicat. Note 1550-6, June 2000.
- ² Elamaram B., Pollard R.D., Iezekiel S., 2000, A bilateral lightwave network analyzer - Architecture and Calibration, IEEE Transactions on Microwave Theory and Techniques, 48 pp. 2630-2636.
- ³ Iezekiel S., Elamaram B., Pollard R.D., 2001, Recent Developments in Lightwave Network Analysis, Electronics & Communication Engineering Journal, 13(2) pp. 85-94.
- ⁴ Paul D. Hale and Dylan F. Williams "Calibrated Measurement of Optoelectronic Frequency Response", IEEE Transactions on Microwave Theory and Techniques, Vol. 51, No. 4, pp. 1422- 1429, April 2003.
- ⁵ D. A. Humphreys, and A. J. Moseley, "GaInAs photodiodes as transfer standards for picosecond measurements," *IEE Proc. Pt. J*, vol. 135, no. 2, pp. 146-152, April 1988.
- ⁶ T. Albrecht, J. Martens, T. Clement, P. D. Hale, and D. Williams, "Broadband characterization of optoelectronic components to 65 GHz using VNA techniques," 62nd ARFTG conference.

Characterization of Multimode Fiber for 10+ Gb/s Operation By Predicting ISI from Bandwidth Measurement Data

John S. Abbott
Corning Inc. SP-PR-1-3
Corning, NY 14831

Introduction

A common way to characterize the quality of data transmission in high speed optical communication networks, for example 1Gb/s or 10-Gb/s Ethernet local area networks, is to use the so-called eye diagram to determine inter-symbol interference [1]-[3]. The degradation in transmission quality is quantified by the amount of eye closure. For multimode fibers in high-speed networks using 10Gb/s VCSEL sources, the ISI penalty depends on the characteristics of both the source and the optical fiber, particularly the mode group delays (a fiber property) and the relative modal power distribution (a source property) [4].

In developing the TIA specifications for sources and fibers for 10Gb/s networks, extensive modeling and simulation of system links were done using estimated distributions of mode delays and mode power distributions [5]-[6]. In addition to ISI, the effective modal bandwidth (EMB) was calculated, and both parameters were used as a measure of the link performance.

Standard models of system performance including a IEEE link model assume a Gaussian pulse shape, allowing ISI to be uniquely determined by the -3dB BW used for EMB [1],[5]. The TIA modeling used a more sophisticated link model developed at IBM [6] including the non-Gaussian nature of pulses in high bit-rate fibers. It was found that many 'outlier' fibers did not follow a correlation between ISI and the -3dB EMB. This complicated the development of specifications both in estimating the link performance and in determining what characteristics of the fiber should be measured.

The purpose of this note is to explain how the ISI/EMB correlation can be improved for non-Gaussian pulses by defining a modified bandwidth metric using the bandwidth measurement data combined with information about the bit rate and length of the system link.

ISI vs. EMB using the standard -3dB metric

The results of the TIA simulation of 10,000 (no-connector) 300m links at 10Gb/s, plotting the ISI penalty in dB/km vs. the -3dB EMB in MHz.km, are given in Figure 1. In the TIA work the ISI requirement for the link is 2.6dB/km and points with $EMB < 1500 \text{ MHz.km}$ will not give satisfactory system performance. The limiting curve crosses $ISI = 2.6 \text{ dB}$ at about 1740 MHz.km . Although statistically the (EMB, ISI) pairs concentrate along a 'limiting curve', there are a large number of outliers making it difficult to

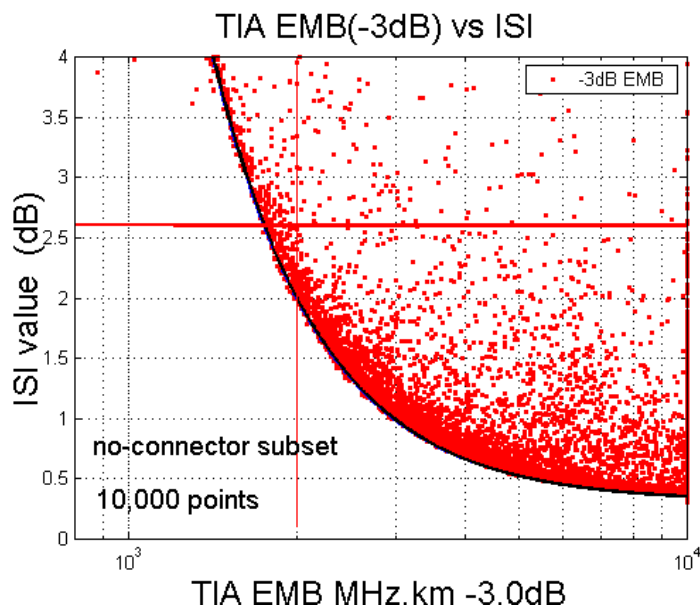


Figure 1. ISI vs. -3dB EMB (TIA modeling [5])

guarantee ISI performance based on the EMB value alone. For example, for an EMB of 5GHz.km the limiting curve is approximately ISI = 0.5dB, but outliers extend up to the 2.6dB line and even a few are above the line.

A modified bandwidth metric based on bit-rate and link length

The suggested multimode bandwidth metric, to achieve a tighter correlation between ISI and EMB, can be explained using Figure 2. Rather than defining the bandwidth as the frequency where the amplitude drops to a specific level (typically -3dB, but -1.5dB has also been used for optoelectronics [7] or to address waves in the Fourier Transform amplitude [8]), we note the bit-rate of the application f_{bit} and determine the amplitude where the frequency equals $f_{\text{bit}}/2$. As an example, for a 10Gb/s system operating literally at a bit rate of 10Gb/s, $f_{\text{bit}}/2 = 10,000/2 = 5,000$ (if the bit rate is actually 10.125Gb/s etc. f_{bit} would be adjusted). If this amplitude is less than -3dB, the normal -3dB bandwidth is less than $f_{\text{bit}}/2$ and can be used. If this amplitude is greater than -3dB, then a Gaussian extrapolation to -3dB can be done and the extrapolated bandwidth will better correlate with the system ISI even if the pulse is non-Gaussian. For a 300m 10Gb/s system, the key frequency $f_{\text{bit}}/2$ corresponds to $5000 * 0.300 = 1500\text{MHz.km}$. In the example Fourier Transform shown in Figure 2, point (a) corresponds to the usual -3dB definition of bandwidth (amplitude = 0.5), while point (b) is the point on the curve corresponding to $f_{\text{bit}}/2$. In this example, extrapolating from point b down to the -3dB level will give a modified bandwidth very close to the -3dB bandwidth; however, the extrapolated value is not sensitive to the wave in the transform between 2.5 and 3.0 GHz.km, which can cause large changes to the -3dB bandwidth with small changes to the original pulse structure.

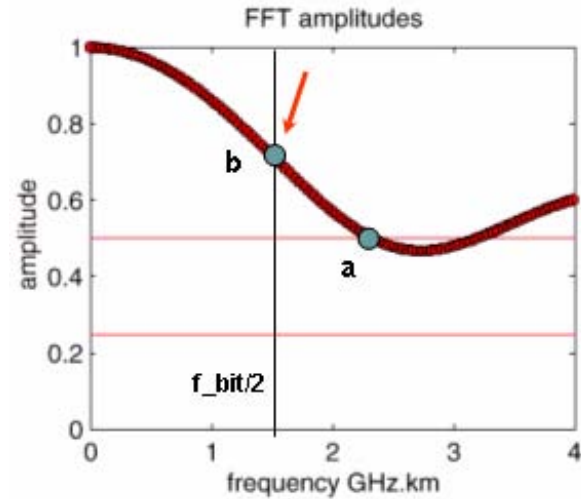


Figure 2. FFT amplitude vs. normalized frequency

ISI vs. EMB using the modified metric

Figure 3 shows a plot of the TIA model results using the modified BW metric. The same ISI values for the 10,000 laser source-fiber pairs are now plotted vs. the modified EMB, where the EMB is now calculated with the modified “frequency bandwidth” metric. This uses the identical laser-fiber pairs as plotted in Figure 1; the ISI values are the same and the only change is the definition of ‘bandwidth’ now depends on the bit rate and link length for the application.

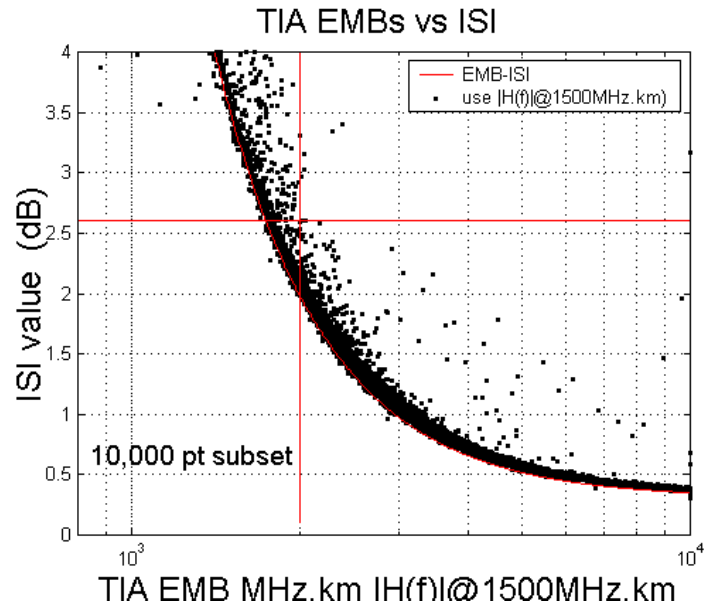


Figure 3. ISI vs. modified EMB using 1500MHz.km

A modified bandwidth metric using Real $H(f)$, the bit rate, and link length

The ISI in the TIA model is somewhat better predicted by the Real part of the Fourier Transform of the impulse response $\text{Re } H(f)$ rather than the amplitude $|H(f)|$. This is motivated physically by noting that in the random bit sequence used to generate an eye diagram and calculate inter-symbol interference, a contribution to ISI comes whether a pulse overlaps with the preceding bit period or the following bit period. The ISI is the same if the pulse is reflected through its centroid (assuming the centroid lies at the center of the bit period) and hence correlates with the symmetric part of the pulse (and hence $\text{Re } H(f)$). By using $\text{Re } H(f) = 0.5$ as the bandwidth criteria the (EMB, ISI) distribution is tightened, and by using $\text{Re } H(f)$ at the frequency $f_{\text{bit}}/2$ the distribution is tightened further. Figure (4) shows the improved tightening of the distribution compared to Figures 1 or 3 so that there is a more deterministic connection between EMB and ISI.

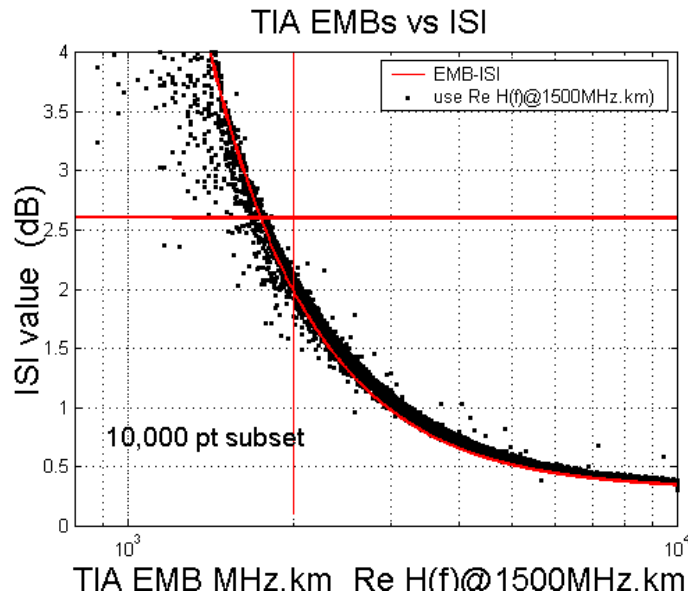


Figure 4. ISI vs. modified EMB using $\text{Re } H(f)$ @1500MHz.km

Conclusion

A significantly improved correlation between ISI and EMB can be made if the BW metric used for EMB is modified to take into account the bit rate and link length of the network application, just as it is needed to estimate ISI. An improvement also occurs by using the real part of the transfer function rather than its amplitude, and further improvement occurs when the two approaches are combined.

References

- [1] Cunningham, D.C., and Lane, W.G., Gigabit Ethernet Networking. Indianapolis: Macmillan Technical Publishing, 1999.
- [2] Pepeljugoski, P., Kuchta, D., Kwark, Y., and Pleunis, P., "15-Gb/s Transmission over 1 km of Next Generation Multimode Fiber", IEEE Photonics Tech. Lett., Vol. 14 No. 5 (May 2002) pp. 717-719.
- [3] Schlager, J.B., Hackert, M.J., and Pepeljugoski, P., "Measurements for Enhanced Bandwidth Performance Over 62.5-um Multimode Fiber in Short-Wavelength Local Area Networks", J. Lightwave Technology, Vol. 21, No. 5 (May 2003) pp. 1276-1285.
- [4] Abbott, J.S., "Characterization of Multimode Fiber for 10 Gbps Operation", NIST Symposium on Optical Fiber Measurements, Boulder, Sept. 2000, pp.29-34.
- [5] Pepeljugoski, P., Hackert, M.J., et al., "Development of System Specification for Laser-Optimized 50-um Multimode Fiber for Multigigabit Short-Wavelength LANs", J. Lightwave Technology, Vol. 21 No. 5 (May 2003) pp. 1256-1275.
- [6] Pepeljugoski, P., Golowich, S.E., et al., "Modeling and Simulation of Next-Generation Multimode Fiber Links", J. Lightwave Technology, Vol. 21 No. 5 (May 2003) pp. 1242-1255.
- [7] Senior, J.M., Optical Fiber Communications, 2nd Edition. New York: Prentice Hall, 1992. p.404
- [8] FOTP-220: Differential Mode Delay Measurement of Multimode Fiber in the Time Domain, Paper TIA/EIA-455-220A, PN 3-0008-RV1.

FIBRE SENSING: SPECIFYING COMPONENTS AND SYSTEMS

Brian Culshaw¹ and Wolfgang Habel²

¹*University of Strathclyde, Electronic & Electrical Engineering
Glasgow, Scotland (b.culshaw@eee.strath.ac.uk)*

²*Federal Institute for Materials Research and Testing (BAM)
Berlin, Germany (wolfgang.habel@bam.de)*

1. INTRODUCTION

Optical fibres have been used in sensing for almost 40 years⁽¹⁾. The first ideas emerged even before the concept of low loss, low dispersion fibres appeared on the horizon. Fibre sensing now has evolved in a very different context from fibre communications. The communications industry is relatively homogeneous especially at the transmission level where fibres have undoubtedly contributed critically to the revolution in the way in which society functions. Communications is also the industry of large corporate interests and to function it relies heavily on interchangeable product and therefore well defined standards and protocols.

The sensing industry is markedly different. This is the domain of the specialist and the small company servicing niche needs. The niches come with their own specific demands. Operating at the bottom of an oil well is radically different from operating in deep space but temperatures and strains are to be measured in both. Some impression of this diversity can be gleaned from the observation that within the UK estimates of the number of companies involved in sensing and measurement using all technologies start at around 1,000 and continue ever upwards - very much greater than the numbers involved in the communications business which of itself has a total turnover far exceeding that in sensing and measurement. These contrasts have a profound effect on the way in which the two industries are operated, standardised and regulated.

These observations are essential background to any discussion on standards and specifications in the context of optical fibre sensors. This paper will endeavour to bring together the issues concerning standards and specification development within the industry. This is a fragmented task. The final customer is interested in measurement capability, reliability and cost. The manufacturer's task is to optimise these trade-offs within the constraints imposed through - typically - a small manufacturing enterprise. The manufacturer assembles his sensor system from components and often these components have been fabricated with an entirely different market in mind and are therefore less than perfectly suited to the need in question. There is always a technical risk implicit in using such components. The fragmentation is important. Chemical, biochemical, biomedical and physical measurands are all addressed using fibre based optical transducers. All operate in very different environments. Consequently, to enable some focus to this discussion, we shall concentrate here on issues concerning fibre sensors to measure physical measurands: strain, pressure, acceleration, temperature, direction and rotation are the most important of these.

The main body of the paper starts with a basic description of the fibre sensor itself to highlight the critical interfaces and the areas in which standards and specification issues are foremost. There is actually relatively little standardisation material at the component level which directly supports the fibre sensor industry. There are some critical areas where recognised measurement processes and procedures would be extremely welcome. We briefly discuss the evolution of one of the most focused standards endeavours - that of fibre gyroscopes which is we believe unique in Optical Fibre Sensing in having been considered by a US based (IEEE) Standards Committee. We also mention some IEC activity. Finally this leads into a discussion on the standard processes which would be desirable, the standards which are needed and how these needs may be approached. To exemplify this we consider the specific case of the fibre Bragg grating.

2. THE FIBRE SENSOR

2.1 Sensor Basics

The fibre sensor is, in principle, a simple concept and is shown in figure 1. An optical fibre feeds light into an interaction zone, where a transduction process takes place through which the light in the fibre is modulated. Hopefully this transduction process is uniquely related to a measurement parameter of interest which can be physical, chemical or biological in origin. The modulated light is then transmitted back to some demodulation and decoding unit in a remote location. The assumption in the fibre sensor - and it is always a very tenuous assumption - is that the interaction between the parameter of interest and the light is constant over long periods of time and further is only related to the measurand of interest. Additionally the transfer characteristics between

source and input fibre, input fibre and modulation region, modulation region and output fibre, and output fibre and detector are also assumed to be constant, not to mention the transfer characteristics of the fibres themselves.

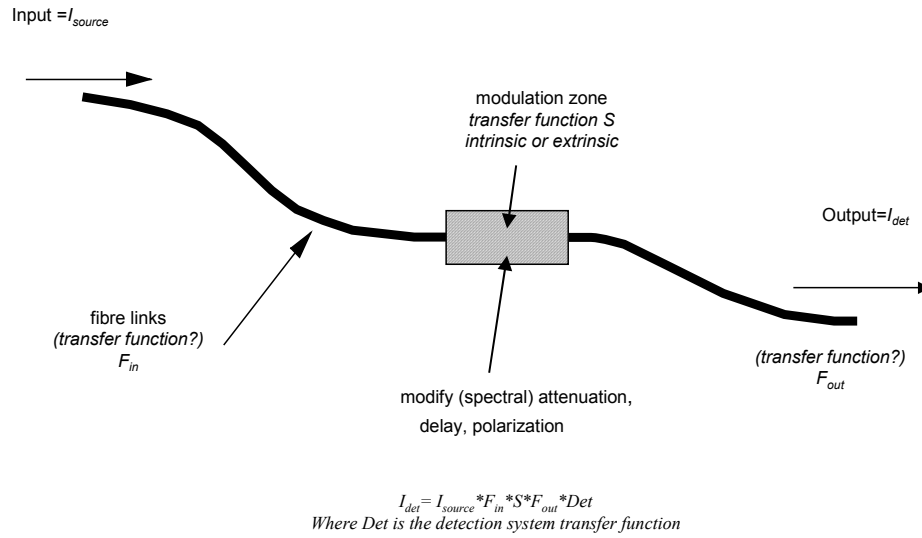


Figure 1: The fibre sensor: illustrating the relationship between what is detected and the measurand

For any form of analogue modulation the characteristics of the transmission regions are almost always variable so recalibration is often the only approach to consistent repeatable measurement. For digital modulation and any form of frequency/wavelength modulation the interface between the measurand and the fibre through various transduction transformers (glues, chemical reagents, coatings, fixings etc) must also be well known and characterised. Further more the stability of the interfaces is always critical whether for analogue or spectral/pulse modulation. The key to a successful sensor lies not so much in ingenious optics but in carefully engineering the package and in ensuring robust data interpretation.

In all cases the sensor decoding system, both electronic and optical, needs careful definition to ensure its performance matches the capability of the sensor itself. Recalibration, direct or implicit, is inherent in the processing: some validation procedure during the sensor lifetime is always desirable, sometimes necessary. Some architectures are self calibrating and can be scaled and set to zero at every reading. There are relatively rare - principally some types of spectroscopic chemical measurements. Recalibration is the norm. This can be implemented against a known signal (e.g. earth rate and zero rotation for gyroscopes) but for remote sensors direct recalibration becomes impossible. Confidence is essential.

The diversity of the parameters involved in determining sensor stability is immense and goes well beyond the domains traditionally considered in optical fibre communication systems. The principal factors which affect the operation of physical sensors include:

- Strain transfer between structure of interest and the sensor element, and the stability thereof.
- Thermal transfer stability and correction as appropriate and as required.
- Fibre and connectors with stable transfer characteristics for the modulated optical signal.
- Demodulators, detectors and signal processing to satisfactorily decode the appropriate information from the received signal.
- Sources with stable spectral and intensity characteristics as required by the modulation protocol in the sensor architecture.

The whole process is inherently far more complex than the simple on/off optical signal which typifies communications systems. The standards and specifications issues associated are consequently extremely diverse and different from the majority of constraints required in communications. In particular very high speed

communication and modulation over long distances has thus far never been required. However there are often specific demands on the optical system - for example those involving Bragg gratings need extremely precise wavelength measurement.

2.2 The Sensor as a System

The sensor manufacturer creates a product which is technically transparent to the user whose interests are simply in making a measurement and communicating it to some kind of monitoring computer. The final specification therefore defines the quality of the interface between the measurand and the output protocol which embraces standards ranging from 4 to 20 milliamps analogue through IEEE bus standards to a number of other specialised military and industrial requirements.

The needs for trading in sensor technology are therefore that the specification language is unambiguous and well understood by supplier and user. This need not be necessarily straightforward: the same measurement can be approached through different rules in different industries and also the optical community sometimes - as in the case of the gyroscope - invents its own language which needs to be translated. This, whilst inconvenient, is straightforward to resolve.

It is these performance and data interface standards which finally matter. None of this is directly influenced at the optical component level. The sensor manufacturer's task then is to identify the interfaces between the optical system and the outside world which determine how well a particular sensor actually works. A discussion of optical fibre sensor technology-specific standards must therefore concentrate on these interfaces through which optical transduction takes place. There is also a precise "language of standards and specifications"⁽²⁾ and of "expression of measurement results"⁽³⁾. It is essential to transfer these definitions into the fibre sensor context. Selected definitions are given in the Appendix.

For the final customer - the sensor system user - there are also some technology specific issues which must be addressed. These include installation, maintenance, calibration and error correction. All these, and other parameters too, need careful attention.

A draft generic fibre sensor specification has been prepared by the IEC⁽⁴⁾. This attempts to encapsulate all sensor mechanisms in all environments and applications and is, in our view, too general to be usefully incorporated into the technical evaluation and definition of a specific sensor or its components.

3. COMPONENTS FOR FIBRE OPTIC SENSORS

3.1 Introductory Comments

There are three principal contributors to the sensor system performance which require attention from precise, standardised and understood measurement processes. These are:

- The operation of the optical modulation zone which may include the properties of the optical fibre within the interaction region (for intrinsic sensors) or the properties of an external modulation process (for extrinsic sensors). In the context of this paper we shall focus predominantly on the optical fibre itself and therefore on intrinsic sensors (figure 2). Extrinsic sensors involve a multiplicity of technologies and therefore the interface between the measurand and the modulator and in turn the modulator and the optical fibre which transmits the signal must be considered on a case by case basis.
- Coatings and cables have a vital role to play in sensor technology. Some cables are themselves an intrinsic part of the sensor (for example in distributed architectures – figure 3) and in all cases the cable between the sensing region and the detector point must be designed to avoid interference with the propagating optical signal.
- Sources, detectors and data processing must be designed, tested and evaluated for stability in the context of the modulation process utilised by the sensor.

We are then restricting this discussion to examining the measurement issues from the perspective of the sensor manufacturer and his procurement procedures. The sensor manufacturer must define the optical needs in the components carefully and precisely in the context of his customer's requirements both environmental and technical.

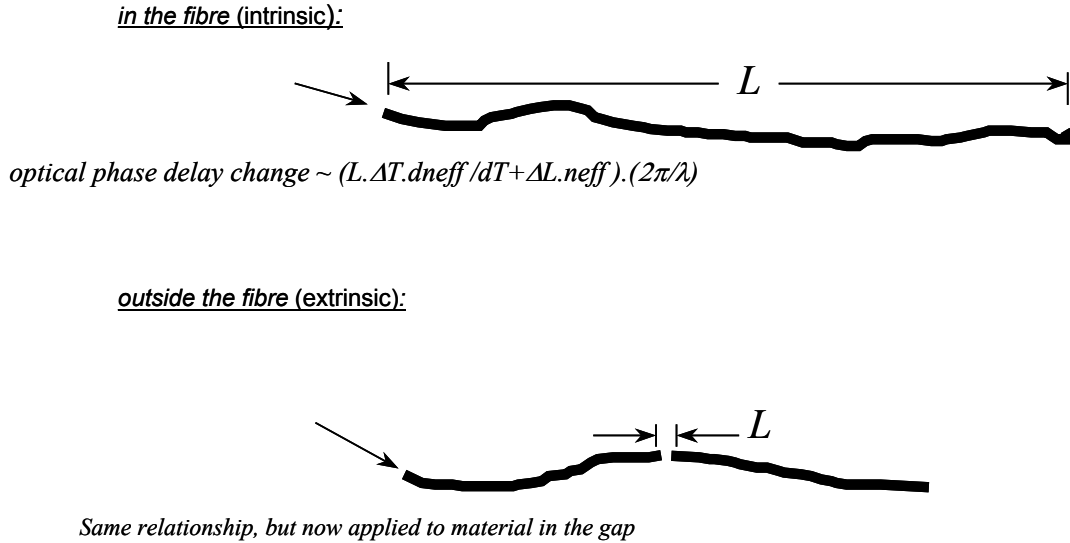


Figure 2: Intrinsic and extrinsic sensors – an example illustrating length measurement within and outwith the fibre

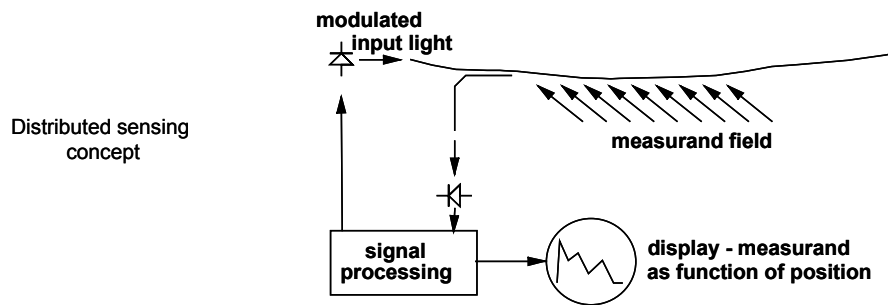


Figure 3: Distributed sensing using fibre optic transducers: obtaining a measurand as a function of position along the fibre

Our focus here is on intrinsic sensors in which the fibre itself performs the optical transduction process either directly or involving an intermediary coating or cabling structure. (except for the fibre gyroscope in which predominantly the geometry of the optical fibre sensing loop is important). In all cases the properties of the fibre itself (plus coatings, cables and packaging) are instrumental in determining sensor response. Furthermore, the demodulation schemes and the source characteristics also play a critical role. We therefore need to carefully characterise these elements for all specific sensor architectures. The principal interactions which determine the relationship between the input measurand and the output reading are highlighted in figure 4. We should note two additional points in this figure. First, interfering measurands, most notably temperature, must always be accommodated and their influence minimised. Secondly, the required relationship between the input measurand and the output reading depends critically on the application context. In particular, the influence of arrays with redundant sensors and equivalently of increasingly robust signal processing algorithms, can substantially alleviate the demands on sensor performance.

In the remainder of this section we shall briefly examine the need for standardisation in fibres themselves, coatings and cables, and detectors and sources

3.2 Coatings and Cables

In communication networks the coatings and cables are simply there to protect the fibre. In intrinsic sensors - with the exception of temperature probes and the fibre gyroscope, the coating and cable are a critical interface between the measurand and the propagating light.

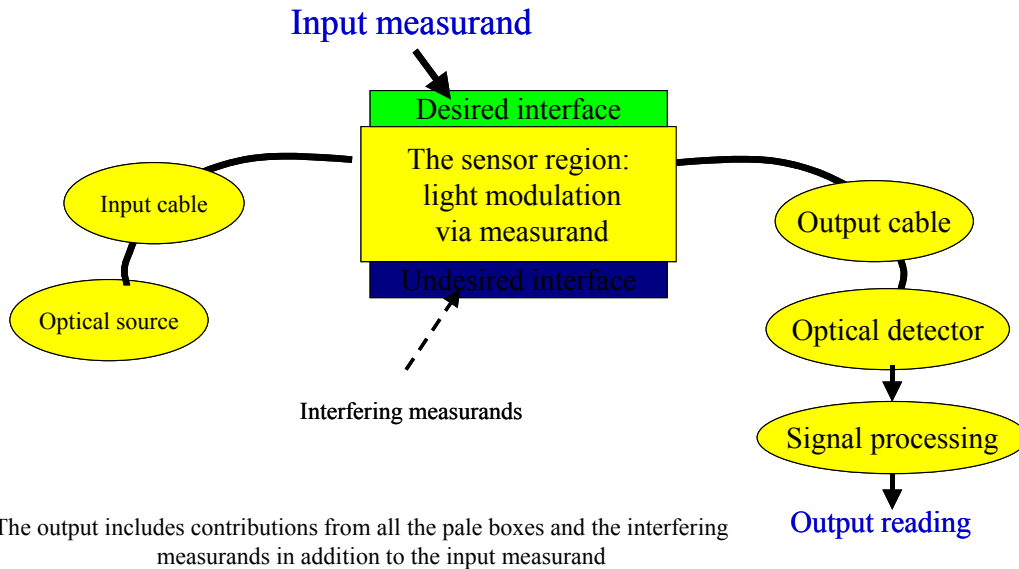


Figure 4: The fibre optic sensor as a measurement tool...illustrating the interfering phenomena which distort the final perceived measurement

For many applications mechanical transfer (strain or pressure) is dominated by the coating and cabling. Strain measurement using optical fibres is a relatively common application and many trial systems based upon Bragg gratings are currently under evaluation. For structurally integrated sensors, e.g. gratings mounted in a carbon or glass fibre composite, the coating material plays a critical part in transferring strain from the host material to the sensor. Techniques for assessing this interface are critical to sensor success. A particularly critical aspect is the interface between the fibre, the fibre coating and the host material. Here push tests (figure 5) show considerable promise⁽⁵⁾.

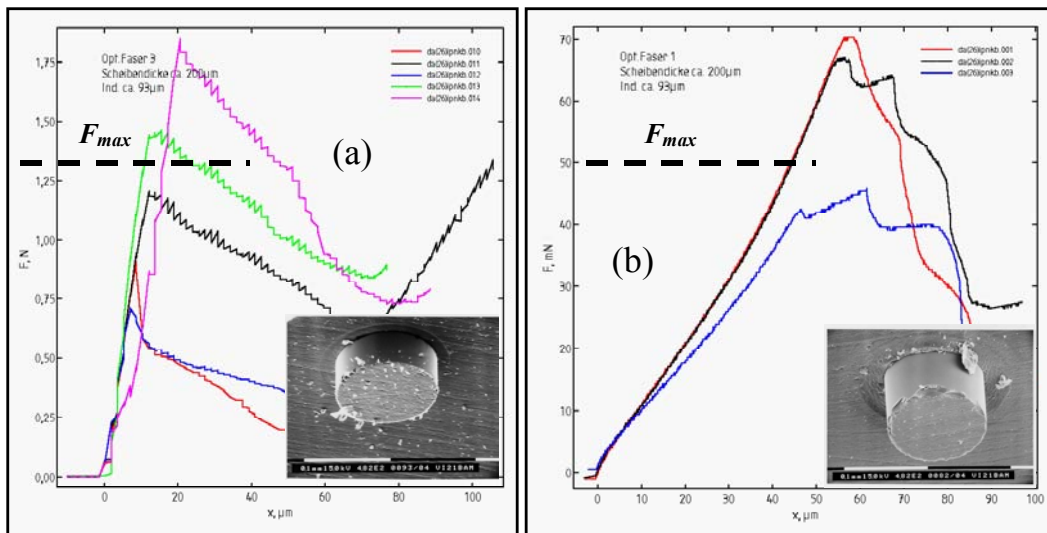


Figure 5: Evaluation of the bonding behaviour of an embedded coated fibre Bragg grating sensors in the epoxy resin matrix of a composite by using the push-in test method⁽⁵⁾. Figure 5(a) shows the bonding failure of a polyimide coated fibre sensor pushed into the matrix at 1.3 N (average). Figure 5(b) shows the failure behaviour of an acrylate coated fibre at already 0.05 N (average).

The SOFO sensor⁽⁶⁾ has been widely exploited in civil engineering. A major contribution to the success of SOFO has been the very satisfactory, stable long-term interfaces between the fibre itself, the sensor packaging and through well defined attachment procedures, the structure under test. Very importantly - and another

function of coatings in sensors - the fibre in the SOFO is mounted under a tension of a few thousand microstrain. This is in complete contrast to communication fibres which are always operated stress neutral. Even small tension can expose micro cracks and induce moisture penetration. Polyimide coatings are particularly appropriate for mechanical sensors. They are thin (typically a few microns), stiff (and therefore give effective strain transfer) and adhere well to both external epoxy based adhesive joints and to the surface of the fibre. Like all polymers these coatings can become hard and brittle with exposure to ultraviolet light and/or high temperatures. When these factors are likely to become problematic, metal coatings can be used, particularly at higher temperatures.

In all sensor architectures the transfer functions of the cabled fibres to and from the sensor region are also important. Ideally these cables should transmit the optical signal which carries the sensor information without any distortion or errors. This requirement is often difficult to meet and must be incorporated into any assessment of fibre sensor applications.

The fibre cable is the means through which the fibre is handled in installation and protected in operation. For many sensor architectures, particularly those concerned with chemical measurements, the cable must be transparent to the environment. Chemically reactive coatings and/or cable structures are often incorporated into distributed chemical sensors. Coating architectures include chemically reactive fluorescent layers used as coating materials and chemo-mechanical transducers which change in shape or volume (typically expand) in response to a chemical measurand. The cables for these sensors must combine providing adequate mechanical protection with providing transparency to the measurand of interest. Once more specific solutions to specific applications are the way forward.

3.4 Sources, Detectors and Demodulation

The influence of sources, detectors and demodulation systems on sensor performance is extremely important. It is also very much determined by the details of the modulation protocol within the sensing transducer. These vary immensely.

The optical fibre Bragg grating when used as a sensor modulates the wavelength of light reflected by the grating. The details for this particular transducer are considered the brief case study which comprises section 5 of this paper. The emphasis is on the long term stability and repeatability⁽⁷⁾ of the wavelength measuring system.

Interferometers are another category of sensors. Here the wavelength of the source and the stability of the reference arm are fundamental to the reliability of the measured result except for nulling interferometers such as SOFO where the distance measurement reference lies within the mechanical control of the tuned arm of the interferometer.

In polarimetric systems polarisation stability is key and again source wavelength comes into play. In intensity based systems source intensity and detector responsivity are fundamental. Changes in optical coupling to fibres may also come into play - for example some sources change their spatial mode spectrum with ageing and/or drive current.

The list is endless. Clearly each case must be treated individually and a careful system analysis is absolutely essential to determine errors in perceived measurements. However much relies upon ingenious design of the sensor architecture and the careful implementation of the optoelectronic source and detector systems. From an optical measurement perspective parameters such as precision wavelength measurement (especially for gratings - see section 5); phase and polarisation state propagation in fibres under varying environmental conditions; or spatial mode stability are important and should be addressed.

3.5 Some General Observations

The diversity of technical requirements in fibre sensors is apparent from the preceding discussion, ranging through the technical measurement needs to the often demanding environmental specifications (thermal, mechanical and biological). These application specific agreements arise predominantly between vendor and supplier and are often so specialised that they sit outside the scope of any international standards and measurement community. There are notable exceptions predominantly where a sensor or a component addresses a diverse market with a range of suppliers. One example of this is the fibre optic gyroscope – a sensor. Another is the Bragg grating - a much used sensor component.

The fibre gyroscope standard⁽⁸⁾ has thus far - to our knowledge - emerged only in draft, a status in which it has lingered for over five years. Furthermore it is a draft written through a US community and the extent to which the international community has acknowledged this standard is far from apparent from published summary data sheets. The evolution of this standard went through a tortuous process during which the vernacular of the fibre gyro community was merged, sometimes painfully, with that of the mechanical gyroscope community to produce a mutually intelligible output. How much this output will benefit the trading community only time will tell.

4. THE DEVELOPMENT OF STANDARD TEST PROCEDURES

Optical Fibre Sensors and their associated instrumentation clearly require comprehensive knowledge of their characteristics under service loading and under operational environmental conditions. To obtain this knowledge the entire sensor system should be characterised using test methods according to well-defined international standard guidelines^(9,10). Through these procedures the all important customer confidence can be assured. The user can compare the capability of different sensor systems available on the market provided that the test procedures are universal and recognised.

The sensor itself, irrespective of its use, has a number of principal parameters which characterise it and which must be clarified:

- The sensor related characteristics including range, resolution, sensitivity
- Uncertainty in the measurements including repeatability and reproducibility taking into account mechanical and thermal hysteresis.
- Long-term stability at constant temperature and the dependence of stability on temperature.
- Long term proof of zero point accuracy (for example position in displacement/ strain sensors) as appropriate to the application.

Often long term sensor use is required and again standard procedures must be determined to provide accurate comparison for parameters such as:

- Creep: depending on temperature and mechanical cycling (for example relaxation in coatings, in support materials, in adhesives etc).
- Drift parameters: a function of temperature and other influences such as moisture associated with this the definition of recalibration procedures where appropriate and available.
- Durability: for the materials within the sensor under the appropriate environmental conditions.

Sometimes sensors must be removed and reinstalled on a regular basis or essential components such as cables, splitters, filters etc may require replacement due to wear, accidents or environmental conditions. Under these circumstances a number of other parameters must be specified including:

- Mating and repeatability of connectors if these are frequently opened.
- Cross sensitivity of components to exterior unwanted measurands (including the sensing element itself, the interconnecting fibres, connectors and splices, optoelectronic decoding systems etc) under both mechanical and thermal influences.
- Characterisation of zero point changes.
- The influence of corrosive or other hostile media within the environment.

The general requirements for testing laboratories are well documented as exemplified in ISO/IEC 1705/2000⁽⁹⁾ and any testing programme must comply with these, or equivalent, recommendations. However the specific situation of fibre optic sensors is somewhat different. There exists a comprehensive standard set concerning fibre optic components as classified under 33.180 in International Classification of Standards⁽¹¹⁾. These standards have been prepared by IEC Technical Committee 86 and cover the necessary methods to characterise components in telecommunication systems. Within this set only one focuses on optical fibre sensors (IEC 61757-1:1998)⁽⁴⁾. The standard defines some terms (for example extrinsic sensor, intrinsic sensor etc) but to date only addresses test and measurement procedures as headline points. This standard, to be useful, requires total revision.

To date, no standards describe explicit methods for test and characterisation of components for fibre sensor systems. Consequently all current trade based on the components for fibre sensors and the sensors themselves

must be executed through local agreement, or through reference to communications standards, as appropriate. The sensing product can however be defined through established processes for the particular application.

As an example, a standard test method should be evolved to identify and characterise the strain transfer mechanisms for structurally integrated fibre Bragg grating sensors. Its test methods should comply with existing generic standards, for example ISO 10012⁽¹⁰⁾. In this particular case appropriate techniques such as push testing must be defined in detail to comply with these generic measurement processes. These procedures, for example, will define an ultimate maximum reliable applied strain value and the necessary properties of any fibre coatings in the measurand:fibre interface.

In all cases an agreed language is essential. There is considerable ambiguity in the vocabulary used by both manufacturers and users to define fibre optic sensor performance. Common usage sometimes differs from precise technical usage. Words like “accuracy” “resolution” “sensitivity” are often misinterpreted. This can lead to sometimes-considerable confusion and avoidable misunderstandings. In order to contribute a little to this debate we have appended the definitions of a selection of important terms. A more comprehensive dictionary can be obtained through the usual standard sources⁽²⁾.

5. THE FIBRE BRAGG GRATING

The fibre Bragg grating is extensively used in sensing predominantly to measure strain fields both dynamic and quasi static⁽¹²⁾. The grating is also temperature sensitive (1°C change in temperature gives an equivalent signal to 10µε) so temperature compensation is an essential. In broad terms the strain coefficient is 1ppm.µε⁻¹, the temperature coefficient is -10ppm.K⁻¹.

The Bragg grating is also used extensively in communication systems, invariably as a wavelength reference standard. There is an immediate contrast: in communications the grating must be kept absolutely stable - the sensor environment is much more demanding.

In sensing the Bragg grating operates by modulating the reflected peak wavelength from a broad input spectrum with the coefficients mentioned above (figure 6) Consequently, 1µε corresponds to around 1pm change in reflected wavelength. Since most strain measuring systems require 10 µε or better resolution, the wavelength measurement can be extremely challenging. The fibre Bragg grating sensor needs an accurate, repeatable and transferable decoder. Ideally one manufacturer’s decoder should give an identical reading to another’s. There has as yet been only one comparison of the numerous decoding systems which are currently available and this study has pointed towards achievable interchangeability with precision references in the tens to 100pm range⁽⁷⁾. In order to improve this reproducibility, reference wavelength standards are necessary. There are a few gas absorption lines in the necessary wavelength region to which curve fitting may be applied, but such procedures need consistent definition.

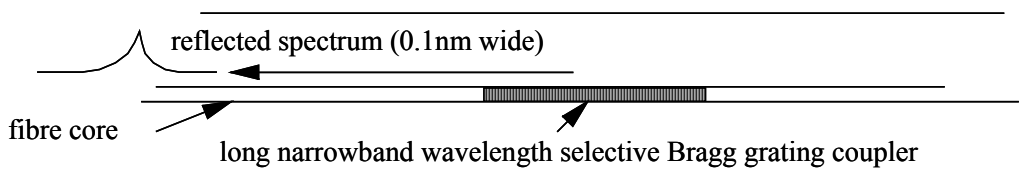


Figure 6: The operating principle of the Fibre Bragg Grating the reflected wavelength varies as the grating period varies. Note that the reflected line width typically exceeds the wavelength measurement precision needed for sensing.

The final issue with Bragg gratings is that of the longevity of the grating itself. This is written into the fibre using a photo degradation process and its permanence is clearly important both in terms of the modulation depth of the grating and its period. Again temperature and strain cycling give the sensor a much more demanding task than the more usual communication technology, especially if as is often the case, the grating is operated under permanent tension.

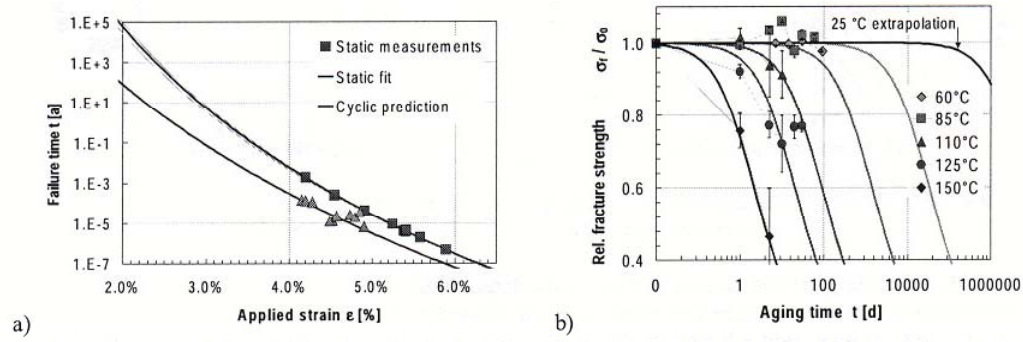


Figure 7: Fibre lifetime estimation by model extrapolation after accelerated aging tests: (a) aging by stress, and (b) aging at low strain but high relative humidity (85%) and increased temperature. (courtesy Phillip Nellen, EMPA)

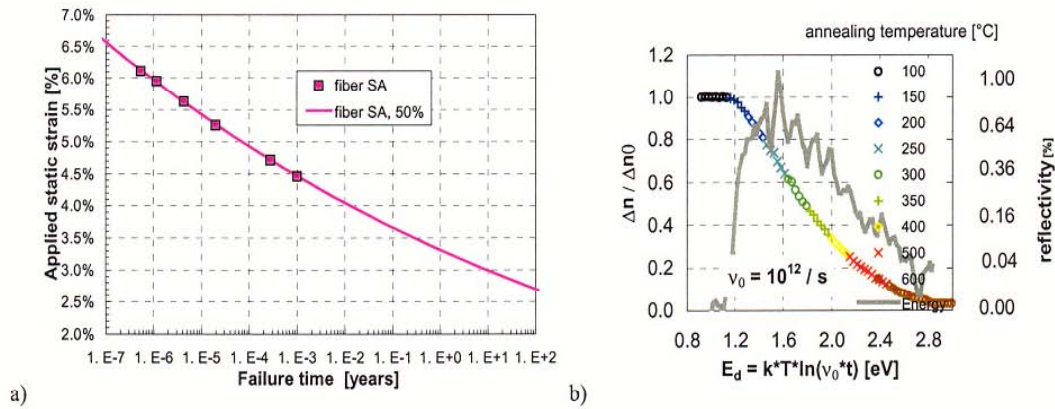


Figure 8: Static lifetime curve (a) of the sensor fibre and reliability master curve (b) of the fibre Bragg gratings (refractive index modulation (right axis) and energy distribution in (a.u)). (courtesy Phillip Nellen, EMPA)

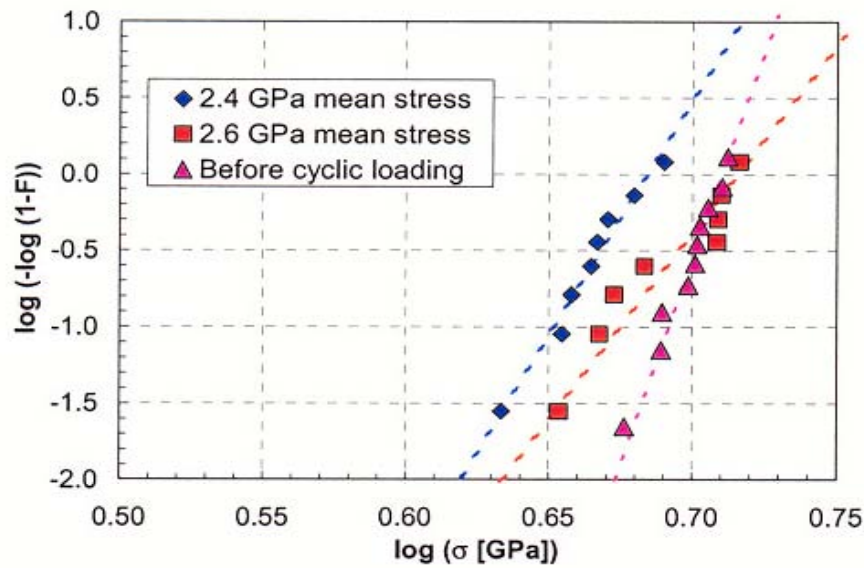


Figure 9: Weibull plots of FBG's measured by dynamic tensile testing at a stress rate of 0.1GPa/sec before and after cyclic loading with a mean stress of 2.4GPa and 2.6GPa. (courtesy Phillip Nellen, EMPA)

Clearly the strain and temperature transfer characteristics themselves require characterisation under a wide range of conditions to give 2-dimensional matrix of strain transfer coefficient at all temperatures and temperature coefficients at all achievable strains. As an additional complication the gratings are also pressure sensitive which is important at the interface between textile layers in composites (local transverse pressure from textile reinforcements) or in high pressure applications (for example down hole in oil exploration). Asymmetric mechanical fields can induce birefringence which broadens or splits the grating reflection spectrum⁽¹³⁾. These last observations apply also to simple intrinsic fibre sensors used in interferometric or polarimetric mode.

The mechanical and thermal longevity of gratings has been extensively evaluated and some example results are shown in figures 7 and 8^(14,15). These results are the most extensive published to date and provide a first rate mechanical and thermal reference on the performance of Bragg gratings. EMPA have also examined reliability under tension (Figure 9). There are however numerous special issues remaining particularly the behaviour of gratings at temperatures over 200°C including the effect of hydrogen on their characteristics and their behaviour with coatings. The measurements are inherently difficult requiring the application of precisely known mechanical fields in addition to a controlled and variable temperature environment. They define the ultimate precision within which the fibre grating can be expected to perform and also determine the long term drift and stability. The gratings must always be used with coatings (see section 3.3), sometimes under extremely demanding thermal and/or mechanical stresses.

There are opportunities here to assist the sensor community in thoroughly understanding this critical basic component. At present such measurements when needed are undertaken on a case by case basis usually by sensor system providers. The results are invariably confidential so the overall technical community has benefited minimally. Some techniques for sharing experiences could also assist enormously in more rapidly advancing the application of this much used sensor element.

6. DISCUSSION AND OUTLOOK

Our paper has endeavoured to present an impression of the issues which surround the evolution of standards and measurement protocols for optical fibre sensors. We have seen that in most cases the need for standards is very specific to a particular application domain and that internationally agreed standards for the optical fibre sensors themselves are driven by a need into that particular application from a multiple supplier base. However, standards for fabrication processes, process outcomes, components and procedures will contribute immensely to the diverse SME culture which services most of the sensor industry.

These standards address three needs. The specification of the sensor itself is an agreement between manufacturer and final user invariably involving external statutory, insurance, liability, process control or operational needs. These can be defined from the existing literature in the application domain on a case by case basis. The second area lies in processes and procedures within the manufacturer. Again these can be defined via reference to the standard set of guidelines encapsulated in, for example ISO 9000 and related documents.

The third areas are technology specific and it is here that considerable contributions could be made from the standardisation communities. We have illustrated the needs in Bragg gratings, some of which have been addressed. There are also needs for reference definitions in the properties of coatings and cables for sensing and in the properties of the fibres themselves, especially for non-linear distributed sensing. Most of all, guidelines to assist in smoothing the manufacturer: user interface would be most welcome. These guidelines would enable the user to become confident in how to utilise this relatively rare technology by highlighting factors which are specific to its use. These could include many of the issues mentioned here concerning measurand transfer, recalibration, stability in measurand transfer, the impact of sources, interconnect fibres and detectors and the generic environments into which fibre sensors can be applied. Such information exists, but brought together and approved through an authority like IEC, it would comprise a valuable tool to enable the fibre sensor manufacturer to work effectively to increase his customer base and the potential user to fully understand the implications of using the technology.

ACKNOWLEDGEMENTS

Many have contributed to the development of this paper including, in no particular order, Daniele Inaudi, Bill Morey, Sam Crossley, Sid Bennett, Dick Dyott, Wolfgang Ecke, Phillip Nellen, Johan Vlekken all of whom have made valuable inputs to the discussion and provided invaluable background information.

REFERENCES

- 1 OFS early history is summarised in: B. Culshaw, *Optical Fibre Sensors and Signal Processing*, Peter Peregrinus, Stevenage, UK 1984
- 2 *International Vocabulary of Basic and General Terms in Metrology*. Beuth Verlag GmbH Berlin Wien Zürich. 1994.
- 3 *Guide to the Expression of Uncertainty in Measurement (GUM)*. ISO, First Edition 1995.
- 4 IEC 61757-1:1998. *Standard: Fibre optic sensors - Part 1: Generic specification*. 1998.
- 5 Habel, W.: *Fiber optic sensors for deformation measurements: criteria and method to put them to the best possible use*. Invited paper, to be published in Proc. of SPIE vol. 5384 (2004), paper 23.
- 6 Inaudi, D.: *Testing performance and reliability of fiber optic sensing system for long-term monitoring*. Proc. of SPIE vol. 5502 (2004) 552-555.
- 7 Dyer, S. D.: *Key metrology considerations for fiber Bragg grating sensors*. To be published in Proc. of SPIE vol. 5384 (2004), paper 25.
- 8 IEEE Standard Specification Format Guide and Test Procedures for Single Axis Interferometric Fiber Optic Gyros.
- 9 Standard EN ISO/IEC 17025:2000 (trilingual version): *General requirements for the competence of testing and calibration laboratories* (ISO/IEC 17025:1999).
- 10 Standard ISO 10012-1:1992: *Quality assurance requirement for measuring equipment; part 1: Metrological confirmation system for measuring equipment*. 1992.
- 11 <http://www.iso.ch/iso/en/CatalogueListPage.CatalogueList>
- 12 Udd, E.; Calvert, S.; Kunzler, M.: *Usage of fiber grating sensors to perform critical measurements of civil infrastructures*. Technical Digest OFS-16 (2003) ISBN 4-89114-036-4, pp.496-499.
- 13 Lebid, S.: *Perturbations in behaviour of fibre Bragg grating sensors introduced by local thermal and mechanical influences*. Dissertation at Dresden Univ. of Technology 2003. BAM Dissertationsreihe vol. 2, ISBN 3-86509-136-9.
- 14 Nellen, Ph. M. et al.: *Reliability of fiber Bragg grating based sensors for downhole applications*. Sensors and Actuators A 103 (2003) 364-376.
- 15 Nellen, Ph. M. et al.: *Reliability in fiber optical sensor applications*. Invit. paper. Proc. of SPIE vol 4940(2003)174-185.

APPENDIX – Some selected important terms and definitions⁽²⁾

- Measurement result:

The result of a measurement is only an approximation or estimate of the value of the measurand and thus is complete only when accompanied by a statement of the uncertainty of that estimate, respectively: $\Delta\epsilon = 20 \mu\text{m/m} \pm 3 \mu\text{m/m}$ (95 %) or $\Delta\epsilon = (20 \pm 3) \mu\text{m/m}$ (95 %). The numerical value following the symbol \pm is the combined standard uncertainty and not a confidence interval. The percentage in parenthesis (here: 95 %) informs about the coverage probability, or in other words, about the level of confidence.

- Resolution:

Resolution is defined as smallest difference between indications of the sensor (including the displaying device) that can be meaningfully distinguished. Resolution is often confused with sensitivity. ‘Resolution’ is related to the achievable measurement uncertainty which should not exceed 10 to 20% of the minimum quantity to be measured; resolution be better than below 10 to 20% of this desired measurement uncertainty. The achievable resolution is always defined by the complete measurement system, not only by the displaying device.

- Precision:

‘Precision’ is a qualitative concept, too. It informs about the closeness of the agreement between the results of successive measurements of the same measurand carried out under the same conditions of measurement (repeatability) or under changed conditions of measurements (reproducibility). Both types of precision may only be expressed quantitatively in terms of the dispersion characteristics of the results (e. g. standard deviation σ , variance σ^2).

- Conventional true value:

‘Conventional true value’ or “trueness” (formerly ‘true value’) informs about the closeness of the expectation of the result of measurement to the reference value. At a given location, the value assigned to the quantity realized by e.g. a reference standard may be taken as a conventional true value. Frequently, a number of results of measurements of a quantity are used to establish a conventional true value. It is sometimes called best estimate of the value, conventional value or reference value; it should not be confused with ‘reference value’ in the sense connected to traceability.

- Sensitivity:

‘Sensitivity’ defines the change in the response of a measuring instrument divided by the corresponding change in the stimulus. The sensitivity coefficient describes how the output estimate y varies with changes in the values of the input estimates x_1, x_2, \dots, x_n . The sensitivity may depend on the value of stimulus and have to be expressed then separately for each value. Its unit of measurement cannot be expressed in % but in related unit, e. g. pm/mm.

- Accuracy:

‘Accuracy’ is a qualitative concept and expresses the closeness of the agreement between the result of a measurement and a true value of the measurand. Every still so accurate measurement represents only an estimate; so that accuracy gives the reciprocal information how inaccurate a measurement is due to unavoidable non-linearities, hysteresis effects, environmental influences, vibrations, drifts, and many other effects. Accuracy includes the terms precision and trueness (conventional true value, best estimate of the value). Therefore, the term precision must not be used for accuracy.

Accurate index profile measurements for fiber Bragg gratings and sensor application

Xavier Chapeleau¹, Dominique Leduc¹, Pascal Casari², Yves Quiquempois³,
Josselin Lebon², Francisco Lopez³, Cyril Lupi¹ and Christian Boisrobert¹

¹*Institut de Recherche en Electrotechnique et Electronique de Nantes-Atlantique (IREENA),
Université de Nantes, 2 rue de la Houssinière, 44300 Nantes, France*

²*Institut de Recherche en Génie Civil et Mécanique (GEM),
Université de Nantes, 2 rue de la Houssinière, 44300 Nantes, France*

³*Laboratoire de Physique des Lasers, Atomes et Molécules (PhLAM), UMR CNRS 8523,
Université des Sciences et Technologies de Lille, 59655 Villeneuve d Ascq, France
xavier.chapeleau@univ-nantes.fr*

Abstract : This paper demonstrates that the combination of the optical low-coherence reflectometry and the layer-peeling algorithm is a suitable method to measure the index profile of fiber Bragg gratings. The high sensitivity of this technique permits to detect index modulation amplitude as small as 10^{-5} . The phase of the grating can also be determined accurately and we demonstrate that this measurement permits to retrieve the axial strain distribution for gratings subjected to strain gradient.

1 Introduction

The determination of the index profiles of Fiber Bragg Gratings (FBGs) is more and more desired in order to improve their spectral and temporal performances in particular for high bite rate transmission systems. Some methods as tranverse diffraction technique, local heating technique or Optical Space Domain Reflectometry (OSDR) can be used but they are more suitable for highly reflective gratings. In general, their sensitivity is not sufficient to detect index modulation amplitude below 10^{-4} . An alternative method is based on the association of the Optical Low-Coherence Reflectometry (OLCR) and an inverse scattering algorithm called layer-peeling [1]. The OLCR measures the complex reflection coefficient which is necessary for the layer-peeling to retrieve the index profile of FBGs. The aim of this paper is to demonstrate the efficiency of this method. The sensitivity of the index modulation amplitude and phase measurements are studied. An application of our method to the determination of axial strain distribution is also presented.

2 OLCR and layer-peeling

FBGs are a periodic refractive index modulation in the core of optical fibers, induced by UV exposure. This index perturbation $\Delta n(z)$ is generally written as the following form :

$$\Delta n(z) = \Delta n_{DC}(z) + \Delta n_{AC}(z) \cos \left[\frac{2\pi}{\Lambda_0} z + \frac{2\pi}{\Lambda_0^2} \int_0^z (\Lambda(z') - \Lambda_0) dz' \right] \quad (1)$$

where Δn_{AC} is the index modulation amplitude and Δn_{DC} is the mean index variation. $\Lambda(z)$ is the period of the grating. For uniform gratings $\Lambda(z) = \Lambda_0$ and for gratings with linear chirp $\Lambda(z)$ is expressed as $\Lambda(z) = \alpha z + \Lambda_0$.

The layer-peeling algorithm is based on the coupled mode theory. By knowing the complex reflexion coefficient, this algorithm gives the coupling coefficient $\Omega(z)$ which is expressed by the following relation :

$$\Omega(z) = \frac{\eta \pi}{2 n_{co} \Lambda_0} \Delta n_{AC}(z) e^{-i \Psi(z)} \quad \text{with} \quad \Psi(z) = \frac{2\pi \eta}{n_{co} \Lambda_0} \int_0^z \Delta n_{DC}(z') dz' + \frac{2\pi}{\Lambda_0^2} \int_0^z (\Lambda(z') - \Lambda_0) dz' \quad (2)$$

where n_{co} is the unperturbed effective index of the fiber and η the fraction of the modal power contained in the fiber core. $\Psi(z)$ corresponds to the phase of the grating. The equation 2 shows that the index modulation amplitude and the phase of the grating can easily be determined. However, the layer-peeling algorithm can only be used if the complex reflexion coefficient of FBGs is measured accurately. The OLCR is admitted as a suitable method to do it. Several papers [2, 3, 4] have demonstrated its efficiency. A description of our experimental set-up and the first results we obtained can be found in [5].

3 Performance of the OLCR technique

As all inverse scattering algorithms, the layer-peeling is hindered due to the presence of noise in the complex reflexion coefficient measurements, especially for high reflexion coefficient. So, it can't determine correctly the index profile of FBGs having reflexion coefficient upper than 90 %. It's the highest limit we obtained so that the index profiles determined by the layer-peeling and the transverse diffraction technique (Krug method [6]) are in good agreement. The figure 1 shows the index modulation amplitudes obtained by both methods for a uniform FBG whose reflexion coefficient is equal to 90 %. We can notice that the index profiles exhibit some ripples. They are not an artefact of the layer-peeling algorithm since they appear also for the transverse diffraction measurement. They are due to internal reflexion in the phase mask. To evaluate the repetability of ten successives measurements, the maximum relative difference has been calculated. In the figure 1, we can see that these differences remain lower than 3 %, which demonstrates the high repetability of our measurements.

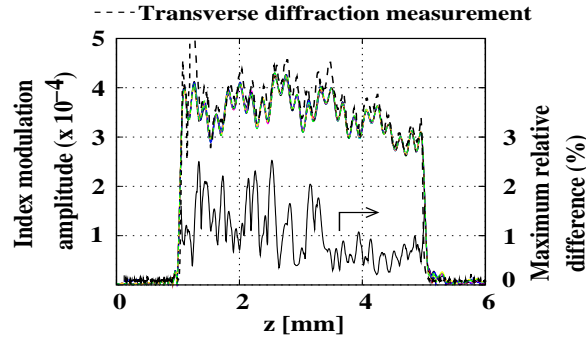


Figure 1: Index modulation amplitude. $R = 90\%$ (10 measurements)

It's clear that the layer-peeling algorithm is most suitable for weak gratings. However, if the coupling strength becomes too small, the noise can hinder the index profile reconstruction. To illustrate this fact, the figure 2 shows the index profile of a grating whose reflexion coefficient is equal to only 1 %. In this case, the index modulation amplitude doesn't exceed 2.5×10^{-5} and we can see that the maximum relative difference is a little higher than in the previous case. Nevertheless, it remains lower than 4 %. It's important to emphasize that the index profile presented in this figure can't be detected by the diffraction technique. This proves the high sensitivity of our method.

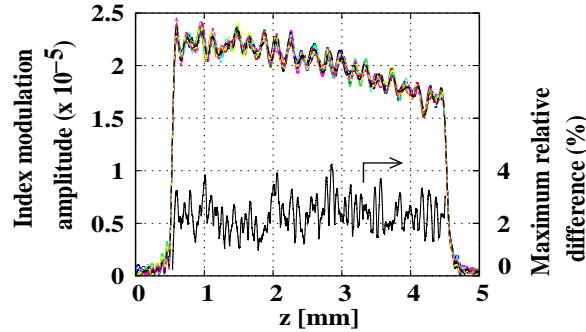


Figure 2: Index modulation amplitude. $R = 1\%$ (10 measurements)

To show more precisely the sensitivity, the index profile of a particular grating has been measured. Seven uniform, $500 \mu\text{m}$ long, gratings were written successively and the index modulation amplitude was divided approximately by two from one grating to the next. The measured index profile reveals well this step structure (cf. figure 3). The first step has a high index modulation amplitude close to 1×10^{-3} . The last step is very small since the index modulation amplitude is below 2×10^{-5} . This results demonstrate that the association of the layer-peeling and OLCR techniques is perfectly suitable for the measurement of index profile whose amplitude is as small as 1×10^{-5} .

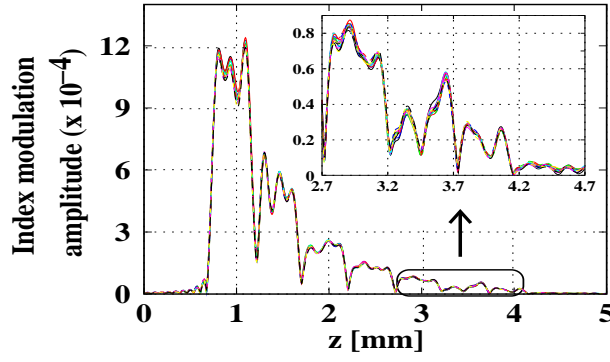


Figure 3: Index modulation amplitude (10 measurements).

4 Phase grating measurement

An other advantage of our technique is that the phase of the grating can be measured. For example, a π phase-shift grating has been studied. Theoretically, if we assume that the mean index $\Delta n_{DC}(z)$ is constant along the grating, the phase grating can be modeled by :

$$\begin{cases} \Psi(z) = \frac{2\pi\eta}{n_{co}\Lambda_0} \Delta n_{DC} z & \text{if } 0 < z < z_0 \\ \Psi(z) = \frac{2\pi\eta}{n_{co}\Lambda_0} \Delta n_{DC} z + \pi & \text{if } z_0 < z < L \end{cases} \quad (3)$$

where z_0 is the position of the phase-shift in the grating.

The figure 4 shows the phase we obtained for this grating. This phase is linear with z and in the middle of the grating, we can see the phase-shift which expands over $50 \mu\text{m}$. Sometimes, it can be less long, this depends on the fabrication process. The figure in insert shows that the amplitude of the phase-shift is close to π as expected. Thus, this result demonstrates the efficiency of our method to measure the phase grating.

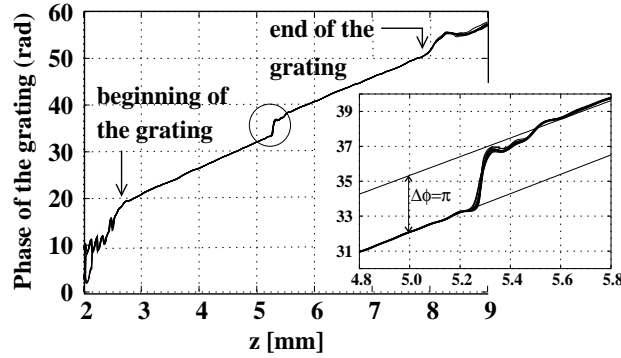


Figure 4: Phase of the π phase-shift grating (10 measurements).

5 Axial strain distribution measurement

When FBGs are subjected to an axial force, both the grating period and the refractive index are modified. Indeed, the refractive index is changed due to the photoelastic effect :

$$\Delta n_{DC} = -\frac{n_{co}^3}{2} [P_{12} - \nu (P_{11} + P_{12})] \epsilon(z) \quad (4)$$

where P_{11} , P_{12} are the strain-optic coefficients and ν the Poisson's ratio of the FBG. The grating period variation is related to the strain by the following relation :

$$\frac{\Delta \Lambda(z)}{\Lambda_0} = \epsilon(z) \quad (5)$$

Taking into account these two effects, the phase of the grating modified by an axial strain becomes :

$$\Psi(z) = \frac{2\pi}{\Lambda_0} \left\{ 1 - \frac{\eta_{\text{nc}}^2}{2} [P_{12} - \nu (P_{11} + P_{12})] \right\} \int_0^z \epsilon(z') dz' \quad (6)$$

So, the axial strain can be obtained simply by differentiating the phase. In order to test this method, an uniform FBG, 4 mm long, has been embedded in a parallelepipedal sample of epoxy resin in which two holes have been drilled symmetrically beside the sensor (figure 5). This scheme permits to obtain a non-uniform strain along the grating.

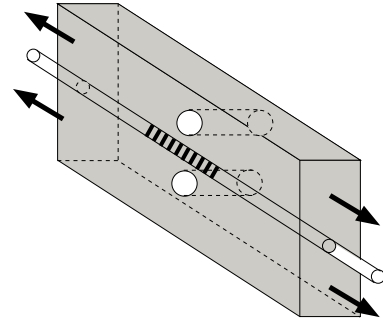


Figure 5: Sketch of the embedded FBG

Figure 6(a) shows the strains obtained from different tensile loads. Without applied force, the strain curve is a straight line despite some small ripples. For a force equal to 1200 N, the curve appears rounded as shows it the figure 6(b). This indicates that the strain is not uniform along the grating. The dissymmetry of the measurement is only due to the fact that the two holes are not perfectly centered to the middle of the FBG.

A finite element model (FEM) has been used in order to predict the strain evolution along the grating. The figure 6(b) shows that the strain obtained by FEM follows exactly the same evolution as the ones measured with the FBG sensor. The excellent agreement between the two results demonstrates the validity of our method for non uniform axial strain measurements.

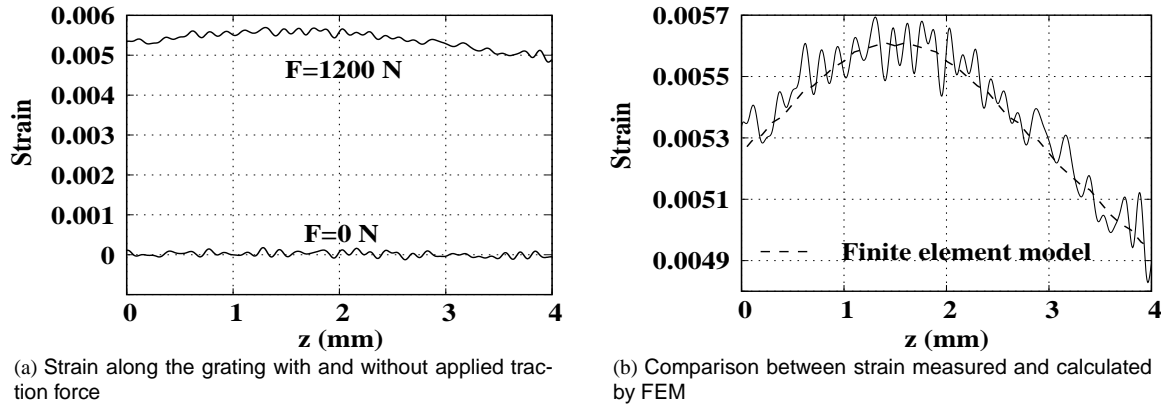


Figure 6: Strain distribution measurement.

6 Conclusion

The association of OLCR and layer-peeling is an efficient method for the index profile of FBGs characterization. Thanks to its high sensitivity, index modulation amplitude variations as small as $1 \cdot 10^{-5}$ can be detected. Moreover, this method gives the phase of the grating, which permits to localize phase-shift or to measure the mean index variation in the case of uniform gratings. Such phase grating measurements can also be used in sensor applications. Indeed, we demonstrated that non-uniform axial strain distribution can be measured.

References

1. J. Skaar, L. Wang et T. Erdogan, "On the Synthesis of Fiber Bragg Gratings by Layer Peeling", IEEE J. Quantum Electron. , **37**(2), 165-173 (2001).
2. D. Leduc, X. Chapeleau, C. Lupi, R. Le Ny et C. Boisrobert, "Accurate low-coherence interferometric relative group delay and reflectance measurements; characterization of a free space optics multiplexeur/demultiplexeur", Journal of Optics A : Pure and Applied Optics, **2**, 51-55, (2003).
3. S. Dyer and K. Rochford, "Low-coherence interferometric measurements of the dispersion of multiple fi ber Bragg gatings", IEEE Photonics Technology Letters, **13**(3), 230-232, (2001).
4. P. Giaccari, H.G. Limberger et R. Salathé, "Local coupling-coeffi cient characterization in fi ber Bragg gratings", Opt. Lett. , **28**(8), 598-600 (2003).
5. X. Chapeleau, D. Leduc, C. Lupi, R. Le Ny, M. Douay, P. Niay et C. Boisrobert, "Experimental synthesis of fi ber Bragg gratings using optical low coherence refectometry", Appl. Phys. Lett. , **82**(24), 4227-4229, (2003).
6. P. Krug and R. Stolte and R. Ulrich, "Measurement of index modulation along an optical fi ber Bragg grating", Optics Letters, **20**(17), 1767-1769, (1995).

Analysis of a Fiber Bragg Grating Writing Process using Low-Coherence Interferometry and Layer-Peeling

R.J. Espejo, M. Svalgaard, and S.D. Dyer
National Institute of Standards and Technology
Optoelectronics Division
325 Broadway, Boulder, CO 80305 USA
email: espejo@boulder.nist.gov

Abstract: We demonstrate accurate measurements of the longitudinal refractive index profile of a fiber Bragg grating (FBG). We measure the impulse response of a FBG with a low-coherence interferometer, calculate the complex spectrum from a Fourier transform of the interferogram, and then apply a layer-peeling algorithm to find the index profile of the measured FBG. We use our results to calibrate and identify systematic errors in a scanning beam/dithered phase mask FBG writing system.

1. Introduction

A written fiber Bragg grating (FBG) is often analyzed by the examination of the reflected power spectrum. This does little to indicate the origins of errors that can degrade the spectral quality. Systematic problems with the writing system such as phase-mask imperfections are difficult to diagnose in this manner. Thus writing often involves a process of trial and error, ending when the correct spectrum is achieved.

Better quality control of the writing process can be accomplished by measuring the FBG's index profile. The exact index profile is particularly important in cases of complicated index profiles, where small deviations from design can greatly affect the resulting spectra. Knowledge of the actual longitudinal index profile that was written into the FBG can be used to identify problems that can then be corrected or compensated for in subsequent writings [1]. This has the potential to greatly improve the quality of the FBGs produced.

We use low-coherence interferometry (LCI) to measure the impulse response of the grating. A layer-peeling algorithm is then used to calculate the complex spatial coupling coefficient of the FBG. We show that our measurements can be used to calibrate a scanning beam/dithered phase mask writing system, and that we can identify systematic errors in written FBGs.

2. Measurement System

The impulse response of the FBG is measured using the fiber-optic Michelson LCI, shown in Fig. 1. We have previously shown that accurate, high-resolution measurements of the dispersive and spectral properties of optical components can be achieved using this measurement system [2].

The FBG to be measured (DUT) is placed in one arm of the Michelson LCI along with a 1319 nm reference grating. The other arm has a variable air path that is capable of scanning a total distance of 1.4 m. The low-coherence signal is provided by a commercial C+L band superfluorescent source. A 1319 nm reference laser tracks the interferometer's total optical path difference as the reference arm mirror is translated. The reference grating

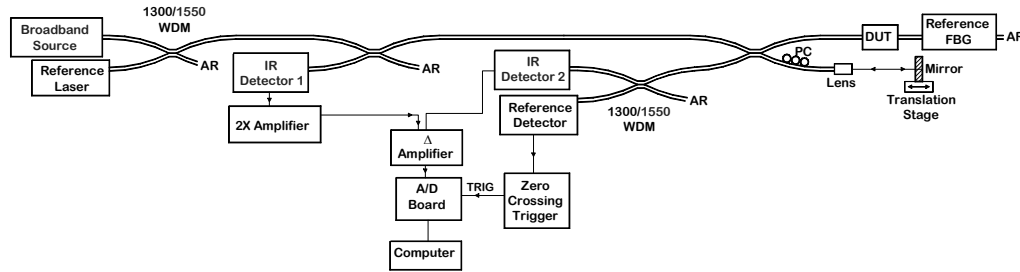


Figure 1. Low-coherence measurement system. DUT: device under test. AR: anti-reflection. PC: polarization control. WDM: wavelength division multiplexer.

provides a narrowband reflection of just the reference laser signal. The low-coherence signal is differentially detected and then digitized with a 16-bit A/D card. Triggering occurs at every zero crossing of the interference signal created by the reference laser, which sets the sample spacing to 659.5 nm. The signal-to-noise ratio (SNR) is greater than 70 dB.

The complex reflection spectrum is found by calculating the fast Fourier transform (FFT) of the interferogram. A layer-peeling algorithm is then applied to the calculated complex spectrum to determine the complex coupling coefficient of the FBG, $q(z)$ [3]. The index modulation amplitude, Δn_{ac} , is calculated from $q(z)$ as follows:

$$\Delta n_{ac}(z) = \frac{|q(z)| \lambda_B}{\pi \eta}, \quad (1)$$

where λ_B is the Bragg wavelength and η is the fraction of power in the fiber core. Assuming that the spatial grating phase is constant, as is ideally the case for a phase mask, the average index change, Δn_{dc} , can be found by

$$\Delta n_{dc}(z) = \frac{\lambda_B}{2\eta} \left(\frac{1}{\Lambda_B} - \frac{1}{\Lambda_{eff}(z)} \right), \quad (2)$$

where Λ_B is the Bragg period, and the effective grating period Λ_{eff} is determined from

$$\Lambda_{eff}(z) = \Lambda_B \left(1 + \frac{\Lambda_B}{2\pi} \frac{d}{dz} \arg(q(z)) \right)^{-1}. \quad (3)$$

The physical interpretation of these grating parameters is shown in Fig. 2.

The spatial resolution of the calculated FBG index profile is limited by the bandwidth of the low-coherence source [3]. A spectral width of 1525 nm-1610 nm gives a maximum resolution of 15 μ m.

3. Calibration of Δn_{ac} as a Function of Phase Mask Dither Voltage

It has been shown that an effective method for controlling the FBG profile during writing is by scanning a narrow ultraviolet (UV) beam across a phase-mask (PM) while the position of the PM is dithered by a piezoelectric transducer (PZT) [4]. Dithering of the PM with an amplitude of one-half the mask period has the effect of completely washing out the fringe visibility; therefore we can control the index modulation written into the fiber by changing the PM dither voltage as the writing beam is scanned across the fiber.

The dither voltage applied to the PZT affects the Δn_{ac} in a cosinusoidal manner, with the period of the cosine determined by the PM period and the PZT's response [4]. These variables necessitate a calibration of the dither voltage applied to the PZT in order to have accurate control over Δn_{ac} for a particular writing system.

To obtain this calibration we wrote a series of gratings with equal exposure times but different dither voltages along a single fiber. The measured Δn_{ac} for each grating is shown in Fig. 3a. In Fig. 3b we show the peak Δn_{ac} of each grating as a function of the dither voltage that was applied when that grating was written. The peak Δn_{ac} of each grating is normalized to the maximum possible index modulation amplitude, which occurs when no dither is applied. We calculated a least-squares cosinusoidal curve fit to the measured data using the cosine period as the free parameter in the fit. Figure 3b allows us to predict the dither voltage needed to achieve a desired Δn_{ac} . By varying the dither voltage as the UV writing beam is scanned along the fiber, gratings with a wide variety of index modulation profiles can be written.

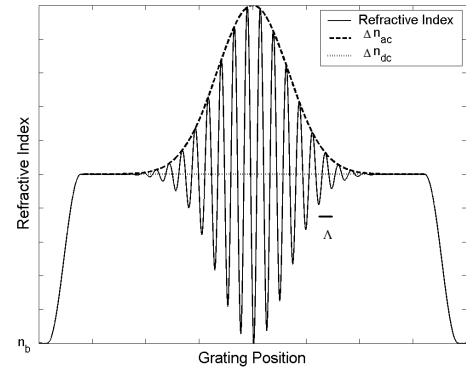


Figure 2. Physical interpretation of Δn_{ac} , Δn_{dc} , and Λ of a FBG. An un-chirped Gaussian apodized FBG shown. The modulation frequency is not shown to scale. n_b : fiber bulk index.

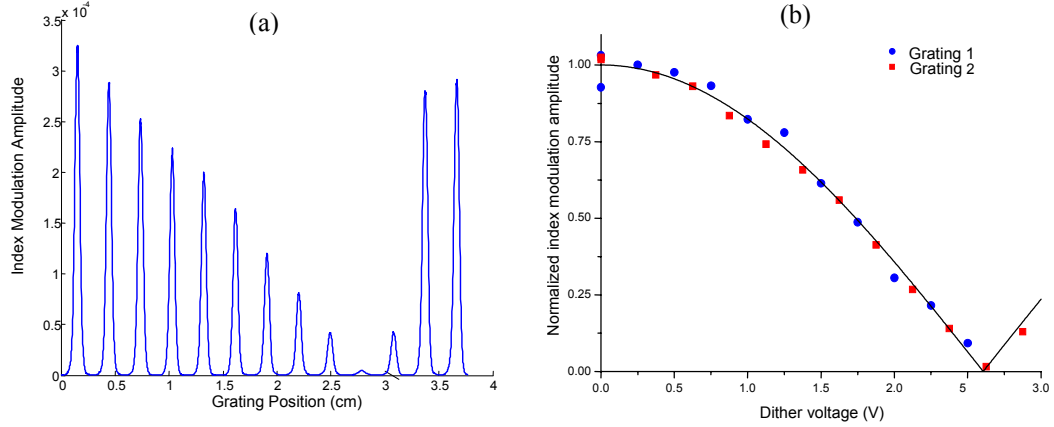


Figure 3. (a): Measured Δn_{ac} of the grating series. Each grating has the same exposure; only the PZT dither amplitude is changed, and each is the width of the writing beam (~ 0.5 mm). Shown is the average of 10 measurements. (b) Index modulation (Δn_{ac}) vs. PM PZT dither voltage. Calibration curve fit is used for determining the appropriate dither voltage needed in order to achieve a desired index modulation when writing a FBG. Two separate grating sets fabricated several weeks apart were used.

4. Troubleshooting Errors in the Grating Writing Process

Our measurements can be used to identify problems in the grating fabrication process, which can lead to unexpected errors in the reflection spectrum of a written FBG. Once these problems are identified and characterized they can then be compensated and the desired spectrum achieved.

4.a. Phase Mask Uniformity

To check the PM for non-uniformities 18 gratings were written under identical conditions across the full width of the mask. Sampling of the PM in this manner was chosen rather than writing a single uniform grating, due to the difficulties in measuring long, strong gratings [5].

The measured Δn_{ac} is shown in Fig. 4. The slight non-uniformity shows a similar trend as seen in direct measurements of the diffraction efficiencies for this mask. Our results show that the achieved index modulation amplitude decreases in a slow manner across the phase mask, with a total variation of $\sim 8\%$. After mapping the PM non-uniformity, we can adjust the PM dither voltage or the UV exposure time when writing subsequent gratings with the same PM to compensate for its non-uniformity.

4. b. Writing Errors

Cosine-apodized FBGs are desirable since their reflection spectra have suppressed side-lobes. We produced a cosine-apodized grating using our scanning beam/dithered PM writing system. The measured spectrum and index profile for this grating are shown in Figs. 5a and b. Although the measured Δn_{ac} fits the intended cosine curve reasonably well, several obvious imperfections can be seen. The one that is labeled “mask defect” appears to be a defect on the PM since it appears in the same location on several other gratings written with this mask. The second, narrow grating seen to the right of the main grating labeled “writing error” is the result of an error that occurred when the writing beam was not shuttered at the appropriate

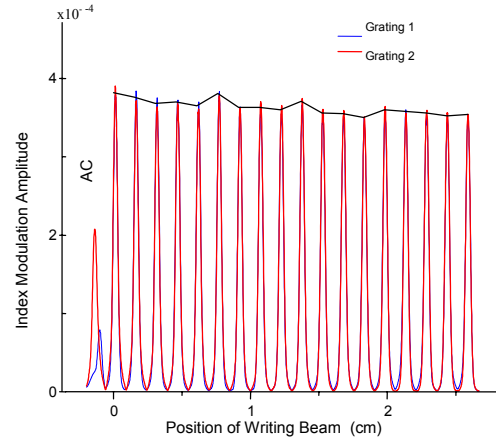


Figure 4. Grating series for mapping phase-mask non-uniformity. For the peak labeled AC (alignment check) the beam was walked on to the edge of the mask to ensure that the writing began in the same place each time. Two different grating sets were used and the results for each are shown. The two curves are practically indistinguishable.

time. Figure 5b shows the Δn_{dc} of the FBG. An ideal apodized FBG should have a constant dc component to its index profile. The linear increase of approximately 7.8×10^{-5} /cm in Δn_{dc} detected in the measured FBG will cause a chirped broadening of the reflection spectrum

We simulated the combined effect of these writing errors on the FBG reflection spectrum using the well known matrix-transfer method [3]. The simulated spectrum is shown in Fig 5c along with the reflection spectrum of an ideal cosine-apodized grating and the reflection spectrum measured by LCI. The measured index profile of the FBG provides valuable information as to why the reflection spectrum does not match the ideal case. It is unlikely that these errors could have been identified by spectral analysis alone.

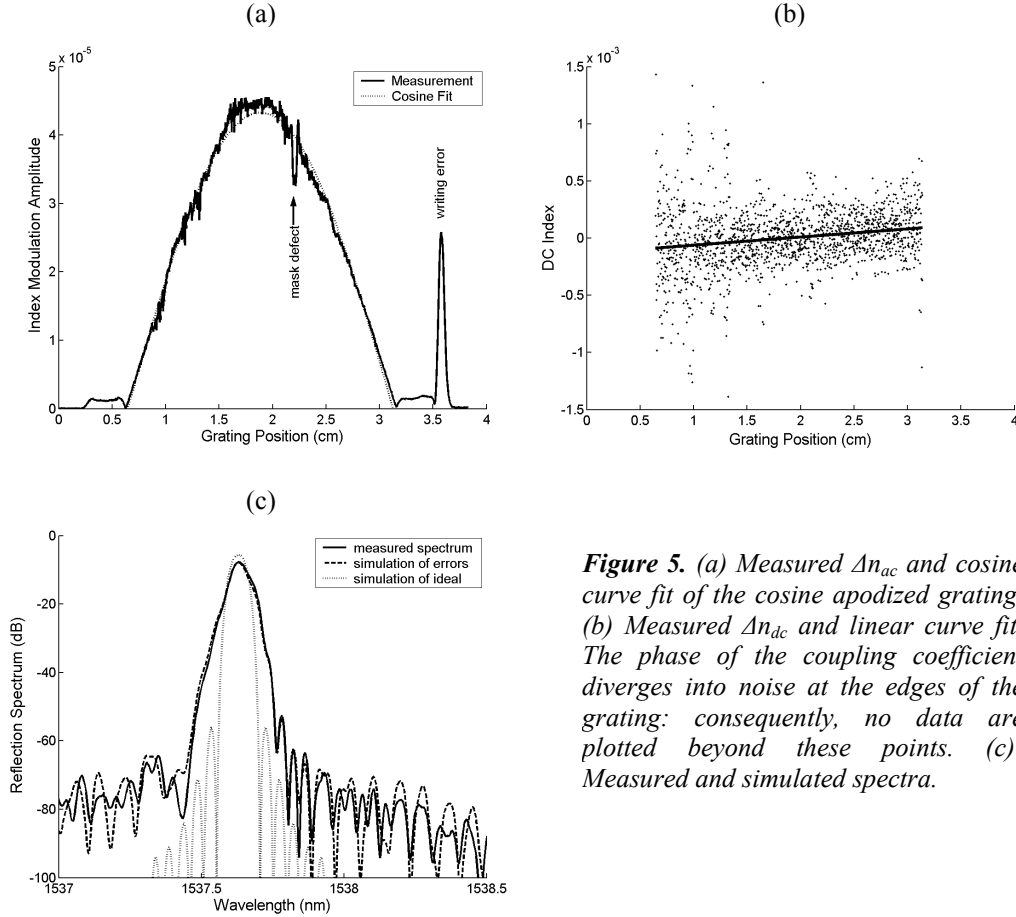


Figure 5. (a) Measured Δn_{ac} and cosine curve fit of the cosine apodized grating. (b) Measured Δn_{dc} and linear curve fit. The phase of the coupling coefficient diverges into noise at the edges of the grating; consequently, no data are plotted beyond these points. (c): Measured and simulated spectra.

5. Conclusion

We have demonstrated a fast and accurate method for the calibration and analysis of a FBG writing process. Our measurement gives high-resolution (15 μ m) spatial characterization of the FBG. We have also shown the ability to identify imperfections in the written grating, and we have shown that these imperfections can have a significant impact on the FBG's reflection spectrum.

6. References.

1. A. V. Buryak and D.Y. Stepanov, "Correction of systematic errors in the fabrication of fiber Bragg gratings," *Opt. Lett.*, vol. 27, no. 13, pp.1099-1101 (2002).
2. S.D. Dyer, R.J. Espejo, and P.A. Williams, "High-Resolution Group Delay Measurements of a Hydrogen Cyanide Gas Cell Using Low-Coherence Interferometry," SOFM 2002, Boulder, CO, NIST Spec. Publ. 988, pp. 45-48 (2002).
3. J. Skaar, L. Wang, and T. Erdogan, "On the Synthesis of Fiber Bragg Gratings by Layer Peeling," *IEEE J. Quan. Elect.*, vol. 37, no. 2, pp. 165-173 (2001).
4. M. J. Cole, W. H. Loh, R. I. Laming, M. Zervas and S. Barcelos, "Moving fibre/phase mask-scanning beam technique for enhanced flexibility in producing fibre gratings with a uniform phase mask," *Elect. Lett.*, vol. 31, pp. 1488-1490 (1995).
5. J. Skaar and R. Feded, "Reconstruction of gratings from noisy reflection data," *J. Opt. Soc. Am. A*, vol. 19, no. 11, pp. 2229-2237 (2002).

CO₂-laser induced LPFG's torsion characteristics depending on the length of the twisted fiber

Yi-Ping Wang and Jian-Ping Chen

State Key Laboratory on Local Fiber-Optic Communication Networks and Advanced Optical Communication Systems, Shanghai Jiao Tong University, Shanghai 200030, China, E-mail: wangyp@sjtu.edu.cn

Yun-Jiang Rao

Department of Optoelectronic Engineering, Chongqing University, Chongqing 400030, China

Abstract: The unique torsion characteristics of the CO₂-laser-induced LPFG depend strongly on the length of the twisted fiber. While the LPFG is much shorter than the twisted fiber, its resonant wavelength and amplitude change wavelike with the twist-rate applied. In addition, the shift of the resonant wavelength is dependent on the twist direction.

1. Introduction:

Long period fiber grating (LPFG) is a promising passive optical fiber device. Lin [1] and Soohie [2] explored the torsion characteristics of LPFGs fabricated by the etched corrugation and the electric arc discharge, respectively. In our previous works [3], it is found that the torsion characteristics of the CO₂-laser induced LPFG whose length is similar to one of the twisted fiber depend strongly on the twist-directions. That is, the resonant wavelength shifts linearly toward the longer wavelength as the LPFG is twisted clockwise, whereas it shifts linearly toward the shorter wavelength as the LPFG is twisted anticlockwise. In this paper, the unique torsion characteristic of the CO₂-laser induced LPFG which is much shorter than the twisted fiber was demonstrated for the first time to our knowledge.

2. Twist experiments:

The experimental set-up testing torsion characteristic of LPFGs is shown in Fig.1[3]. L and L' are the length of the twisted LPFG and the twisted fiber, respectively. One end of the fiber with a LPFG in the middle was fixed and the other end was glued on the axis of the disk. A 5g mass was attached to the fiber in order to keep the LPFG straight. The twist-rate of the LPFG can be shown as

$$\tau = \frac{\pi\beta}{180L'} \quad (1)$$

where β is the turning angle of the disk. The tested LPFG was written in Corning SMF-28 fiber by the high-frequency CO₂-laser pulses exposure technique reported by authors previously [4]. The LPFG's resonant wavelength and loss peak amplitude are 1541.8nm and 22.565dB, respectively. The length of the twisted fiber including LPFG is $L' = 625\text{mm}$, which is much longer than the twisted LPFG of $L = 27\text{mm}$, i.e. $L' \gg L$. Firstly, the disk was turned anticlockwise by a total angle of -1620° , i.e. an anticlockwise twist-rate of $-45.2\text{rad} \cdot \text{m}^{-1}$. That is, the anticlockwise twist-rate increased gradually. Secondly, the twisted LPFG was loosened gradually to be free. That is, the anticlockwise twist-rate decreased gradually. Thirdly, the disk was turned clockwise by a total angle of 2000° , i.e. a clockwise twist-rate of $55.9\text{rad} \cdot \text{m}^{-1}$. That is, the absolute value of the clockwise twist-rate increased gradually.

The changes of the resonant wavelength and loss peak amplitude of the LPFG with the twist-rate applied are shown in Fig. 2. The resonant wavelength shifted wavelike toward the longer and shorter wavelength as the LPFG was twisted clockwise and anticlockwise, respectively, and the loss peak amplitude decreased wavelike with the twist-rate applied. The repeatability of the wavelength and amplitude change was observed during the twist-rate increasing and decreasing. As shown in Fig. 2, the periodic wave of the resonant wavelength and amplitude appeared once whenever the disk was turned by an angle of 360° ($\sim 10\text{rad} \cdot \text{m}^{-1}$). Therefore, it seems as if the resonant wavelength change is composed of one periodic function with a period of 360° and another linear function with a slope of $\sim 0.024\text{nm}/(\text{rad} \cdot \text{m}^{-1})$. And, the loss peak amplitude change seems to be composed of one period function and another function, too.

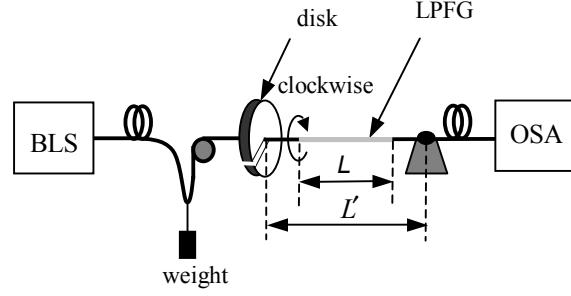


Fig.1 Experimental set-up for testing torsion characteristics of LPFGs, BLS: broadband light source, OSA: optical spectrum analyzer

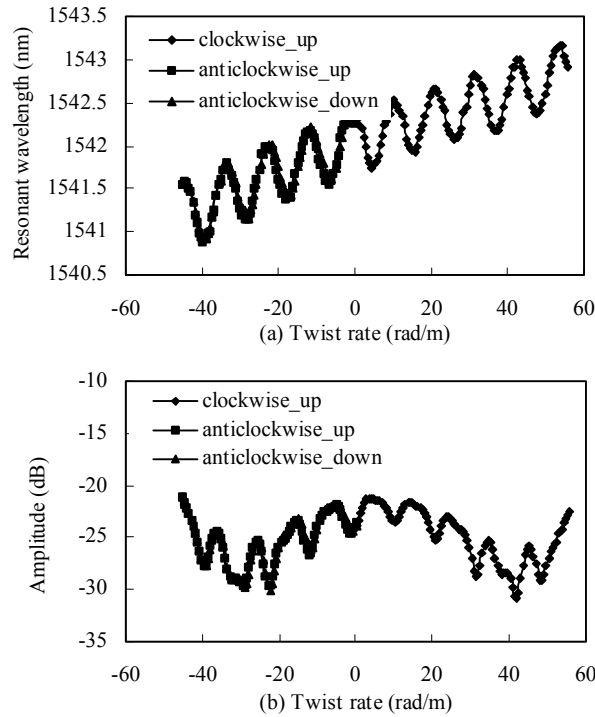


Fig. 2 Torsion characteristic of LPFG in the case of $L' \gg L$, (a) resonant wavelength, (b) loss peak amplitude; '◆' shows the clockwise twist-rate increasing; '■' and '▲' show the absolute value of the anticlockwise twist-rate increasing and decreasing, respectively

3. Discussion and analysis:

When a LPFG is written in the fiber using high-frequency CO₂-laser pulses, the single side incident CO₂-laser results in an asymmetric refractive index profile within the cross-section of the LPFG [3-5]. Therefore, the linear birefringence exists in the LPFG induced by high-frequency CO₂-laser pulses. The elliptical birefringence results from twisting the LPFG with linear birefringence [3, 6]. Whereas, the circular birefringence results from twisting the fiber without linear birefringence [6]. The twist direction dependence of the torsion characteristics of the CO₂-laser induced LPFG has been analyzed using the twist-induced elliptical birefringence in Ref. [3]. By comparing fig. 2 in this paper with fig. 2 and fig. 3 in Ref. [3], it is known that, in the case of $L' \gg L$, the torsion characteristics of the LPFG owe to the twist effect in the both LPFG and fiber. That is, the trends of the resonant wavelength linear shift and the amplitude change result from the twist of the LPFG, and the periodic waves of the resonant wavelength and amplitude result from the twist of the fiber. The twist-fiber-induced circular birefringence repeats once whenever the

end of fiber is turned by an angle of 360° , which results in the resonant wavelength and amplitude changing a period. Therefore, in the case of $L' \gg L$, the twist-induced circular birefringence in the fiber cause the periodic wave of the resonant wavelength and amplitude.

When the fiber is strongly twisted, which is the usual case for the twist experiment on LPFGs, the change of the state of polarization of the input light can be shown as $\Delta C = g\tau L'$ on the Poincare sphere [6], where g is the photoelastic coefficient, L' is the length of the twisted fiber. Thus, the effect, resulting from the twist-fiber-induced circular birefringence, on the torsion characteristics of the LPFG is proportional to the length of the twisted fiber. Therefore, only if the twisted fiber is much longer than the twisted LPFG, i.e. $L' \gg L$, the twist-fiber-induced effect on the torsion characteristics of the LPFG, i.e. the periodic wave of the resonant wavelength and amplitude, can be observed. In contrast, the effect can not be observed in the case of $L' \cong L$, which reasons is that the twist-fiber-induced effect is submerged in the twist-LPFG-induced effect.

4. Conclusions:

The torsion characteristics of the CO₂-laser induced LPFG are dependent on the length of the twisted fiber. In the case of $L' \gg L$, the resonant wavelength of the CO₂-laser induced LPFG shifts wavelike toward the longer and shorter wavelength as the LPFG is twisted clockwise and anticlockwise, respectively, and its loss peak amplitude decreases wavelike with the twist-rate applied. The twist-induced elliptical birefringence in the LPFG causes that the resonant wavelength shift of the LPFG is dependent on the twist-directions. And the twist-induced circular birefringence in the fiber causes that the resonant wavelength and amplitude of the LPFG change wavelike. Furthermore, the effect, resulting from the twist-fiber-induced circular birefringence, on the torsion characteristics of the LPFG is proportional to the length of the twisted fiber. These unique torsion characteristics could find important applications in the field of optical fiber communication and sensor.

5. Acknowledge:

This works was done in Chongqing University and supported by both the National Natural Science Foundation of China under the Outstanding Young Scientist Program (No. 60025515) and the China Postdoctoral Science Foundation (No. 2003034258).

References

- [1] Lin C. Y. and Wang L. A.: 'Loss-tunable long period fibre grating made from etched corrugation structure', Electronics Lett., 1999, **35**(21): 1872-1873
- [2] Soohye I., Chul C., and Hojoon L., The resonance wavelength-tuning characteristic of arc-induced by diameter modulation. 15th Optical Fiber Sensors Conference, Portland U.S.A., 2002, TuP2, 131-134
- [3] Wang Y. P., and Rao Y. J., Long period fibre grating torsion sensor measuring twist rate and determining twist direction simultaneously, Electronics Lett., 2004, **40**(3), 164-166
- [4] Rao Y. J., Wang Y. P., Ran Z. L., Zhu T., Novel fiber-optic sensors based on long-period fiber gratings written by high-frequency CO₂ laser pulses. J. of Lightwave Technology, 2003, **21**(5): 1320-1327
- [5] VanWiggeren G. D., Gaylord T. K., Davis D. D., Anemogiannis E., Garrett B. D., Braiwich M. I. and Glytsis E. N., Axial rotation dependence of resonances in curved CO₂-laser-induced long-period fibre gratings. Electronics Lett., 2000, **36**(16): 1354-1355
- [6] Ulrich R. and Simon A., Polarization optics of twisted single-mode fibers. Applied Optics, 1979, **18**(13): 2241-2251

AUTHOR INDEX



Abbott, J.S.	175	Guo, L.Q.	167
Allen, C.	91	Habel, W.	179
Araki, N.	69	Hall, T.J.	115
Arrowsmith, P.	153	Hallam, A.G.	73
Audet, F.	103	Hansen, K.P.	119
		Hansen, T.P.	119
Barber, Z.	1	Haywood, J.H.	127
Bartels, A.	1	Hernanz, M.L.	7, 37, 107, 149
Bassett, I.M.	127	Hiskett, P.	159
Baxter, G.	55	Hollberg, L.	1
Boisrobert, C.	191	Hong, J.-X.	59
		Hoyt, C.	1
Cao, J.-R.	41	Hughes, R.J.	159
Capmany, J.	131	Humphreys, D.A.	171
Carrasco-Sanz, A.	7, 37, 107, 149	Huntington, S.T.	55
Carter, G.M.	95		
Casari, P.	191	Ives, D.	111
Channon, N.D.	73	Izumita, H.	69
Chapeleau, X.	191		
Chapuran, T.E.	159	Jackel, J.	159
Chen, J.-P.	59, 199	Jakobsen, C.	119
Choi, S.-J.	41	Jørgenson, C.G.	11
Connelly, M.J.	167		
Connibear, A.B.	103	Kemp, N.J.	137
Corredera, P.	7, 37, 107, 149	Kim, R.K.	29
Culshaw, B.	179	Kim, S.K.	29
Cyr, N.	85	Kim, W.J.	41
		Kondamuri, P.K.	91
Dapkus, P.D.	41	Koshikiya, Y.	69
Davé, D.P.	137	Kuang, W.	41
Desfonds, É.	115		
Diddams, S.	1, 11	Lebon, J.	191
Dorrer, C.	63	Leduc, D.	191
Dyer, S.D.	195	Legré, M.	47, 119, 123
		Leitch, A.W.R.	103
Espejo, R.J.	195	Li, X.-W.	59
		Lopez, F.	191
Feder, K.	11	Lupi, C.	191
Fleming, S.	51	Lyytikainen, K.	51
Garren, J.	153	Marin-Naranjo, L.D.	99
Gignac, D.	153	Marks, B.S.	95
Gilbert, S.L.	15	Martín-López, S.	7, 37, 107, 149
Gisin, N.	47, 119, 123	Matar, M.	127
González- Herráez, M.	7, 37, 107, 149	McCabe, K.	159
Goodman, M.S.	159	McNown, S.	159
Gordon, B.	127		

Méndez, J.A.	107	van Eijkelenborg, M.A.	51
Menyuk, C.R.	95	Vayshenker, I.	145
Michie, A.	127	Visser, F.J.	103
Mies, E.	153		
Milner, T.E.	137	Wang, Y.P.	59, 199
Moon, H.S.	29	Washburn, B.R.	11
Morel, J.	81	Watanabe, T.	153
Murdoch, S.G.	77	Wegmuller, M.	47, 119, 123
		Wei , Z.-J.	41
Nakamura, M.	69	Wesson, L.	153
Namihira, Y.	33	Westbrook, P.S.	11
Newbury, N.R.	11	Wilpers, G.	1
Nicholson, J.W.	11		
Nordholt, J.E.	159	Xu, H.	95
O'Brien, J.	41	Yan, L.	95
Oates, C.W.	1	Yang, S.	145
Ortega, B.	131	Ye, A.-L.	59
Pastor, D.	131	Zeng, K.-C.	19
Pelayo, J.	107	Zhang, X.-H.	59
Peterson, C.G.	159	Zhao, Y.C.	51
Pimenov, K.	115	Zhou, J.-H.	59
Pradhan, S.	153	Zweck , J	95
Quiquempois, Y.	191		
Rao, Y.-J.	199		
Richards, D.L.	91		
Roberts, A.	55		
Ruffin, A.B.	23		
Runser, R.J.	159		
Rylander, C.G.	137		
Sales, S.	131		
Salmi, R.	103		
Seo, J.-C.	29		
Shih, M.-H.	41		
Sidiroglou, F.	55		
Stapleton, A.	41		
Stern, R.	55		
Suurmann, R.	153		
Svalgaard, M.	195		
Svendsen, D.A.	77		
Swafford, R.	145		
Swann, W.C.	15		
Taylor, M.G.	163		
Toliver, P.	159		
Tyagi, K.	159		

APPENDIX I - PROGRAM



Tuesday, September 28, 2004

9:00 **Opening Remarks:** G.W. Day, National Institute of Standards and Technology, Symposium General Chair, P.A. Williams, National Institute of Standards and Technology, Symposium Program Chair

Session I. Wavelength Metrology, Chair: Sarah Gilbert, National Institute of Standards and Technology

- 9:15 **INVITED:** The Era of Coherent Optical Frequency References, L. Hollberg, C.W. Oates, S. Diddams, G. Wilpers, A. Bartels, C. Hoyt, Z. Barber, *National Institute of Standards and Technology*
- 9:45 Generation of Standard Frequency References over the C and L Bands Using an Acetylene Cell and Four-Wave Mixing Enhanced by Raman Amplification, A. Carrasco-Sanz, S. Martín-López, M. González-Herráez, P. Corredera, M.L. Hernanz, *Instituto de Física Aplicada (CSIC)*
- 10:00 Infrared Frequency Comb for Frequency Metrology Based on a Tunable Repetition Rate Fiber Laser, B.R. Washburn, S.A. Diddams, N.R. Newbury, *National Institute of Standards and Technology*; J.W. Nicholson, K. Feder, P.S. Westbrook, *OFS Laboratories*; C.G. Jørgenson, *OFS Fitel*
- 10:15 Accuracy Limits for Simple Molecular Absorption Based Wavelength References, W.C. Swann, S.L. Gilbert, *National Institute of Standards and Technology*
- 10:30 Fast-Fourier-Transformation De-convolutions for a Fabry-Perot Filter Based OSA: Demonstration of 15.0 dB Increase of Optical-Rejection-Ratio at ± 25.0 GHz from Peak, K.-C. Zeng, *Sunrise Telecom, Inc.*
- 10:45 **BREAK**

Session II. Nonlinear Measurements, Chair: Mark Wegmuller, University of Geneva

- 11:15 **INVITED:** Stimulated Brillouin Scattering: An Overview of Measurements, System Impairments, and Applications, A.B. Ruffin, *Corning, Inc.*
- 11:45 Coherence Effect on the Measurement of Optical Fiber Nonlinear Coefficient in Continuous-Wave Dual Frequency Method, S.K. Kim, H.S. Moon, R.K. Kim, J.-C. Seo, *Center for Information and Telecommunication Standards Korea Research Institute of Standards and Science*
- 12:00 ITU-T Round Robin Measurement for Nonlinear Coefficient (n_2/A_{eff}) of Various Single Mode Optical Fibers, Y. Namihira, *University of the Ryukyus*
- 12:15 Broadband Continuous-Wave Source Based on Fiber Nonlinearity, M. González-Herráez, S. Martín-López, P. Corredera, M.L. Hernanz, A. Carrasco, *Instituto de Física Aplicada (CSIC)*
- 12:30 **LUNCH**

Session III. Fiber Characterization, Chair: Timothy Drapela, National Institute of Standards and Technology

- 2:00 **INVITED:** Characterization of Photonic Crystal Structures, J. O'Brien, J.-R. Cao, A. Stapleton, M.-H. Shih, W. Kuang, W.J. Kim, Z.-J. Wei, S.-J. Choi, P.D. Dapkus, *Department of Electrical Engineering, University of Southern California*
- 2:30 Ultrasensitive Measurement Method for Refractive Index Difference between Two Wavelengths, M. Légré, M. Wegmuller, N. Gisin, *GAP-Optique, University of Geneva*
- 2:45 Tomographic Reconstruction for Arbitrary Refractive Index Distribution of Optical Fibre Preforms, Y.C. Zhao, S. Fleming, K. Lyytikainen, M.A. van Eijkelenborg, *Australian Photonics CRC, Optical Fibre Technology Centre, University of Sydney*

- 3:00 Micro-Analytical Techniques for Imaging Erbium Doped Optical Fibers, F. Sidirolou¹, S.T. Huntington¹, R. Stern², G. Baxter³, A. Roberts¹, ¹*School of Physics, University of Melbourne*; ²*School of Communications and Informatics, Victoria University*; ³*Centre for Microscopy and Microanalysis, University of Western Australia*
- 3:15 Measuring Electro-Optic Coefficients of Poled Polymers Using Fiber-Optic Mach-Zehnder Interferometer, Y.-P. Wang, J.-P. Chen, X.-W. Li, J.-X. Hong, X.-H. Zhang, J.-H. Zhou, A.-L. Ye, *State Key Laboratory on Local Fiber-Optic Communication Networks and Advanced Optical Communication Systems, Shanghai Jiao Tong University*
- 3:30 **BREAK**

Session IV. OTDR and Chromatic Dispersion, Chair: Casey Shaar, Photon Kinetics

- 4:00 **INVITED:** Concepts and Techniques for Short Optical Pulse Characterization, C. Dorrer, *Bell Laboratories-Lucent Technologies*
- 4:30 High Spatial Resolution PON Measurement Using an OTDR Enhanced with a Dead-Zone-Free Signal Analysis Method, N. Araki, H. Izumita, Y. Koshikiya, M. Nakamura, *NTT Access Network Services Systems Laboratories, NTT Corporation*
- 4:45 A Bi-Directional Optical Time Domain Reflectometry Technique Optimised for Short LAN Fibers, N.D. Channon, *Megger Limited*; A.G. Hallam, *Halcyon Optical Services*
- 5:00 An Improved Method for the Distributed Measurement of the Chromatic Dispersion of an Optical Fiber Using a Wavelength Tunable OTDR, S.G. Murdoch, *Department of Physics, University of Auckland*; D.A. Svendsen, *Photon Kinetics (UK), Ltd.*
- 5:15 Inter-Comparison of Chromatic Dispersion Reference Fibre Measurements: Results of Euromet Project 666, J. Morel, *Swiss Federal Office of Metrology and Accreditation (metas)*
- 5:30 **SESSION CLOSE**
- 6:30 **RECEPTION, MILLENNIUM HARVEST HOUSE**



Wednesday, September 29, 2004

Session V. PMD, Chair: Greg Schinn, EXFO

- 9:00 **INVITED:** Generalized Interferometric Method for Accurate Match with DGD Measurements and Comparison against Standard References, N. Cyr, *EXFO Electrical Optical Engineering*
- 9:30 Study of Variation of the Laplacian Parameter of DGD Time Derivative with Fiber Length Using Measured DGD Data, P.K. Kondamuri, C. Allen, *Lightwave Communications Systems Laboratory, Information and Telecommunications Technology Center (ITTC), University of Kansas*; D.L. Richards, *Sprint Corporation*
- 9:45 The Long-Term Distribution of Differential Group Delay in a Recirculating Loop, H. Xu¹, B.S. Marks^{1,2}, J. Zweck³, L. Yan¹, C.R. Menyuk¹, G.M. Carter^{1,2}, ¹*Department of Computer Science and Electrical Engineering, University of Maryland Baltimore County*; ²*Laboratory for Physical Sciences*; ³*Department of Mathematics and Statistics, University of Maryland, Baltimore County*
- 10:00 Experience in Reflectometry and PMD Measurements for WAN in Costa Rica, L.D. Marin-Naranjo, *University of Costa Rica, Photonics and Laser Laboratory LAFTLA, Electrical Engineering School, Engineering Department*
- 10:15 Locating High PMD Sections of an Overhead Cable Using Polarization-OTDR, A.B. Connibear¹, F.J. Visser², F. Audet³, R. Salmi³, A.W.R. Leitch¹, ¹*University of Port Elizabeth*; ²*Telkom S.A.*; ³*EXFO*
- 10:30 **BREAK**

Session VI. PMD and Polarization, Chair: Tom Hanson, Corning, Inc.

- 11:00 Effects of Polarization-Mode Dispersion on Four-Wave Mixing Efficiency, M. González-Herráez, J. Pelayo, P. Corredera, M.L. Hernanz, J.A. Méndez, S. Martín-Lopez, A. Carrasco, *Instituto de Física Aplicada (CSIC)*

- 11:15 Calibration of a Polarisation Rotator, to Launch Defined Polarisation States, D. Ives, *National Physical Laboratory*
- 11:30 Extraction of Orthogonal Incident State of Polarization Spectra Using Mueller Matrix Approach, É. Desfonds, K. Pimenov, *MetroPhotonics, Inc*; T.J. Hall, *University of Ottawa*
- 11:45 Detailed Polarization Properties Comparison for Three Completely Different Species of Highly Birefringent Fibers, M. Wegmuller, M. Legré, N. Gisin, *GAP-Optique, University of Geneva*, K.P. Hansen, T.P. Hansen, C. Jakobsen, *Crystal Fibre A/S*
- 12:00 Determination of the Phase and Group Birefringence of Single-Mode Optical Fibers Based on the Twist, M. Legré, M. Wegmuller, N. Gisin, *GAP-Optique, University of Geneva*
- 12:15 An Improved Lyot Fibre Depolariser, M. Matar¹, I.M. Bassett¹, B. Gordon², J.H. Haywood¹, A. Michie¹, ¹*Australian Photonics CRC, Optical Fibre Technology Centre*; ²*Cochlear, Ltd*
- 12:30 LUNCH**

Session VII. Optoelectronics Applications, Chair: Janet Jackel, Telcordia

- 2:00 **INVITED:** Measurement Issues in Microwave Photonics, J. Capmany, D. Pastor, B. Ortega, S. Sales, *Optical Communications Group, IMCO2 Research Institute Universidad Politécnica de Valencia*
- 2:30 **INVITED** Applications of Metrology for Optical Coherence Tomography, T.E. Milner, N.J. Kemp, C.G. Rylander, D.P. Davé, *Department of Biomedical Engineering, The University of Texas at Austin*

Session VIII. Fiber Optic Power and Loss, Chair: Janet Jackel, Telcordia

- 3:00 High-Power Nonlinearity of Optical Fiber Power Meters, I. Vayshenker¹, R. Swafford², S. Yang¹, ¹*National Institute of Standards and Technology*; ²*OZ Optics, Ltd.*
- 3:15 Characterization of a High Power and High Accuracy Integrating Sphere Radiometer for Fiber Applications, P. Corredera, M.L. Hernanz, M. González-Herráez, S. Martín-López, A. Carrasco-Sanz, *Instituto de Física Aplicada (CSIC)*
- 3:30 Insertion Loss Measurement of Low Loss Fiber Optic Splices, L. Wesson, *Aurora*; P. Arrowsmith, R. Suurmann, *Celestica*; D. Gignac, *Nortel Networks*; S. Pradhan, *Sanmina-SCI*; J. Garren, *Soletron*; T. Watanabe, *Sumitomo Electric*; E. Mies, *Vytran*
- 3:45 **BREAK**
- 4:15 **SOFM Workshop – Fiber to the Masses: Metrology and Motivation for the “Last Mile”**
 Overview of Active Network Solutions - Mathieu Tallegas, Director of Product Management, *World Wide Packets*
 Overview of Passive Optical Networks – David Cleary, Vice President of Advanced Technology, *Optical Solutions, Inc.*
 Unique Metrology Issues in the Last Mile – Marc Breton, Chief Metrologist, *EXFO*
- 5:45 **SESSION CLOSE**



Thursday, September 30, 2004

Session IX. Network Measurements, Chair: William Reed, OFS

- 9:00 **INVITED:** Quantum Cryptography in Optical Networks and Supporting Metrology, R.J. Runser¹, P. Toliver¹, S. McNown², T.E. Chapuran¹, M.S. Goodman¹, J. Jackel¹, R.J. Hughes³, J.E. Nordholt³, C.G. Peterson³, K. Tyagi³, P. Hiskett³, K. McCabe³, ¹*Telcordia Technologies*; ²*Laboratory for Telecommunication Science*; ³*Los Alamos National Laboratory*
- 9:30 Measurement of Phase Diagrams of Optical Communication Signals Using Sampled Coherent Detection, M.G. Taylor, *Optical Networks Group, Department of Electronic and Electrical Engineering, University College London*

- 9:45 Demonstration of Birefringence in a Bulk Semiconductor Optical Amplifier and Its Application to All-Optical Wavelength Conversion, L.Q. Guo, M.J. Connelly, *Optical Communications Research Group, Department of Electronic and Computer Engineering, University of Limerick*
- 10:00 Effects of Optical Coherence and Polarization in Optical ANA, D.A. Humphreys, *National Physical Laboratory*
- 10:15 Characterization of Multimode Fiber for 10+ Gb/s Operation by Predicting ISI from Bandwidth Measurement Data, J.S. Abbott, *Corning, Inc.*
- 10:30 **BREAK**

Session X. Fiber Bragg Gratings and Fiber Sensors, Chair: Gordon Day, National Institute of Standards and Technology

- 11:00 **INVITED:** Fibre Sensing: Specifying Components and Systems, B. Culshaw, *University of Strathclyde, Electronic and Electrical Engineering*; W. Habel, *Federal Institute for Materials Research and Testing (BAM)*
- 11:30 Accurate Index Profile Measurements for Fiber Bragg Gratings and Sensor Application, X. Chapeleau¹, D. Leduc¹, P. Casari², Y. Quiquempois³, J. Lebon², F. Lopez³, C. Lupi¹, C. Boisrobert¹, ¹*Institut de Recherche en Electronique de Nantes-Atlantique (IREENA), Université de Nantes*; ²*Institut de Recherche en Génie Civil et Mécanique (GéM)*; ³*Laboratoire de Physique des Lasers, Atomes et Molécules, Université des Sciences et Technologies de Lille*
- 11:45 Analysis of a Fiber Bragg Grating Writing Process Using Low-Coherence Interferometry and Layer-Peeling, R.J. Espejo, M. Svalgaard, S.D. Dyer, *National Institute of Standards and Technology*
- 12:00 CO₂-Laser Induced LPFG's Torsion Characteristics Depending on the Length of the Twisted Fiber, Y.P. Wang, J.-P. Chen, *State Key Laboratory on Local Fiber-Optic Communication Networks and Advanced Optical Communication Systems*; Y.-J. Rao, *Department of Optoelectronic Engineering, Chongqing University*
- 5:45 **SYMPOSIUM CLOSE**



SYMPOSIUM COMMITTEE

G.W. Day, NIST, General Chair
P.A. Williams, NIST, Program Chair

M. Artiglia, *Pirelli*
A. Barlow, *PerkinElmer*
T.J. Drapela, *NIST*
S.C. Fleming, *Sydney University*
D. Franzen, *NIST*
N. Gisin, *University of Geneva*
M. Hackert, *U.S. Navy*
T.A. Hanson, *Corning*

D. Humphreys, *NPL*
J. Jackel, *Telcordia*
J. Jones, *Heriot-Watt University*
W. Reed, *OFS*
K.B. Rochford, *NIST*
G. W. Schinn, *EXFO*
C. Shaar, *Photon Kinetics*
K. Takada, *Gunma University*

NIST Technical Publications

Periodical

Journal of Research of the National Institute of Standards and Technology—Reports NIST research and development in metrology and related fields of physical science, engineering, applied mathematics, statistics, biotechnology, and information technology. Papers cover a broad range of subjects, with major emphasis on measurement methodology and the basic technology underlying standardization. Also included from time to time are survey articles on topics closely related to the Institute's technical and scientific programs. Issued six times a year.

Nonperiodicals

Monographs—Major contributions to the technical literature on various subjects related to the Institute's scientific and technical activities.

Handbooks—Recommended codes of engineering and industrial practice (including safety codes) developed in cooperation with interested industries, professional organizations, and regulatory bodies.

Special Publications—Include proceedings of conferences sponsored by NIST, NIST annual reports, and other special publications appropriate to this grouping such as wall charts, pocket cards, and bibliographies.

National Standard Reference Data Series—Provides quantitative data on the physical and chemical properties of materials, compiled from the world's literature and critically evaluated. Developed under a worldwide program coordinated by NIST under the authority of the National Standard Data Act (Public Law 90-396). NOTE: The Journal of Physical and Chemical Reference Data (JPCRD) is published bimonthly for NIST by the American Institute of Physics (AIP). Subscription orders and renewals are available from AIP, P.O. Box 503284, St. Louis, MO 63150-3284.

Building Science Series—Disseminates technical information developed at the Institute on building materials, components, systems, and whole structures. The series presents research results, test methods, and performance criteria related to the structural and environmental functions and the durability and safety characteristics of building elements and systems.

Technical Notes—Studies or reports which are complete in themselves but restrictive in their treatment of a subject. Analogous to monographs but not so comprehensive in scope or definitive in treatment of the subject area. Often serve as a vehicle for final reports of work performed at NIST under the sponsorship of other government agencies.

Voluntary Product Standards—Developed under procedures published by the Department of Commerce in Part 10, Title 15, of the Code of Federal Regulations. The standards establish nationally recognized requirements for products, and provide all concerned interests with a basis for common understanding of the characteristics of the products. NIST administers this program in support of the efforts of private-sector standardizing organizations.

Order the following NIST publications—FIPS and NISTIRs—from the National Technical Information Service, Springfield, VA 22161.

Federal Information Processing Standards Publications (FIPS PUB)—Publications in this series collectively constitute the Federal Information Processing Standards Register. The Register serves as the official source of information in the Federal Government regarding standards issued by NIST pursuant to the Federal Property and Administrative Services Act of 1949 as amended, Public Law 89-306 (79 Stat. 1127), and as implemented by Executive Order 11717 (38 FR 12315, dated May 11, 1973) and Part 6 of Title 15 CFR (Code of Federal Regulations).

NIST Interagency or Internal Reports (NISTIR)—The series includes interim or final reports on work performed by NIST for outside sponsors (both government and nongovernment). In general, initial distribution is handled by the sponsor; public distribution is handled by sales through the National Technical Information Service, Springfield, VA 22161, in hard copy, electronic media, or microfiche form. NISTIR's may also report results of NIST projects of transitory or limited interest, including those that will be published subsequently in more comprehensive form.

U.S. Department of Commerce
National Bureau of Standards and Technology
325 Broadway
Boulder, CO 80305-3328

Official Business
Penalty for Private Use \$300